Universitat Autònoma de Barcelona

PHYSICO-CHEMICAL PROPERTIES OF CHONDRITIC METEORITES CLUES ON THE ORIGIN AND EVOLUTION OF THEIR PARENT BODIES

Carles Eduard Moyano Cambero

PHYSICO-CHEMICAL PROPERTIES OF CHONDRITIC METEORITES

CLUES ON THE ORIGIN AND EVOLUTION OF THEIR PARENT BODIES

Carles Eduard Moyano Cambero

Advisor: Dr. Josep Maria Trigo i Rodríguez

Institut de Ciències de l'Espai (IEEC/CSIC)

Tutor: Prof. Dr. David Jou i Mirabent

Universitat Autònoma de Barcelona (UAB)

Departament de Física

Universitat Autònoma de Barcelona

This doctoral thesis is submitted for the degree of

Doctor of Philosophy in Physics

Cerdanyola del Vallès, novembre 2017

Pleasure to me is wonder-the unexplored, the unexpected,

the thing that is hidden and the changeless thing that lurks behind superficial mutability.

Howard Phillips Lovecraft

ACKNOWLEDGEMENTS

First of all, I would like to thank my advisor, Josep M. Trigo Rodríguez, for the supervision of this thesis. Few people show more dedication and enthusiasm for this field as he does, and it's catchy! Also, he provided me many amazing opportunities to travel, participate in conferences, work with different teams… basically, to learn and grow as a person and scientist. Thanks to you, I discovered in the study of meteorites a very wide and complex world that turned out to be amazing. Gràcies!

I also want to thank the many coauthors of the papers and abstracts published during the gestation of this thesis. I would like to thank Antonella Barucci and Sonia Fornasier for welcoming me at the Observatoire de Paris, and for all they taught me. Also Albert Rimola, and his contribution to the interpretation of the IR spectra. I would like to thank F. Javier Martín Torres, for the few days we shared in Madrid, in which your enthusiasm gave me renewed strength. A special mention to M. Isabel Benito and Jacinto Alonso, whose knowledge about geology and mineralogy proved to be completely crucial to publish our paper on ALH 84001; it took a very long time, but thanks to you… ¡Lo conseguimos! I'm very thankful to Jordi Sort and Eva Pellicer for their dedication and help that resulted in which is probably the best paper I have published so far, moltes gràcies! I also want to thank Martin R. Lee, Iwan P. Williams, Jürgen Blum, Patrick Michel, Michael Küppers and Ivan Lloro for their invaluable contributions. Particularly important are the contributions of Jordi Llorca, Narcís Mestres and Jordi Fraxedas, who besides from contributing to the papers granted us access to some of the instrumental techniques described here. Oh, and Belén Ballesteros, Marcos Rosado and Alfredo Fernández, for the technical support with the SEM, EDS and EMP. I also need to mention the people from the Carnegie Institution of Washington, in particular Larry Nittler, Jemma Davidson, and Conel Alexander, for the time we spent together in D.C., which was amazing. Also the Rosetta-VIRTIS team for providing the Lutetia spectrum in digital form, the NASA Meteorite Working Group, and the Johnson Space Center, for providing the samples of Antarctic meteorites, and Professor Addi Bischoff, who kindly provided the Chelyabinsk thin section used in this thesis. Finally, I would like to thank Marina Martínez, coauthor and coworker: hem estat companys de moltes penúries, però també hem rigut amb el surrealisme de tot plegat. I qui m'ho havia de dir, al final seràs tu qui m'ensenyarà el camí. Sort, i ja ens veurem!

A mis padres. No estéis orgullosos de mí, pues todo lo que soy sale de vosotros y mis logros son vuestros logros. Nos habéis dado la vida, y todas las oportunidades que vosotros no tuvisteis. Habéis dado vuestra vida para que nosotros solo tuviéramos que escoger un camino y seguirlo, y eso ha hecho posible esta tesis. Por todo ello, y mucho más, os doy las gracias. A la yaya, por enseñarme a escuchar, a tener paciencia, y a respetar a todo el mundo. A mi hermano, porque todo lo que me ha fascinado en esta vida (¡O casi!), primero te fascinó a ti. Tú caminaste por las rutas peligrosas; yo solo tuve que fijarme en tus huellas. Y al resto de mi familia, en general, por ser tan diferentes y tener tantos puntos de vista, por todo lo que he aprendido de vosotros, por el caos que somos todos juntos (¡Aunque del caos sale el orden!)… y por muchas otras cosas ¡Gracias!

No em puc deixar tots els meus companys i companyes de batalletes a l'ICE. Des del cyber fins al flamant new building, hem viscut tantes i tantes coses plegats... La temperatura Sahariana al cyber, els coffees, seguir treballant quan sonen les alarmes d'incendi, l'epicness als Pirineus, Port aventura, la casa de l'Esquirol (i les golfes misterioses!), l'oasi del SAF, Montserrat, bodes, dinars, riures, bogeries, bikinis, cartells, ping-pongs, tontades vàries, reptes absurds, acudits massa frikis per ser tolerats... i sobretot, el que més ens ha ajudat a tots a complir amb la nostra tesi: el Lamatube; long live the Lama! M'agradaria mencionar-vos un/a per un/a, perquè hi ha tant a dir de cadascun de vosaltres! Heu fet d'aquests casi 5 anys una època molt memorable, i només espero que els nostres camins es tornin a trobar. Gràcies, gracias, thank you! De la mateixa manera, hauria de mencionar moltes altres persones que d'una manera o altra han fet que això hagi estat possible: als distingits membres del bus sharing i els seus horaris de servidor públic, que tan bé m'han vingut, les seves converses sobre paternitat, el cafè matiner, i, sobretot, les litrones! A tots els meus companys i companyes del cau, per tot el que he crescut amb ells/es i per ensenyar-me una manera diferent de viure la vida. Als meus amics, per acostumar-se a no veure'm el pel i esforçar-se en mantenir el contacte, malgrat tot... i tanta altra gent que m'oblido.

Y finalmente a Amaia, por las aventuras que hemos vivido, por la paciencia que has tenido, por quererme a pesar de mis silencios, por tu locura, que me recuerda que no estoy solo en este mundo, por cada día que hemos pasado juntos (los buenos y los malos), por lo mucho que me has enseñado sobre mí mismo, por ser mi cielo (¡Lleno de meteoritos!) y mi compañera de viaje… ¡Muchas, muchas gracias!

ABSTRACT

In the first million years of the solar nebula, specific conditions triggered, from aggregation and melting of dust and presolar grains, the formation of the first solid materials of the Solar System. Among them, a variety of igneous glassy spherules known as chondrules can be found. These materials progressively aggregated together with dust and interplanetary particles to form larger bodies, such as asteroids, planetesimals, and finally planets. From those, some experienced chemical segregation due to heating and melting of their materials. The bodies that did not melt, called undifferentiated, still conserve some of these very primordial materials of the Solar System. The meteorites coming from these objects, known as chondrites from the chondrules that they contain, are therefore samples of materials formed in the protoplanetary disk around the Sun about 4,600 million years ago.

This thesis studies chondrites with a multidisciplinary approach, starting with the exploration of several instrumental techniques applied to a Martian meteorite. Those techniques allow the study of several physico-chemical properties of chondrites, and therefore provide clues about the complex accretionary histories of their parent bodies. The specific mineralogy and features related to thermal metamorphism, aqueous alteration, and the effects of shock of two chondrites are described here in the context of their possible parent asteroids. Besides, spectroscopic techniques are applied as suitable method to link the meteorite samples to specific asteroids currently populating the Solar System.

Retrieving samples directly from asteroids is a very complex concept, and therefore terrestrial collections of meteorites become a very available source of samples. The information obtained from chondrites can be extrapolated to better understand the composition, structure, and physical properties of asteroids. Thus, the study of chondrites can facilitate the practical applications on asteroids, such as space mining or the concept explored in this thesis: the deflection through solid projectiles of asteroids that suppose a potential thread to life on Earth, one of the goals the ESA and NASA collaboration known as the AIDA mission. Most of these potentially dangerous objects are made of chondritic materials, and therefore the study of chondrites can provide valuable information about them, which is key in order to be prepared for the possible future catastrophic impact events.

RESUM

Durant els primers milions d'anys del Sistema Solar, condicions específiques van propiciar, començant per l'agregació i fusió de pols estel·lar i grans presolars, la formació dels primers materials sòlids del Sistema Solar. Entre ells s'hi pot trobar una varietat d'esferes ígnies anomenades còndrols. Aquests materials es van anar agregant amb pols i partícules interplanetàries per formar cossos més grans, com els asteroides, planetesimals, i finalment els planetes. Alguns d'aquests cossos van experimentar segregació química com a resultat de l'escalfament i la fusió dels seus materials. Els que no es van fondre, anomenats "no diferenciats", encara conserven alguns d'aquests materials primitius del Sistema Solar. Els meteorits que provenen d'aquests cossos, anomenats condrites a causa dels còndrols que contenen, són per tant mostres dels materials formats al Sistema Solar fa uns 4.600 milions d'anys.

Aquesta tesi estudia les condrites des d'una aproximació multidisciplinària, començant amb l'exploració de diverses tècniques instrumentals aplicades a un meteorit marcià. Aquestes permeten l'estudi de les propietats fisicoquímiques de les condrites, i per tant proporcionen pistes sobre les complexes històries d'agregació dels seus cossos progenitors. La mineralogia i característiques específiques relacionades amb el metamorfisme tèrmic, l'alteració aquosa, i els efectes de xoc de dues condrites, es descriuen aquí en el context dels seus possibles cossos progenitors. A banda, s'apliquen tècniques espectroscòpiques com un mètode adequat per vincular les mostres de meteorits a asteroides concrets que actualment poblen el Sistema Solar.

Recuperar mostres directament dels asteroides és un concepte molt complex, i per tant les col·leccions terrestres de meteorits esdevenen una font de mostres perfectament disponible. La informació obtinguda de les condrites pot ser extrapolada per entendre millor la composició, estructura i propietats físiques d'asteroides. Així, l'estudi de les condrites pot facilitar aplicacions pràctiques en asteroides, com la mineria espacial o el concepte que s'explora en aquesta tesi: el desviament mitjançant projectils sòlids d'asteroides que suposen una amenaça potencial a la vida a la Terra, un dels objectius de la col·laboració entra la ESA i la NASA coneguda com la missió AIDA. La majoria d'aquests objectes potencialment perillosos estan formats per materials condrítics, i per tant l'estudi de les condrites pot proporcionar informació valuosa sobre ells, el que resulta clau per tal d'estar preparats per futurs possibles impactes catastròfics.

CONTENTS

Although being a thesis in physics, this study uses terminology often referring to mineralogy and geochemistry. To facilitate the reading of those not familiar with these subjects, a glossary has been included in the annex. All the words highlighted in the thesis through the use of *italics* are explained there.

LIST OF TABLES

LIST OF FIGURES

1 INTRODUCTION

1.1 First solids formed in the Solar System

1.1.1 Early processes in the Solar System

It can be considered that the formation of our Solar System started around 4.6 Gyr ago, as this is the oldest age calculated so far for any material formed in it (Bouvier & Wadhwa, 2010). There are many theories to explain how the Solar System formed (for a review see, e.g., Woolfson, 2000). The one with highest acceptance, although it presents many difficulties not yet solved (Woolfson, 2000), is the solar nebular disk model (SNDM), which implies collapse of a region inside a molecular cloud to produce a *protostar* surrounded by a disk of gas and dust (Cameron, 1963; Cameron, 1993; Montmerle et al., 2006). This region, which maybe started collapsing by the effect of a shock wave introduced by a nearby supernova (Cameron & Truran, 1977; Williams, 2010), flattened into a protoplanetary disk due to gravity, gas pressure, magnetic fields and rotation (Lewis, 1995; Williams & Cieza, 2011), while forming a hot dense *protostar* at the center (Greaves, 2005). Within the next 50 million years, before the temperature and pressure in its core were high enough to start hydrogen fusion, the Sun could have become a *T Tauri star* (Caffee et al., 1987).

In this hot environment the first solid materials of the Solar System condensed, settle into the disk plane, and formed primordial aggregates exemplified by the porous Interplanetary Dust Particles (IDPs) that are still found nowadays (Figure 1.1). Those mixtures were posteriorly melted under the action of different heat sources, and later

solidified into the first surviving solar solids. Several studies have provided clues to evaluate when the formation of these primitive materials occurred. Radionuclide dating techniques, such as the U^{235}/Pb^{207} system, the Pb-Pb ages, and the Al chronometer, have been used to dating the formation of these materials (Macpherson & Russell, 1997; Amelin et al., 2002; Macpherson, 2003). According to the age calculated for a Ca and Al-rich *refractory* inclusion (CAI) found in the Northwest Africa (NWA) 2364 meteorite, that heating process took place at least ~4,568.2 Myr ago (Bouvier & Wadhwa, 2010), in a lapse of time shorter than 0.3 Myr, while the protosun was fastly accreting matter (Göpel et al., 1994; Allègre et al., 1995). CAIs, composed mainly by Ca-Al-Ti-rich *refractory silicates* and oxides, are therefore considered the oldest processed materials conserved from the beginnings of the Solar System. Other solid materials were melted from the gas phase to slide in the shape of nearly round submillimeter Mg-Fe *silicates*, called chondrules, which are one of the main components found within most primitive meteorites (Brearley & Jones, 1998; Jones et al., 2000). Radionuclide dating, together with the differing oxygen isotopic compositions between CAIs (^{16}O-rich) and chondrules (usually ^{16}O-poor), suggests that CAIs must have formed before chondrules, assuming that the nebula became progressively more ^{16}O-poor (Krot et al., 2005). Chondrule formation started 1 to 5 Myr after CAI formation, in a time when the protosun was accreting at a slower rate, and lasted for 1 to 3 Myr (Kita et al., 2005; Scott & Krot, 2005), although some chondrules could have formed later through impacts between planetary embryos (Rubin et al., 2003). In any case, the formation times inferred from radiogenic dating are consistent with the lifetimes of circumstellar disks (Reipurth, 2005).

Many hypotheses have been proposed to describe the heat source or sources that participated in the thermal processing of the first solids, but only few of them are currently considered (Rubin & Brearley, 1996; Rubin & Krot, 1996). The X-wind model, which in agreement with the SNDM suggests that the Sun was a *T Tauri star* at some point of its beginning (Figure 1.3), is usually taken as the preferred option to explain the thermal processing of the first solids formed in the Solar System (Reipurth, 1990; Shu et al., 1997; Reipurth, 2005). It considers that a flow of gas and dust accreting through the disk and into the star could have experienced Fu Orionis outbursts, called X-winds, that form when magnetic field lines of opposite polarities from the star and the disk contact, which truncates the accretion disk as the gas presses onto the magnetic field (Shu et al., 2001).

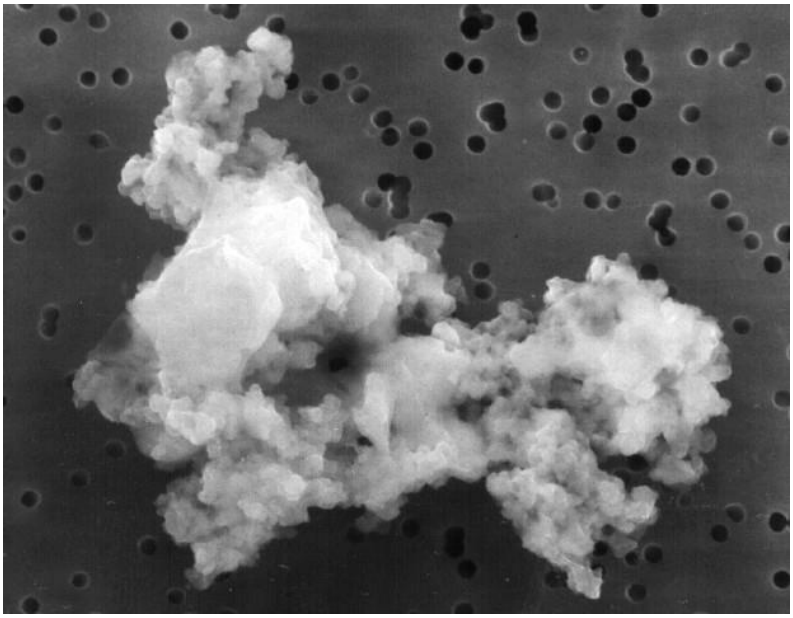

Figure 1.1: First solid condensates formed aggregates of micron to submicron-size minerals that, under the action of heat, were transformed into CAIs and chondrules. Some of those first solid aggregates survived in cometary bodies and today reach Earth's top of the atmosphere as IDP (credit: NASA/JPL).

The plasma confined in the large magnetic loop between the disk and the protosun produces, due to magnetic reconnection events, flares with the capacity of accelerating coronal ions and electrons to very high energies (Reames, 1995; Montmerle et al., 2006). By *bremsstrahlung effect*, those energetic electrons emit hard X-ray photons when they collide with ambient matter (Shu et al., 2001), generating the so called X-wind that pushes away the gas and drags the precursor materials due to a strong gas-grain coupling, deviating part of the accreting mass in an outflow (Shu et al., 1997; Shu et al., 2000; Montmerle et al., 2006). With gas and dust being pushed away, the precursor materials were not anymore protected by the disk from the direct solar radiation, and were rapidly heated (Jones et al., 2000).

A theoretical thermodynamically-based study found that the ambient nebular temperature at which CAIs formed should have been around 1400-1500 K, which vaporized the most *volatile* elements leaving CAIs and other *refractory* inclusions depleted in the moderately *volatile* elements that can be found in the bulk composition of chondrules (Wasson, 1985; Alexander et al., 2012). Indeed, the temperature for chondrule formation should have been below 970 K in order to preserve moderately

volatile elements such as Na and S, assuming that they survived from the precursor materials (see e.g. Wasson, 1985). With high temperatures lasting hour to days, the precursor materials would have melted and formed CAIs after cooling (Shu et al., 1997), but the *crystalline* and *amorphous silicates* precursors of chondrules would have evaporated, although their origin requires local high melting temperatures approaching 2200 K (Shu et al., 1997). Further theoretical studies suggest that to facilitate the retention of moderate *volatiles* and relict grains, the melting interval for chondrules should have been of less than a few minutes (Hewins & Connolly Jr., 1996; Connolly Jr. et al., 1998). This evidence suggests that chondrules and CAIs were melted due to fast heating events, such as solar flares.

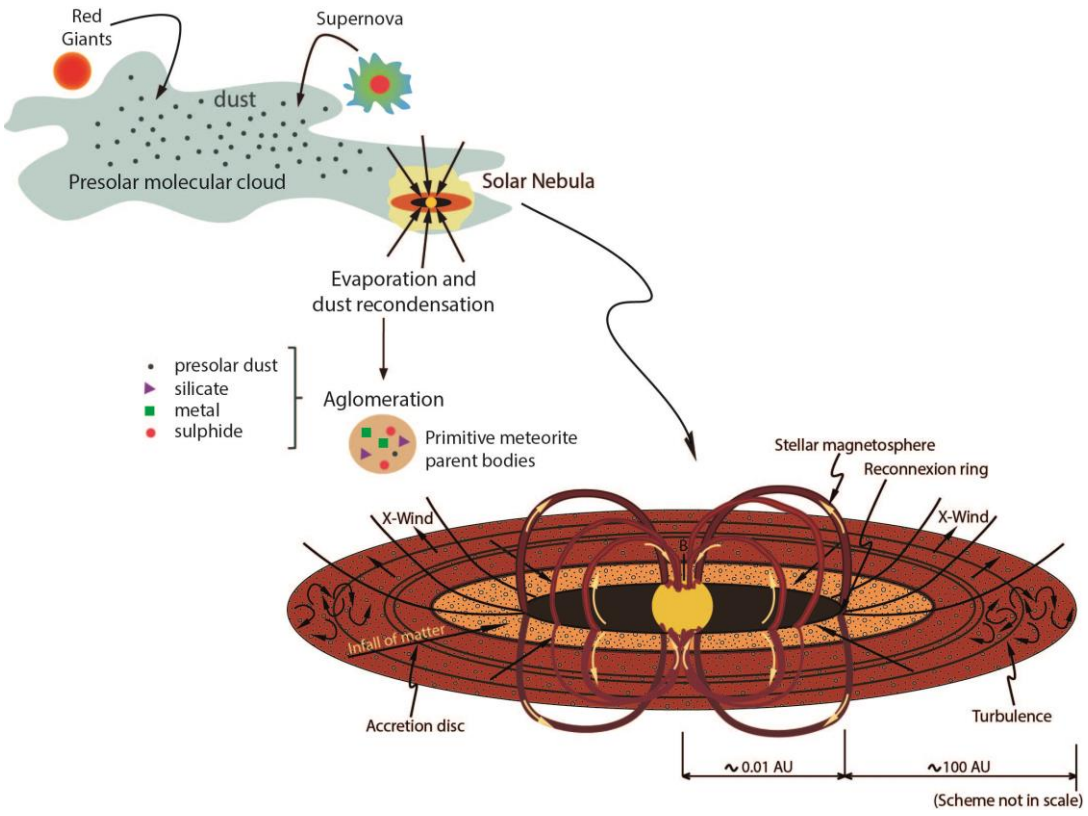

Figure 1.2: Scheme showing the model described here for the formation of the first solid materials in the Solar System in the primitive solar nebula (Martínez-Jiménez et al., 2017).

The cooling rates should also have been pretty fast in order to be in agreement with the textures and mineral bulk chemistry found for these chondritic components; around 50-1000 K/hr for chondrules and 2-50 K/hr in the case of CAIs, which implies cooling to solar nebula temperatures in hours or days (Hewins et al., 1997). These rates are lower

than expected for radiative heat loss to the ambient nebular gas, which implies the presence of a heat-buffering effect, like a high dust/gas ratio insolating the formation regions, or the presence of a hot compressed gas (see e.g. Sahagian and Hewins, 1992). After they cooled, some solidified particles were pushed farther by the X-wind, and while the smallest material remained coupled to the gas and were pushed to interstellar space, larger particles stayed close to the inner disk or were carried to the relatively cold interplanetary regions (Shu et al., 2000).

Posteriorly, chondrules and *refractory* inclusions reached different reservoirs, where they were compacted together with fine-grained dust available at the protoplanetary disk, including ancient interstellar grains, to become the precursors of larger bodies (Jones et al., 2000; Brownlee et al., 2006; Moyano-Cambero et al., 2016a). Actually, it seems that this materials could have reached distances far enough to even be included in the formation of comets (Ogliore et al., 2012). This combination of *igneous crystalline* components (CAIs and chondrules), metal and *chromite* grains, *sulfides*, and an *amorphous* fine-grained material (usually forming the *matrix*), is what we can find nowadays in chondrites (primitive undifferentiated meteorites, which will be described later). Therefore, the study of primitive meteorites allows access to these first solid materials, which provides an opportunity to date and better understand the first steps in the evolution of the early Solar System, and the formation of the first building blocks of planets.

1.1.2 Refractory inclusions

It is common, when speaking about CAIs, to just call them *refractory* inclusions. By *refractory* we mean that they are the first materials predicted to condense from a cooling gas of solar composition, and also among the last materials to evaporate during heating (Jones et al., 2000). However, there is another type of *refractory* inclusions in meteorites, called Amoeboid-*Olivine*-Aggregates (or AOA, composed of *forsterite* and Ca-Al-Ti mineral aggregates), and both are closely related, although CAIs formed at higher nebular temperatures (Connolly Jr., 2005; Scott & Krot, 2005). This type of inclusions seems to have formed simultaneously or slightly later than CAIs (Itoh et al., 2002).

There are several different types of CAIs: A (rich in *melilite*, divided in Fluffy Type A or FTA, and in Compact Type A or CTA), B (with abundant Ca-Ti-*pyroxene*, and

divided in B1, B2 and B3) and C (rich in *anorthite*), but there could be more (Macpherson et al., 1988). A type CAIs are fine-grained and irregular, while B and C, also called *igneous* CAIs, are coarse-grained and *crystal*lized from melts (Connolly Jr., 2005). The formation process for *igneous* CAIs should be related and consistent with the formation of chondrules under the X-wind model (Shu et al., 1997). Some CAIs contain minerals that are only stable above 1650 K, like *corundum*, *hibonite* and *perovskite*, but it is much more common to find CAIs containing *spinel*, *melilite*, C-Ti-*pyroxene* and *anorthite*, minerals stable at 1400-1500 K (Scott & Krot, 2005). By the other hand, AOAs contain *anorthite*, Ca-*pyroxen* and *spinel* surrounded by *forsterite*, minerals stable at 1350-1450 K (Krot et al., 2004).

AOAs and FTA CAIs are irregularly shaped and fine-grained, probably formed by condensation of minerals in the nebula (Scott & Krot, 2005). Some clues in FTA CAIs point indeed toward a condensation in the nebula, after loss of a very *refractory* element (Boynton, 1975). It seems also that they re*crystal*lized at high temperatures, since they are aggregates of intergrown *crystals* (Macpherson, 2003). AOAs probably formed in a region where the most *refractory* materials were not removed before, and show different textures, from porous aggregates to re*crystal*lized, coarser aggregates (Krot et al., 2004; Scott & Krot, 2005). *Igneous* CAIs (B and C type), by the other hand, show spheroidal shapes (Scott & Krot, 2005) and a highly *refractory* core surrounded by a moderately *refractory* mantle, which can be the result of both being melt and behaving like immiscible liquids during a flare, and after several liquifications and resolidifications (Shu et al., 2001). In fact, some CAIs seem to have been reheated 1-2 times after their formation, and during the formation of chondrules (Scott & Krot, 2005).

1.1.3 Chondrules

Chondrules probably were initially composed by aggregates of fine-grained dust of different composition, which mostly were molten in the X-wind scenario, except for some preserved relict grains (Jones et al., 2000; Moyano-Cambero et al., 2016a). Their formation conditions were more oxidizing than for CAIs, and also with a higher dust/gas ratio and lower in temperatures, which allowed liquids to be stable for a longer time (Scott & Krot, 2005). It has been suggested that there were several different chondrule reservoirs in the Solar System, with variations in composition and level of oxidation, as represented differences found between the chondrite meteorite groups (Grossman et al., 1988; Jones et al., 2000). In fact, despite many similarities, chondrules

from separated chondrite groups show different sizes, oxygen isotopic ratios, bulk compositions, and specific petrographic features (Figure 1.3), among other differences (Krot et al., 2005; Jones, 2012). The chondrules from each of these reservoirs must have similar overall properties, such as bulk or oxygen isotopic compositions, but simultaneously more than one chondrite group could have generated on some of these regions, showing smaller variations that allow us to classify chondrites in subgroups (Grossman et al., 1988). In order to avoid homogenization of the reservoirs by processes occurred in the protoplanetary disk, the parent bodies of chondrites should have accreted pretty fast after chondrule formation (Cuzzi et al., 2010).

The major minerals in chondrules are low-calcium *pyroxene* and *olivine*, and they also commonly contain *troilite* (FeS) and metallic NiFe (Scott & Krot, 2005). Chondrules can be divided as a function of their differences in composition. Most of them are ferromagnesian (i.e., dominated by Fe and Mg), showing variation in the Mg/(Mg+Fe) ratios (Grossman et al., 1988). Others are Al-rich, showing the gap of compositions between ferromagnesian chondrules and CAIs, and containing a higher amount of *feldspar* than other chondrules (Macpherson & Russell, 1997). The content in SiO can change the amount of specific *silicates* available, increasing the ratio between *pyroxene* and *olivine* with higher SiO (Jones et al., 2000). Also, they can be classified in FeO-poor reduced chondrules (called type I chondrules, with Mg/(Mg+Fe)>0.9 in *silicate* minerals, and containing metallic Fe) and FeO-rich oxidized chondrules (also called type II chondrules, with Mg/(Mg+Fe) ratios between 0.6 and 0.9, and containing minor metallic Fe), according to several studies (e.g., Grossman et al., 1988; Wasson, 1993). Both classes show evidence of some melting and evaporation, while type I also seem to have undergone condensation and accretion of solid and melted materials, and type II apparently formed in an environment with higher dust to gas ratios (Scott & Krot, 2005).

Consistently with the idea of being molten and then *crystal*lized, most chondrules (both type I and type II) show *igneous* textures, the presence of *glass*, and partially rounded outlines, indicating that they behaved at some point as melt droplets (Jones et al., 2000). The differences in texture allow us to separate chondrules in *porphyritic* and non-*porphyritic*. First ones usually are more irregular, as a consequence of the partial melting of fine-grained material, and they also had a slow enough cooling to allow the formation of *crystals* up to hundreds of μm in size (Grossman et al., 1988; Rubin,

2000). Non-*porphyritic* chondrules are more spherical, as they apparently were heated more extensively and cooled faster, melting sufficiently to allow surface tension to round their shape and providing them finer grain (Scott & Krot, 2005). Some chondrules underwent more complicated evolutions, including collisions between molten or at least hot solid grains, which allowed growth of particles from dust (Rubin, 2000). There were also collisions between chondrules, as can be seen in some examples of chondrules fused together, and of fragments of chondrules inside other chondrules (Wasson et al., 1995). High temperatures during the aggregation of these materials melted *silicates* enough to stick them together, and to weld their grains (Scott & Krot, 2005). In other occasions some thermal annealing took place instead of the complete melting of chondrules, which is often evidenced in *mafic* chondrules as a Fe-rich layer surrounding a more Mg-rich core.

Porphyritic type I chondrules can also be divided in type IA (*olivine* and Ca-rich) and type IB (*pyroxene* and *volatile*-rich), division that probably comes as a consequence of condensation in the nebula (Rubin, 2010). Actually, it seems that *olivine*-rich type I chondrules, also rich in *refractory* inclusions, formed first, and some of them evolved in the nebula under several effects into *pyroxene*-rich type I chondrules (Pack et al., 2004). Type II chondrules, by the other hand, only show a small variation in the amount of *volatiles*, which imply an important difference in the formation conditions (Scott & Krot, 2005). Some non-*porphyritic* chondrules have textures that suggest a formation by condensation of a melt (Krot et al., 2002). There is also a small fraction of chondrules that seem to have formed by selective impact melting on the surface of an asteroid (Rubin, 2003).

1.1.4 Further processing of refractory inclusions and chondrules

Both *refractory* inclusions and chondrules can show thin layers, or rims, around them (Boynton & Wark, 1985). If the precursor materials for CAI or chondrule formation were vaporized by an extended heating, the remaining atoms could have condensed as rims in the preexisting materials. After a first launching cycle of the X-wind, the initial *refractory* inclusions and chondrules fell back into the midplane, and could undergo the same process again, which could result in the formation of a thick layered mantle around them (Davis & MacPherson, 1996). Also, several flares may have reheated chondrules, implying some recycle of its material, which is consistent with several

evidences pointing toward multiple heating events in some chondrules (Rubin & Krot, 1996).

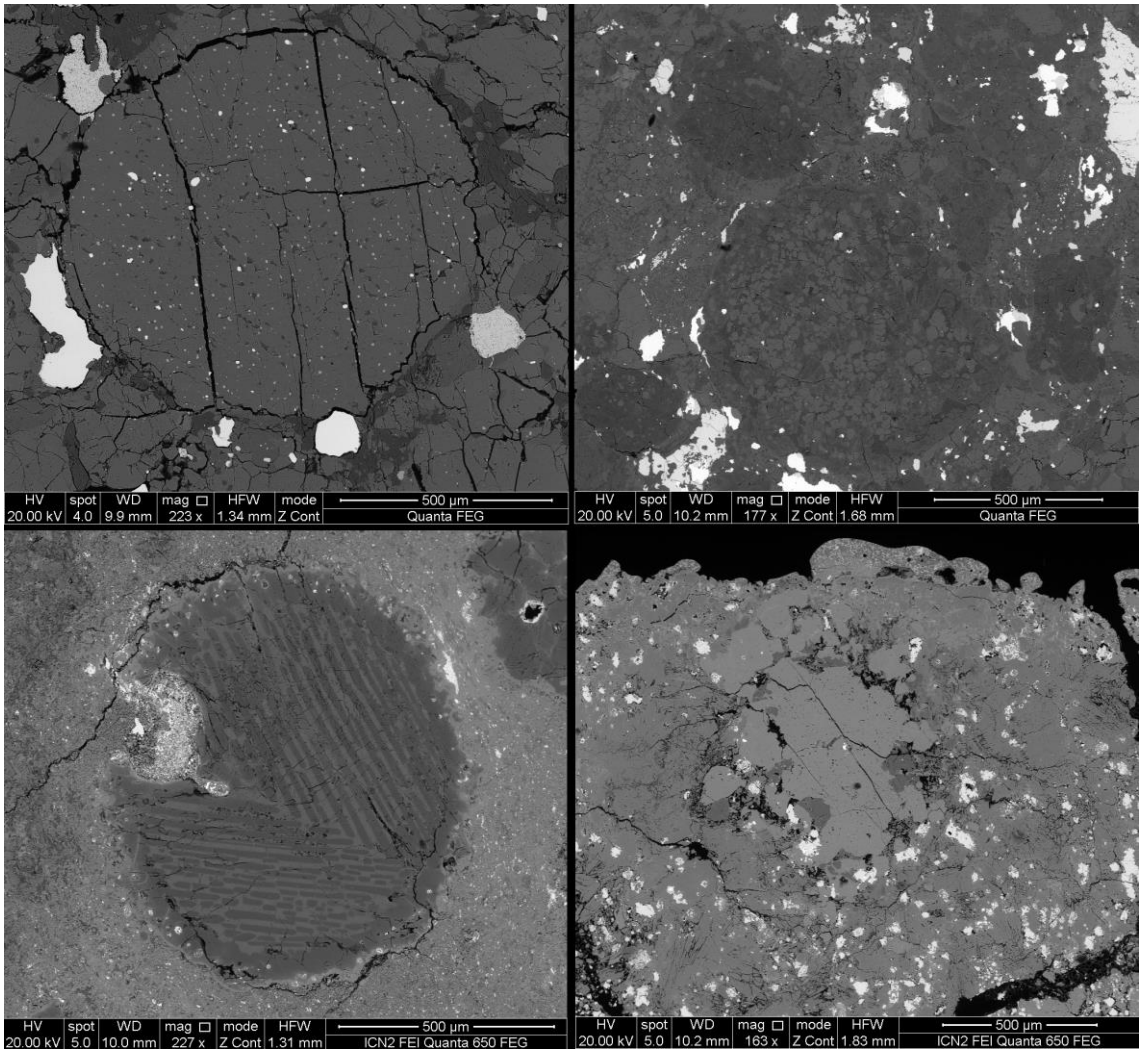

Figure 1.3: A selection of chondrules seen under a Scanning Electron Microscope, and found on different chondritic meteorites: the Ardon L6 ordinary chondrite (top left), the Cali H/L4 ordinary chondrite (top right), the Allende CV3 carbonaceous chondrite (bottom left), and the PCA 82500 CK4/5 carbonaceous chondrite (bottom right). Images obtained at the Institute of Space Sciences (IEEC-CSIC).

The composition of those rims is very similar to the *matrix* found in meteorites between chondrules, CAIs and other inclusions, interpreted to be dust adhered to chondrules that escaped the heating process (Jones et al., 2000). Actually, primitive primary chondrules, or even CAIs, can be found in the inside of secondary larger chondrules, formed around

the first one as a consequence of heating and melting of fine-grained dust (Wasson et al., 1995). Accretionary rims composed mainly of *forsterite*-rich *olivine* and *refractory* inclusions similar to AOAs, can also be found outside the melt rims (Scott & Krot, 2005). Besides, some chondrules, and even CAIs, show the presence of relict grains, which apparently are pieces from a previous generation of chondrules or CAIs, according to their chemistries and oxygen isotopic compositions (Jones et al., 1998).

In general it can be concluded that the thermal processing of the solids that later accreted into chondritic planetesimal was extensive. It has been found that the *matrix* trace element abundances are characteristic for a given chondrite meteorite group, and are depleted relative to the pristine Sun composition (Anders & Grevesse, 1989; Bland et al., 2005). However, the *matrix* appears enriched relative to bulk compositions of their parent meteorites, particularly in *volatile* elements (Bland et al., 2005; Martínez-Jiménez et al., 2017). This enrichment coincides with a complementary depletion in chondrule compositions, implying that both components were thermally altered and interchanged *volatile* elements (Bland et al., 2005). In other words, chondrule formation from micron-sized minerals and heat lead to an exchange of *volatile* elements between chondrules and *matrix*. Chondrule-*matrix* chemical complementarity supports the thermal processing of chondritic components in the same region of the protoplanetary disk.

1.2 Accretion and evolution of planetesimals and minor bodies

1.2.1 From the first cm-meter-size aggregates to km scale bodies

Experimental studies have simulated the conditions in which the large bodies in the Solar System formed, and demonstrated that this accretion of primordial materials took place in relatively short timescales (Blum et al., 2006). It is generally accepted that these bodies were formed by the relatively fast agglomeration of dust and ice through low speed (below 1 m/s) inelastic collisions, combined with adhesive surface forces (Weidenschilling & Cuzzi, 1993). First, Brownian motion, differential sedimentation, and gas turbulence, dictated collision velocities and promoted the formation of fractal dust agglomerates (Wurm & Blum, 1998; Blum et al., 2000). Due to differential settling of those agglomerates toward the midplane of the accretion disk, the largest fractal aggregates were formed in a few hundred or tens of thousands of years, with sizes between a few cm at 1 AU and ~100 μm at 30 AU (Blum, 2004). As the bodies grew in

size and mass, drift velocities and impact energies increased, which resulted in compaction of the dust aggregates and the beginning of nonfractal growth (Blum & Wurm, 2000). Collision velocities increase linearly with agglomerate sizes, which led to fragmentation processes when the bodies grew to several cm at 1 AU, and ~1 mm at 30 AU (Blum, 2004).

Above these sizes, the growing processes are less understood. With collision velocities higher than 1 m/s, the interactions between agglomerates are defined by compaction and fragmentation (Blum & Münch, 1993). With moderate collision velocities, compaction allows the formation of very porous objects, but with increasing velocities porosity decreases while mass density grows (Blum et al., 2006). Larger mass densities imply the formation of compacted dusty bodies and a further increase in collision velocities, which results in fragmentation or crater formation, and hinders aggregation (Wurm et al., 2005). However, by aerodynamic interaction with the ambient gas of the solar nebula (Wurm et al., 2004), or also by electrostatic charging of the colliding bodies (Blum, 2004), the fragments resulting of impacts can be carried back to the largest body. Indeed, it is believed that most asteroids currently populating the Solar System are formed by the re-aggregation of large rock fragments resulting from the catastrophic disruption of a previous asteroid by impacts, forming what is known as a rubble pile, i.e., a low density asteroid with large cavities between the boulders that form their structure (Holsapple, 2001).

In the ~2 Myr after the formation of CAIs these aggregates continued growing until eventually they became porous bodies in the km scale, large enough to attract each other through their mutual gravity. These bodies, called planetesimals, experienced a final stage of formation that has been described with a runaway growth scenario (Weidenschilling & Cuzzi, 1993), qualitatively similar to the aerodynamic and electrostatic accretion processes described above, together with the continuous accumulation of the remaining smaller dust agglomerates. To fully describe the collisional and aggregation processes occurring at that scale, the structure, morphology and mechanical properties of these large bodies are required, but they are not completely understood, yet. Over the lifetime of the Solar System these planetesimals suffered a large number of collisions from different-sized impactors at random velocities, which compacted and fragmented them, successively reducing their primitivism, in a continuous process known as collisional gardening (Beitz et al., 2016).

Some of these large bodies became the planets and moons currently existing in our system. From the rest, some survived as minor planets and comets in the outer regions of the solar System, while a large fraction remained as asteroids in the Main Asteroid Belt (hereafter MB) between Mars and Jupiter (Beitz et al., 2016).

According to the Nice model, after the dissipation of the primordial gas and dust of the Solar disk, Saturn, Uranus and Neptune scattered planetesimals inwards while moving outwards to preserve angular momentum, while the larger gravity of Jupiter sent those planetesimals to highly elliptical orbits or out of the Solar System, until Jupiter and Saturn entered a 1:2 resonance that strongly destabilized the planetary system and scattered 99% of the planetesimals, sending most to the outer Solar System and some to the inner Solar System, also originating the *Late Heavy Bombardment* (Gomes et al., 2005; Morbidelli et al., 2005; Tsiganis et al., 2005). This way, most of the mass of the asteroid belt was lost during the first few hundred Myr, and the remaining size distribution has not changed significantly from that time (Davison et al., 2013). Since then, the remaining asteroids of the MB have experienced continuous collisions with other objects of variable sizes (de Elía & Brunini, 2007; Beitz et al., 2016), with the largest ones producing considerable amounts of impact ejecta (O'Keefe & Ahrens, 1985). Asteroids with sizes above few km gravitationally recaptured more than 50% of these ejected material, forming a regolith layer on their surface (O'Keefe & Ahrens, 1985). Posterior impacts compacted this regolith layer in the largest asteroids, reducing its bulk porosity while partially protecting the surface, although the crust was compacted to some degree due to the shock waves penetrating through the regolith (Beitz et al., 2016). This way, the continuous bombardment not only modified the shape of asteroids by cratering processes, but also the physical properties of such bodies, changing the conditions for later impacts (Trigo-Rodríguez & Blum, 2009; Beitz et al., 2013). At the same time, the interior of large enough bodies was further compacted by cold isostatic pressing due to the effect of self-gravitation (Gail et al., 2014).

1.2.2 Internal heat of planetesimals

In the first few Myr of the Solar System the main heat source for differentiation and metamorphism of planetesimals was the decay of radioactive nuclei. Although impacts can also be a source for heat, they only played a minor role in bodies smaller than ~1000 km (Keil et al., 1997). These bodies were first heated by the decay of short-lived nuclei, mainly ^{26}Al but possibly also ^{60}Fe, and later by long-lived isotopes such as ^{235}U,

^{232}Th and ^{40}K, although their contribution was much less important (Yomogida & Matsui, 1984; Gail et al., 2014). The relatively low half-life of ^{26}Al implies that bodies with an early accretion had a stronger heat source than those that accreted later. When these short-lived nuclides decay they release energy in the form of radiation, which travels across the body and escapes to space through its surface, if it's not absorbed on its path. The larger the body, the more radiation is retained, which implies a further increase in temperature. In the deep interior of planetesimals, where both the pressure due to self-gravity and the temperature increase due to radioactive decay are higher, compaction processes due to hot pressing, known as sintering, are triggered (Henke et al., 2012). This process results in considerable compaction at temperatures below the solidus point (i.e., the temperature at which melting begins) for *silicates* and metals, and the *crystallization* of *amorphous* ice and phase transition of *volatiles* in icy bodies (Gail et al., 2014). If the radiogenic heating is strong enough, metals and *silicates* start melting when they reach their respective solidus temperatures, which implies the beginning of differentiation (Figure 1.4) with the appropriate conditions (Gail et al., 2014). It starts with the melting of iron, which sinks to the core of the body, while the *silicate* melts travel towards the surface, due to their lower density, although in icy bodies the melting of ice takes place before iron melts (Yomogida & Matsui, 1984). The degree of melting and differentiation of a body depends to some extent on its composition, but mainly on its size, with larger sizes implying higher pressures and temperatures, and its accretion time, that determines the amount of short-lived radionuclides that the body can gather before they decay.

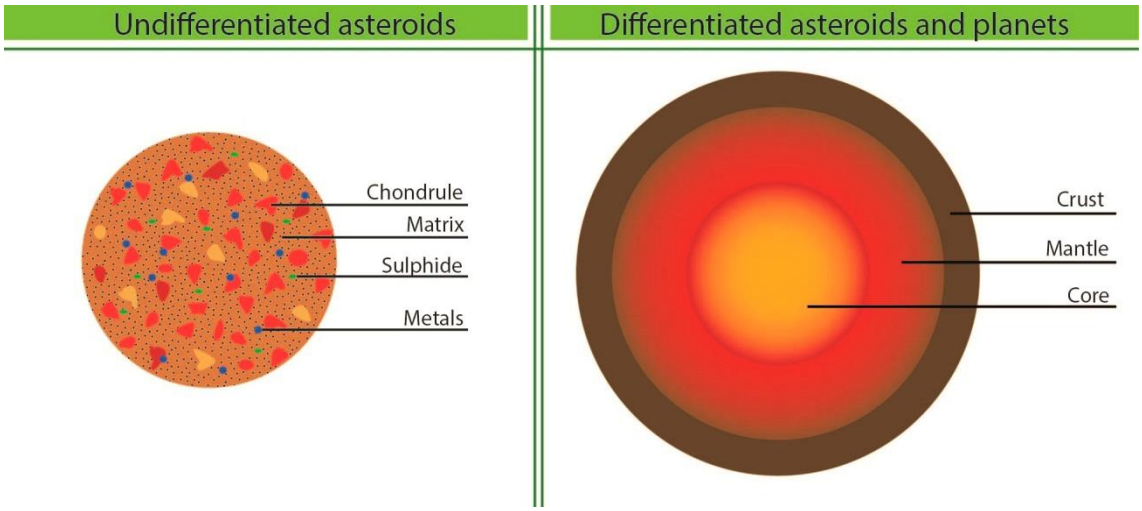

Figure 1.4: A schematic representation of undifferentiated asteroids, which conserve primordial materials embedded in a *matrix*, and differentiated bodies, with their materials segregated in different layers (Martínez-Jiménez et al., 2017).

Sintering becomes active at temperatures ~700 K (Yomogida & Matsui, 1984), and while temperatures grow the associated compaction implies a strong decrease in porosity in the inner layers of bodies. As a consequence, these bodies shrink in size losing more than 15% of their radius (Gail et al., 2014). Compaction also implies an increase in thermal conductivity, and therefore a more efficient transport of heat from the core to the outer layers of the body (Krause et al., 2011). The porous regolith layer at the surface of these bodies is much less thermally conductive, and then the necessary threshold temperature to trigger sintering is only achieved in the deeper parts of the regolith (Yomogida & Matsui, 1984). This way, a porous regolith layer survives in the surface of planetesimals, but its relative thickness decreases in bodies where radioactive decay has been more important, i.e., those large enough or which started their accretion sooner (Gail et al., 2014).

For bodies with sizes of a few km or less melting would only happen if they accreted shortly after the formation of CAIs, because otherwise the abundance of ^{26}Al would not be enough to heat the body up to the melting point of metals (Henke et al., 2012; Neumann et al., 2012). Even for larger bodies, melting becomes more difficult if they accreted more than 3 Myrs after the formation of CAIs, and therefore differentiation would be very unlikely (Neumann et al., 2012), except maybe for bodies with a very high content in *volatiles*, and its associated relatively low melting point (Gail et al., 2014). Those bodies that are heated to the point of starting sintering and even melting processes, but not differentiation, have a temperature distribution that follows an onion-like structure, with temperature decreasing towards the surface (Henke et al., 2012). The materials composing such bodies are modified by the effect of heat (which is known as thermal metamorphism) as a function of the depth where they are found within the body (Henke et al., 2012). Bodies that reach the appropriate conditions for differentiation have their materials redistributed, at least partially, to form the core-mantle-crust structure that can be found in planets (Neumann et al., 2012). Different models describe possible scenarios and relative timing for the differentiation between the core and the mantle, and between the mantle and the crust (see, e.g., Gail et al., 2014, and references therein). These models differ mainly in the timing of core

formation with respect to *silicate* melting, in how the presence of minor phases affects differentiation, in the amount of melt that has to be achieved before the materials can migrate inside the body to properly differentiate, and in the specific transport mechanisms (Neumann et al., 2012, and references therein). Despite their differences, most thermochemical models of planetesimal heating suggest that the great majority of bodies in the few km scale or above are in a state of partial differentiation (Neumann et al., 2012). The structure would be that of a differentiated interior formed by an iron core and a *silicate* mantle, covered by an undifferentiated layer that is compacted and sintered on its bottom, while porous on its top (Neumann et al., 2012; Gail et al., 2014; Neumann et al., 2014).

The presence of water can have important implications for the thermal and structural evolution of planetesimals. Water ice can absorb substantial amounts of heat during melting, which moderates the temperature increase, and the resulting warm water can redistribute heat within the body while it moves through porous material or due to hydrothermal convection (Grimm & McSween, 1989). Water also allows exothermic and endothermic processes that can modify the evolution of water-rich and icy bodies, like the *crystallization* of *amorphous* ice and the formation of hydrous *silicates* (Gail et al., 2014). Differentiation processes can even lead to the presence of layers of liquid water or ice, although in bodies that reached high temperatures these processes can also result on a dehydrated planetesimal as water vaporizes and escapes the accreting body (McCord & Sotin, 2005).

1.2.3 Petrologic types

Due to the heating processes described above, undifferentiated bodies have been modified to some extent by heat. The degree to which a body has been affected by these processes is known as petrologic type. This way, meteorites coming from undifferentiated bodies are divided in a 1 to 6 scale of petrologic type (Figure 1.5), following the scheme originated by Van Schmus and Wood (1967). As will be explained later, not all meteorites from undifferentiated bodies span the same range of petrologic types. This scheme can actually be divided in two different schemes, with types 1 and 2 describing the degree of aqueous alteration, and types 3 to 6 describing the degree of thermal metamorphism (Van Schmus & Wood, 1967; Weisberg et al., 2006). Although useful, this scheme can sometimes be confusing. For example, some meteorites have been aqueously altered and posteriorly heated high enough to

experience thermal metamorphism, but the scheme considers these two different types of alteration as mutually exclusive. Although two different scales to measure aqueous alteration and thermal metamorphism would probably be more descriptive (Weisberg et al., 2006), this description of petrologic types is widely used in the study of meteorites for classification purposes.

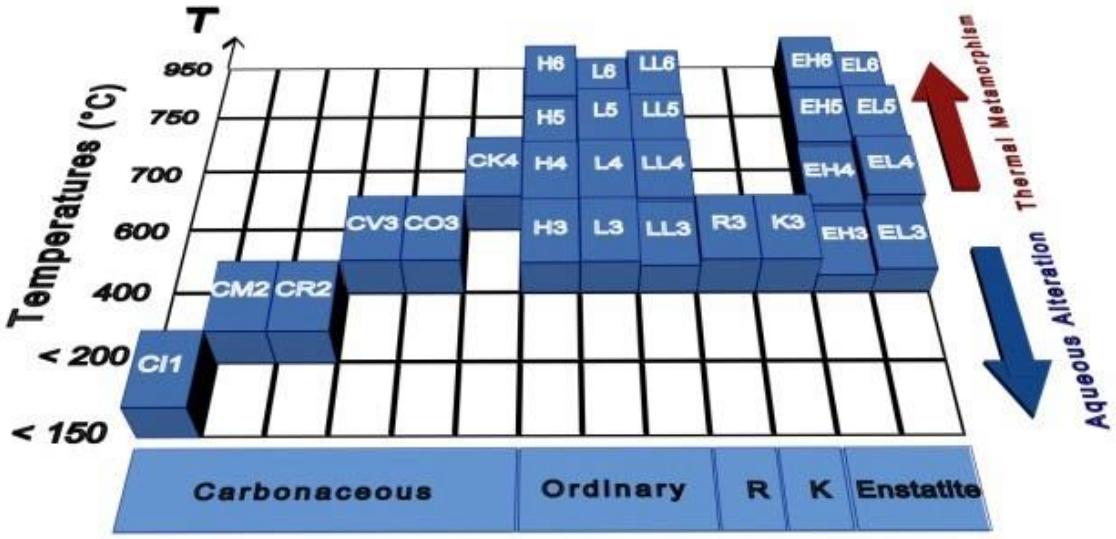

Figure 1.5: A schematic representation of the petrologic types in chondrites that are reminiscence of the thermal metamorphism and aqueous alteration experienced by their parent asteroids (Courtesy E. Dotto).

Petrologic type 1 indicates meteorites that experienced extensive aqueous alteration in their parent bodies at temperatures between ~320 and 420 K, often lacking chondrules and with most of their *olivine* and *pyroxene* altered to hydrous phases (Van Schmus & Wood, 1967; Weisberg et al., 2006). Type 2 are envisioned to be the result of extensive aqueous alteration between ~470 and 600 K, still not enough to produce thermal metamorphism, and allowing chondrules and some unaltered *olivine* and *pyroxene* to survive (Van Schmus & Wood, 1967). This type has been divided in subtypes between 2.0 and 2.6 reflecting progressive aqueous alteration (Rubin et al., 2007). Types 3 to 6 describe a continuous sequence of changes in mineralogy and texture due to different degrees of thermal metamorphism, with only little evidence of aqueous alteration in some cases (Brearley & Jones, 1998; Huss et al., 2006). Together with types 1 and 2, type 3 is described as unequilibrated, because the minerals in these meteorites show compositions reflecting the primitive conditions in the solar nebula (Van Schmus & Wood, 1967). With a very low to absent degree of thermal metamorphism, type 3

meteorites show the nearly pristine conditions as when they accreted to the parent asteroid (Van Schmus & Wood, 1967). This petrologic type, heated between 600 and 900 K, approximately, is subdivided in types 3.0 to 3.9, with increasing thermal metamorphism promoting diffusion of their elements between grains of different composition, starting in the *matrix* and spreading to chondrules (Sears et al., 1980; Huss et al., 2006). Types 4 to 6 have been heated to between ~900 and 1200 K, and are already equilibrated, with the composition of most minerals becoming homogeneous and the *matrix recrystallizing* and increasing in grain size (Van Schmus & Wood, 1967; Huss et al., 2006). With increasing degree of thermal metamorphism chondrules in type 5 meteorites become indistinct and the *matrix* is hardly distinguished, and by type 6 chondrules begin to integrate with the *matrix*, while other minerals coarsen their grain and new *metamorphic* minerals, such as *feldspar*, form (Van Schmus & Wood, 1967; Huss et al., 2006). Above ~1200 K, the parent bodies of these meteorites started melting and differentiating (Henke et al., 2012; Neumann et al., 2012).

Following the onion shell model for the formation of planetesimals, the meteorites of petrologic types 3 to 6 would be representing the evolution histories of materials formed at different conditions of temperature and pressure in their parent bodies (Göpel et al., 1994). Meteorites formed in the same planetesimal but with distinct petrologic types are exemplifying the conditions available at different depths in the structure of their parent body, and therefore carry valuable information about the thermal history and *metamorphic* processes that took place in that body (Gail et al., 2014). This way, primitive type 3 meteorites would have formed in the exterior colder layers or large planetesimals, in bodies that never grew above the few km scale, or in bodies that accreted relatively late (Yomogida & Matsui, 1984; Göpel et al., 1994; Henke et al., 2012).

1.3 Chondritic meteorites

1.3.1 From undifferentiated parent bodies to meteorites

Meteorites are the main available samples of the first solids and planetesimals in the Solar System, much more abundant and easy to get than materials obtained by sample-return space missions. Most meteorites are fragments of the planetesimals formed during the accretion processes that took place in the first few Myr of the Solar System, with only a few being samples of bodies that were differentiated with a metallic core, a

silicate mantle and a crust. Differentiated meteorites suffered *igneous* processes from which their chemical contents were equilibrated, changing their primordial bulk composition and melting the chondrules, and they are consequently called achondrites. Inside this group meteorites from Mars and the Moon can be found, together with HED meteorites, probably originated in the ~500 km asteroid (or minor-planet) 4 Vesta (Drake, 2001). Other achondrites have not been assigned to specific bodies, yet, possibly because their parent planetesimals were destroyed after large impacts and only small shattered pieces remain. There is also a category known as primitive achondrites, which despite reaching melting temperatures or experiencing equilibration, still conserve some properties of undifferentiated meteorites, such as relic chondrules or isotopic ratios resembling those of chondrites (Keil et al., 1997; Weisberg et al., 2006).

However, a great majority (~86%) of the more than 50,000 meteorites recovered so far are undifferentiated, conserving simultaneously a fine-grained *volatile*-rich *matrix*, and primitive solids mostly in the form of CAIs and chondrules, which is the reason why these meteorites are called chondrites (see Van Schmus & Wood, 1967, and references therein). They are the result of impacts on asteroids from the MB, which can release large fragments with the potential to reach Earth. It has to be taken into account that most of the fragments produced after impacts on bodies with sizes above the ~100 km are reaccreted by their parent asteroid, forming the regolith layer described before (O'Keefe & Ahrens, 1985). This is consistent with the fact that a relatively large amount of chondrites are actually breccias, i.e., meteorites formed by multiple broken rock fragments held together by a fine-grained *matrix*, which can be of the same composition but with different *metamorphic* properties (thus originated at distinct depths in the parent body), or fragments of different objects (Bischoff et al., 2006).

Some fragments produced after relatively large impacts on MB asteroids escape the gravitational pull of their parent bodies. They often contain evidence of thermal metamorphism, aqueous alteration, and impacts in their parent bodies, and therefore become samples of the most primitive materials in the Solar System. While travelling through the MB some of them enter in orbital resonances with Mars, Jupiter, or even Saturn, which can eventually send them into highly eccentric Earth's crossing orbits (Morbidelli & Nesvorný, 1999). Indeed, most asteroids of the Near Earth Asteroids (NEAs) population (those whose orbits bring them into proximity with Earth, and at less than 1.3 AU from the Sun), are tens to several hundred meters fragments of larger chondritic bodies that are crossing the near-Earth space thanks to those dynamical

resonances. If they arrive to our planet and survive the entrance through Earth's atmosphere, they become meteorites that can potentially be recovered and studied, which provides clues about the evolution of their parent asteroids (Llorca et al., 2005; Blum et al., 2006). Measuring how much time have meteorites been exposed to the cosmic-rays (which is known as the Cosmic-Ray Exposure Age or CREA), the time they spent travelling from their parent asteroids to Earth can be calculated. It turns out that most of those fragments have only being travelling for a few tens of Myr (Eugster et al., 2006), which means that they were separated from their parent asteroids in relatively recent collisions occurred in the MB (Keil et al., 1994).

Most impacts on the regolith layer of large planetesimals hardly produce high pressures in the materials below, but with high impact velocities a pressure wave is generated that compacts the ejected material and the material below the crater, occasionally producing shock melted-rocks (Beitz et al., 2016). As a result regolith-free fragments in the km scale are released, and they experience high impact pressures due to subsequent impacts, which leads to meteorites with high shock features (Beitz et al., 2016). Those features can be seen in the form of undulatory extinction of light transmitted through thin sections of the samples, fracturing and *mosaicism* of its minerals, and the presence of high-pressure mineral phases, among others (Stöffler et al., 1991). Using these features, meteorites are assigned a specific degree of shock pressure that ranges between S1 (unshocked) and S6 (strongly shocked at pressures up to 90 GPa), although the degree of shock can vary within the same meteorite sample (Stöffler et al., 1991).

Although all chondrites represent relatively primitive undifferentiated material, there are differences in major element ratios, oxygen isotopic compositions, concentration of *refractory lithophile* elements, and abundance of Fe in metallic or oxidized form, among other minor factors, that allow for distinction of several classes (see Weisberg et al., 2006, and references therein). These differences between classes are thought to be the consequence of formation at variable distances with respect to the Sun and different regions of the Solar System, each containing a specific reservoir with particular composition and level of oxidation (see, e.g., Alexander et al., 2007; Rubin, 2011). This way, meteorites are divided in the following classes: ordinary chondrites (hereafter OCs), which is the major class, carbonaceous chondrites (hereafter CCs), with significant amounts of carbon and water, and *enstatite* chondrites (hereafter ECs), which

is the most reduced class of chondrites. OCs, CCs and ECs are also divided in clans, i.e., meteorites formed in the same region of the solar nebula, or with the same evolutionary history, but that experienced different secondary processes like brecciation, impacts, or hydrothermic alteration (Kallemeyn & Wasson, 1981; Weisberg et al., 2006). These clans are similarly divided in groups, each one reflecting a unique composition that can potentially be assigned to a specific parent body (Burbine et al., 2002a). Also, as described before, chondrites belonging to the same group can show different petrologic types, which can be indicative of different thermal and pressure conditions in the same parent body. Finally, there are several meteorites that do not fit exactly into the description of any of those classes, and therefore belong to minor groups or remain ungrouped (Weisberg et al., 2006).

1.3.2 Ordinary chondrites

OCs is the major class of undifferentiated meteorites, representing ~85% of the meteorite samples recovered so far and more than 90% of all chondrites. They are characterized by a high abundance of chondrules (60-80% of the material composing the meteorites) opposed to a very minor presence of CAIs (less than 1%), with the *matrix* representing ~10-15% of the material composing those meteorites, and dominated by thermal *metamorphism* (Figure 1.6), with petrologic types ranging between 3 and 6 (see Weisberg et al., 2006, and references therein). Some of the least thermally metamorphosed OCs show evidence for a low degree of aqueous alteration, mainly in the *matrix* (see, e.g., Sears et al., 1980). The normalized with respect to Mg abundance of *refractory lithophile* elements (RLE) is closer to Earth's than in the case of CCs (Rubin, 2011), and the O-isotopic compositions of OCs plot above what is called the Terrestrial Fractionation Line (TFL) that represents Earth's O-isotopic composition (Clayton & Mayeda, 1991).

OCs are divided in three different groups: H, L and the least common LL chondrites. Generally they show similar petrologic characteristics (like chondrule size and main minerals composition) and O-isotopic compositions, and therefore the three groups are considered members of the same clan. The main distinction between the three groups of OCs comes from the abundances of total iron, iron in metallic form, and iron oxide in *silicates* (mostly through *fayalite*, the Fe-rich endmember of *olivine*), although this last feature is only reliable in equilibrated chondrites, i.e., of petrologic type 3 or close (Weisberg et al., 2006). H chondrites show the highest content in iron

(hence the abbreviation as H chondrites), mostly in metallic form, with a low abundance of *fayalite*; L chondrites show a lower content in iron (hence the abbreviation as L chondrites), with less metal, and a higher abundance of *fayalite*; LL chondrites show the lowest content in iron and metal (hence the abbreviation as LL chondrites), but the highest abundance of *fayalite* (Kallemeyn et al., 1989). Chondrule sizes also vary between them, with average sizes of ~0.3 mm for H chondrites, ~0.7 mm for L chondrites, and ~0.9 mm for LL chondrites (see, e.g., Weisberg et al., 2006). Other chondrites show intermediate states between those groups, or properties that do not fit exactly in any of them, which could be indicative of, at least, a fourth parent body for ordinary chondrites (Kallemeyn et al., 1989; McCoy et al., 1994).

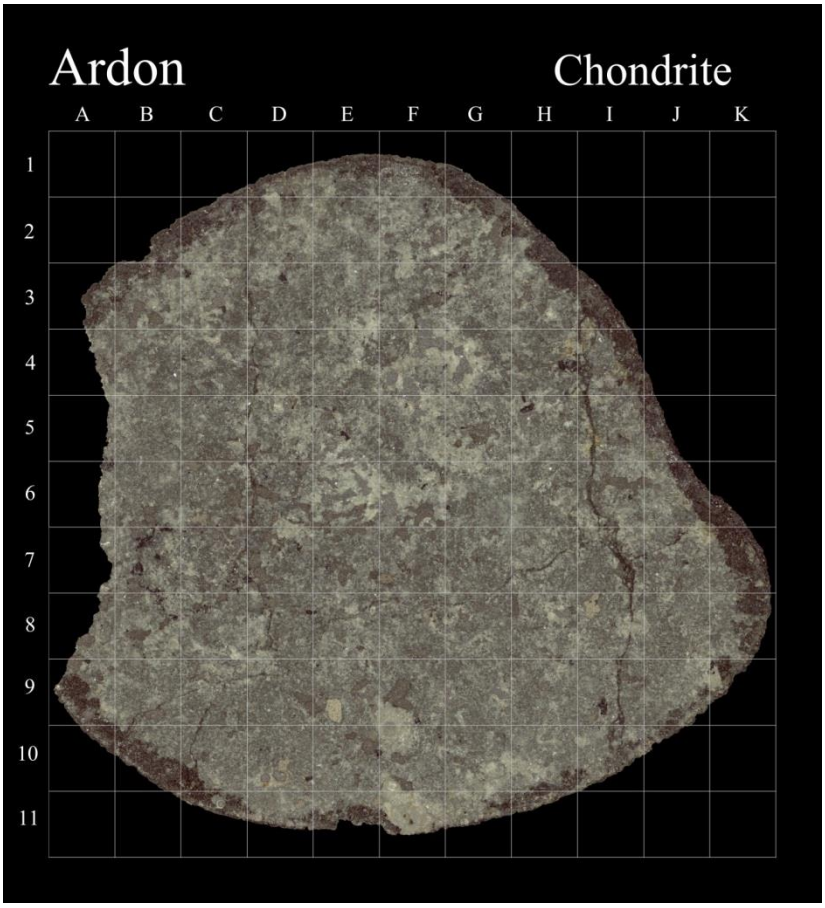

Figure 1.6: High resolution reflected light optical mosaic of one thin section of the Ardón L6 ordinary chondrite (see chapter 2 for more technical information). Image obtained at the Institute of Space Sciences (IEEC-CSIC).

1.3.3 Carbonaceous chondrites

CCs are the second class in number, with more than 2,100 samples that represent ~4% of all chondrites, and are usually characterized by particularly high abundances in C and water. Indeed, it is believed that this type of meteorites and their parent bodies acted as catalysts of prebiotic scenarios (see, e.g., Rotelli et al., 2016, and references therein). Oppositely to OCs, CCs show abundances of RLE, normalized to Mg, above the terrestrial values (Rubin, 2011), and O-isotopic compositions that plot below the TFL (Clayton & Mayeda, 1999). Their classification is much more complex than that of OCs, with abundance of chondrules varying between ~1 and 70%, amount of *matrix* ranging from above 99% to less than 1%, CAIs representing between 0.1 and 13% of the samples volume, and content in metal between 0 and 80% of the volume (see Scott & Krot, 2003, and references therein)(Figure 1.7). They also show a high variability in the sizes of chondrules, and their petrographic type varies between the highest degree of aqueous alteration (type 1) to a very high thermal metamorphism (type 6), although most groups belong almost completely to the unequilibrated type 3 (see Weisberg et al., 2006, and references therein). Following that high variability, CCs are divided in four different clans, which include 8 different groups and even 5 subgroups (see Weisberg et al., 2006, and references therein).

The CI group, named after the Ivuna meteorite that fell in Tanzania in 1938, is at the same time an independent clan, since nothing seems to link them to the other groups (Kallemeyn & Wasson, 1981). These very rare CCs (only 9 samples have been identified so far), are considered some of the most primitive meteorites, because their bulk composition is very close to that of the solar photosphere (Anders & Grevesse, 1989). They all belong to the petrologic type 1, which implies a very extensive aqueous alteration, and they are composed mostly by highly-porous fine-grained *matrix* including ~20% in weight of water, although in the form of *phyllosilicates* (Kallemeyn & Wasson, 1981). Apart from some rare isolated fragments, these meteorites are devoid of chondrules and CAIs, but it is not clear if they never contained those materials or rather the aqueous alteration was so extensive that mostly destroyed both CAIs and chondrules (Weisberg et al., 2006).

The CM and CO groups of chondrites are the most abundant, with more than 500 samples each recovered so far, and together they form the CM-CO clan. These two groups are linked by similarities in the size of chondrules, the composition of *anhydrous* minerals, the abundances of RLE, and the O-isotopic compositions of high-temperature

minerals (Kallemeyn & Wasson, 1981). CM chondrites are named after the Mighei meteorite that fell in Ukraine in 1889, and are characterized by a 20% volume of chondrules with sizes of an average of 0.3 mm, a 70% volume of *matrix*, and ~5% volume of CAIs that have been partially or completely replaced by phyllosilicates (Weisberg et al., 2006). All CM chondrites have experienced different degrees of aqueous alteration, and while most belong to the petrologic type 2, and some have been classified as petrologic type 1, the reported differences between specimens suggest a progressive alteration with petrologic subtypes between 2.0 and 3.0 (Zolensky et al., 1997; Rubin et al., 2007). CM chondrites have apparently been distributed widely in the early Solar System, since CM-like materials have been commonly found as clasts in other chondrites and achondrites (Zolensky et al., 1996). CO chondrites are named after the Ornans meteorite that fell in France in 1868, and are characterized by close to a 50% volume of chondrules with sizes of an average of 0.15 mm, ~30% volume of *matrix*, and the highest volume in CAIs found in any chondrite group, above the 10%. (see Scott & Krot, 2003, and references therein). With petrologic types ranging between 3.0 and 3.7, those are some of the least altered chondrites, although the ones with higher petrologic type contain minerals resulting from metamorphism (Rubin, 1998).

The CV and CK groups of chondrites, with ~400 and more than 300 samples, respectively, form the CV-CK clan. The meteorites of these groups with low petrologic types (type 3) have a similar range of O-isotopic and mineralogical compositions, which allows to classify them as the same clan and even as fragments of the same parent body, although this connection needs to be studied in further detail (Greenwood et al., 2010; Wasson et al., 2013). CV chondrites are named after the Vigarano meteorite that fell in Italy in 1910, and are characterized by a 45% volume of large chondrules with an average size of 1 mm, ~40% volume of *matrix*, and a large abundance of CAIs of ~10% of volume (see Scott & Krot, 2003, and references therein). All CVs are classified as petrologic type 3, but specific variations have allowed to divide the members of this group in three subgroups: reduced CVs (CVred), oxidized Allende-like CVs (CVoxA), and oxidized Bali-like CVs (CVoxB) (Weisberg et al., 1997). These subgroups show differences in *matrix*/chondrule ratios (increasing from CVred to CVoxB), metal/*magnetite* ratios (decreasing from CVred to CVoxB), slight differences in ^{16}O abundance, and even the presence of phyllosilicates that would allow to classify some CVoxB as petrologic type 2 (see Weisberg et al., 2006, and references therein). This division in subgroups may represent a complex multi stage alteration suffered by the

parent body of CV chondrites. CK chondrites are named after the Karoonda meteorite that fell in Australia in 1930, and are characterized by a 15% volume of mostly *porphyritic* chondrules with an average size of ~0.7 mm, a large abundance of *matrix* of ~75% volume, and an abundance of CAIs of ~4% of volume (see Scott & Krot, 2003, and references therein). This is the only group of CCs with petrologic types above 3, and they show the whole range of thermal metamorphism from type 3 to 6, with most of them being type 4 or 5. The members of this group show a high content in *fayalite*, a very low content of metal (both features related to high levels of oxidation), and O-isotopic compositions and RLE abundances within the range of CO and CV chondrites (Kallemeyn et al., 1991).

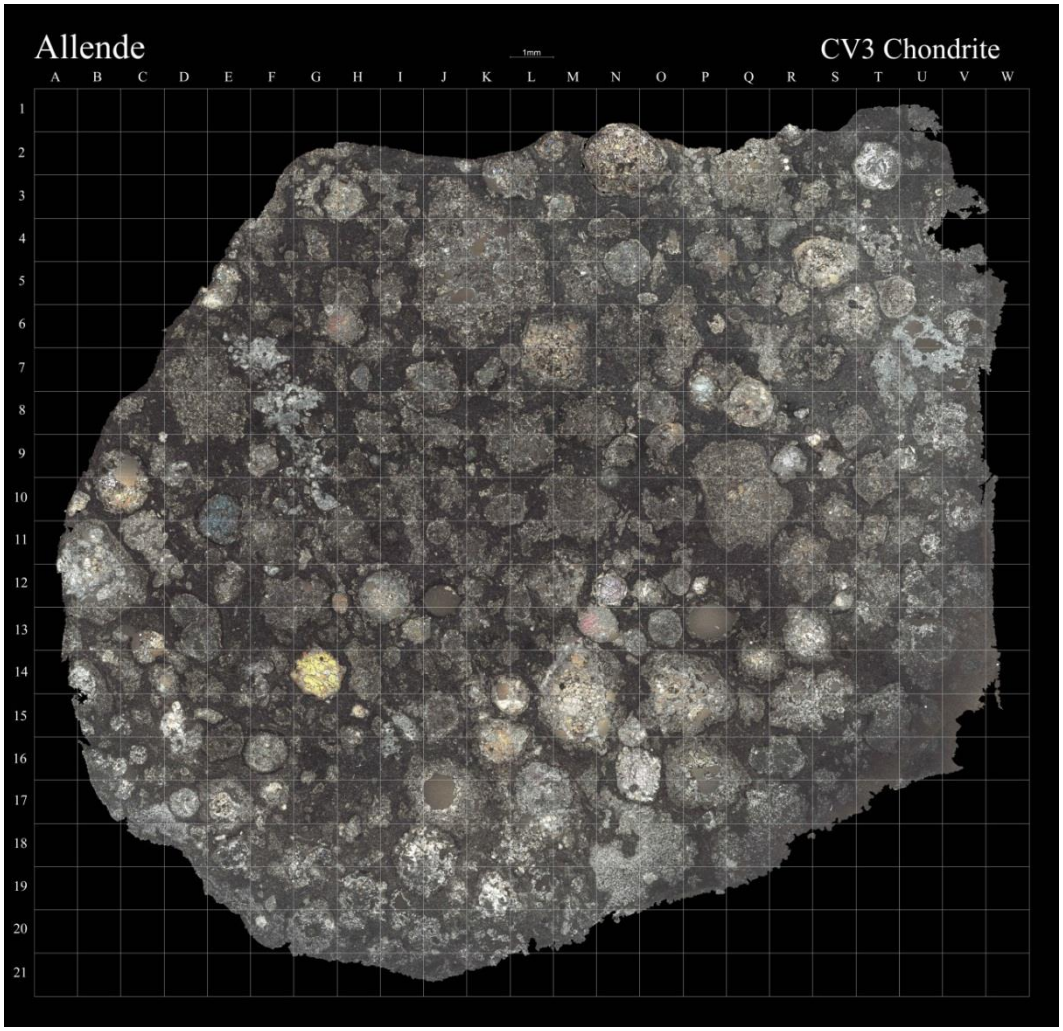

Figure 1.7: High resolution reflected light optical mosaic of one thin section of the Allende CV3 carbonaceous chondrite (see chapter 2 for more technical information). Image obtained at the Institute of Space Sciences (IEEC-CSIC).

The CR group of chondrites, with less than 200 samples, and the CH and CB groups, both with ~20 samples, form what is known as the CR clan. Although these groups show differences in petrographic characteristics and bulk chemistry, they share a particularly high abundance of primitive Fe-Ni metal with a large compositional range (between 5 and 70% in volume), bulk O-isotopic compositions that plot in the CR-mixing line, mostly Mg-rich *anhydrous mafic silicates*, heavily hydrated parts of the *matrix* with *phyllosilicates*, positive anomalies in N-isotopic composition that suggest a heavy N carrier no yet identified, a whole-rock RLE abundance close to Solar, and a high depletion of moderately *lithophile* elements (Rubin, 2000; Krot et al., 2002). CR chondrites are named after the Renazzo meteorite that fell in Italy in 1824, and are characterized by a 50-60% volume of chondrules with an average size of ~0.7 mm, ~30-50% volume of *matrix*, a low abundance of CAIs of ~0.5% of volume, and a Fe-Ni metal content between 5 and 8%, which is above the values for the carbonaceous chondrites described previously in this thesis (see Scott & Krot, 2003, and references therein). Most CRs are classified as petrologic type 2, with a few samples being closer to type 1, due to their highly hydrated *matrix* containing *phyllosilicates*, *magnetites*, *carbonates* and *sulfates* (Kallemeyn et al., 1994; Krot et al., 2002). Their contain Fe-poor reduced metal-rich chondrules (type 1), dark clasts of *matrix*-like material, and primitive Fe-Ni metal inclusions that show a large compositional range (Kallemeyn et al., 1994). CH chondrites (with the H meaning 'high-metal') are characterized by the highest abundance of chondrules among the CCs (~70% of volume), although they are also the smaller chondrules with an average size of ~0.05 mm, a low volume of *matrix* of only ~5%, a very low abundance of CAIs and *refractory* inclusions of ~0.1% of volume, and a high Fe-Ni metal content of ~20% in volume (see Scott & Krot, 2003, and references therein). They are all classified as petrologic type 3, although contain heavily hydrated *matrix*-like clasts instead of interchondrule *matrix*. CHs have bulk RLE abundances close to those of CIs, and their N-isotopic positive anomalies are even larger than in CRs (see, e.g., Wasson & Kallemeyn, 1990). CB chondrites, all classified as petrologic type 3, are named after the Bencubbin meteorite found in Australia in 1930, and are characterized by a 30-40% volume of large *cryptocrystalline* and barred chondrules with an average size of ~1 mm, a low volume of *matrix* below the 5%, a very low abundance of CAIs below the ~0.1% of volume, and a very high Fe-Ni metal content between 60 and 80%, far above the content in any other chondrite group (see Scott & Krot, 2003, and references therein). Compared to the other groups of the CR

clan, CBs have even larger depletion in moderately-*volatile-lithophile* elements and enrichment in N-isotopes (Weisberg et al., 2001). This group is divided in two different subgroups: CBa chondrites, with very large chondrules that reach the cm-scale, ~60% volume of metal, and a very high enrichment in N-isotopes, and CBb chondrites, with more than 70% volume of metal, smaller chondrules with an average size of ~0.5 mm, and a lower enrichment in N-isotopes (Weisberg et al., 2001). Peculiar features in CH and CB have been interpreted both as clues of an origin as highly primitive materials condensed from the solar nebula, or as materials formed in the vapor cloud resulting of a large impact event on a chondritic planetesimal (Wasson & Kallemeyn, 1990; Weisberg et al., 2001).

1.3.4 Enstatite chondrites

ECs, with less than 600 samples recovered so far, are mainly defined by the predominance in their chondrules of the *silicate enstatite*, the Mg-rich endmember of *pyroxene*. They also show a variety of unique mineralogical features that are mostly absent in other chondrites, and which are described as the consequence of formation under highly reducing nebular conditions: Fe-poor *silicates*, metals containing Si, and sulphides formed by elements that generally form oxides (Keil, 1968). All ECs show a range of petrologic types between 3 and 6, and there are even some meteorites defined as *enstatite* achondrites or melts, chemically and isotopically similar to ECs but heated to the point of melting, as a result of impacts or internal melting (McCoy et al., 1995). The chondrule and *refractory* inclusions abundance in ECs is very similar to that of OCs, with a 60-80% volume of chondrules and a very low volume of CAIs and other *refractory* inclusions below the 0.1%, but they show a lower abundance of *matrix* (between 0.1 and 10% in volume) and a higher abundance of metal clasts (between 8 and 15% in volume) (Keil, 1968). Their O-isotopic composition is particularly interesting, since it plots on the TF line, very close to that of the Earth and Moon (see, e.g, Rubin, 2000, and references therein). All ECs are classified as members of a single clan, but they are divided in two different groups: EH (the H stands for 'high-iron') and EL (the L stands for 'low-iron') chondrites. They differ in average chondrule size (~0.2 mm for EHs, ~0.6 mm for ELs), and metal content (~8% volume in EHs, ~15% volume in ELs), but the main differences are consequences of a higher degree or reduction in EH chondrites: higher abundance of Si (up to 3% in EHs, below 1% in ELs) and lower abundance of Ni in the Fe-Ni metal clasts, higher variation in the abundance of sulphides, and lower abundance of *enstatite* (Keil, 1968).

1.3.5 Other chondrites

Although CCs, ECs and mainly OCs encompass the vast majority of chondritic meteorites, some undifferentiated meteorites do not share the common features associated to any of those three classes, and therefore are classified as independent groups, or as ungrouped chondrites (Weisberg et al., 2006).

The largest of these groups is that of Rumuruti chondrites (hereafter RCs), with 181 samples identified so far and named after the Rumuruti meteorite found in Kenya in 1934. They are characterized by a volume of chondrules above the 40% with an average size of ~0.4 mm, a volume of *matrix* ~35%, a very low abundance of CAIs below the ~0.1% of volume, and a nearly absence of Fe-Ni metal, below the 0.1% in volume (see Scott & Krot, 2003, and references therein). They show RLE abundances and O-isotopic compositions very closely resembling those of OCs, but they contain higher abundances of Mn, Na and some *volatiles*, are highly oxidized, with FeO-rich *olivine* containing NiO, and their abundance of *matrix* is more close to that of CCs (Bischoff et al., 2011). Most RCs are thermally *metamorphosed*, with petrologic types usually above 3 and up to 6, and often are brecciated meteorites.

Kakangari chondrites (hereafter KCs), named after the Kakangari meteorite found in India in 1890, are the only other group of independent chondrites generally accepted, although it is formed by only 4 samples. They are characterized by a volume of chondrules between 20 and 30%, with an average size of ~0.6 mm, a volume of *matrix* ~70%, a very low abundance of CAIs below the ~0.1% of volume, and a content in metal around the 6-8% in volume (see Scott & Krot, 2003, and references therein). Although they have metal, RLE, and *volatile* abundances close to that of OCs, their O-isotopic compositions plot below the TF line, near the line described by the CR clan, and they are reduced to an intermediate oxidation state between H chondrites and ECs. Their *matrix*, which abundance resembles that of CCs, is minerallogically unique, composed largely of *enstatite* (see Scott & Krot, 2003, and references therein).

There are also ~60 ungrouped chondrites that do not fit exactly into any of the chondrite groups defined so far, although many have intermediate characteristics between those groups, which means that they could be members of new groups, but also anomalous samples of the currently existing groups. There are even some breccias, containing simultaneously materials associated to CCs, OCs and ECs (see, e.g., Weisberg et al., 2006, and references therein).

1.4 The parent bodies of chondritic meteorites

Earth is subjected to a continuous flux of interplanetary material of approximately 40,000 tons per year, mostly reaching the top of the atmosphere as micron-sized dust particles up to cm-sized meteoroids, but part of this material is formed by meter-sized rocks (Brownlee, 2001; Trigo-Rodríguez & Williams, 2017). Chondrites dominate the flux of objects large enough to survive the entrance through Earth's atmosphere, producing ~90% of meteorite falls (Zolensky et al., 2006). This way, chondritic meteorites are an important source of information about the bodies that deliver meteorites to our planet, and therefore about future meteorite falls and even possible catastrophic impacts on Earth (see, e.g., Moyano-Cambero et al., 2017a; Moyano-Cambero et al., 2017c, and references therein). However, from the millions of asteroids populating the Solar System only a few have had close enough approaches by space missions to have detailed information about their surface mineralogy and composition, and there have been only two successful sample return missions to asteroids or comets: the Stardust mission, which in 2006 brought to Earth dust from the tail of the comet 81P/Wild 2 (Brownlee et al., 2006), and the Hayabusa mission, which in 2010 brought samples from the asteroid 25143 Itokawa (Nakamura et al., 2011). Therefore, the vast majority of data about asteroids is obtained remotely, which besides from information about their size, density, orbits and rotation, can provide clues about their mineralogy when studied using spectroscopy in the range between the ultraviolet and the infrared (see, e.g., Trigo-Rodríguez et al., 2014a; Moyano-Cambero et al., 2016; Moyano-Cambero et al., 2017c). Indeed, one of the methods commonly used to classify asteroids is based in their reflectance spectra (see Bus & Binzel, 2002a; DeMeo et al., 2009, for more information about the asteroid spectral types).

Some achondrites have been successfully connected to the Moon and Mars thanks to the samples returned by the Apollo missions, and the analysis of Martian materials and atmosphere performed by the several spacecrafts, landers, and rovers that have studied the red planet in the last decades (Bogard & Johnson, 1983; Marvin, 1983). As mentioned before, HED achondrites have been related to the asteroid 4 Vesta (or simply Vesta), due to their similarities in the visible and near-infrared spectral ranges that suggest a common surface mineralogy, and to the analysis of Vesta's surface elemental bulk composition performed by the Dawn mission (Drake, 2001), although other asteroids resembling Vesta could also be the parent bodies of these meteorites (Reddy et al., 2015). Another example of the use of spectroscopy to establish possible

connections, is that of the *enstatite* achondrites called aubrites and the spectral E-type asteroid (3103) Eger, which show common albedos, flat reflectance spectrum, and absorption features (Burbine et al., 2002a). The only perfect link between an asteroid and a meteorite is that of the asteroid 2008 TC3, which was spectroscopically studied and classified as a spectral C or M-type asteroid, and the meteorites recovered after it fell on Sudan in 2008, which turned out to be *olivine-clinopyroxene*-rich achondrites called ureilites (Jenniskens et al., 2009).

With respect to chondrites, the ~200 km asteroid 6 Hebe has been related to H chondrites (and also of IIE iron achondrites) considering spectral parameters and the location near appropriate resonances to send fragments to Earth (see Reddy et al., 2015, and references therein). L chondrites have been related to the asteroid 1272 Gefion and its family due to consistencies in estimated ages and travelling times from resonances to Earth, although several members of the Gefion family are not consistent spectroscopically with L chondrites (see Reddy et al., 2015, and references therein). LL chondrites, although being the least common OCs, seem to be representative of ~two-thirds of the population of S and Q-type NEAs, according to their spectral features and interpreted mineralogies (Vernazza et al., 2008). LL chondrites have also been associated to the asteroid family of 8 Flora, and the samples recovered from both the asteroid Itokawa and the Chelyabinsk fall are LL chondrites, as well (Nakamura et al., 2011; Galimov, 2013). CCs, particularly CM chondrites, have also been tentatively related to the Ch-type asteroids 13 Egeria and 19 Fortuna (Fornasier et al., 2014), which is consistent with the typical association of CCs to low reflecting (dark) asteroids (Vilas & Gaffey, 1989). But, for most chondrites, there has only been a very general linkage to asteroids of specific spectral types, with OCs being associated with S and Q-type asteroids, CCs with C-type asteroids (although K and X-type asteroids also could be associated to specific CC groups), and ECs with X-type asteroids (Burbine et al., 2002a; DeMeo et al., 2009). However, and oppositely to what is suggested by the amount of each chondrite type recovered on Earth, C-type asteroids are more abundant than S or Q-type asteroids (Zellner, 1979). This is because C-type are mostly found in the outer regions of the MB, while S-type are in the inner MB, where more orbital resonances able to bring asteroids to Earth take place (see, e.g., Morbidelli & Nesvorný, 1999; Dunn et al., 2013a). Also, asteroids of CC composition are more fragile than those similar to OCs (Popova et al., 2011), and therefore it is harder for them to survive both impacts during their space travel and the entrance through Earth's atmosphere, which

implies that the meteorites found on Earth are biased with respect to the asteroid population, and explains why most CCs show only low degrees of shock (Trigo-Rodríguez & Blum, 2009).

Establishing consistent links between chondrite groups and specific asteroids is a very challenging issue. First of all, it has to be taken into account that the bodies that cross Earth's atmosphere and become meteorites are just fragments of much larger asteroids, and therefore could be representative of only specific regions of the original parent asteroid. Also, those fragments would have been separated from their parent asteroid for periods of tens of Myr, according to their CREAs (Llorca et al., 2005), which can imply very different posterior impact processing and space weathering alteration for the parent asteroid and the travelling fragment (Clark & Johnson, 1996; Chapman, 2004). Furthermore, the spectral information obtained from asteroids is only representative of their surface, usually covered by regolith, while meteorites can be samples from deeper layers of the asteroid released by strong impacts, and therefore affected to different extents by thermal metamorphism, aqueous alteration and/or impact processing, which can modify their spectra (Clark et al., 1992; Keil et al., 1992; Vernazza et al., 2008; Gaffey, 2010).

1.5 Outline and goals of the thesis

As have been explained above, chondrites are still samples of the early objects populating our Solar System, due to the undifferentiated nature, and are also representative of the building blocks that aggregated to form asteroids and rocky planets. In this thesis chondrites are studied from this point of view, exploring the properties of specific meteorite samples in order to understand the formation and evolution processes that took place in their parent asteroids, and extrapolate that information to learn about the properties of the bodies currently populating our Solar System.

The first step is to perform laboratory analysis of the samples, which, if performed properly and rigorously, will provide great insight about the formation and evolution of a specific meteorite. All experimental techniques and specific instruments used in the different parts of this thesis are briefly explained in chapter 2, as an accessible summary. As a practical example, a Martian meteorite is explored with a wide selection of instruments in chapter 3. Although not being a chondrite, this differentiated meteorite is one of the oldest samples of Mars recovered so far, and therefore is representative of

an epoch not long after the red planet evolved from a large planetesimal to a proper planet, as an example of the final step of evolution from the first chondritic aggregates to planets (see, e.g., Lapen et al., 2010). The specific features explored in this sample are the consequences of shock and aqueous alteration, which can be representative of similar effects found in large differentiated (or partially differentiated) asteroids. Besides, the aqueous alteration and shock features found in this meteorite can be connected to the event known as *Late Heavy Bombardment*, in which a large amount of chondritic asteroids impacted the terrestrial planets, imprinting a high degree of shock on some regions of the Martian surface, and probably providing the necessary amounts of water and carbon to produce the identified aqueous alteration features (Gomes et al., 2005). Moreover, the selected Martian meteorite has been studied extensively in the last 30 years, and therefore the data obtained here can be compared to previous results to validate the experimental methods applied here. At the same time, however, it requires a very deep study in order to find clues not yet explored about this meteorite and its formation (Moyano-Cambero et al., 2017b)

Most meteorites have their origin in asteroids from the NEA population, which at the same time had their origin in the MB, but besides from the case of those originated at the Moon and Mars, their parent asteroids are mostly unknown. In order to be able to extrapolate the information obtained in meteorites to learn about the properties of specific asteroids, it is necessary to find a method to connect the meteorite samples studied in the laboratory with the information remotely obtained from asteroids. In chapter 4, the properties found in CH CCs are compared to those inferred from the remote data obtained from the asteroid 21 Lutetia, approached by the Rosetta mission in 2010 (see, e.g., Sierks et al., 2011). Besides from comparing information from the bibliography about both objects, an extensive comparison of the spectra obtained from the two in the ultraviolet to infrared range is performed (Trigo-Rodríguez et al., 2014a; Moyano-Cambero et al., 2016b). It provides a possible connection between a chondrite group and an asteroid (or similar asteroids), but it is also useful to explore possible formation scenarios for the parent body of CH chondrites, and the specific asteroid studied here. This way, this chapter becomes an extensive example of how meteorites and asteroids can be connected.

Chapters 5 and 6 explore the properties of an OC breccia that can be considered a good example of the materials composing most of the asteroids populating the NEA

region (Vernazza et al., 2008): the Chelyabinsk meteorite, fallen in Russia in 2013. Chapter 5 explores the nanoindentation technique, which has only been applied to meteorites in a few occasions so far, and therefore opens the door for innovative studies. It analyses the mechanical properties in a non-destructive way, allowing the study of fragile samples without damaging them (Moyano-Cambero et al., 2017a). Chapter 6 explores the extension of shock effects in the different *lithologies* of this meteorite, and how the mechanical properties change between these separated regions, due to the variable effects of shock and other features (Moyano-Cambero et al., 2017c).

Considering the asteroid-meteorite connection described in chapter 4, plus the results of chapter 5, chapter 6 explores how the degree of shock and the mechanical properties are reflected in the ultraviolet to near-infrared spectra obtained from meteorite samples, and therefore how these properties can be partially inferred from the remotely obtained spectra of asteroids. Extrapolating properties such as composition and physical properties of an asteroid from the study of chondrites is of great interest for future practical applications, such as asteroid mining (Martínez-Jiménez et al., 2017). Chapters 5 and 6 are developed with a specific practical application in mind: the deflection of asteroids that can potentially become a thread to our planet. This way, those chapters try to determine, through the mechanical properties, which regions of an asteroid would be more efficiently deflected by a projectile, and how these areas can be recognized remotely using spectroscopy in the surface of heterogeneous asteroids. Although really catastrophic impact events of kilometre scale asteroids are expected to be very rare, much smaller asteroids, in the tens of meters scale, can be source of considerable damage, as exemplified by the 2013 Chelyabinsk event (see, e.g., Borovička et al., 2013). In the last years, there has been a growing interest in defining strategies to prevent the potential thread represented by asteroids in the near-Earth region, as exemplified by the collaboration between ESA and NASA in the Asteroid Impact and Deflection Assessment (AIDA) mission (Michel et al., 2015a). In this context, these two chapters consider an almost unexplored approach to provide new data that can be helpful for this and similar missions.

As a summary, the goals of this thesis can be described as follows. First, to apply a wide selection of instrumental techniques to explore different aspects of meteorites, and particularly chondrites, in order to learn as much as possible about them, and at the same time inferring information from their parent bodies. Then, the methods commonly used to establish links between meteorites and asteroids are applied to a practical case,

showing their strengths and weaknesses. Finally, a new technique is combined with the information from the previous chapters in a practical case, exemplifying the great interest that the study of the physico-chemical properties of chondrites can have, and opening the door for future studies.

2 EXPERIMENTAL METHODS

Research groups dedicated to the study of meteorites are usually focused in specific properties of the samples, and therefore each will use those analytic techniques that better fit their needs. Since the goal of this thesis is to study different aspects of chondrites to better understand the processes at work during the evolution of their parent asteroids, a multidisciplinary approach using, varied instrumentation, is required. Therefore, to facilitate the appropriate characterization of the meteorites from different points of view (chemical composition, mineralogy, mechanical properties) several techniques were combined in order to establish connections between meteorites and their possible parent bodies. See below a short description and specifications for each of the laboratory techniques used during the gestation of the thesis.

2.1 Petrographic microscopy

Several samples of previously selected meteorites were studied using three distinct petrographic microscopes. A Zeiss Scope Axio petrographic microscope, with magnifications up to 500×, and a Motic BA310Pol Binocular polarization microscope, which has a rotating platen that enables preliminary characterization of minerals using the polarizer, were used at the Institute of Space Sciences (ICE, IEEC-CSIC). Both instruments allow the identification of Regions of Interest (hereafter ROIs) for their study with other techniques. The third microscope is a Nikon Eclipse LV100NPol at the Universidad Complutense de Madrid, working with magnifications up to 600×. The combined capabilities of the three microscopes allow working with reflected light (RL), transmitted light (TL, particularly useful to recognize features on samples with a size of

tens of μm), crossed nicols (for identifying mineral phases in TL), and with bright field (high contrast and differentiation between more and less dense materials), or dark field illumination (use of scattered light to increase the visibility of low relief features). These techniques enable a great deal of information to be obtained from the ROIs. Here, the microscopes were used to take several images from each meteorite sample at different magnifications, varying between 50× and 500×, using TL whenever the samples where thin enough (in the tens of μm scale). High-resolution mosaics of each sample were built merging those detailed images, in order to use them as maps to navigate around the samples, and to establish target features and ROIs to be analyzed with other techniques. A grid (square size of 1 mm^2) was superimposed to every map, which facilitates moving around the section and positioning the interesting features.

2.2 Cathodoluminescence microscopy

A Technosyn cold cathodoluminescent (CL) MK4 microscope operated at 20–24 kV/350–400 mA was used at the Universidad Complutense de Madrid. This technique performs electron bombardment on a sample, which consequently emits light with values of intensity and wavelength that depend on its chemical composition and *crystal*lographic structure (Burns, 1993). Even trace amounts of some elements can act as activators or quenchers of CL and the energy of the electron beam can also have an influence on its emission (Götze et al., 2000; Akridge et al., 2004). Therefore, to correctly interpret CL results it is important to constrain the mineralogy of the sample being studied. For example, iron-free minerals can be particularly luminescent, as iron is a typical quencher (Burns, 1993).

2.3 Scanning Electron Microscopy

Three Scanning Electron Microscopes (SEMs) were used in order to study the microstructure of the samples: a FEI Quanta 650 FEG with a Back Scattered Electron Detector (BSED), at the Catalan Institute of Nanoscience and Nanotechnology (ICN2), a JEOL JSM7600F at the National Center for Electron Microscopy (ICTS) at the Universidad Complutense de Madrid, and a Zeiss Merlin field emission (FE) SEM at the Autonomous University of Barcelona (UAB). This type of microscope produces images by scanning the surface of a sample with a focused beam of electrons, which interact with atoms and produce signals that contain information about the sample's surface topography and composition. Nonconductive samples collect charge when

scanned by the electron beam, which can cause image artifacts, and therefore their surfaces are usually covered in an ultrathin electrically conductive coating (usually made of graphite in the case of meteorites). To avoid that, nonconductive samples can be imaged without coating using low-vacuum conditions. That was the case for the Quanta 650 SEM, which was operated in low-vacuum mode with the thin section uncoated. These microscopes can use Secondary Electron (SE) imaging, which uses the electrons generated as ionization products close to the specimen surface to produce very high-resolution images, or Back-Scattered Electron (BSE) imaging, which uses electrons reflected by elastic scattering from deeper locations within the sample to provide information about the atomic number and distribution of different elements. Both SE and BSE were used to study in detail ROIs in the sample, and at magnifications of up to 27,000×. The SEM was also used to select ROIs and points of interest for subsequent chemical analysis by electron microprobe.

2.4 Energy-Dispersive X-ray Spectroscopy

Working together with the SEMs, Energy-Dispersive X-ray Spectroscopy (EDS) was used to create elemental maps of the ROIs. Two different EDS detectors were used: an Inca 250 SSD XMax20 with a Peltier cooling, an active area of 20 mm^2, and working at accelerating voltages of 20 kV, attached to the SEM at the ICN2, and the Zeiss Merlin SEM, which also allowed for the acquisition of EDS patterns working at accelerating voltages of 15 kV. This technique focuses a high-energy electron beam into the sample, which produces the ejection of electrons from the inner shells of atoms that are consequently substituted by electrons from higher-energy shells, releasing the excess energy in the form of X-rays. The energy of those X-rays is representative of specific atomic structures, and therefore allow for measuring the elemental composition of the samples. Since the samples where uncoated, any carbon detection by EDS analysis was not from the coating. The normalization of the results was done to 100% totals.

2.5 Electron microprobe

Quantitative chemical analyses and BSE images were obtained using a JEOL JXA-8900 electron microprobe (EMP) at the Universidad Complutense de Madrid. This technique is based in the same principles operating for SEM and EDS, i.e., and electron beam focused on the sample and releasing X-rays with energies that depend in the elements being analyzed. However, while SEM and EDS are optimized in order to provide high-

resolution images, EMP is much more specialized in providing analytical results, being able to focus in much smaller points. The EMP used here is equipped with five wavelength-dispersive spectrometers, which allows for the simultaneous analysis of 5 distinct elements. It was used to obtain punctual analysis at an accelerating voltage of 15 kV, with a beam current of 10 nA, and a spot size of 1 μm. With this setup, the counting time for spot analyses is 30 seconds per element, which combined with the low voltage and beam current minimizes beam damage. Several continuous profiles (i.e., the electron beam moves describing a line and providing the composition at each step interval) were also obtained, using the same accelerating voltage but a beam current of 100 nA, and spot size and step interval of 1 μm diameter (dwell time = 1000 ms).

2.6 Micro-Raman spectroscopy

Micro-Raman spectra were acquired using a Jobin-Yvon T-64000 Raman spectrometer at the Institute of Material Sciences of Barcelona (ICMAB-CSIC). This technique uses a monochromatic light that changes the energy state of the excitations in the system (vibrations, phonons…), which produces a shift in the energy of the laser photons scattered inelastically. The specific shifts depend on the vibrational modes of the system, and therefore provide information about the materials being analyzed. The instrument used here was attached to an Olympus microscope and equipped with a liquid nitrogen-cooled CCD detector, and was operated in backscattering geometry at room temperature using the 5145 Å (green) line of an argon-ion laser. The lateral spatial resolution was ~ 1 μm, and the laser power onto the sample was maintained between 0.6 and 0.7 mW to avoid degradation or excessive heating. High-resolution spectra were acquired in working windows between 100 and 1,400 cm^{-1}. The instrument was used to better characterize mineralogy, composition and possibly also to detect shock features.

2.7 UV-Vis-NIR spectroscopy

A Shimadzu UV3600 ultraviolet-visible-near infrared (UV-Vis-NIR) spectrometer was used to obtain the reflectance spectra of meteorite samples in the 0.2 to 2.2 μm range (Moyano-Cambero et al., 2013; Trigo-Rodríguez et al., 2014a), at the Politechnical University of Catalonia (UPC). In the ultraviolet-visible spectroscopy, light in that range is used to illuminate the sample, which excites some specific electrons producing electronic transitions, and the wavelength of the reflected light is dependent on the energy gap between the excited state and the ground state. Near-infrared spectroscopy is

based in the excitations of the molecular vibrations of the system, i.e., in the excitation from the ground state to overtone or harmonic states, and how they reflect the near-infrared applied to the sample. Although is not particularly sensitive and the bands are quite broad, it penetrates deeper in the sample than the ultraviolet-visible light, and is very useful to see bulk material composition with little or no sample preparation. The spectrometer used here has multiple lamps to work in those two ranges during the same measurement. The standard stage for this spectrometer is an Integrating Sphere (which produces uniform light scattering minimizing the effect of the original light direction and conserves power, although spatial information is lost) with a working range of ~0.2 to 2.6 μm. The sample beam interacts with the section to be studied at a phase angle of 8º. For calibration of the detector a standard baseline was created using a conventional $BaSO_4$ substrate, which provides close to a 100% reflectance signal better than 1 σ. The area sampled corresponds to a slot of 1.0×0.5 cm^2. The scanned area corresponds to a 2×6 mm^2 area, which is below the size of the sample and therefore avoids any contribution from the epoxy or the glass in which the section is mounted. The spectra obtained this way typically show small baseline noise between 0.77 and 0.89 μm, and larger noise due to working under normal laboratory conditions (non-vacuum) and to system hardware between 2.2 and 2.6 μm. There are also peaks of instrumental origin between 1.4 and 1.55 μm, and between 1.9 and 2.2 μm, approximately. To avoid showing unreliable data we applied some corrections. The region between 0.77 and 0.89 μm was deleted from most spectra, but in some occasions it was approximated by the result of a polynomial equation, as we expect the spectrum there to be mainly flat and it is visually preferable. The peaks at the regions from 1.4 to 1.55 μm and from 1.9 to 2.2 correspond to an unsuccessful instrumental correction applied by the software to remove the presence of the $BaSO_4$ substrate from the final spectra. A correction was applied to the spectra in order to get rid of those peaks, but the final result in those regions became slightly noisy, which could hide some faint feature of interest. Finally, to avoid the loss of uniformity above 2.0 μm, only data up to 2.2 μm was used. With this technique, the absolute reflectance (compared to a $BaSO_4$ standard) of a meteorite section can be obtained, allowing for the comparison with the remote spectra of asteroids (Trigo-Rodríguez et al., 2014a).

2.8 IR spectroscopy

A Nicolet Fourier transform infrared (FT-IR) spectrometer, equipped with a Smart Orbit Attenuated Total Reflectance (ATR) accessory, was used to obtain the reflectance spectra of meteorite samples in the middle to far infrared range (2.5 to 30.0 μm, or 4000 to 333 cm^{-1}, approximately). This technique works similarly to near-infrared spectroscopy, although in the mid-infrared range (2.5 to 25 μm) it studies the fundamental vibrations and the rotational-vibrational structure, and in the far-infrared (above 25 μm and up to 1000 μm) it works with the rotational structure. FT-IR spectroscopy collects high spectral resolution data over a wide spectral range, using a Fourier transform to convert the raw data into a spectrum. The Smart Orbit ATR accessory uses a *crystal* to produce several reflections in the surface of the sample, and the light beam is then measured as it exits the *crystal*, which produces a high resolution spectrum, whose peaks have the same positions but different relative intensities than an equivalent absorption IR (Chemtob & Glotch, 2007). Data in this spectral range are often expressed in μm (wavelength) or in cm^{-1} (frequency, or wave number), and both units are used in this thesis to facilitate the comparison with previous and future studies. In order to use this device meteorite powders are required, which are obtained after grinding small samples (chips) with an agate mortar. The spectrometer uses a diamond-based detector, which has a wide spectral range plus a good depth of penetration, and is inert, particularly interesting feature when working with meteorites. It has a spectral resolution of ~1 cm^{-1} and the data sampling is every ~0.5 cm^{-1}. Although the spectral window of the spectrometer goes from 2.5 to 45.5 μm (4000 to 200 cm^{-1}, approximately), we discard the data above 30 μm (~333 cm^{-1}) which are much noisier or scattered (Trigo-Rodríguez et al., 2012). This kind of device is mainly used to analyze molecular structures, which allows determining the presence of organic molecules and hydrous components. It is also useful to detect *silicate* minerals, reasons why is widely used in mineralogy and geology.

2.9 Nanoindentation

An Ultra Micro Indentation System (UMIS) from Fischer-Cripps Laboratories from the Autonomous University of Barcelona (UAB) was used to measure the mechanical properties of thin meteorite samples. Nanoindentation consists in applying a controlled load into a sample through the use of a hard indenter, which in this case consists in a Berkovich pyramidal-shaped diamond tip. The indenter pushes the surface while

increasing load, up to a specific maximum load. The maximum depth achieved is then measured. When the indenter is unloaded, the sample surface pushes back due to elasticity. The obtained load-displacement curves provide information about the deformation mechanisms (elastic, and plastic), and the *elastic recovery*, through the loading and unloading curves, respectively. *Hardness* (*H*) and reduced *Young's modulus* (E_r) values can be determined from the load-displacement curves at the beginning of the unloading segment (Oliver & Pharr, 1992). The *elastic recovery* values, W_{el}/W_{tot} (where W_{el} and W_{tot} are the elastic and total indentation energies), can be evaluated from the area between the unloading curve and the displacement axis (W_{el}) and between the loading curve and the displacement axis (W_{tot}), respectively. Proper corrections for the contact area (in this case, calibrated with a fused quartz specimen), initial penetration depth, and instrument compliance, must be applied (Fischer-Cripps, 2004).

3 CARBONATES IN THE MARTIAN METEORITE ALLAN HILLS 84001

Abstract

Martian meteorites are *igneous* rocks produced in Mars, and consequently classified as achondrites. They can provide valuable information about aqueous alteration, weathering, and shock processes in planetary bodies like Mars. Indeed, Martian meteorites have already proved valuable to gain insight about past environmental conditions on Mars. In this chapter the notorious Martian meteorite Allan Hills 84001 is analyzed with several techniques. It was formed more than 4 Gyr ago, and has been extendedly studied by several authors since it was found in Antarctica in 1984. The study of this meteorite allows, then, for comparison with previous studies, and therefore gaining expertise using multiple laboratory techniques to analyze the samples. Also, it is particularly interesting considering the formation age of the samples, as it is representative of the old Martian crust and reflects a very early epoch in Mars, not very long after the formation of the planet itself and possibly coincidental with the *Late Heavy Bombardment*, in which a considerable amount of chondritic asteroids would have impacted Mars. It is therefore an example of the final stage of the planetesimals that reached differentiation. This *orthopyroxenite* contains several features of great interest in the study of meteorites: a highly fractured texture bearing shocked minerals, gases trapped during one or more impact events or during formation of the rock, and

spherical Fe-Mg-Ca *carbonates*. These *carbonates* were formed under the presence of liquid water, and therefore its study provides clues about the presence of water on the early stages of Mars, and about the aqueous alteration in meteorites. This chapter focuses on the formation context of these *carbonates* using a range of techniques, in order to explore whether they record multiple precipitation events. The petrographic features and compositional properties of these *carbonates* indicate that at least two pulses of Mg- and Fe-rich solutions saturated the rock. Those two generations of *carbonates* can be distinguished by a very sharp change in compositions, from being rich in Mg and poor in Fe and Mn, to being poor in Mg and rich in Fe and Mn. Between these two generations of *carbonate* is evidence for fracturing and local corrosion. It is a clear example of features that can provide clues on floods in the early Mars. The results of this chapter have been published in *Meteoritics and Planetary Science* (Moyano-Cambero et al., 2017b).

3.1 Introduction

Most Martian meteorites are *igneous* achondrites. A possible exception is Northwest Africa (NWA) 7034 (and paired meteorites), whose classification is debated, although it is officially described as a *basaltic* breccia (Agee et al., 2013). Historically the Martian meteorites have been referred to as 'SNC', although it is now known that some of them do not fit into the three traditional families referenced by the acronym: shergottites, nakhlites, and chassignites (Mittlefehldt, 1994; Agee et al., 2013). Martian meteorites have a characteristic mineralogy, bulk chemistry, and oxygen isotope composition (with NWA 7034 and its pairs being an exception, according to Agee et al., 2013) that distinguish them from other extraterrestrial rocks (McSween, 1994; Treiman et al., 2000). The incontrovertible evidence of their Martian origin is the isotopic composition of trapped gas in shock-formed *glass*, which matches that of the planet's atmosphere as measured by the Viking lander (Owen et al., 1977; Bogard & Johnson, 1983).

Allan Hills (ALH) 84001, a 1.93 kg meteorite that was found in Antarctica in 1984, is studied on this chapter. It was ejected from Mars 15 Myr ago (Nyquist et al., 2001), and fell to Earth ~13,000 years ago (Jull et al., 1995). Several different *crystallization* ages have been reported for ALH 84001 (Nyquist et al., 2001; Lapen et al., 2010), thus highlighting the difficulty in dating a meteorite in an open system with a complex post-*crystallization* history including aqueous alteration and shock metamorphism (Treiman, 1998). It is accepted by the scientific community that ALH 84001 is the oldest known

Martian meteorite, with the only exception being some older materials found in the Martian breccia NWA 7533, probably paired with NWA 7034 (Humayun et al., 2013). It formed ~4.1 Gyr ago (calculated using ^{176}Lu-^{176}Hf chronometry by Lapen et al., 2010), and during a period of intense bombardment (Frey, 2008). Therefore, ALH 84001 is a fragment of Noachian crust (oldest Martian terrains, formed 4.5 to 3.5 Gyr ago), which forms the ancient highlands of Mars (Hamilton et al., 2003). As this meteorite the only non-brecciated sample we have of the oldest Martian crust, it is a very valuable source of information about the earliest conditions and subsequent evolution of Mars (Bridges et al., 2001).

Once it was recognized as a Martian meteorite, ALH 84001 was classified as an *orthopyroxenite* (the only one found so far), and therefore is not part of the traditional SNC family (Mittlefehldt, 1994). It contains 97 vol. % of *orthopyroxene* ($Fs_{27.3}Wo_{3.3}En_{69.4}$) as grains up to 6 mm in size. Other constituents include 2 vol. % of *euhedral* to *subhedral chromite* clasts, and 1 vol. % of *augite*, *olivine*, *pyrite*, *apatite*, *plagioclase* (mostly transformed into *maskelynite* or *glass*, by shock), *phosphate* and SiO_2 (Mittlefehldt, 1994). The minor minerals in this meteorite are mostly remnants of trapped interstitial melt.

ALH 84001 has a highly fractured texture (Figure 3.1), most probably due to progressive deformation by impacts while it was still on Mars (Treiman, 1995). In fact, the meteorite has a complicated shock history, which may have moved it progressively closer to the spallation zone of the impact that ejected it (Melosh, 1984). At least two impact events are responsible for its shock features (Treiman, 1995); the first event led to brecciation and relocation of the rock closer to the planet's surface, and the second higher intensity event transformed *plagioclase* into *maskelynite* or shock-modified *plagioclase glass*. As a consequence, it has been affected by shock-induced metamorphism. The *orthopyroxene* and *chromite* in ALH 84001 are in cumulus phases due to the formation of discrete *crystals* forming a primary precipitate during slow cooling in a surrounding magma, conforming thus to an *orthopyroxene* adcumulate (for a description of *igneous cumulates* see e.g. Hall, 1987). The uniform chemical composition of the *pyroxene* could indicate that ALH 84001 cooled more slowly than other Martian meteorites during magmatic or *metamorphic recrystallization* (Mittlefehldt, 1994), probably at a depth of ~40 km (Kring & Gleason, 1997).

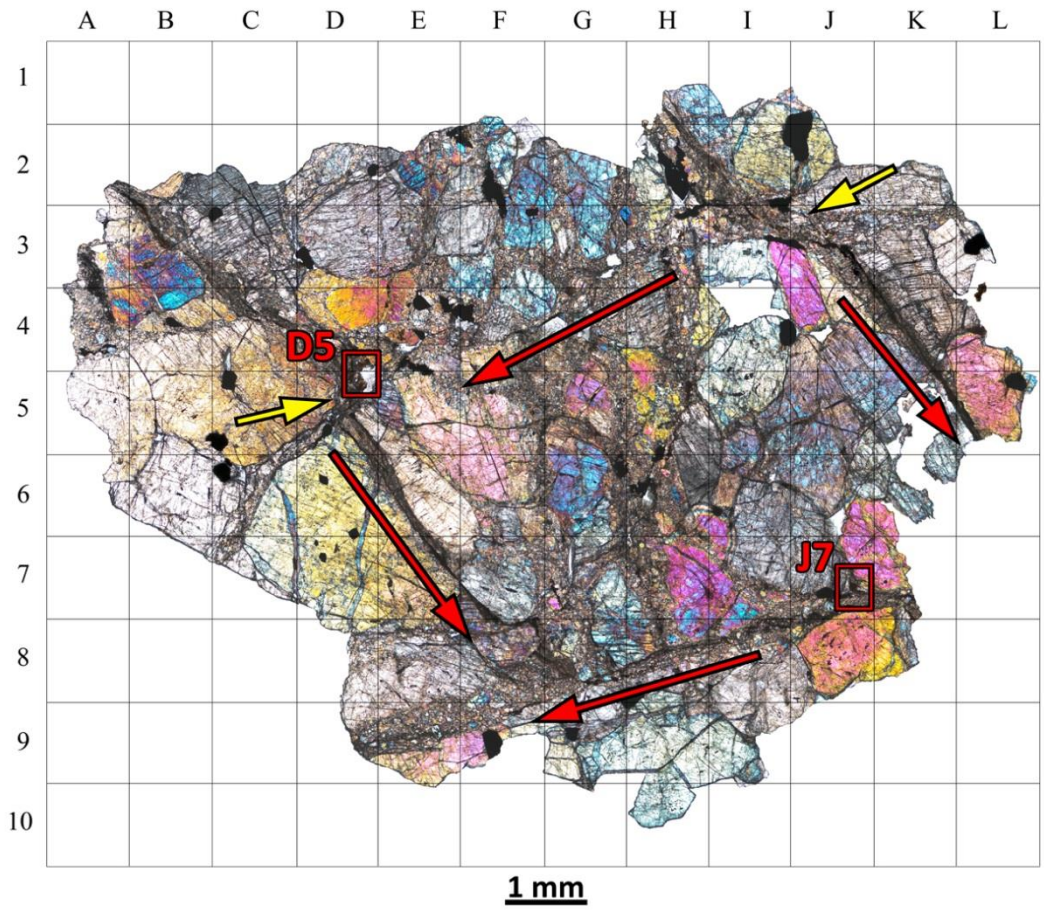

Figure 3.1: High resolution TL with crossed nicols mosaic of the ALH 84001,82 thin section. Red arrows show the orientations of the two main fracture systems. Yellow arrows point to where the fractures intersect. D5 and J7 are the two *carbonate*-containing regions studied.

One of the most interesting features of ALH 84001 is the presence of Mg-Fe-Ca *carbonates* along fractures and in cataclastic areas (Scott et al., 1998). The study of Martian *carbonates* is important as these minerals precipitate from aqueous fluids and thus can be used to explore the history of water at the planet's surface and crust (Bridges et al., 2001; Tomkinson et al., 2013). *Carbonate* outcrops have been found on the Martian surface by orbiters, landers and rovers (Bandfield et al., 2003; Ehlmann et al., 2008; Boynton et al., 2009; Morris et al., 2010). *Carbonate* deposits that may represent sites of paleolakes support the idea that Mars had a warmer and wetter past (Wray et al., 2011). In particular, the amount of *carbonates* present at the surface are a powerful tool for understanding the duration of the warmer and wetter period of Martian history. Additionally, *carbonates* can contain microstructures that form by high shock

pressures and temperatures, thus enabling them to be used to explore the magnitude and frequency of impact events (Treiman, 1998).

The *carbonates* in ALH 84001 are known to be Martian because they are cut by and predate some of the fractures mentioned previously, and so have received considerable attention. The detailed study by Corrigan & Harvey (2004) described them as "rosettes" (here termed "globules"), planiform "slabs", "post-slab" *magnesites*, and as interstitial *carbonates*, but they have been classified in several other ways (e.g. Saxton et al., 1998; Scott et al., 1998; Holland et al., 1999; Corrigan et al., 2003; Niles et al., 2005; Meyer, 2012, and references therein). One early interpretation of their origin was that it was associated with early biologic activity on Mars (McKay et al., 1996), but subsequent studies have shown that their precipitation can also be explained by abiotic processes (Scott et al., 1998; Warren, 1998; Golden et al., 2001; Treiman et al., 2002; Corrigan & Harvey, 2004; Steele et al., 2007; Niles et al., 2009; Meyer, 2012). However, what make these *carbonates* objectively interesting are their formation process and their ~3.9 Gyr age (calculated using ^{87}Rb-^{86}Sr chronometry by Borg et al., 1999). The anomalies in magnetization of these *carbonates* could indicate that the Martian magnetic field shut off between the formation of these *carbonates* and the transition from the late Noachian to Hesperian, ~3.5 Gyr ago (Weiss et al., 2002). ALH 84001 is not the only Martian meteorite containing *carbonates*, since they have also been described in the much younger nakhlites (Carr et al., 1985; Bridges & Grady, 2000; Tomkinson et al., 2013). However, and although the formation process for those *carbonate* could be fairly similar (Bridges & Grady, 2000; Bridges et al., 2001), their petrography and composition are clearly different (Tomkinson et al., 2013). This is why this chapter focuses in the study of the *carbonates* in ALH 84001, since they are much older evidence of water availability in Mars and, therefore, provide information about the conditions on Mars long before the *carbonates* found on nakhlites were formed (Bridges et al., 2001).

The distribution of *carbonates* throughout ALH 84001 provides clues about the environmental conditions under which they formed, and can help to establish a link to the *carbonates* that have been found at the surface of Mars. Following several studies, two main formation scenarios at ~3.9 Gyr have been proposed: (i) precipitation at low temperature (e.g., Treiman, 1995; McKay et al., 1996; Valley et al., 1997; Golden et al., 2000; Eiler et al., 2002; Halevy et al., 2011); (ii) precipitation from a fluid with high

concentrations of CO_2, possibly over a short time, at high temperatures (e.g., Mittlefehldt, 1994; Harvey & McSween, 1996; Scott et al., 1997; Scott et al., 1998). This second scenario may have been the consequence of an impact event and subsequent hydrothermal activity (Harvey & McSween, 1996; Treiman et al., 2002), or *crystallization* of shock melted material (Scott et al., 1997; Scott et al., 1998). The terrestrial *carbonates* described in Treiman et al. (2002) support, by analogy, formation due to Martian hydrothermal processes. Indeed, the *carbonates* found in ALH 84001 are compositionally different from the common *carbonates* (or any of their solid solutions) found on Earth (Moyano-Cambero et al., 2017b). In fact, there are just a few regions on Earth where similar (but not identical) *carbonates* occur (Treiman et al., 2002), and they are out of the range of terrestrial *carbonate* solids solutions. This chapter provides complementary information for the multi-generational *carbonate* model that was described by previous authors (e.g., Corrigan & Harvey, 2004). Indeed, textural and compositional evidence for precipitation of the *carbonates* by at least two different fluids are described here (Moyano-Cambero et al., 2017b).

3.2 Sample selection and experimental techniques

The meteorite selected for this study, ALH 84001, was found in the Far Western Icefield of Allan Hills by the Antarctic Search for Meteorites (ANSMET) program in 1984. A preliminary study provided a terrestrial weathering degree of A/B (minor to moderate rust acquired while on Earth) and a 'fracturing category' of B, which is equivalent to an S4-5 shock grade of the classification used currently (Score & Macpherson, 1985). The NASA Johnson Space Center (JSC), responsible for the curation of the ANSMET collection, provided the 30 μm thin section ALH 84001,82 (see Meyer, 2012, for the specific location of this sample in the original rock). In order to comprehensively characterize *carbonates* in this sample, several laboratory techniques were used: TL and CL microscopy, EMP, micro-Raman spectroscopy, SEM and EDS.

The three petrographic microscopes described in chapter 2 were used to observe the sample with detail, which allowed for selection of the regions to be studied with other techniques. First, 500× RL and TL images of the whole ALH 84001,82 section were obtained. The TL images were merged to create a high-resolution mosaic to be used as a reference map (Figure 3.1). The petrographic microscopes also allowed observing the results of applying CL to the sample. This technique is of great interest for the study of

the *carbonates* in ALH 84001, since they are zoned, with some layers being particularly Mg-rich and Fe-poor (Saxton et al., 1998). Being iron a typical quencher of CL, iron-free minerals can be particularly luminescent (Burns, 1993), and therefore those Fe-poor layers should show a red luminesce (Akridge et al., 2004). To show that, a CL mosaic of the thin section was created, and higher magnification and resolution images were obtained (Figure 3.2 and Figure 3.3).

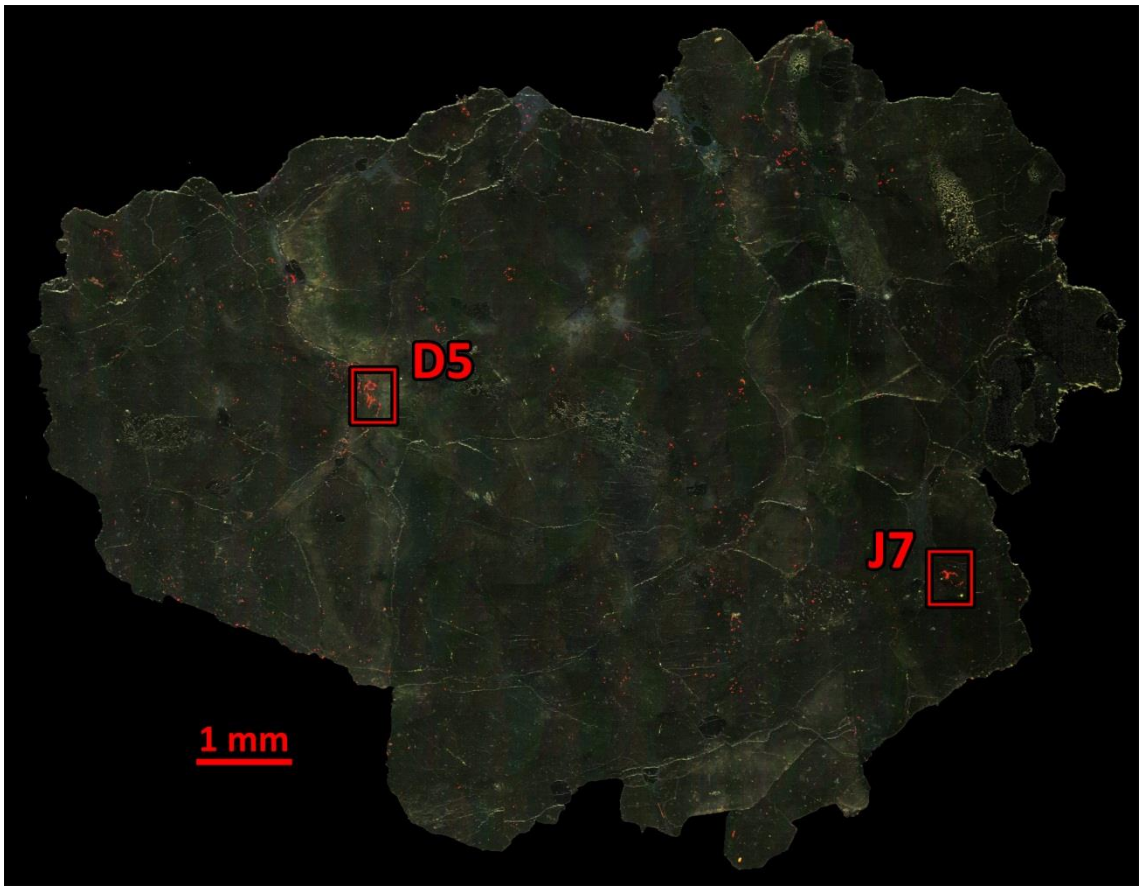

Figure 3.2: High resolution CL mosaic of the ALH 84001,82 thin section that can be compared directly with Figure 3.1. Bright red areas correspond to very Fe-poor and Mn-rich layers in *carbonates*.

The two SEMs from ICN2 and ICTS were also used with this sample. SE and BSE imaging allows for observing the sites of interest previously identified with the petrographic microscopes and CL technique, at magnifications up to 27,000×. Combined with EDS, illustrative elemental maps of the regions of interest were constructed (Figure 3.4), but this technique was not used to perform quantitative

chemical analyses. Instead, SEM was used in order to select the regions where chemical analysis by EMP should be performed.

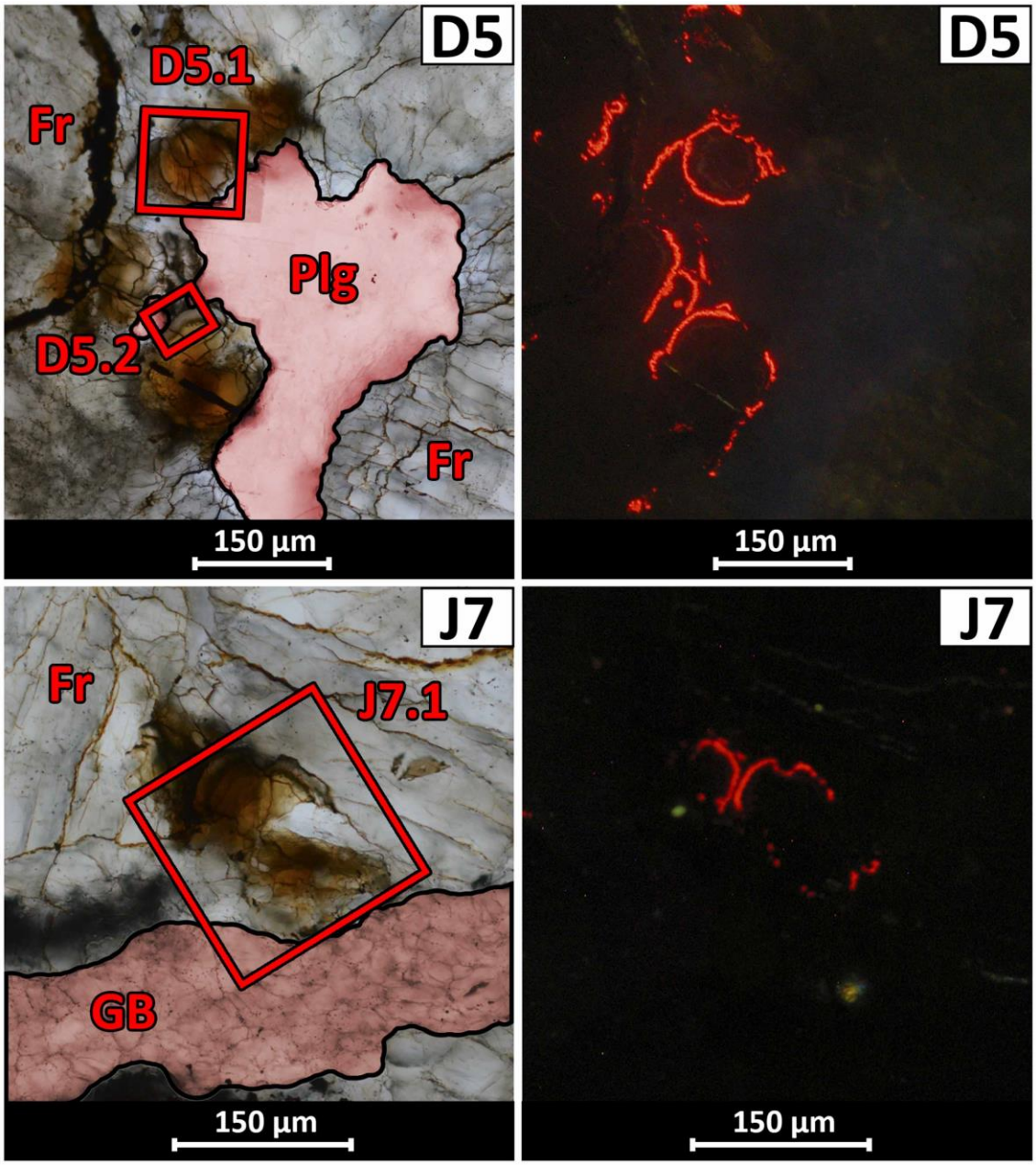

Figure 3.3: Detail of the two regions of interest highlighted in Figure 3.1 and Figure 3.2 (D5 and J7); TL left, CL right. *Carbonates* are the brown to orange areas in TL, while their Fe-poor and Mn-rich layers are the red rims in CL. In the TL images we draw attention to the fractures around regions where the *carbonates* are present (Fr). The *maskelynite* or shock modified *plagioclase glass* solidified in a fracture or pore after formation of the *carbonates* at D5 (Plg, highlighted in red), and in one of the so-called granular bands (Mittlefehldt, 1997) next to the

carbonate **at J7 (GB, painted in red). Three areas that are in some of the later Figures (D5.1, D5.2 and J7.1) are also highlighted.**

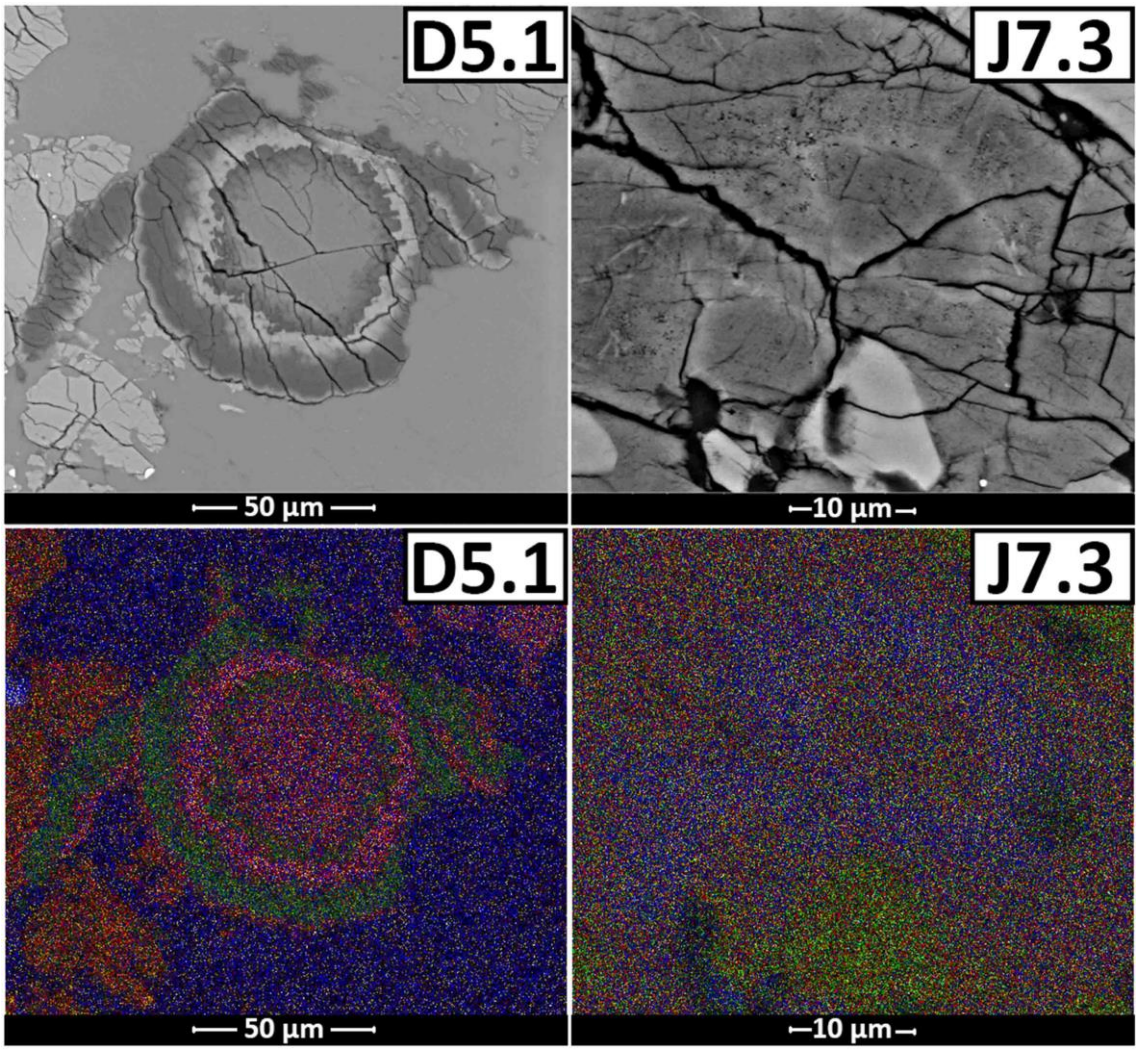

Figure 3.4: BSE images of the areas D5.1 and J7.3 (see Figure 3.3Figure 3.2 and Figure 3.5 for the location of J7.3) with corresponding EDS maps revealing the distribution of Ca (blue), Fe (red), Mg (green) and Mn (yellow). In D5.1, the Fe-rich and Mg-rich rims of the *carbonate* can be clearly observed. Also note that the outer layers of the globules are partially corroded, and that the surrounding mineral (*maskelynite*, or shock modified *plagioclase*) incorporates fragments of the *carbonate*. In J7.3 the *carbonate* is compositionally more homogeneous, apart for the most outer part of layer #2 (see J7.3 in Figure 3.8), whose Ca-rich composition is shown more clearly by the EDS map than by the BSE image.

Once the regions that showed potential for the goals of this study had been selected, both micro-Raman and EMP analysis could be performed. Micro-Raman microscopy was used to better characterize the composition of the *carbonates* and possibly also to detect shock features (Figure 3.5). With the EMP more than 160 spot analyses and several line profiles from the *carbonate* globules were acquired (Figure 3.6). The standards used were *siderite* for Fe and Mn, and *dolomite* for Mg and Ca. Measured precision was better than ± 0.0014% for Mg, ± 0.009% for Ca, ± 0.005% for Fe, and ± 0.19% for Mn. Detection limits were 150–180 ppm for Mg, 150–200 ppm for Ca, 350–500 ppm for Fe and 400–510 ppm for Mn. Elemental compositions were given as element oxides % and were recalculated to mole % of $MgCO_3$, $CaCO_3$, $FeCO_3$ and $MnCO_3$.

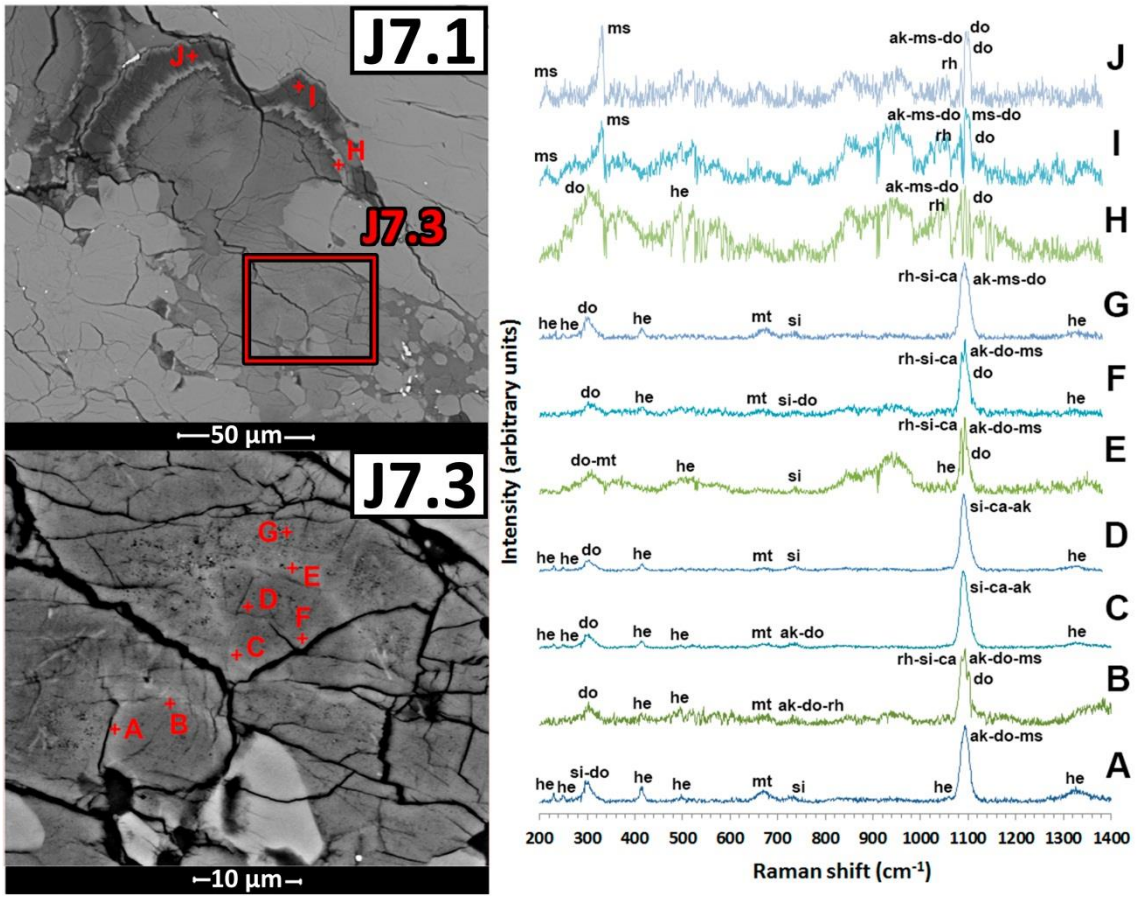

Figure 3.5: BSE images of areas J7.1 and J7.3 (see Figure 3.3), where Raman spectroscopy was performed (left) and corresponding Raman spectra (right). The minerals that match each peak have been suggested (according to the data in the RRUFF catalogue, Lafuente et al., 2015): ms (*magnesite*), ak (*ankerite*), do (*dolomite*), rh (*rhodochrosite*), he (*hematite*), mt (*magnetite*), si (*siderite*), ca (*calcite*). The positions of the peaks are listed in Table 3.1.

3.3 Results

This work has focused on *carbonates* in the regions marked D5 and J7 on the TL and CL high-resolution mosaics (Figure 3.1, Figure 3.2, and Figure 3.3). D5 contains abundant *carbonate* globules attached to the walls of a former pore (Figure 3.3), while J7 is a large globule that lies next to a granular band (Figure 3.3), and has a rhombohedral core (J7.3 in Figure 3.4, Figure 3.5, Figure 3.6, and Figure 3.7). In these regions, both of which are close to fractured areas, the space between *carbonate* globules contains *maskelynite*, which has probably formed by shock transformation of *plagioclase* (Figure 3.3)

Table 3.1: Position (in cm^{-1}) of the main peaks found by Raman spectroscopy (see Figure 3.5). Those in bold were clearly distinguishable from noise before the background was removed. Other minor peaks, plus some whose origin was not determined, are not listed.

Point	Detected Peaks on Each Point													
A	n.d.	230	250	296	415	498	670	733	n.d.	n.d.	1094	n.d.	n.d.	1326
B	n.d.	229	253	303	414	496	679	722	n.d.	1086	1094	1100	1103	n.d.
C	n.d.	229	250	303	413	497	668	725	n.d.	n.d.	1090	n.d.	n.d.	1326
D	n.d.	229	249	303	416	500	681	735	n.d.	n.d.	1090	n.d.	n.d.	1323
E	n.d.	n.d.	247	310	n.d.	507	658	734	1056	1086	1093	1099	n.d.	n.d.
F	n.d.	n.d.	n.d.	303	415	497	670	730	n.d.	1087	1093	n.d.	1102	1314
G	n.d.	234	249	302	415	n.d.	675	734	n.d.	1088	1093	n.d.	n.d.	1333
H	n.d.	n.d.	n.d.	303	n.d.	497	658	734	1057	1085	1093	1094	1103	1332
I	216	n.d.	n.d.	331	n.d.	497	660	n.d.	1056	1085	1095	1098	1103	1330
J	214	n.d.	252	332	n.d.	497	663	736	1055	1085	1096	1100	1102	1326

n.d. = not detected.

3.3.1 Petrographic context and microstructures of the carbonates

Two main fracture orientations can be identified in Figure 3.1; one is aligned NNW-SSE, and the other ENE-WSW. As the ENE-WSW fractures cross-cut and displace the other set, they must be younger (Figure 3.1). CL imaging highlights some of the layers in *carbonates* by their high intensity of red luminescence in comparison to the rest of the sample (which is largely non-luminescent; Figure 3.2). The high CL intensity is inferred to be the consequence of a particularly low content of Fe, which would otherwise quench the Mn–activated luminescence (Machel et al., 1991). Areas with blue to grey CL (pale areas under TL) are *maskelynite* or *plagioclase glass* (Plg in Figure 3.3). Non-luminescent grains are *chromite* (a few can be seen in Figure 3.2). As expected, *carbonates* were found in or close to fractures, and also dispersed throughout the meteorite (Figure 3.1, Figure 3.2, and Figure 3.3).

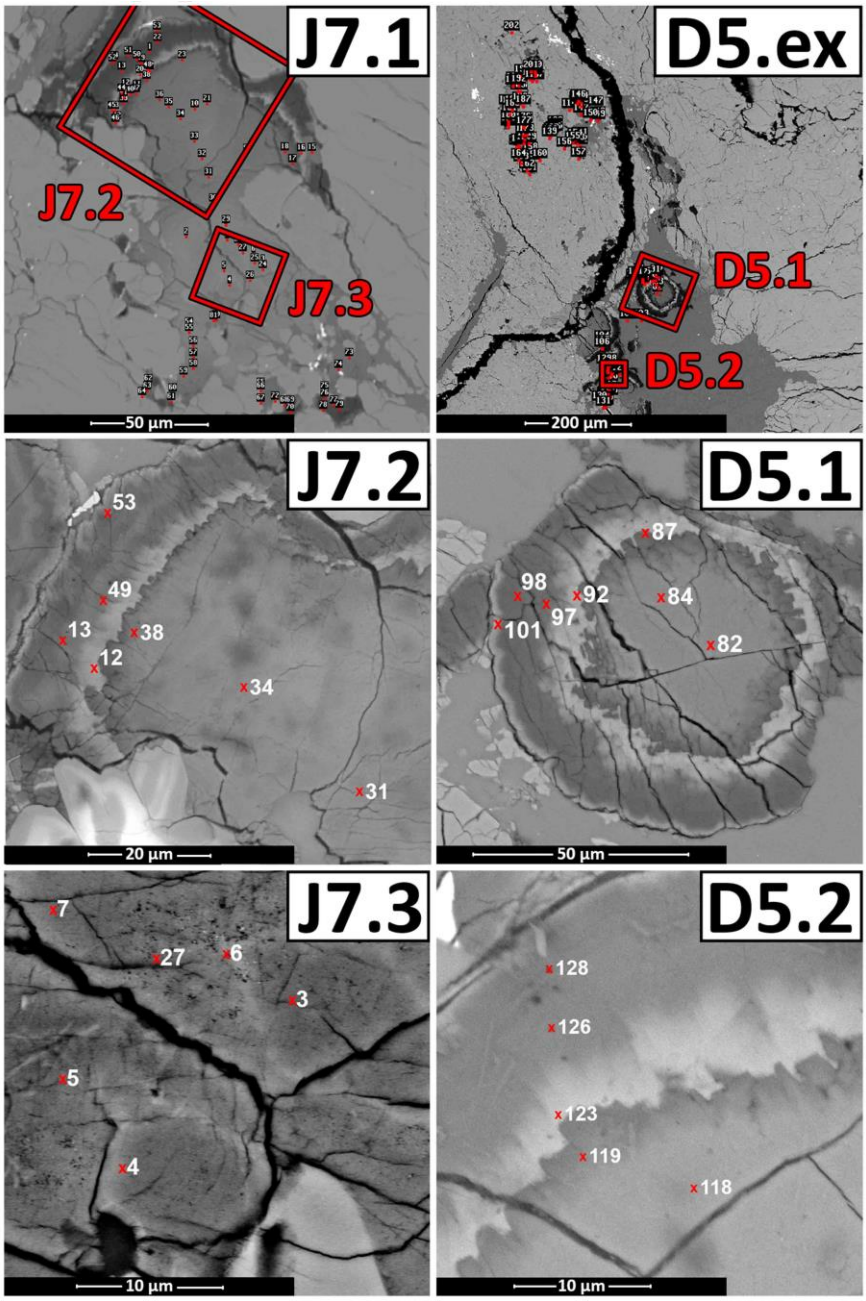

Figure 3.6: BSE images of the *carbonate* globules studied, including the locations of the 160 microprobe spots. J7.1 is highlighted in Figure 3.3, and J7.2 and J7.3 are showing detail of this area. D5.ex is a region showing D5 (see Figure 3.1, Figure 3.2, and Figure 3.3) but also the area above, where some *carbonates* were analyzed. D5.1 and D5.2 are also showing specific areas in greater detail, and both were already highlighted in Figure 3.3. All the data obtained are shown in Figure 3.11. Only some example points can be seen in J7.2, J7.3, D5.1, and D5.2; the data obtained from these points are listed in Table 3.2.

Table 3.2: Chemical compositions obtained from the *carbonate* globule by EMP analyses in Figure 3.6.

Point	Layer	$MgCO_3$	$FeCO_3$	$CaCO_3$	$MnCO_3$

31 (J7.2)	#3	57.91	30.89	10.38	0.81
34 (J7.2)	#3	57.86	31.04	10.33	0.77
38 (J7.2)	#3	71.00	22.19	6.38	0.43
12 (J7.2)	#5	36.21	52.07	9.97	1.75
49 (J7.2)	#6	89.26	7.46	3.26	0.01
13 (J7.2)	#6	91.80	4.75	3.41	0.04
53 (J7.2)	#7	81.94	11.62	6.01	0.43
3 (J7.3)	#1	50.80	32.43	14.53	2.23
4 (J7.3)	#1	50.41	32.38	14.60	2.60
6 (J7.3)	#2	45.18	33.68	16.63	4.52
27 (J7.3)	#2	40.31	30.15	22.96	6.58
5 (J7.3)	#2	38.21	29.86	24.64	7.29
7 (J7.3)	#3	50.20	32.25	15.01	2.53
82 (D5.1)	#3	60.86	30.02	8.87	0.25
84 (D5.1)	#3	66.24	25.95	7.26	0.54
87 (D5.1)	#4	87.79	8.39	3.46	0.35
92 (D5.1)	#5	60.49	32.45	6.17	0.89
97 (D5.1)	#6	86.65	8.62	4.62	0.11
98 (D5.1)	#6	93.96	1.11	4.79	0.13
101 (D5.1)	#7	77.37	15.58	6.27	0.77
118 (D5.2)	#3	65.34	27.21	7.05	0.40
119 (D5.2)	#4	85.06	9.61	5.19	0.14
123 (D5.2)	#5	43.46	45.43	9.31	1.80
126 (D5.2)	#6	91.49	4.86	3.56	0.09
128 (D5.2)	#6	92.51	0.78	6.52	0.19

The values are mole *% carbonates*.

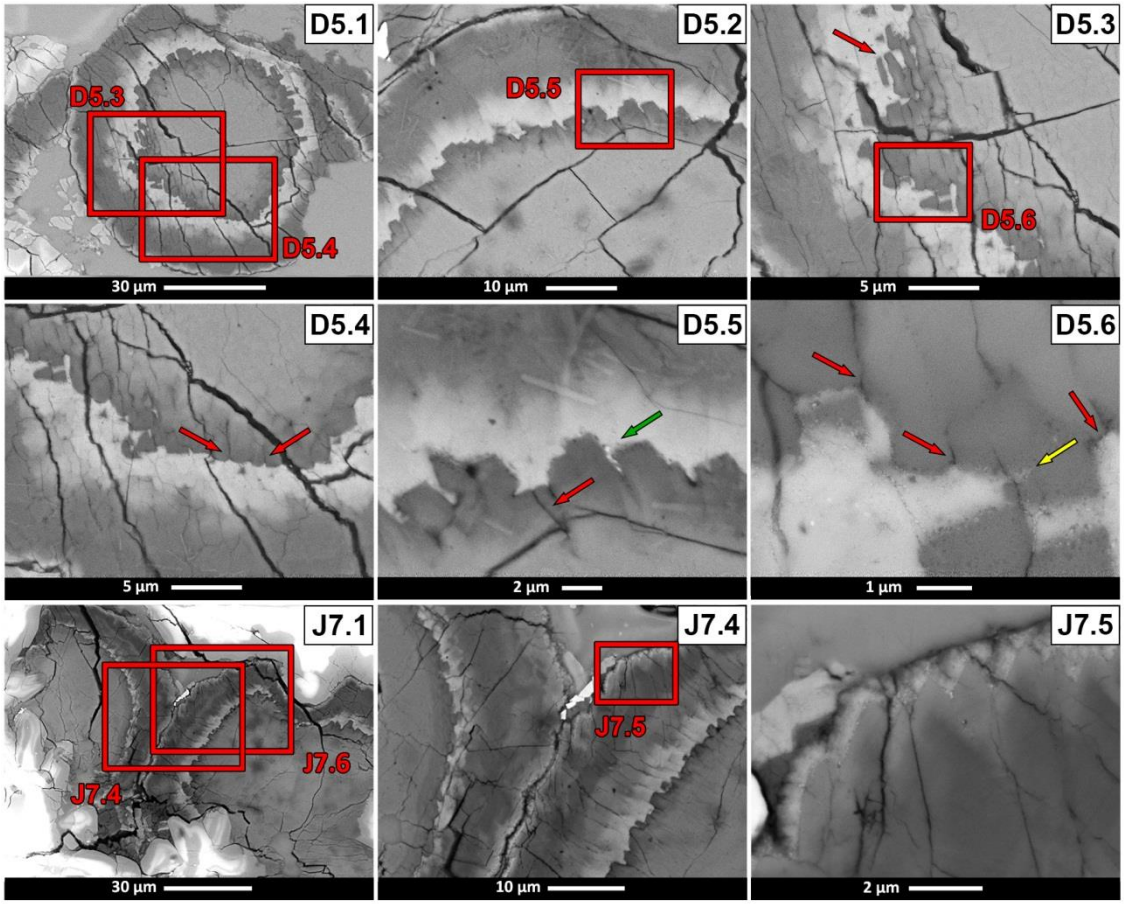

Figure 3.7: Detailed BSE images showing the boundary features between layers #4 and #5 (D5.1-D5.6) on *carbonate* globules (see also D5.1 in Figure 3.8). Red arrows point to the small fractures that terminate at the end of layer #4. The green arrow indicates small high atomic number inclusions. The yellow arrow shows corrosion at the end of layer #4. J7.1, J7.4 and J7.5 show the complex gradation in color (and composition) between layers #5 and #7 (see J7.6 in Figure 3.8).

In regions where the two fracture systems cross-cut, globules seem to be bigger and more abundant, (e.g., D5), and *plagioclase* is also more abundant (Figure 3.1, Figure 3.2, and Figure 3.3).

SEM work shows that the *carbonate* globules are characterized by a very clear and previously well documented zonation that divides them into several 'layers' (Saxton et al., 1998; Holland et al., 1999; Golden et al., 2001; Corrigan & Harvey, 2004). This zoning can be readily characterized by BSE imaging (Figure 3.4, Figure 3.5, Figure 3.6, and Figure 3.7) and EDS element mapping (Figure 3.4). The layers are differentiated using the scheme in Figure 3.8. The pattern of layering is comparable between globules, although in J7 the oldest part can be recognized (J7.3 in Figure 3.4, Figure 3.5, Figure

3.6, and Figure 3.8). A preliminary description of this 'core' was provided by Moyano-Cambero et al. (2014). It is likely to be equivalent to the central regions of other globules, but is surrounded by a thin rim that is lighter grey in BSE images (and therefore has a higher mean atomic number). The core has a rhombohedral shape, which is consistent with the *carbonate* solid solutions (i.e., *calcite*, *siderite*, *magnesite*, *rhodocrosite*, *ankerite* or *dolomite*). Hereafter the core and its rim are described as layers #1 and #2, respectively (see J7.3 in Figure 3.8). Layer #2 is followed by a much thicker and uniform layer (#3) that is comparable to layer #1 in BSE images (see J7.6 in Figure 3.7 and Figure 3.8). Layer #3 is equivalent to the first-formed zone that has been distinguished in other globules found in this sample (e.g., D5.1 in Figure 3.4, Figure 3.5, Figure 3.6, and Figure 3.7), which is also called layer #3 (Figure 3.8). *Carbonate* globules in the two selected areas (D5 and J7) gradually become darker in BSE images (lower in mean atomic number) until their *euhedral* terminations at the margins of layer #4 (Figure 3.7 and Figure 3.8). It is interesting to note the presence of small fractures that terminate at the end of layer #4 and do not affect layer #5 (Figure 3.7). Also, it was observed that although the boundary between layers #4 and #5 is mostly *euhedral*, in some areas a small-scale corrosion can be seen affecting the outermost part of layer #4 (Figure 3.7). Layer #5, distinctive in BSE images, gradually grades into layer #6, which has a lower mean atomic number. Finally, the zonation ends in a very thin and clear area (layer #7), although it is not present in all globules (Figure 3.8). At the boundaries between layer #4 and #5, and between #6 and #7, are small inclusions of high atomic number, which are petrographically compatible with Fe oxides and *sulfides* (Figure 3.7, D5.5). However, the very small size of these minerals (<500 nm) meant that they could not be characterized properly. Nevertheless, the areas containing these minerals have overall higher content of Fe than the surrounding *carbonate*, and lower concentrations of Na, Cr and locally S (less than 1%), which are not detected in the surrounding *carbonate*.

3.3.2 Carbonate and oxide mineralogy

The micro-Raman spectrometer was used to analyze the *carbonates* in J7 (Figure 3.5). Crystalsleuth software (Laetsch & Downs, 2006) was used to compare the spectra obtained with those in the RRUFF catalogue (Lafuente et al., 2015), and to remove the background from the spectra. As a consequence, the particularly fluorescent spectra obtained at points H, I and J were very noisy, but interesting features could nonetheless be distinguished (Figure 3.5). The main peaks obtained (Table 3.1) are not easily

attributed to a specific *carbonate* mineral. As shown in Figure 3.5 several minor peaks (~230, 250, 300, 415 and 1320 cm^{-1}) can be related to *hematite*, which is consistent with previous studies suggesting the presence of *microcrystalline* grains of this mineral within the *carbonates* (Steele et al., 2007). The peak that occurs in all the spectra at ~300 cm^{-1}, which is common in *carbonates* but varies with composition, can be modified by one peak of *hematite* existing at approximately the same wavenumber. Therefore, and although in most cases they seem similar to the *dolomite* peak, the exact position of this peak cannot be truly associated to that of a specific *carbonate* mineral (except for I and J, where the typical 330 cm^{-1} peak of *magnesite* can be clearly recognized). The peak at ~730 cm^{-1} also proved to be difficult to attribute, as most spectra show Raman shifts that are too high compared to the common values for *carbonates*. This is why in Figure 3.5 those peaks are mainly associated with *siderite*, because it is the *carbonate* showing a highest shift for this peak. Something similar happens with the peak at ~1100 cm^{-1}. Apart for a minor possible influence of *hematite* in the peak position, all the analyzed points (apart for A, C and D) show between 2 and 4 peaks in the 1085 to 1103 cm^{-1} region (Table 3.1). Also of interest is a peak at between 660 and 680 cm^{-1} that can be clearly distinguished in several of the spectra (Figure 3.5) and is interpreted to indicate the presence of *magnetite*, whose most prominent peak is at ~660 cm^{-1}. This finding of *magnetite* is consistent with previous studies (McKay et al., 1996; Cooney et al., 1999), although according to our Raman results it seems to be present all around the *carbonate* at J7 (Figure 3.5).

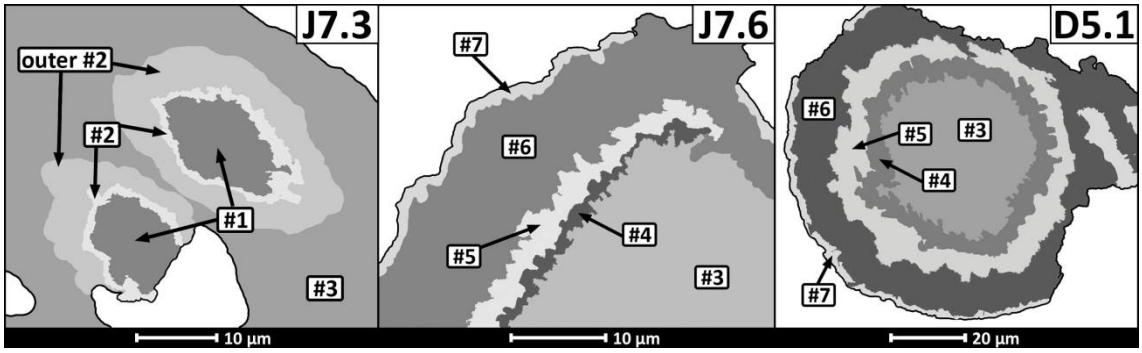

Figure 3.8: Schematic images showing the different layers in the *carbonates* studied. The area indicated as 'outer #2' is the portion of layer #2 that is distinguishable as a blue ring in the element map (Figure 3.4).

3.3.3 Carbonate compositional zoning

EDS element maps of D5.1 (Figure 3.4) show the alternating Fe-rich (red) and Mg-rich (green) nature of the layers. The ~160 points analyzed with EMP were used to quantify *carbonate* chemistry (Figure 3.6) and to show the progressive compositional trends in the globules. The overall composition of each layer is shown in Table 3.1 and the microprobe profiles and spot analyses of globules D5 and J7 are in Figure 3.9 and Figure 3.10, respectively. A subset of these data (the spots marked at J7.2, J7.3, D5.1 and D5.2 in Figure 3.6) are listed in Table 3.2.

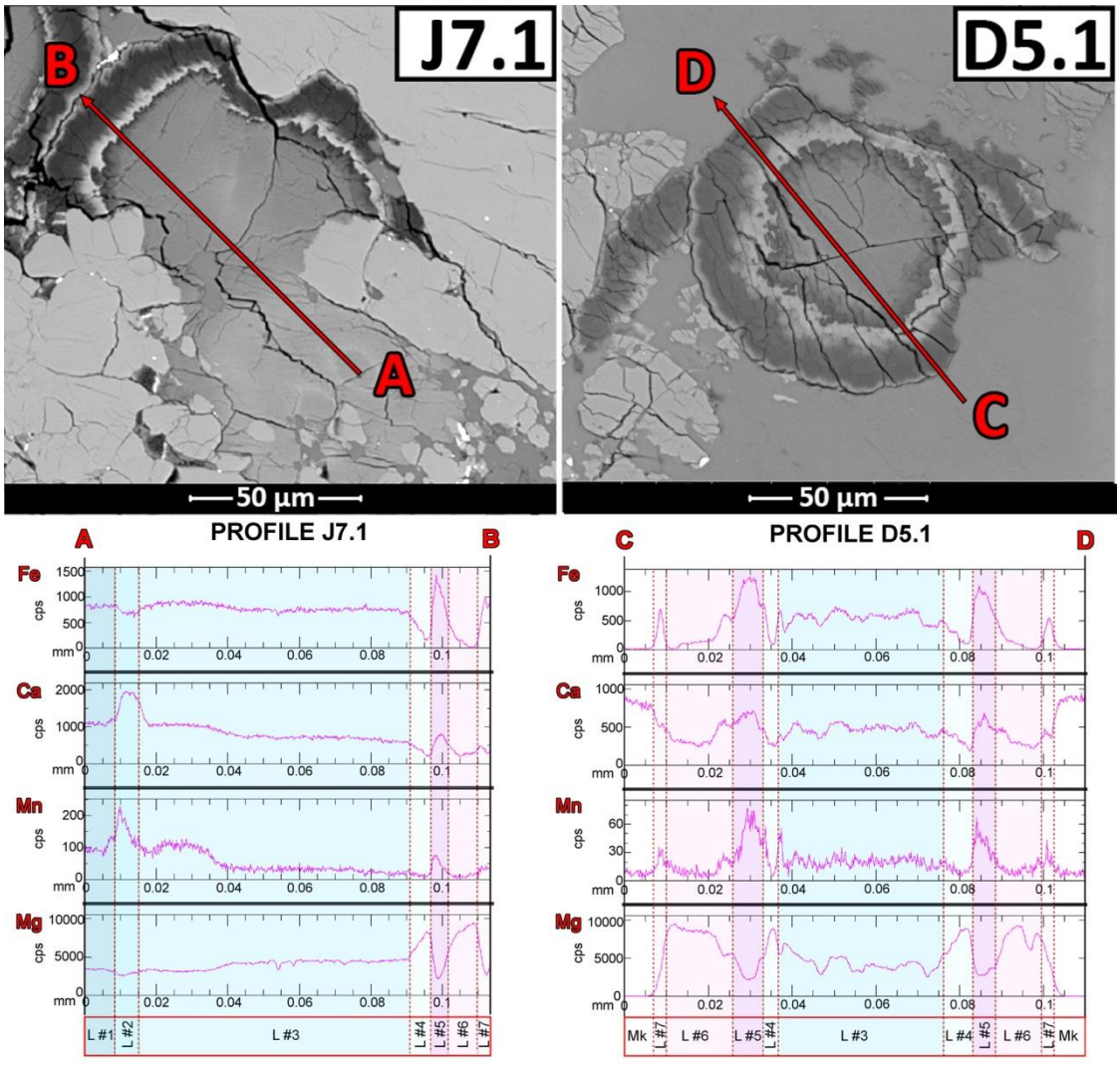

Figure 3.9: Elemental profiles obtained by EMP showing progressive geochemical variations along two globules. In the upper part the lines along which the profiles where obtained are indicated, in J7.1 and D5.1. Cps: counts per second; L: layer; Mk: *maskelynite* (or shock modified *plagioclase glass*).

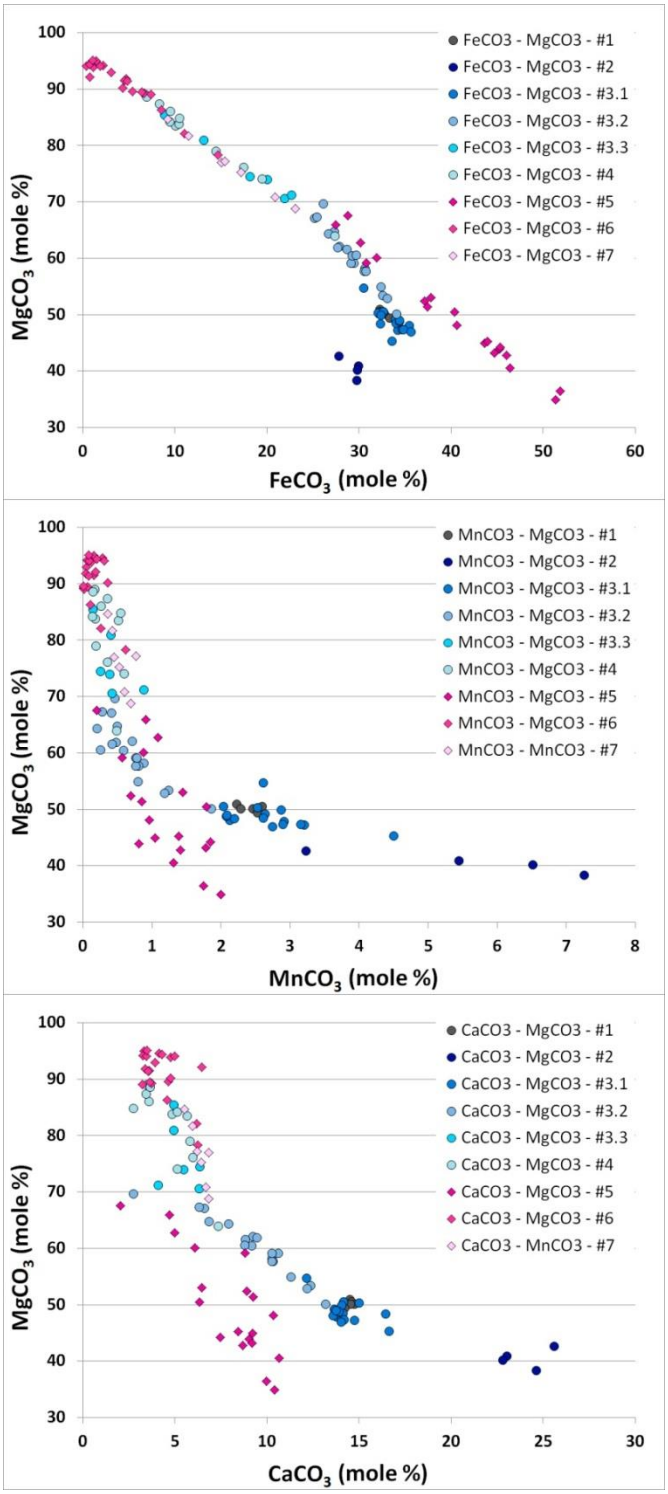

Figure 3.10: Plots of $MgCO_3$ versus $FeCO_3$, $MnCO_3$ and $CaCO_3$ (in mole %) derived from microprobe analyses (see J7.1 and D5.ex in Figure 3.6). Each layer is marked with a different colour. Also, layers #1 and #4 are represented by bluish circles, while layers #5 to #7 are represented by purple to pink diamonds. As compositions vary within layer #3 (see Figure 3.8), it is subdivided into #3.1 (slightly clearer, just after layer #2), #3.2 (intermediate between layers #2 and #4) and #3.3 (slightly darker, just before layer #4).

Layers #1 and #2, are visible only in the *carbonate* at J7 (points 3, 4 and 6 at J7.3). They differ from other zones in having intermediate concentrations of Fe and Mg, and the highest Ca compositions, plus relatively high Mn values (Figure 3.9, Figure 3.10, and Table 3.3). The main differences between the two layers are that #2 has a lower Mg, and greater Ca, Mn and Fe concentrations. The outer part of layer #2 (indicated as 'outer #2' in Figure 3.8) shows high Ca and Mn compared to any other regions in the *carbonates*, and simultaneously very low Fe and Mg abundances (Figure 3.9, Figure 3.10 and Table 3.3, and points 27 and 5 at J7.3 in Figure 3.6 and Table 3.2). This specific portion of layer #2 cannot be clearly resolved in BSE images, but can be easily identified as a blue ring (Ca-rich region) in the elemental map at J7.3 (Figure 3.4). Layer #3 is characterized by a progressive decrease in Ca, Mn, and Fe with a concomitant enrichment in Mg (Figure 3.9, Figure 3.10 and Table 3.3; see points 7, 31, 34, 82, 84 and 118 in Figure 3.6 and Table 3.2). This compositional progression was divided in three phases: #3.1 (the closest area to layer #2, still quite Ca- and Mn-rich), #3.2 (main layer #3, the wide area between layers #2 and #4) and #3.3 (the closest area to layer #4). Layer #4 (like in points 38, 87 and 119, Figure 3.6) follows the variation in composition started in layer #3 but at greater intensity, until reaching very high contents in Mg (Figure 3.9, Figure 3.10). Layer #5 shows an abrupt change in globule composition compared to layer #4 (Figure 3.10, Figure 3.11): Mg content strongly decreases whereas Fe, Ca and Mn concomitantly increase (Figure 3.10, Figure 3.11; points 12, 92 and 123, Figure 3.6). This sharp change in *carbonate* composition coincides with the presence of local corrosion and the small fractures affecting the end of layer #4 and not affecting layer #5 (Figure 3.7). In layer #6 (points 49, 13, 97, 98, 126 and 128, Figure 3.6) there is again a progression towards a very Mg-rich *carbonate* (Figure 3.9, Figure 3.10; points 98 and 128 in Figure 3.6 and Table 3.3). This layer has the lowest Fe contents, thus accounting for its high luminescence intensity. Some globules have a thin Fe, Ca and Mn-rich rim (layer #7, represented by point 101, Figure 3.6) which exhibits higher Fe, Ca and Mn contents than layer #6 (Figure 3.9, Figure 3.10).

The microprobe data were plotted in a ternary diagram (Figure 3.11) for comparison with the results of previous studies, with terrestrial *carbonates*, and with the distribution of *carbonate* solid solutions (Chang et al., 1996). According to the ternary diagrams (Figure 3.11), the studied *carbonates* are not in the range of terrestrial *carbonate* solid solutions, and have a composition that is intermediate between *dolomite*, *ankerite* and

the *siderite-magnesite* solid solutions. The *carbonates* studied in this chapter are compositionally similar to those analyzed by previous authors (Mittlefehldt, 1994; Harvey & McSween, 1996; Valley et al., 1997; Scott et al., 1998; Holland et al., 1999; Eiler et al., 2002; Corrigan & Harvey, 2004; Holland et al., 2005; Halevy et al., 2011), as shown in Figure 3.11. However, some of those authors observed a very Ca-rich *carbonate* phase in bulk samples of ALH 84001, and in thin sections ALH 84001,119, ALH 84001,287, ALH 84001,302 and ALH 84001,303, which is not observed in the sample studied here, ALH 84001,82.

Table 3.3: Mean and range in chemical composition (maximum and minimum values) calculated from the results of the EMP analyses of the globule layers.

Layer	n	$MgCO_3$		$FeCO_3$		$CaCO_3$		$MnCO_3$	
		mean	range	mean	range	mean	range	mean	range
1	5	50.3	50.9 - 49.5	32.5	33.3 - 32.2	14.5	14.7 - 14.2	2.4	2.6 - 2.2
2	4	40.6	42.7 - 38.4	29.3	29.9 - 27.8	24.0	25.6 - 22.8	5.6	7.3 - 3.2
3.1	16	48.8	54.8 - 45.4	33.7	35.6 - 30.5	14.2	16.6 - 12.1	2.7	4.5 - 2.0
3.2	25	61.0	71.6 - 50.2	28.7	34.0 - 20.5	9.1	13.2 - 2.7	0.7	1.9 - 0.2
3.3	7	77.1	85.5 - 70.6	16.9	22.6 - 8.8	5.0	6.3 - 3.0	0.4	0.9 - 0.2
4	12	81.7	89.1 - 64.0	12.5	27.3 - 6.8	4.7	7.4 - 2.7	0.3	0.6 - 0.1
5	19	49.8	67.5 - 35.0	40.1	51.9 - 27.4	7.9	10.7 - 2.0	1.2	2 - 0.2
6	21	90.9	95.1 - 78.3	4.4	14.7 - 0.3	4.3	6.5 - 3.2	0.2	0.6 - 0.0
7	7	76.5	84.7 - 68.8	16.0	23.1 - 9.2	6.3	6.8 - 5.5	0.5	0.8 - 0.4

The values are mole % *carbonates*.

n = number of analyses.

3.4 Discussion

3.4.1 Environment of carbonate precipitation

It has been suggested that most of the ALH 84001 *carbonates* formed from a CO_2-enriched aqueous fluid penetrating an already brecciated rock (Harvey & McSween, 1996). These processes are interpreted to have coincided with impact metamorphism,

perhaps with the solutions sourced from a transient impact crater lake (Warren, 1998). Formation of the *carbonate* in a low temperature near surface environment over short timescales has been suggested (Berk et al., 2011), maybe by a mixture of subsurface and atmosphere-derived fluids or within an alkaline spring environment (Niles et al., 2005; Halevy et al., 2011).

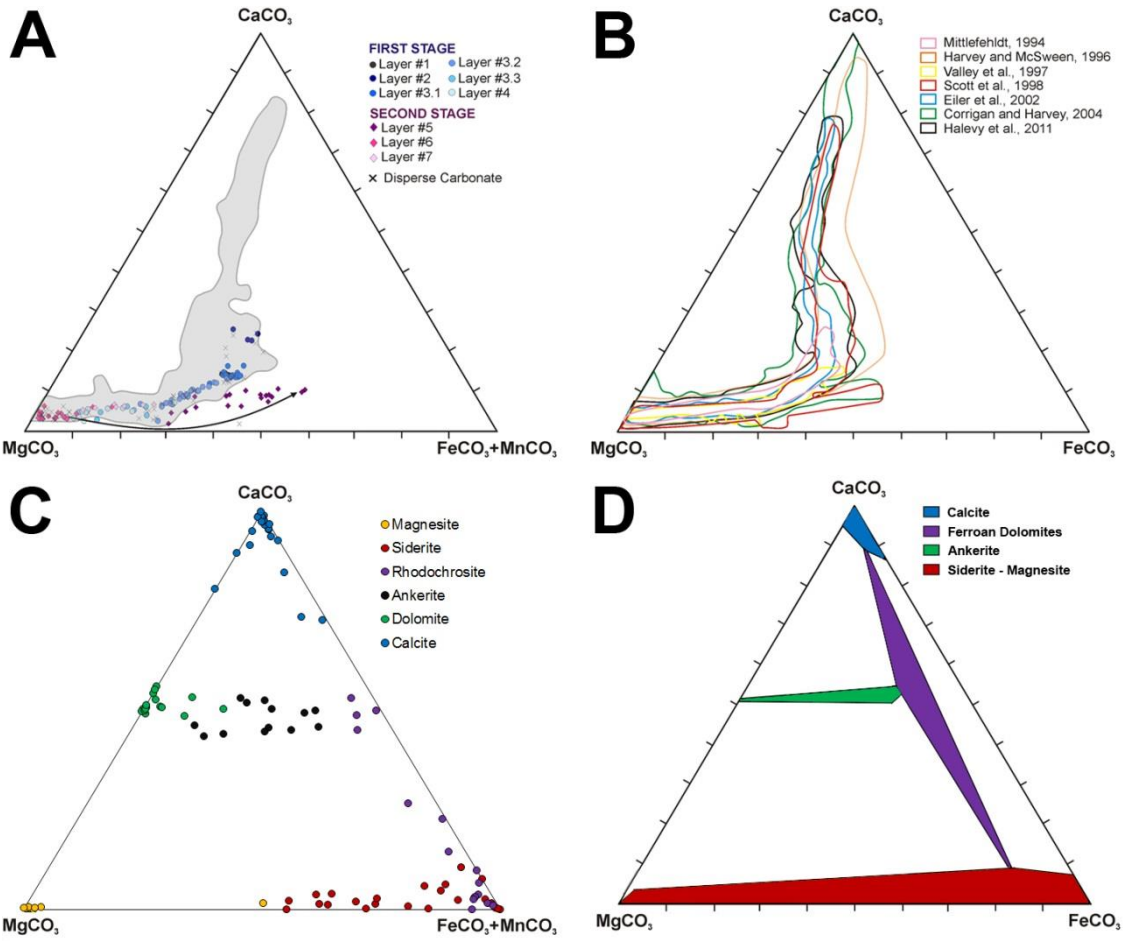

Figure 3.11: Ternary diagrams showing: A. The data obtained by EMP from ~160 different spots (see J7.1 and D5.ex in Figure 3.6 and Table 3.3). Note the progressive compositional change between layers #1 and #4 and the sharp compositional change between layers #4 and #5 (black arrow). The shaded area shows published *carbonate* compositions of ALH 84001 (based on data published by Holland et al., 1999; Holland et al., 2005, who plotted Fe+Mn contents). B. Ternary diagram showing, in different colors, *carbonate* compositions of ALH 84001 published by different authors (Mittlefehldt, 1994; Harvey & McSween, 1996; Valley et al., 1997; Scott et al., 1998; Eiler et al., 2002; Corrigan & Harvey, 2004; Halevy et al., 2011), who only plotted Fe contents. C. Compositions of several terrestrial *carbonates* (data taken from Chang et al., 1996). D. Distribution of the *calcite* solid solutions (blue), Fe-rich *dolomites* with less than 20% Fe substitution (purple), *ankerite* solid solutions (green), and *siderite-magnesite* solid solutions

(red), at 450ºC (adapted from Rosenberg, 1967). The diagrams show the mole % of $MgCO_3$, $CaCO_3$, $FeCO_3$ and $MnCO_3$.

Similar *carbonates* have been found only in a few places in Earth, and the presence of *magnesite* rather than *hydromagnesite*, the C and O isotope ratios consistent with near-surface reservoirs and ocean water, respectively, and the lack of uniformity in the distribution of *carbonates*, point toward a hydrothermal origin for them (Treiman et al., 2002). Due to the similarities between these terrestrial *carbonates* and those in ALH 84001, an origin in a hydrothermal system has been proposed for the last (Treiman et al., 2002).

3.4.2 Relative chronology of carbonate precipitation

There have been several interpretations of the proposed ages of these *carbonates* (Nyquist et al., 2001), and the information presented here suggests that different types, and maybe different generations, are present (Mittlefehldt, 1994; Moyano-Cambero et al., 2017b). According to the petrographic and geochemical results described here, the formation of these *carbonates* can be divided in at least two phases of precipitation (Moyano-Cambero et al., 2017b). In the studied section, *carbonate* globules are found mostly in regions that had been previously highly fractured (Figure 3.1, Figure 3.2, and Figure 3.3), like the points where the two fractures systems intersect. The presence of these distinct fractures systems, with the one aligned NNW-SSE being traversed and displaced by the one aligned ENE-WSW, suggests that the sample also experienced at least two shock events. Granular bands (i.e., 'GB' in Figure 3.3), have been previously interpreted as being older than the fractures (Mittlefehldt, 1997), pointing towards more than two shock events. However, the granular bands are considered here to be contemporary with the fractures. Indeed, these types of bands typically form as a product of friction during terrestrial fracturing (see e.g. Brodie et al., 2007, where they are named cataclasites). These bands could actually show a high *carbonate* content due to their greater original porosity.

In common with previous models (e.g. Schwandt et al., 1999), this chapter suggests that the most plausible scenario for *carbonate* formation is initial precipitation from Mg- and Fe- rich solutions, followed by the formation of *maskelynite* or shock modified *plagioclase glass* (Figure 3.3) during a shock event (Mittlefehldt, 1994; Treiman, 1995;

Scott et al., 1997; Treiman, 1998; Cooney et al., 1999; Corrigan et al., 2003). These solutions would have filled the shock-produced fractures at different times, leading to the precipitation of *carbonates* in at least two events. Indeed, *carbonates* are partially corroded at their contact with *maskelynite* or *plagioclase glass* (Figure 3.4, D5.1). The density of fractures also differs dramatically between the *carbonate* and *glass* (Mittlefehldt, 1994), which supports the suggestion that out of these two components, the *carbonates* formed first. The presence of these solutions, along with other evidence (described, e.g., in Niles et al., 2006, and at the references therein) imply that liquid water was relatively abundant on Mars ~3.9 Gyr ago. In fact, those *carbonates* could be just a small sample of the products of quite a common phenomenon on the subsurface of Mars (Michalski & Niles, 2010).

The characteristic compositional zoning of ALH 840001 *carbonates* (e.g. Saxton et al., 1998; Corrigan & Harvey, 2004) indicates that they precipitated in a manner whereby each zone formed when saturation was reached (Halevy et al., 2011). This zonation has been described as a consequence of chemical variation of their parent fluid, driven by the *carbonate* precipitation since Fe-, Mn- and Ca-rich solutions are more kinetically favored to precipitate than Mg-rich solutions (Harvey & McSween, 1996; Saxton et al., 1998; Corrigan et al., 2003; Corrigan & Harvey, 2004; Niles et al., 2009, among others). The last *carbonates* to precipitate are therefore Mg-rich, only when the initial fluid is much more depleted in Fe, Ca and Mn than it was at the beginning. Despite other differences, this zonation is equivalent between the globules and the interstitial *carbonates* precipitated within *pyroxene crystals* (see e.g. Scott et al., 1998, for the distinction between *carbonates*). A similar trend in the chemical evolution of the *carbonates* can be observed twice (from layers #1 to #4, and from #5 to #6) (Figure 3.10, Figure 3.11), which together with evidence described later suggests that these *carbonates* precipitated in at least two events.

3.4.3 Carbonate mineralogy

None of the *carbonate* spectra in the RRUFF database precisely fit any of our Raman results. This finding, together with the multiplicity of peaks and the clear asymmetry of some of them (Figure 3.5 and Table 3.1), could suggest that the ALH 84001 *carbonates* are a mixture of several phases, or compositionally heterogeneous on the submicroscopic scale (Cooney et al., 1999). However, the results presented in this chapter suggest the presence of a single and compositionally unusual mineral with

varying compositions, like the *carbonates* described by Treiman et al., (2002). This phase has yet to be properly characterized, and doing so will require further work using techniques such as X-ray diffraction and transmission electron microscopy. Raman spectroscopy has demonstrated the presence of *hematite* and *magnetite* in those *carbonates* that were analyzed here (Figure 3.5). *Hematite* affects the positions of several *carbonate* peaks, and therefore should be taken into account carefully when studying ALH 84001. The presence of *magnetite*, whose most prominent peak lies at ~660 cm^{-1}, is consistent with results of previous studies (McKay et al., 1996; Cooney et al., 1999), although it seems to be present throughout these *carbonates* (Figure 3.5).

As previously noted, the evidence presented here suggests that ALH 84001 *carbonates* precipitated in at least two different episodes. Consistently, the fracturing and local corrosion of the *euhedral crystals* of layer #4 prior to precipitation of layer #5 (Figure 3.7, D5.3-D5.6) indicate that layers #1 to #4 correspond to the first stage of precipitation, while layers #5 to #7 formed in the second stage and as an overgrowth. Moreover, the sharp transition in *carbonate* compositions between #4 and #5 suggests a change in solution chemistry and saturation state (e.g., the concentration in CO_2 or pH), between formation of the inner (#1 to #4) and outer (#5 to #7) layers. The microprobe data reveal two trends (Figure 3.10, Figure 3.11) that add further weight to the idea of at least two episodes of precipitation. Indeed, the contrasting compositional trends imply that the ambient fluids differed in chemistry, pointing to distinct aqueous alteration events (Figure 3.7). The distribution coefficients for Fe and Mn into *carbonates* are much higher than 1, meaning that any Fe^{2+} or Mn^{2+} in the fluid will preferentially partition into the *carbonate* (e.g. Chang et al., 1996; Rimstidt et al., 1998). Moreover, the distribution coefficients are not strongly temperature dependent due to the fact that all solubility products of *carbonate* minerals change with temperature in almost the same way, at least between 273 and 373 K (Rimstidt et al., 1998). Assuming that the system was closed so that the aqueous solutions were not being continually replenished, Fe and Mn would progressively be depleted relative to Mg as *carbonate* precipitated from this fluid. This process may be responsible for the chemical patterns observed between layers #2 to #4 and layers #5 to #6 (Figure 3.10, Figure 3.11). Layer #1 probably represents an initial precipitation, from a relatively Mg- and Fe-rich fluid. Once the concentration on Fe became lower, the precipitation of a more Ca- and Mn-rich *carbonate* started (layer #2). After that, successive layers are progressively depleted in Fe and Mn and enriched in Mg (layers #2 to #4, and posteriorly #5 to #6),

representing precipitation from an evolving fluid, which was progressively depleted on Fe and Mn as *carbonate* precipitated. Thus, the sharp change from Fe- and Mn-poor layer #4 to the Fe- and Mn-rich layer #5, would imply the input of a new fluid. Indeed, the presence of small fractures and local corrosion formed prior to layer #5 (Figure 3.7) suggests that a new hydrous event introduced a Fe-rich fluid into the system, responsible for the precipitation of layers #5 and #6. The possibility of an additional fluid influx between layers #6 and #7 (layer #7 has higher Fe and Mn content than layer #6) cannot be discounted. This interpretation is in accordance with experimental data obtained by Golden et al., (2001), who performed a multiple step precipitation process to produce chemically and mineralogically zoned synthetic *carbonate* globules (see their Table 3.1 and Figure 3.1). In the first step they added Ca, Fe, and Mg to the starting solution, and as a result a globule with a Ca-Fe rich core precipitated, progressively grading outwards to a more Mg-rich *carbonate*.

Small high atomic number inclusions occur between *carbonate* layers #4 and #5 (Figure 3.7, D5.5), but their small size prevented identification. They could be the *pyrrhotite* and/or *magnetite* inclusions that other authors have observed in *carbonate* rosettes rims, which are interpreted to have possibly precipitated when the *carbonate* was invaded and partially melted by shock-generated liquids (McKay & Lofgren, 1997; Scott et al., 1997; Bradley et al., 1998). Indeed, the small fractures observed in Figure 3.7 (red arrows) are consistent with shock between the precipitation of layers #4 and #5. These apparently *amorphous magnetite* inclusions, intermixed with iron *sulfide*, and the voids where they formed, can be the direct result of local *carbonate* decomposition by an impact (Scott et al., 1997; Barber & Scott, 2002). However, a strong shock melting of the *carbonates* would make the borders of layer #4 to be corroded and *anhedral*, but the boundary between layers #4 and #5 is mostly *euhedral*. The melting produced by shock should then have been of sub-micrometer scale.

Microprobe data reveal that the studied *carbonates* fall between *dolomite*, *ankerite*, *siderite* and *magnesite* (Figure 3.6, Figure 3.11, Table 3.2 and Table 3.3). The compositions of ALH 84001,82 *carbonates* do not correspond to any known mineral (Harvey & McSween, 1996). Also, there is no solid solution series in terrestrial *carbonates* from *calcite* to *dolomite* or *ankerite*, and nor from those minerals to *magnesite* or *siderite* (see e.g. Chang et al., 1996). Therefore there is no mineral intermediate between these phases, because the substitution of Ca by Mg or Fe is not straightforward. These *carbonates* with intermediate compositions are unusual on Earth,

and their presence suggests a terrestrially uncommon formation scenario. For example, different and variable aqueous solutions under changing environmental circumstances (see e.g. Fernández-Remolar et al., 2011) supported by kinetic stabilization of these metastable compositions (McKay & Lofgren, 1997). Compositionally similar *carbonate* globules have been found on Earth in specific contexts like the volcanic centers in Spitsbergen (Norway), and other few places (Treiman et al., 2002, and references therein). Those *carbonates* are also described as discs, with cores called 'ASM' due to their compositions lying between *ankerite*, *siderite* and *magnesite* (Treiman et al., 2002).

3.5 Conclusions

Several laboratory techniques were used here to analyze the ALH 84001,82 thin sample, and each proved to be a useful in the study of meteorites. Although not being a chondrite, ALH 84001 is one of the oldest known Martian meteorite and so is a unique source of information on the environmental conditions of early Mars. Therefore, it is representative of the processes that could take place in the largest planetesimals, and the effect that the accretion of chondritic asteroids could have on them. Also, this meteorite has been studied extensively, which allows for comparison with previous experimental results and studies, and therefore developing the appropriate laboratory skills for the study of meteorites. The main conclusions of this chapter are as follows:

1. In order to study meteorites and comprehend their formation and evolution, a multidisciplinary approach involving physics, mineralogy and chemistry, among other disciplines, is required. A minimum domain of at least some the laboratory techniques described in this chapter provides the necessary resources and skills to identify ROIs, and to appropriately read and understand the data obtained from the analyses.

2. Petrographic microscopy showed the presence of at least two sets of fractures in this *igneous* achondrite. This supports previous studies showing that the constituent minerals of this meteorite have suffered at least two shock events. With prior knowledge of how the *carbonate* globules should look like, two ROIs were found between cracks with a high abundance of *carbonates*.

3. Since those *carbonates* contain Mn and some Fe-poor layers, CL has proven to be very useful as a support technique. It showed the presence of several smaller *carbonates* that would have been very difficult to find with other techniques. However, its usefulness when it comes to the search of specific minerals is very limited to the particular composition of those minerals.

4. SEM and EDS allow for a more detailed observation of the ROIs. Working with BSE allows for distinction between regions with different atomic number, and therefore to observe the chemical variations within a mineral. This capability was particularly useful to distinguish the different layers of these *carbonate* globules. Thanks to the high magnification and resolution of the SEMs, several features suggesting at least two precipitation events from different generations of fluids became evident: the *euhedral* shape observed at the boundary between layers #4 and #5, the small inclusions at the margins of layer #4 (described by other authors as *magnetite* and *sulfide*), and the small fractures that do not extend from layer #4 to #5. After precipitation of layers #1 to #4 from a Mg- and Fe-rich aqueous solution, a shock event created the fractures and introduced a second fluid, which precipitated further *carbonate* as layers #5 and #6, at least. Layer #7 could be the result of a third precipitation event from a later fluid, but the evidence is less clear. Although EDS allows for elemental analyses of specific spots in a sample, EMP performs much better to that end. Still, EDS combined with SEM provides in situ chemical maps of the regions of interest, and therefore a fast first characterization.

5. Micro-Raman spectroscopy was used to identify the specific *carbonate* minerals forming the globules. The resulting spectra were compared to a very extensive catalogue. Besides from the possible presence of *hematite* and *magnetite* in the *carbonates*, the Raman spectra showed that those *carbonates* could not easily be classified as any of the known *carbonate* solid solutions.

6. EMP provided a much more detailed elemental analysis of the sample. As suggested by previous studies, the composition of those *carbonates* is very uncommon on Earth. Indeed, this phase evolves across the immiscibility areas between Fe-, Mg- and Ca-rich *carbonates*, constituting metastable minerals that

require a more comprehensive characterization, opening the door to future analysis on ALH 84001. This technique also supports the idea of the two precipitation events. First, it shows a very sharp change in composition between layers #4 and #5, which suggests the presence of a new fluid after precipitation of layers #1 to #4. Also, it shows at least two distinct compositional trends between layers #1 and #7, which again supports the two fluid hypotheses.

7. The evidence compiled here demonstrates a temporally differentiated fluid environment within the region of the Martian crust that was sampled by ALH 84001. Two, or possibly three, generations of fluids formed the *carbonates* in different stages. *Carbonate* precipitation incrementally changed the aqueous environment to promote the precipitation of more Fe- and Mg-rich *carbonates*. The model outlined in this thesis is consistent with previous studies suggesting a hydrothermal origin for the *carbonates*.

4 CONNECTION BETWEEN CH CARBONACEOUS CHONDRITES AND THE ASTEROID 21 LUTETIA

Abstract

Chondrites provide an opportunity to study undifferentiated asteroids, and thus some of the oldest materials of the Solar System, without the economic cost of a sample return mission. Through their study much can be learnt about their parent bodies and the asteroids currently populating the Solar System, but in order to do so it becomes crucial to identify which asteroids (or asteroid groups) are the parent bodies of each type of chondrite. As sort of a practical example, this chapter focuses in the feasibility of a connection between asteroids similar to 21 Lutetia, encountered by the Rosetta mission in July 2010, and the CH3 (i.e., CH chondrite of petrologic type 3) carbonaceous chondrite Pecora Escarpment 91467 (PCA 91467). Most of the information about the composition of asteroids is obtained from their reflectance spectra in different ranges, and that offers an opportunity for comparison with meteorites. With that in mind, several spectra of the PCA 91467 meteorite were acquired in the ultraviolet to near-infrared (0.3 to 2.2 μm) and in the mid-infrared to thermal infrared (2.5 to 30.0 μm or 4000 to ~333 cm^{-1}), and they are compared in this chapter to spectra from the asteroid 21 Lutetia. There are several similarities in absorption bands and overall spectral

behavior between this CH3 meteorite and 21 Lutetia. Considering also that the bulk density of Lutetia is similar to that of CH chondrites, it is suggested here that this asteroid could be similar, or related to, the parent body of these meteorites, if not the parent body itself. However, the apparent surface diversity of Lutetia pointed out in previous studies indicates that it could simultaneously be related to other types of chondrites. This implies a considerable difficulty to establish a solid link with specific meteorites, but at the same time requires exploring the available techniques and data with great attention, providing an opportunity to learn the most of it. Future discovery of additional unweathered CH chondrites could provide deeper insight in the possible connection between this group of metal-rich carbonaceous chondrites and 21 Lutetia or other featureless, possibly hydrated, high-albedo asteroids. The results of this chapter have been published in *Meteoritics and Planetary Science* (Moyano-Cambero et al., 2016b)

4.1 Introduction

Establishing relationships between meteorites and their parent asteroids has always been quite a tricky task, as there are many differences in the observing conditions, resolutions and methods used for the study of these primordial objects (see e.g. Clark et al., 2010; Clark et al., 2011). To complicate the overall puzzle it is obvious that the physical processes at work in each one of the parent bodies of meteorites have been remarkably different depending on their particular evolutionary stories (Binzel et al., 2010). In this chapter, evidence is presented about the similitude, and even plausible connection, between almost featureless, possibly hydrated, high-albedo asteroids, and the CH group of metal-rich chondrites. Few asteroids fit this description: 21 Lutetia, 77 Frigga, 135 Hertha, 136 Austria, and possibly others (Hardersen et al., 2011). Since 21 Lutetia (or simply Lutetia), encountered by the Rosetta mission in July 2010, has been studied in greater detail than the others, it was selected in this chapter for comparison to the CH chondrites on the basis of spectral similarities in the ultraviolet to thermal infrared (UV-IR) range, and considering the information gathered so far by the scientific community on both the asteroid and this type of meteorites.

Lutetia is a large MB asteroid. Some of its spectra are flat and almost featureless in the 0.15 to 2.5 μm range (Birlan et al., 2004; Ockert-Bell et al., 2010; Coradini et al., 2011; Hardersen et al., 2011; Sierks et al., 2011), but others can show faint signatures, depending mostly on the region sampled (see, e.g., Birlan et al., 2006; Weaver et al.,

2010; Barucci et al., 2012), which makes the spectral type classification of this asteroid quite difficult. Tentatively, and due to its moderately-high albedo and presumably high metal content, it has been considered as an M taxonomic type asteroid into the X-group according to the Tholen classification (Barucci et al., 1987; Tholen, 1989). In the Small Main-Belt Asteroid Spectroscopic Survey (SMASS) classification, it has been described as an uncommon Xk transition type asteroid into the X-group or one of the very rare Xc transition type asteroids, due to its spectral slope and absorption bands (Bus & Binzel, 2002b; Ockert-Bell et al., 2008; DeMeo et al., 2009; Shepard et al., 2010). Both its albedo and bulk density are too low to be considered a largely metallic asteroid (Weaver et al., 2010), but they are also too high for the typical C-class asteroids (Shepard et al., 2008). Indeed, its albedo seems to be more consistent with *enstatite* chondrites, CH chondrites, or *silicate* bearing iron meteorites (Shepard et al., 2008).

In addition to spectral shape comparison, similitudes between the CH group and Lutetia are also explored in this chapter on the basis of the mineralogy of these meteorites and their relatively high reflectance, compared to most CCs. The reflectance of CHs is probably associated with their high abundance of metal grains (Campbell & Humayun, 2004; Trigo-Rodríguez et al., 2014a; Moyano-Cambero et al., 2016b). Indeed, the albedo of asteroid Lutetia is also higher than expected for the kind of dark asteroids commonly associated with CCs. Besides, the spectra obtained from several regions of this asteroid, which usually show few features, are consistent with the commonly flat spectra characteristic of most CCs, pointing towards a closer relation with this class of meteorites than with other chondrites. However, it must be taken into account that some of the spectra associated to Lutetia show features consistent with other meteorites, which could imply that, even if CH meteorites are indeed connected to asteroids similar to Lutetia, they could not be representative of the entire surface of their parent body. Indeed, impact gardening has had an important processing effect enhancing the heterogeneity in the surfaces of asteroids (Beitz et al., 2016).

4.2 Sample selection and experimental techniques

4.2.1 Rationale for sample selection

Several attempts to establish asteroid Lutetia as the parent body of different meteorites groups have been done before. Primitive meteorites (of petrologic type 3 or close) have been related to this body due to observations in the UV-NIR range (e.g. Nedelcu et al.,

2007, where meteorite and asteroid spectra are compared using a χ^2 fitting test). CCs also seem to match some of the spectral properties of Lutetia, and indeed, it has been related to COs and CVs due to its mid-to-far-infrared features and polarimetry data (Lazzarin et al., 2004; Barucci et al., 2008; Lazzarin et al., 2009; Belskaya et al., 2010; Barucci et al., 2012). However, most spectra of Lutetia do not show the lack of the drop-off below 0.55 μm which is common in CVs (Gaffey, 1976), and both groups of CCs show the 1 μm band related to the presence of *olivine* (Vernazza et al., 2011). Despite the relatively high abundance of mostly featureless (in the UV-NIR range) *matrix* on those meteorites, the 1 μm band is still too strong considering that it has not been reported on Lutetia. Actually, rather than making those features disappear the presence of *matrix* material darkens the spectra of these meteorites, which makes them less reflective than expected for a meteorite whose parent asteroid is Lutetia (Drummond et al., 2010). This asteroid has also been compared with meteorites with a very high content in metal, due to its moderately high albedo around 0.2 (see e.g. Mueller et al., 2006, for a summary of albedo determinations for Lutetia in table 5, and Sierks et al., 2011, for more recent result obtained with the cameras onboard Rosetta), but the inferred density of this asteroid, ~3400 kg/m^3 (Weiss et al., 2012), is too small for an object dominated by metallic components, even assuming a typical porosity of 10-15% (Weaver et al., 2010; Patzold et al., 2011). It has been suggested that ECs match the spectra of 21 Lutetia better than most CCs (see, e.g., Ockert-Bell et al., 2010; Vernazza et al., 2011). Indeed, FeO-free *enstatite* is almost featureless in the UV-NIR range (see e.g. Klima et al., 2007; Vernazza et al., 2011). Furthermore, a few Lutetia spectra show a weak band at ~0.9 μm (see e.g. Birlan et al., 2006) that could be indicating the presence of *enstatite* on the asteroid's surface (Klima et al., 2007; Vernazza et al., 2011). Lutetia spectra in the mid-infrared apparently implies that the *silicates* on its surface are most likely iron free, like *enstatite* (Vernazza et al., 2011), and that this asteroid has not suffered from aqueous alteration (Coradini et al., 2011; Vernazza et al., 2011), consistently with ECs of petrologic types 3 to 6 (Weisberg et al., 2006). However, other studies suggest that the far-infrared Spitzer data of Lutetia does not match that of ECs (Barucci et al., 2008; Perna et al., 2010), and that these meteorites neither show the Christiansen peak, related to mineralogy and grain size, around 9.3 μm (~1075 cm^{-1}), reported in a spectrum of 21 Lutetia and common in CCs (Izawa et al., 2010; Barucci et al., 2012). Additionally, ECs do not show the features in the visible

related to aqueous alteration and hydrated minerals that have been found in some Lutetia spectra (Lazzarin et al., 2009; Hardersen et al., 2011; Rivkin et al., 2011).

Some authors (e.g. Lazzarin et al., 2009; Shepard et al., 2010; Coradini et al., 2011) took into account the metal-rich CR clan in the analysis of Lutetia spectra. It has been shown that the densities of these meteorites are consistent with that of the 21 Lutetia asteroid (Coradini et al., 2011), specifically in the case of CHs, with a bulk density of ~ 3650 kg/m^3 (Macke et al., 2010). The geometric albedo of this asteroid, determined precisely in situ by the Optical, Spectroscopic, and Infrared Remote Imaging System (OSIRIS) instrument onboard Rosetta, has a value of 0.19 ± 0.01 (Sierks et al., 2011). This value corresponds to zero phase angle, and therefore in previous studies it has been corrected using Lutetia phase function, in order to be compared to albedos of meteorites (usually measured at angles of ~7 to 10 degrees), obtaining a value in the range of 0.13-0.16 (Belskaya et al., 2010). It is larger than the usual values for other primitive bodies and most CCs, and lower than the ones for metal meteorites (Gaffey, 1976), but in agreement with metal-rich CCs (Weiss et al., 2012; Trigo-Rodríguez et al., 2014a). However, the particle size can have a strong effect on albedo, so the fact that Lutetia is probably covered in fine-grained regolith has to be taken into account to do a proper comparison with the spectral properties of meteorites (Belskaya et al., 2010). Moreover, Lutetia shows surface heterogeneities (see Barucci et al., 2012, and references therein), indicating the presence of different *lithologies* and therefore the possibility that more than one class of meteorites could have their origin in such a parent body (Nedelcu et al., 2007). Therefore, these metal-rich CCs could be are considered in this chapter as possible analogues of certain regions of similar asteroids, which does not mean that the whole body shows metal-rich carbonaceous composition.

Previous studies have concluded that each chondrite group exhibits distinctive reflection spectra (see, e.g., Cloutis et al., 2012a; Cloutis et al., 2012c; where they use spectra from powders of different grain sizes, and Trigo-Rodríguez et al., 2014a, where we mostly obtained spectra from meteorite thin or thick sections). CCs belonging to the CR clan show rather high reflection degrees, increasing from CRs to CBs. This is probably due, at least partially, to their high content in metal grains. However, this relationship is not linear as the distribution of metal in these three groups is heterogeneous: while CHs have most of their metal in the *matrix*, CRs show metal grains mostly inside the chondrules, which would not necessary imply a high increase of the albedo of their parent body (Krot et al., 2002; Trigo-Rodríguez et al., 2014a). On

the other hand, CBs have much higher metal abundances mostly out of the chondrules, so their parent body should show a particularly high albedo in the same way that the meteorite samples show a very high reflectance spectrum (Trigo-Rodríguez et al., 2014a; Moyano-Cambero et al., 2016b). The 0.13-0.16 reflectance of Lutetia at phase angles between 7 and 10 degrees is low compared to iron meteorites and CBs, and high compared to other CCs, including CRs, but it is comparable to the absolute reflectance obtained for a CH chondrite in a previous study, between 0.10 and 0.20 in the 0.2 to 2.0 μm range. (see, e.g., Fig. 1d in Trigo-Rodríguez et al., 2014a, paper). This is why among the CR clan, CH chondrites are considered here as the more plausible candidates to be related to Lutetia or similar asteroids.

For this chapter, some samples of the Pecora Escarpment (PCA) 91467 CH3 chondrite were obtained. This meteorite was recovered by the Antarctic Search for Meteorites (ANSMET) program in 1991, and nowadays belongs to the NASA Antarctic collection. These samples consist of a small chip, the thin section PCA 91467,25, and the thicker section PCA 91467,16, from which a second thin section was obtained. Although a weathering grade of B/C (moderate to severe rustiness) has been indicated for this meteorite (Bischoff et al., 1994), these samples show a remarkably pristine interior that can be representative of the forming materials of its progenitor asteroid, if the differences in scale and other factors are taken into consideration appropriately. This particular CH chondrite is consistent with the other members of its group, with abundant *lithic* fragments and few relatively small chondrules, Mg-rich *pyroxenes* and *olivines* with mostly Fs_{1-5} and Fa_{1-4} composition, and abundant NiFe metal and hydrated materials, such as *magnetite* (Bischoff et al., 1994; Cloutis et al., 2012c).

The Zeiss Scope Axio petrographic microscope was used to take several images from the thin samples at magnifications varying between 50× and 500×. Metal inclusions are mostly opaque to TL, and therefore in this chapter RL was preferred in order to obtain the images to be merged in a high-resolution mosaic of the PCA 91467,25 thin section (Figure 4.1). In this case, the mosaic was used as reference and with illustrative purpose, since no search for specific features was performed. Instead, spectroscopic techniques provided spectra from the samples as a whole, and as a consequence there was no need for a reference map.

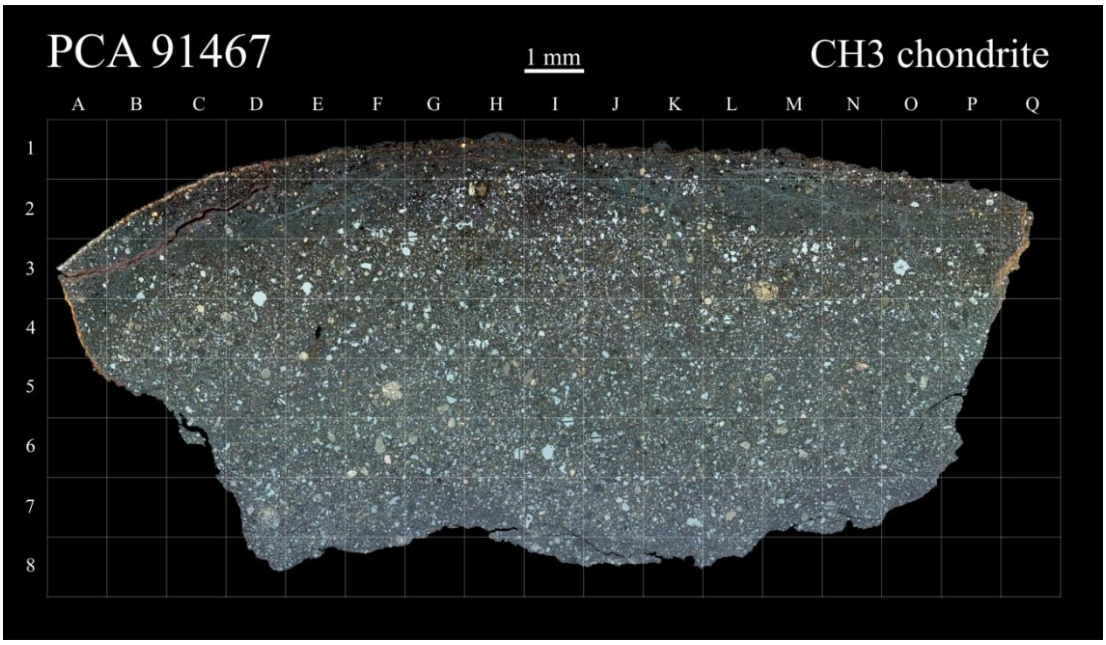

Figure 4.1: High resolution RL mosaic of the PCA 91467,25 thin section. A thin *fusion crust* and a 1 mm thick rusty surface that suffered terrestrial weathering can be found at the top. The light blue inclusions are metal grains more abundant below the altered region.

4.2.2 Spectroscopy in the 0.3 to 2.2 μm range

The Shimadzu UV3600 spectrometer was used to obtain reflectance spectra in the UV-NIR range (from 0.3 to 2.2 μm) from the two thin sections and the thick section of PCA 91467. The absolute reflectance of a meteorite section can be obtained with this technique, which can be compared to the remote spectra of asteroids (Trigo-Rodríguez et al., 2014a). As explained in chapter 2, the spectra obtained with this spectrometer show some noise and instrumental errors that need to be corrected before comparing with asteroid spectra. Such corrections were applied to the spectra from the samples of PCA 91467 (Figure 4.2, A). As can be seen, the region between 0.8 and 0.9 μm is very noisy and therefore does not include usable data. In this example (Figure 4.2, A) that spectral region was approximated by a polynomial equation for aesthetic reasons, but in the other figures it was just deleted to avoid false data. The peaks at the regions from 1.4 to 1.6 μm and from 1.9 to 2.2 were corrected to get rid of the effect of the $BaSO_4$ substrate. To avoid the loss of uniformity above 2.0 μm, we only include data until 2.2 μm, although the noise here is already quite strong (Figure 4.2). Also, comparing the spectra of both a thick and a thin version of the same sample it can be seen that the contribution from the *glass* is very small, if any at all (Figure 4.2, B).

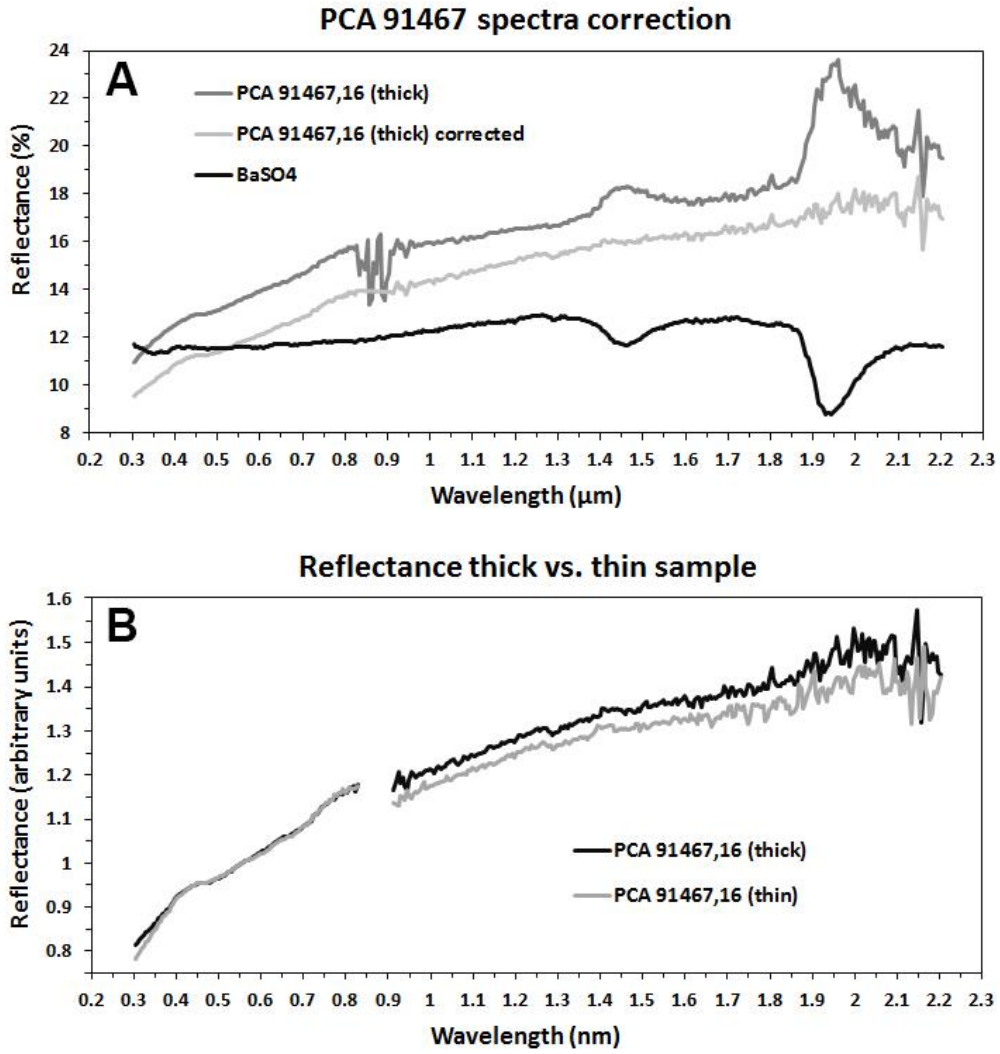

Figure 4.2: Analysis of the PCA 91467 spectra in the UV-NIR (0.3 to 2.2 μm). In A the corrections applied to the spectra can be seen. When comparing to the $BaSO_4$ spectrum, it becomes clear that the peaks between 1.4 and 1.6 and between 1.9 and 2.2 are due to some contribution by the substrate of the spectrometer. As can be seen, above 2.0 μm the signal becomes very noisy and hardly useful. In B the spectra obtained from a thick and a thin section are compared, and as can be appreciated the differences are rather small.

There are obvious differences between the PCA 91467 spectra obtained with the Shimadzu UV3600 spectrometer in this range and the spectrum shown by Cloutis et al. (2012c), (Figure 4.3), which nowadays is the only CH3 spectrum in the RELAB (Reflectance Experiment Laboratory) catalogue. It was acquired from a <75 μm grain size powder at the NASA RELAB facility, in bidirectional reflectance mode with a

source and phase angle of 30º, and a 5 nm resolution. Both the 0.9 and the 1.9 μm bands in the RELAB spectrum, which are due to the presence of almost pure *enstatite* (Klima et al., 2007), are hidden in the spectra acquired for this chapter by the baseline noise between 0.8 and 0.9, and by the noise produced after correcting the instrumental peak from 1.9 to 2.2, respectively. However, in the RELAB spectrum those bands are quite weak, and according to Cloutis et al. (2012c), they are deepened by the effect of terrestrial weathering. Therefore we can expect those peaks in the parent body to be even fainter.

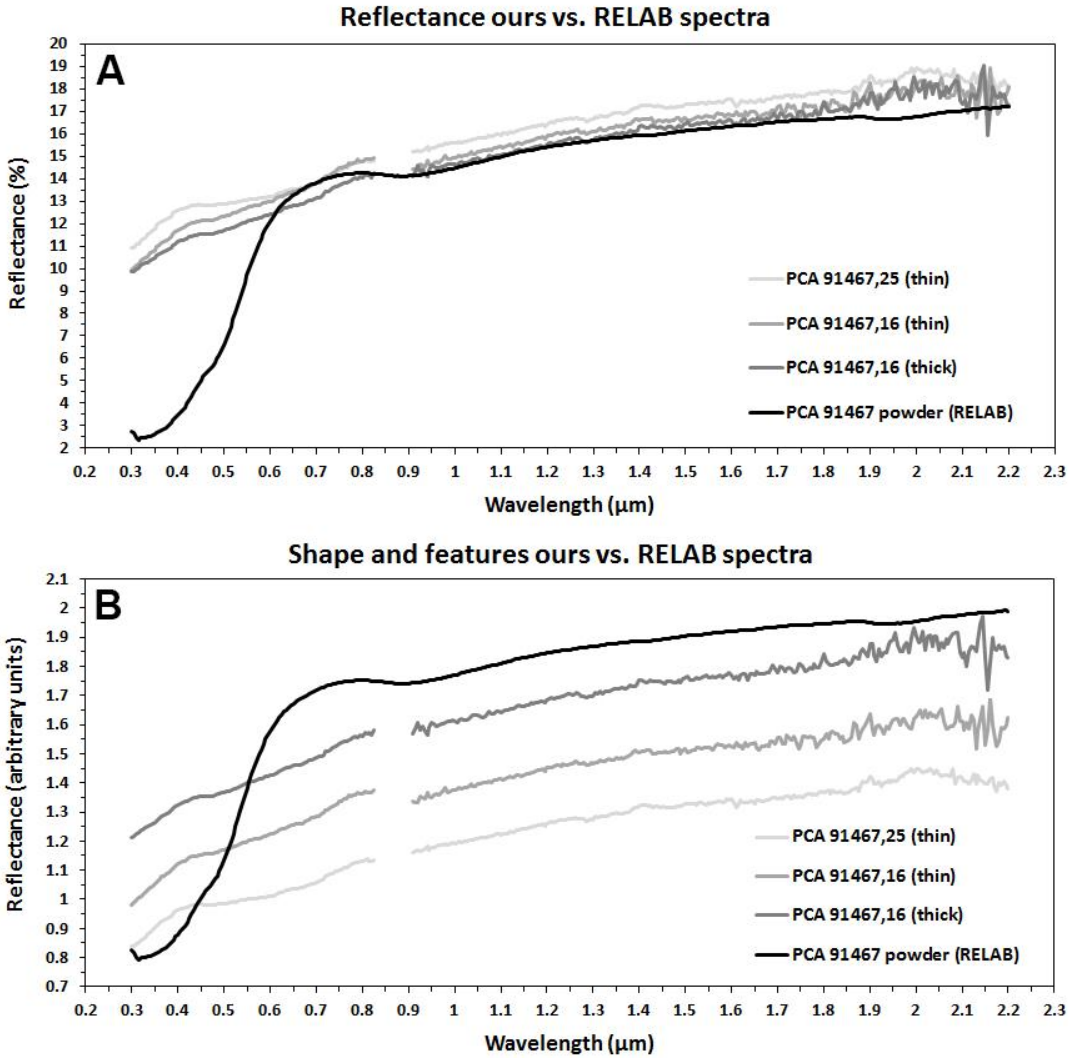

Figure 4.3: Comparison between the spectra obtained for this chapter from thin and thick sections, and the RELAB spectrum of the PCA 91467 CH3 chondrite, obtained from a powder. In A the reflectance is compared, showing that, from 0.6 μm onwards, the difference is smaller than 2%. In B the four spectra are displayed (normalized and then shifted to avoid superposition).

The most notable difference between those spectra is the absence of the deep steep below 0.6 μm in the spectra from the samples studied in this chapter. The presence of this strong ultraviolet absorption can be produced as a result of terrestrial weathering (Cloutis et al., 2012c). Although the spectra used here were obtained from regions where the terrestrial alteration is not significant (Trigo-Rodríguez et al., 2014a), some minor terrestrial weathering in the selected areas is plausible. A strong heating can make this feature disappear (Hiroi et al., 1993), but this is not consistent with a mostly unaltered CH3 chondrite (Bischoff et al., 1994). Hendrix and Vilas (2006) provided another explanation for the disappearance of this feature, showing that space weathering (represented by addition of nanophase iron), resulted on a decrease of slope in this spectral region, but again this is hardly the case as the effects of space weathering are rarely seen on meteorites. However, they also explained how minerals with high iron content produce a similar effect (Hendrix & Vilas, 2006). Indeed, in NiFe metals a higher content in Fe implies flattening between 0.4 and 0.6 μm, while higher Ni provides reddening of the spectra between 0.35 and 1.2 μm (Cloutis et al., 2010). As cut polished sections were used for this chapter, their metal content becomes more 'visible' from a spectroscopic point of view than in the powder used in RELAB. Indeed, the spectra from the thick and thin sections seem to be dominated by spectrally featureless and red-sloped Fe-rich metal phases (Gaffey et al., 2002; Cloutis et al., 2010), and not by the presence of *enstatite* like in the RELAB spectrum (Klima et al., 2007; Cloutis et al., 2012c). As a consequence, the features and the deep steep below 0.6 μm become much weaker in a very similar way as what happens in space weathered asteroids (Hendrix & Vilas, 2006), which means that the samples selected here are good candidates for meteorite-asteroid comparison. Other differences between the spectra obtained from thin sections and powders could be considered here, but that issue is beyond the purpose of this chapter. However, the strongest variations due to grain size are on overall slope (mostly after ~0.6 μm), and reflectance (Johnson & Fanale, 1973), and it can be seen that those particular features are very similar between all the spectra presented here. The spectra studied here are therefore considered as complementary to the spectra obtained from a <75 μm powder of the same meteorite (Cloutis et al., 2012c).

4.2.3 Spectroscopy in the 2.5 to 30.0 μm (4000 to 333 cm^{-1}) range

The chip from PCA 91467 was grounded into powder with an agate mortar, in order to be studied with the Nicolet FT-IR spectrometer. As mentioned in chapter 2, it is important to take into consideration that this spectrometer is equipped with a Smart Orbit ATR accessory, whose peaks have the same positions but different relative intensities than an equivalent absorption IR spectrum, much more commonly used in the study of meteorites (Chemtob & Glotch, 2007).

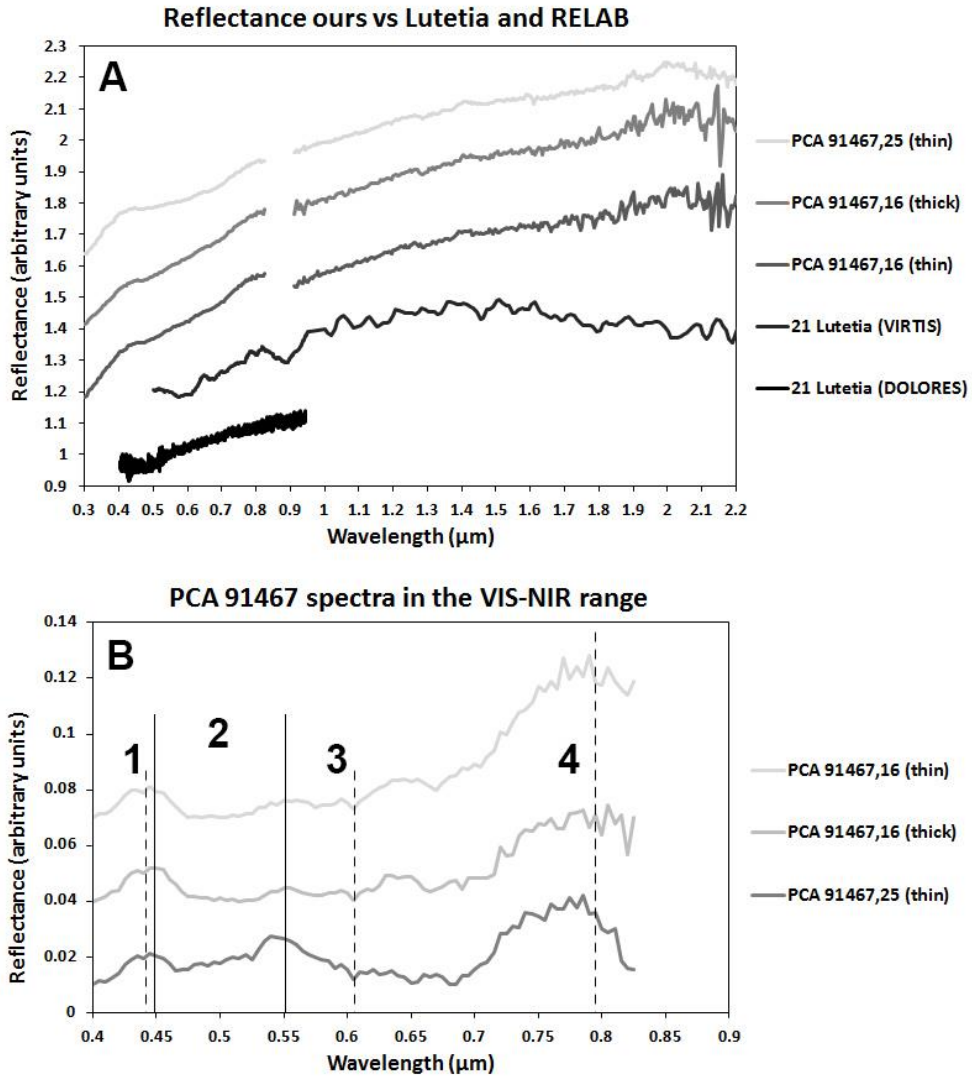

Figure 4.4: The reflection spectra from the PCA 91467 sections are compared in A to the Lutetia spectra in the UV-NIR range as measured by VIRTIS and DOLORES. They are shifted for visibility purposes. In B the PCA 91467 spectra in the 0.40 to ~0.85 range are compared. The continuum was removed from them to properly compare the absorption bands and features. They are also shifted.

4.2.4 Comparison with data from 21 Lutetia

To directly compare the spectra obtained of meteorite PCA 91467 with information from the asteroid 21 Lutetia in the 0.3 to 2.2 μm range, a Lutetia spectrum taken from the Visible and InfraRed Thermal Imaging Spectrometer (VIRTIS) onboard Rosetta in the 0.5 to 5 μm range (Belskaya et al., 2010; Coradini et al., 2011; Sierks et al., 2011) was selected. This spectrum includes some undesired instrumental features mostly in the visible (~0.4 to 0.7 μm) region (Coradini et al., 2011). This is why a Lutetia spectrum from groundbased observations (visible range) was also used. It was obtained with the DOLORES (Device Optimized for the LOw RESolution) instrument in the Telescopio Nazionale Galileo (TNG, more details about this spectrum and the instrument in Belskaya et al., 2010), and was also used by Sierks et al. (2011) (Fig. S6 online material) to compare the OSIRIS Narrow Angle Camera (NAC) and Wide Angle Camera (WAC) spectrophotometry taken in flight during the Lutetia fly-by. In Figure 4.4 the PCA 91467 spectra obtained here are compared with the mentioned spectra from VIRTIS and DOLORES. To properly compare their shape and features, they were normalized to 1 at 0.55 μm. Band center positions were mostly decided using visual criteria, as only an approximate determination is required for the purposes of this chapter.

For the comparison in the 2.5 to 25.0 μm (4000 to 400 cm^{-1}) range, the VIRTIS spectrum between 2.5 and 4 μm (4000 to 2500 cm^{-1}), plus information obtained from Lutetia with the Infrared Spectrograph (IRS) of the Spitzer Space Telescope (SST), which covers the wavelength range from 5.2 to 38.0 μm (1923 to 263 cm^{-1}, approximately), were used. The IRS covered the whole rotational period of the asteroid with a total of 14 full wavelength spectra, which were averaged to obtain the mean emissivity (or emittance) spectrum used here (see Barucci et al., 2008, and Lamy et al., 2010, for more details). Note that in the IRS data, the region between 13.2 and 15 μm suffers from an excess emission, and therefore features there should be considered carefully (Vernazza et al., 2011). An emissivity spectrum depends in the radiant flux emitted, and its intensity pattern differs from what can be seen in an ATR spectrum as the one obtained for this study. The position of the peaks is apparently consistent between these two types of IR spectroscopy, according to previous studies, to the point of direct comparison (see, e.g., Morlok et al., 2014). However, a conservative approach is considered here, since there are too many differences between these techniques to directly compare their shape, and therefore the spectra are used separately. In the first

place, some of the features present in the ATR spectrum are analyzed (Figure 4.5). Separately, in Figure 4.6, some features present in the VIRTIS spectrum are studied, comparing them with information obtained about metal-rich carbonaceous chondrites in previous studies (Osawa et al., 2005). To complement that information, the IRS spectrum was compared with spectra of several meteorites from the ASTER (Advanced Spaceborn Thermal Emission and Reflection Radiometer) (Baldridge et al., 2009) and RELAB spectral catalogues, in a similar way as done before by other authors (Nedelcu et al., 2007; Barucci et al., 2008; Lazzarin et al., 2009). The goal was to see the overall resemblances and differences between them (Figure 4.7). There is only one PCA 91467 spectrum in the RELAB catalogue, and none in ASTER, so that spectrum was intentionally selected for the comparison. The other meteorite spectra were selected automatically performing a χ^2 test between the Lutetia spectrum and all the meteorite spectra on this two catalogues, and only taking into consideration the ones showing a higher correlation with the Lutetia spectrum. They were all normalized and shifted in order to simplify the visual comparison between them. All the spectra selected from the catalogues where obtained from powders with grain sizes < 75 μm, except for the KLE 98300 EH3 spectrum which comes from a sample with a grain size < 5 μm. With respect to the techniques, the spectra from RELAB are biconical reflectance spectra collected with an Off-Axis FT-IR Thermo Nicolet Nexus 870 with PIKE AutoDiff, while the spectra from ASTER are bidirectional reflectance spectra obtained with a Nicolet 520FT-IR spectrometer equipped with a Labsphere integrating sphere (Baldridge et al., 2009).

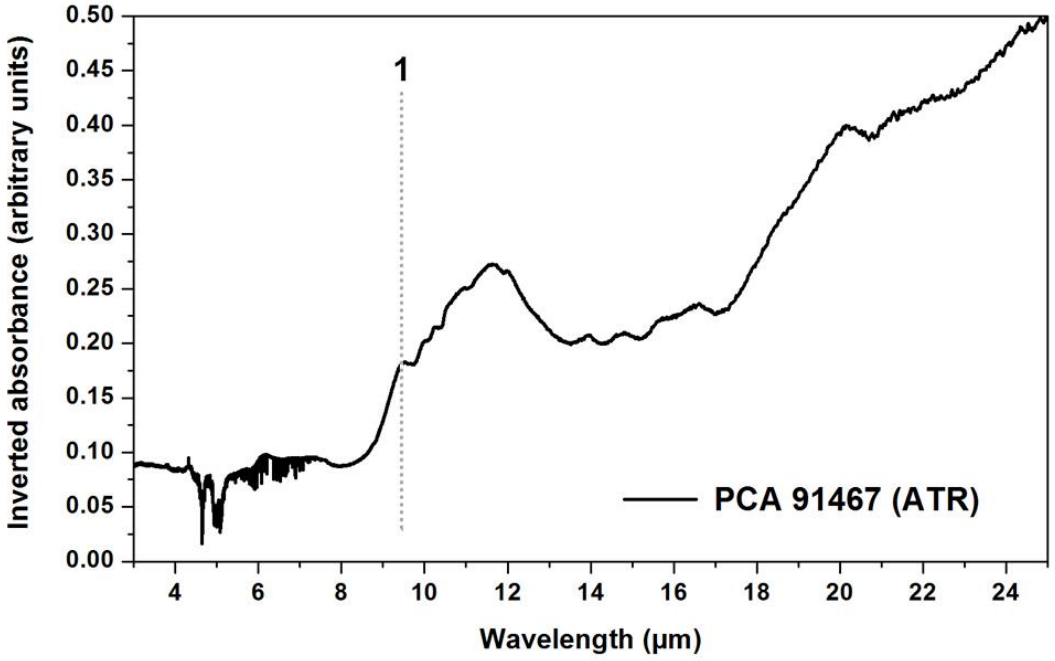

Figure 4.5: ATR inverted absorbance spectrum of a chip of PCA 91467. The grey vertical dotted line indicates the position of the Christiansen feature.

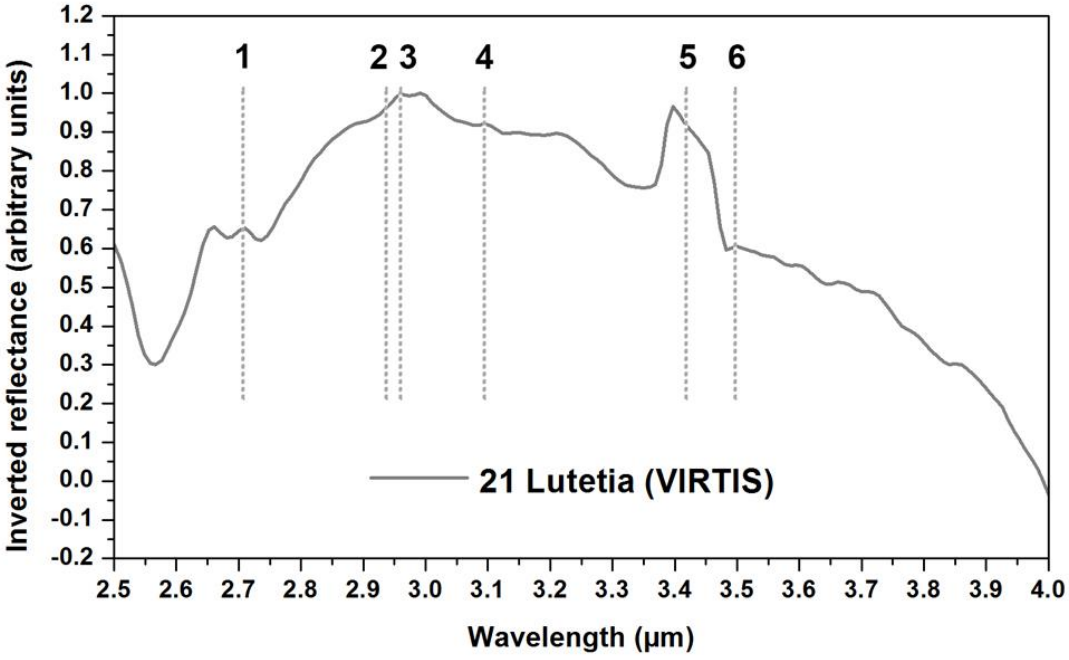

Figure 4.6: Inverted VIRTIS spectrum of the asteroid 21 Lutetia in the 2.5 to 4.0 μm (and 3800 to 2800 cm^{-1}) range. The grey vertical dotted lines indicate the position of several features related to CH chondrites in Osawa et al. (2005), and are explained in more detail in the text.

4.3 Results

4.3.1 Results in the 0.3 to 2.0 μm region

The UV-NIR spectra from Lutetia are usually featureless, except for some faint absorption bands, which are in general understood as different effects of aqueous alteration (see Barucci et al., 2012, and references therein). Indeed, asteroids larger than 100 km are commonly affected by water related processes, probably because they retained water ice that was melted by internal heating and reached the surface by hydrothermal circulation (Grimm & McSween, 1989; Fornasier et al., 2014). Another plausible scenario to explain the presence of features related with hydrous minerals, suggests low velocity collisions with primitive hydrated asteroids (Gaffey et al., 2002; Shepard et al., 2008), which would be consistent with the heterogeneity on Lutetia's surface (Rivkin et al., 2011; Barucci et al., 2012).

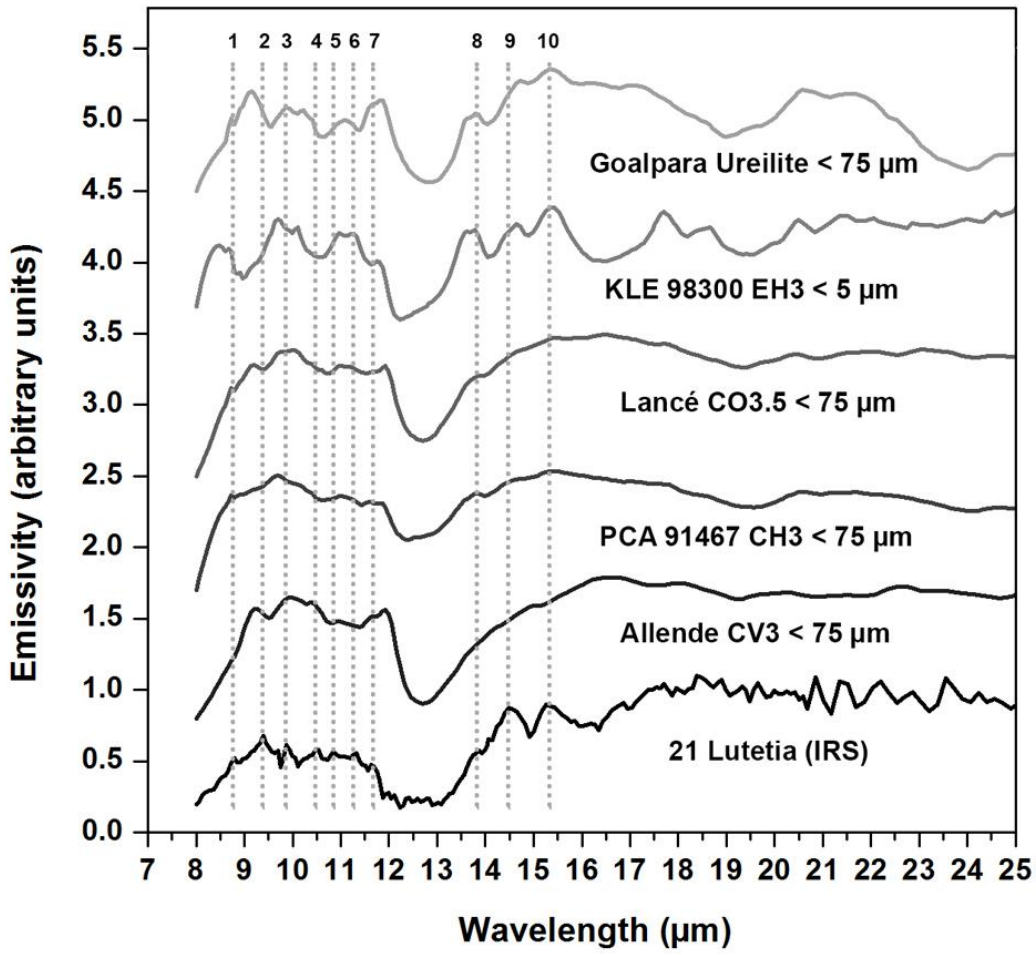

Figure 4.7: IRS spectrum of the asteroid 21 Lutetia in the 8.0 to 25.0 μm (1250 to 400 cm^{-1}) range, compared to five IR spectra from different meteorites. The grey

vertical dotted lines indicate the position of several peaks in the spectrum of 21 Lutetia (see text, Table 4.1 and Table 4.2 for a more detailed explanation). Every spectrum is labeled with its name, meteorite group, and grain size. The Allende and Lancé spectra were taken from the ASTER catalogue, while Goalpara, KLE 98300 and PCA 91467 were extracted from RELAB.

Several bands have been reported on the different Lutetia spectra so far. First, a narrow band at 0.43 μm, attributed to spin-forbidden *crystal* field transition related with ferric iron (Hunt & Ashley, 1979), appears in several spectra (Lazzarin et al., 2004; Belskaya et al., 2010). A broader band between ~0.45 and 0.55 μm, or centered around 0.48 μm, which has also been attributed to the Fe^{3+} spin forbidden (Cloutis et al., 2012c) has been seen in some Lutetia spectra (Lazzarin et al., 2009; Belskaya et al., 2010; Perna et al., 2010). Perna et al. (2010) also identified the Fe^{3+} charge transfer transition in iron oxides band at ~0.6 μm (Feierberg et al., 1985) in spectra obtained from the south pole of Lutetia. Another common band is found between 0.8 and 0.9 μm (Bus & Binzel, 2002b; Barucci et al., 2005; Birlan et al., 2006; Belskaya et al., 2010; de León et al., 2011), as a result of Fe^{3+} charge transfer transition in iron oxides (Hunt & Ashley, 1979). Although those features can be found heterogeneously around the asteroid (Barucci et al., 2012), the typical 3 μm band widely attributed to aqueous alteration (Lebofsky, 1978) seems to be more common in the southern hemisphere (Rivkin et al., 2011; Barucci et al., 2012), indicating that aqueous alteration is more extended in those regions of Lutetia (Birlan et al., 2004; Rivkin et al., 2011; Vernazza et al., 2011). It also should be noticed that the usual aqueous alteration band at 0.7 μm attributed to Fe^{2+} -> Fe^{3+} transfer absorption on phyllosilicates (Vilas & Gaffey, 1989), is not found on the Lutetia spectra (Barucci et al., 2012). Although the 0.7 and the 3 μm bands are often associated, some mechanisms like the transformation of all Fe^{2+} into Fe^{3+} or heating to ~ 800 – 900 K can explain the weakening and even disappearance of the first (Cloutis et al., 2011b). However, although the importance of the 3 μm band as an indicator of the fundamental O-H stretching bands of H_2O/OH (Lebofsky, 1978), this band is not necessarily associated to aqueous alteration (Gaffey et al., 2002; Rivkin et al., 2002), and can be a consequence of the presence of *mafic silicates* containing structural OH, *troilite*, solar-wind implanted H, and other *anhydrous* origins (see Gaffey et al., 2002, and references therein). Therefore, the lack of the 0.7 μm band could talk against

aqueous alteration on Lutetia, but most studies indicate otherwise (see Barucci et al., 2012, and references therein).

The specific asteroid spectra used here, coming from the VIRTIS and DOLORES observations, are just two examples of the space and ground based data obtained observing Lutetia in the ultraviolet to near-infrared range in the last 30 years (Barucci et al., 2012). They cover and represent different regions of the asteroid, showing therefore the variable presence of features described before. The VIRTIS spectrum used here for comparison combines information from about 50% of Lutetia's surface, from the north pole to around the equator (Coradini et al., 2011). The DOLORES spectrum comes from the southern hemisphere (Belskaya et al., 2010). In Figure 4.3 those two spectra of 21 Lutetia are plotted together with the obtained spectra of the CH3 chondrite PCA 91467. They show very similar shape up to 0.9 μm, considering the instrumental origin of the bands at 0.6 μm and 0.9 μm in the VIRTIS spectrum (Coradini et al., 2011). Between 0.9 and 1.4 μm the slope is still considerably close, but after this wavelength the VIRTIS spectrum becomes bluer. In fact, several spectra obtained from this asteroid so far show a relatively high variability in slope in the range between 0.9 and 2.4 μm (Nedelcu et al., 2007).

The 0.9 and 1.9 μm bands in the RELAB PCA 91467 spectrum (Figure 4.3) clearly correspond to *enstatite* with only a minor content on Fe (Fs_{1-5}) (Bischoff et al., 1994; Klima et al., 2007; Cloutis et al., 2012c). The red slope between 0.9 and 2.2 μm is consistent with the high content of Fe-Ni metal (Bischoff et al., 1994; Cloutis et al., 2010; Cloutis et al., 2012b), in both the RELAB spectrum and the spectra collected for this chapter. Those show a slight decrease in reflectance between 0.43 and 0.83 μm. The continuum was removed in this region, in order to see if the minor bands described for Lutetia between 0.4 and 0.9 μm are producing this effect (Figure 4.4, B). The very narrow band at 0.43 μm in the DOLORES spectrum can possibly be distinguished as a very faint feature in the PCA 91467 spectra studied in this chapter (1 in Figure 4.4, B, marked as a dotted line), but it is probably a false band as a consequence of the lower resolution of the Shimadzu UV3600 spectrometer compared to DOLORES. The band described between ~0.45 and 0.55 μm for some Lutetia spectra (Lazzarin et al., 2009; Belskaya et al., 2010; Perna et al., 2010) is seen in the three PCA 91467 spectra (marked as 2 in Figure 4.4, B, between two solid lines). The very faint band at 0.61 μm (3 in Figure 4.4, B, marked as a dotted line) can also be considered as the 0.6 μm band described before for Lutetia (Perna et al., 2010). A drop-off starting at 0.8 μm in the

PCA 91467 spectra (4 in Figure 4.4, B, marked as a dotted line) could be the beginning of the band between 0.8 and 0.9 μm described for some Lutetia spectra (Bus & Binzel, 2002b; Barucci et al., 2005; Birlan et al., 2006; Belskaya et al., 2010; de León et al., 2011), and the 0.9 *enstatite* band in CH chondrites (Cloutis et al., 2012c).

Many factors can be the origin of the differences between the spectra obtained from the surface of an asteroid and the polished sections of a meteorite. First, the nature of Lutetia's surface, and the effect it can have on the spectra obtained from the asteroid, should be considered. Grain size of this material is an important trait to take into account. It has been shown that variations in grain size produce some degree of reddening in the slope of meteorite spectra (Johnson & Fanale, 1973). For example, decreasing the average grain size of CM chondrites usually results in redder spectra (Johnson and Fanale, 1973; Hiroi et al., 1993; Cloutis et al., 2011; among others). The bluer slope seen in the Lutetia spectra could therefore be indicative of a grain size in the surface of the asteroid larger than 75 μm (the grain size of the RELAB sample, which shows an equivalent spectral slope to the samples studied in this chapter, as explained before). That would be consistent with the Gundlach and Blum (2013) paper, where they described a mean grain radius of surface regolith for Lutetia of 210 μm (although with a large indetermination between +340 μm and -170 μm). However, polarimetric observations indicate that the regolith surface of Lutetia could be covered, at least partially, by material with a mean grain size of less than 20 μm, due to the accumulation of small particles and fragments coming from impact gardening around the asteroid (Belskaya et al., 2010). If this is correct, a different scenario should be considered. According to Cloutis et al. (1990) the presence of *magnetite* seems to have a bluing effect (reflectance decreasing toward longer wavelengths) on the spectra of asteroids: the finer the grain size of *magnetite* the bluer the spectra. This mineral has been found in PCA 91467 and other CH chondrites (see e.g. Sugiura, 2000; Greshake et al., 2002; Chan et al., 2015) and its presence is consistent with the band at 0.48 μm, both in the meteorite and the asteroid (Perna et al., 2010; Cloutis et al., 2012c, and references therein). Although the amount of *magnetite* on CH chondrites is very small (Greshake et al., 2002), this kind of opaque minerals tend to dominate the spectral signature (Gaffey et al., 2002). Furthermore, a fine grain size can have a deepening effect in absorption bands (Johnson & Fanale, 1973) which could also explain why the 0.43 μm band is far more visible in the DOLORES Lutetia spectrum. Another possibility would require a strong heating mechanism for Lutetia beyond 770 K, as high enough temperatures have

a bluing effect on spectral slope (Hiroi et al., 1993). Considering Lutetia as analogous to the parent body of PCA 91467, with the same or similar evolutionary process, this strong heating scenario must have taken place after the meteorite was released from the asteroid's surface, as CH chondrites show low to no evidence of metamorphism on its parent body (Krot et al., 2002).

4.3.2 Results in the 2.5 to 25 μm (4000 to 400 cm^{-1}) region

The ATR spectrum of a chip of the meteorite PCA 91467 (inverted to be more easily compared to emissivity spectra from asteroids), between 3.0 and 25.0 μm, is shown in Figure 4.5. The thermal infrared spectra of meteorites and asteroids in this range are usually studied through the Christiansen peak, the Reststrahlen bands and the Transparency features (Barucci et al., 2008; Vernazza et al., 2011, and others). In any case, the presence of these features in the ATR spectrum cannot easily be compared with the features seen in IR spectra obtained with other techniques (see e.g. Morlok et al., 2006; Lane et al., 2011, for examples about the shape of IR spectra obtained by different spectroscopic techniques). However, a Christiansen peak related to mineralogy and grain size (Salisbury, 1993), which was identified in the IRS spectrum of Lutetia by Barucci et al. (2008) at 9.39 μm or 1065 cm^{-1}, can be tentatively identified in the ATR spectrum at 9.46 μm or 1057 cm^{-1}, as pointed out in Figure 4.5 (indicated by a dotted line labeled as 1). This peak, that always occurs between 8 and 9.5 μm (1250 and 1050 cm^{-1}) for *silicates* (Salisbury, 1993), has been identified at around 8.3 μm (1205 cm^{-1}) for ECs (Izawa et al., 2010), which could imply that Lutetia is less related with these meteorites than with CH3 chondrites. In the 8 to 13 μm (1250 to 770 cm^{-1}) region, where the main peaks to compare can be found (Barucci et al., 2008; Morlok et al., 2014), the comparison of specific peaks implies many difficulties. The astronomical data usually have lower signal to noise ratios than laboratory data (see e.g. Barucci et al., 2008). Besides, most asteroids spectra lack specific features probably due to the fine particulate regolith that covers their surface (Lim et al., 2005). Also, the IRS spectrum covers a wide region of the asteroid slightly south of the equator, encompassing a higher mineralogical variability than what can be found on a meteorite sample, and even small changes in composition can affect the position of most mineralogical peaks.

The Lutetia IRS spectrum was also examined in the beginning of the mid-infrared range, from 2.5 to 4 μm (4000 to 2500 cm^{-1}), as in this spectral region several features related with water and organics can be found (see Figure 4.6). Considering the CC

spectra analyzed by Osawa et al. (2005), the Lutetia IRS spectrum seems much more similar to CB and CH chondrites spectra than to any other CC spectra analyzed there. First of all, the peak at 2.709 μm (3692 cm^{-1}, indicated with a dotted line labeled as 1 in Figure 4.6) attributed to free O-H stretching vibrations of *chrysotile*, was only found in one CB and two CH chondrites. Notice that it is different from the peak at 2.714 μm (3685 cm^{-1}) found in CI chondrites and corresponding to the *serpentine* mineral *lizardite* (Osawa et al., 2005). In the Lutetia spectrum this first peak is preceded by another one at 2.66 μm (3758 cm^{-1}) which does not appear in any of the CCs spectra in Osawa et al. (2005), and that could not be identified for this chapter. A very broad peak centered around 2.94 μm (3400 cm^{-1}, dotted line labeled as 2) is also representative of CH chondrites, and similar to the O-H stretching vibrations of CI chondrites (Osawa et al., 2005). In fact, the two peaks at 2.963 and 3.091 μm (3375 and 3235 cm^{-1}, respectively, corresponding to the dotted lines labeled as 3 and 4) are typical features related with hydrated phyllosilicates and widespread aqueous alteration (Dyar et al., 2011). Although, as explained before, the peaks closer to 3 μm could also have an *anhydrous* origin, the interpretation supported in this chapter is based on the several previous studies suggesting a certain degree of hydration for Lutetia (see e.g. Barucci et al., 2012, and references therein), and do not take into consideration other minor contributions to these features. The next two dotted lines, labeled as 5 and 6, are at 3.419 μm (2924 cm^{-1}) and at 3.504 μm (2854 cm^{-1}). In the Lutetia IRS spectrum, peak 5 is much higher than the equivalent identified in Osawa et al. (2005), and looks shifted to a lower wavelength, while peak number 6 is very weak. Those two peaks have been attributed to symmetric and asymmetric C-H stretching vibrations of *aliphatic* (CH_2 and CH_3) organics (Sandford et al., 1991), whether they are the consequence of terrestrial contamination (which is obviously not an option for Lutetia) or they have an extraterrestrial origin.

Finally, in Figure 4.7 the IRS spectrum of Lutetia is compared to five spectra from the ASTER and RELAB catalogues. The selected spectra correspond to one spectrum of the CV3 chondrite Allende and one spectrum of the CO3.5 Lancé (ASTER), plus a spectrum of the CH3 PCA 91467, one from the EH3 KLE 98300, and one spectrum from the ureilite Goalpara (RELAB). As mentioned CVs, COs and ECs have been studied before as possible analogs for the asteroid 21 Lutetia (Lazzarin et al., 2004; Barucci et al., 2008; Lazzarin et al., 2009; Belskaya et al., 2010; Ockert-Bell et al., 2010; Vernazza et al., 2011; Barucci et al., 2012; among others), while some ureilites,

despite being achondrites (with a high content in carbon), have been proved to have similar spectra in the thermal infrared (Lazzarin et al., 2009). CH chondrites have also been suggested in previous studies (Lazzarin et al., 2009; Coradini et al., 2011). Unfortunately, there is only one spectrum of a CH in these two catalogues, and more data would be necessary for a detailed comparison.

The main peaks in the ~8 to 12 μm (1250 to 833 cm^{-1}) plateau of the IRS spectrum, which arises from the O-Si-O asymmetric stretching vibration (Salisbury, 1993), plus three peaks in the ~13.5 to 15.5 μm (740 to 645 cm^{-1}) region (they are highlighted with dotted lines in Figure 4.7, while Table 4.1 shows the relative strength of each peak in every spectrum), were also studied. It has to be taken into account, however, that some of the selected peaks are not very strong, and therefore could be a product of noise, instead of real peaks. Also, that peaks 8 and 9 in the IRS spectrum of Lutetia are in a region that suffers from an excess emission and should be considered carefully (Vernazza et al., 2011). Based on literature data, Table 4.2 reports a plausible assignment of them all, attributed to the presence of *silicates* and *phyllosilicates*. The most abundant classes of *silicates* in space are *olivine* and *pyroxene*, while *phyllosilicates* (also called hydrous *silicates* because they form from hydration of *anhydrous silicates*) are commonly present in interplanetary dust particles and different CC types, in which a shallow band at 2.75 μm (3636 cm^{-1}), associated with OH-bonded *silicate* vibrations, attests to partial hydration of the *silicate* component. The main diagnostic band that indicates the presence of cosmic *silicates* is near 9.8 μm (1020 cm^{-1}). Dorschner et al. (1995) identified bands at 9.80 and 9.78 μm (1020 and 1022 cm^{-1}) associated with *olivine glasses*. Thus, band 3 in Figure 4.7 (9.87 μm or 1013 cm^{-1}) can be due to the presence of *amorphous olivines*. In contrast to the single peak for *olivines*, *pyroxenes* (and in particular *enstatite*) present two characteristic bands at 9.4 and 10.8 μm (1064 and 926 cm^{-1}) according to Zaikowski et al. (1975). These two bands (2 and 5 in Figure 4.7) are present in the meteorites samples at 9.39 and 10.84 μm (1065 and 923 cm^{-1}). It is known that *crystalline silicates* are present in PCA 91467 in the form of *enstatite* and small amounts of Mg-rich *olivine* (Bischoff et al., 1994), and band 6 (centered at 11.33 μm or 883 cm^{-1}) matches with the diagnostic band at 11.3 μm (885 cm^{-1}) for *crystalline forsterite* (Bouwman et al., 2001). In the same way, bands 7, 9 and 10 (at 11.63, 14.49 and 15.25 μm, respectively, or 860, 690 and 656 cm^{-1}) can be due to the presence of *crystalline* forms of *enstatite* as they match to the featured bands at 11.6, 14.5 and 15.4 μm (862, 690 and 649 cm^{-1}) of synthetic *crystalline clinoenstatite* (Jäger

et al., 1998). Band 8, at 13.87 μm (721 cm^{-1}) can also be related to *crystalline enstatite* (Jäger et al., 1998). It is worth mentioning that bands 3 and 9 (9.87 and 14.49 μm, or 1013 and 690 cm^{-1}) can also be contributed by the presence of *talc*. The presence of this mineral can be understood by the hydration of *enstatite* and its presence has been detected in natural *enstatite* samples from peaks at 9.8 – 9.9 μm (1020 – 1010 cm^{-1}) and 14.6 – 15.0 μm (685 – 667 cm^{-1}) (Jäger et al., 1998). Moreover, other *phyllosilicates* can also be present since band 4 (10.48 μm or 954 cm^{-1}) can be attributed to *chlorite*, a *phyllosilicate* with a characteristic band at 10.5 μm (952 cm^{-1}), and band 2 (9.39 μm or 1065 cm^{-1}) can also result from the presence of *serpentine*, which has a featured band at 9.3 μm (1075 cm^{-1}) (Zaikowski et al., 1975). Finally band 1 (8.79 μm or 1138 cm^{-1}) can be due to the presence of pure *silica* SiO_2 component, but only considering, very tentatively, a broad band centered at 8.6 μm (1163 cm^{-1}) present in the spectral region of a sample of Herbig Ae/Be stars (Bouwman et al., 2001).

Table 4.1: Subjective comparison between peaks of the spectra in Figure 4.7.

Spectrum	**1**	**2**	**3**	**4**	**5**	**6**	**7**	**8**	**9**	**10**
μm	**8.79**	**9.39**	**9.87**	**10.48**	**10.84**	**11.33**	**11.63**	**13.87**	**14.49**	**15.25**
cm^{-1}	**1138**	**1065**	**1013**	**954**	**923**	**883**	**860**	**721**	**690**	**656**
21 Lutetia	sm	md	md	sm	sm	sm	sm	sm	lg	lg
Allende	nd	md[a]	md	sm	sm	nd	lg[a]	nd	nd	nd
PCA 91467	sm	md[a]	nd	nd	sm	nd	sm[a]	sm	sm	sm
Lancé	sm	md[a]	md[a]	nd	sm	nd	md[a]	sm	nd	sm
KL 98300	sm	lg[a]	md[a]	nd	lg	lg	sm[a]	lg[a]	md[a]	lg
Goalpara	sm	lg[a]	md	nd	md[a]	nd	lg[a]	md[a]	md[a]	md

[a] The peak (if the same) is notably shifted.

nd Not detected or shifted in such a way that can be confused with another peak.

sm Relatively small peak.

md Relatively medium peak.

lg Relatively large peak.

In the transparency feature between ~12 and 13.5 μm (833 to 740 cm^{-1}) and the region above 16 μm (625 cm^{-1}), the general shape is considered, but not the peaks, as they are poorly defined probably as a consequence of the low signal to noise ratio (Barucci et al., 2008). The general shapes of the five spectra match quite well the Lutetia spectrum, but going into more detail several differences can be seen. First, the slope of the smooth plateau between ~13.5 to 15.5 μm (740 to 645 cm^{-1}) is similar in all the spectra, but the CCs match better the general relative intensity of the peaks and deep of the bands, although none of them show exactly the same features as Lutetia. Concerning the Christiansen peak, all the catalogue spectra show it shifted by a maximum of ± 0.25 μm with respect to the IRS spectrum (to the point of being confused or mixed with other peaks). The spectrum that apparently shows the closest transparency feature between ~12 and 13.5 μm (833 to 740 cm^{-1}) is the one from PCA 91467. For the peaks in the ~13.5 to 15.5 μm (740 to 645 cm^{-1}) region, they are absent in Allende and very faint in the other CCs, while they are quite strong in the spectra of Lutetia, the EC and the ureilite. In the region above 16 μm (625 cm^{-1}) Allende shows the more similar slope and general behavior, while PCA 91467 and Lancé have slightly bluer spectra and the spectra from KLE 98300 and Goalpara show much more strong features than the IRS spectrum. Several reasons can explain the differences between these spectra. Besides specific variations in mineralogy and composition, the grain size of the samples can affect the general slope and the depth of bands, an effect that seems to be more important in CCs than in ECs (Barucci et al., 2012, and references therein). Other variations can be the result of using different techniques. As a summary, it seems that all of them show some spectral similarities with the asteroid 21 Lutetia at those wavelengths, so none of them can be completely discarded or selected as a proper analogue without a more detailed comparison, at least not from a thermal infrared point of view.

Table 4.2: Assignment of the IR bands presented in Figure 4.7.

Band position		**Presence of**	**Reference**
μm	cm^{-1}		
8.79	1138	SiO_2	(Bouwman et al., 2001)
9.39	1065	*enstatite*	(Zaikowski et al., 1975)

		serpentine	(Zaikowski et al., 1975)
9.87	1013	*olivines*	(Dorschner et al., 1995)
		talc	(Zaikowski et al., 1975)
10.48	954	*chlorite*	(Zaikowski et al., 1975)
10.84	923	*enstatite*	(Zaikowski et al., 1975)
11.33	883	*crystalline olivines*	(Jäger et al., 1998)
		crystalline forsterite	(Bouwman et al., 2001)
11.63	860	*crystalline enstatite*	(Jäger et al., 1998)
13.87	721	*crystalline enstatite*	(Jäger et al., 1998)
14.49	690	*crystalline enstatite*	(Jäger et al., 1998)
		talc	(Zaikowski et al., 1975)
15.25	656	*crystalline enstatite*	(Jäger et al., 1998)

4.4 Discussion

As described, the interpretation of 21 Lutetia spectra seems to indicate the presence of reducing minerals such as *enstatite*, and also the presence of water-related features. The simultaneous presence of both elements most likely requires formation in an environment with variable conditions and chemical mixing, such as the middle region of the main asteroid belt (Grimm & McSween, 1993; Hardersen et al., 2011), where Lutetia belongs (Barucci et al., 2005). The apparent dissimilitude between Lutetia and this particular CH chondrite could be envisioned in the context described by Davis et al. (1989), in which large asteroids were collisionally disrupted, losing partially their surface layers in the case of asteroids larger than 100 km. Such scenario has been recently modeled successfully for 21 Lutetia (Beitz et al., 2016), and demonstrates that most of the asteroidal surface must have been gardened by large impacts. In the case of objects with internal ice, heating from decay of their radioactive elements would melt the ice and produce water mobilization and aqueous alteration on portions of the asteroids, possibly close to the surface (Grimm & McSween, 1989), while the interior could be heated to a degree in which thermal metamorphism would be important

(Grimm & McSween, 1993). This scenario assumes that water was present on Lutetia before being heated, but an alternative scenario would be considering that CC-type material (and therefore rich in water and carbon) was accreted to its surface, or maybe a water-rich object impacted Lutetia at a slow speed, thus avoiding the vaporization of water (Gaffey et al., 2002; Shepard et al., 2008; Vernazza et al., 2011). That would explain the abundance of *phyllosilicates* on CH chondrites and their possible detection in the IRS spectrum of Lutetia, while a large portion of the asteroid's surface seems to be dry. PCA 91467 would have been formed, or accreted, in the cold surface of such an asteroid, where the aqueous alteration due to internal heating would be very small, or even absent in some regions. Posterior collisions would gave the surface material the breccia constitution that can be recognized on PCA 91467, with a high proportion of fragmented components (Bischoff et al., 1994; Bischoff et al., 2006), and increase the formation of *phyllosilicates*. Indeed, CH chondrites (but also CR and CB chondrites) have been affected to some degree by melting, vaporization, outgassing, condensation and size-sorting in a cloud of impact ejecta (Wasson & Kallemeyn, 1990). Later, the parent fragment of PCA 91467 would be ejected from the parent asteroid, which surface would finally be reshaped by posterior collisional processes, uncovering superior layers with materials more affected by aqueous alteration, and deeper thermally *metamorphosed* regions. Applied to Lutetia, that model would partially explain the heterogeneity of its surface (Rivkin et al., 2011; Barucci et al., 2012).

4.5 Conclusions

Spectroscopic techniques in the UV-NIR and IR range were used in this chapter in order to obtain spectra from CH3 meteorite PCA 91467. The spectroscopic results obtained in the context of this chapter were compared with spectral data from previous studies. The outcome of this effort was to establish a plausible connection between CH chondrites and 21 Lutetia or similar asteroids. Since 21 Lutetia was fly-bied by the Rosetta spacecraft, a considerable amount of information from this asteroid is available to be studied. The main conclusions of this chapter are as follows:

1. In order to establish links between meteorites and asteroids, a careful deciphering of the spectra obtained from asteroids in different wavelengths is required. They can be compared with the spectra from meteorite samples, but the important differences between a regolith-covered asteroidal surface and a small polished meteorite section must be taken into account. Therefore, an extensive

understanding of the key spectral features provided by those techniques, together with information about their bulk physical properties, is required to determine the parent bodies of chondrites with reasonable certainty. In that sense, future sample-return missions like OSIRIS-Rex or Hayabusa 2 will provide samples from asteroids to be compared with current known chondrite groups, and continue identifying the parent bodies of meteorites reaching our planet.

2. The distinctive slope and features, together with the degree of absolute reflection, allow establishing a possible relationship between PCA 91467 and asteroids resembling Lutetia. This asteroid has been related to M-type asteroids in the Tholen taxonomy, and to the asteroids belonging to the X-complex in the Bus-DeMeo taxonomy. Consistently, CH chondrites exhibit reflectance and mineralogical properties that suggest that their parent bodies can be found among moderate albedo asteroids with mostly featureless spectra. Also, the peculiar combination of a high content on carbon and metal common in CH chondrites can explain many of the special properties of Lutetia, or at least of some regions of this asteroid. Finally, the inferred density of this asteroid is quite close to the bulk density calculated for CH meteorites.

3. In the UV-NIR comparison it was found that the selected spectra from Lutetia and PCA 91467 are reasonably similar, considering the differences between polished sections and the regolith-covered surface expected for Lutetia. The intermediate to high reflectance of PCA 91467 is consistent with the intermediate albedo of Lutetia. The differences are probably a consequence of some posterior evolution of the parent body, and also due to the space weathering affecting its surface.

4. The IRS spectrum of Lutetia was compared to several spectra of different meteorites extracted from the RELAB and ASTER catalogues. The several features identified were tentatively related to mineralogy. Despite all spectra compared in Figure 4.7 show a certain degree of correlation with Lutetia, none of them can be established as a perfect analogue for this specific spectrum of the asteroid. This is expected, as this specific IRS spectrum is the mean of 14 different spectra, probably showing a heterogeneous combination of

mineralogies. The position of particular features clearly differs between Lutetia and ECs, and also from the COs and CVs used in this chapter for comparison. Those three constitute the main types of meteorites suggested before as analogues to Lutetia. The peaks analyzed suggest a possible detection of *phyllosilicates* in the surface of Lutetia.

5. In the specific comparison between the 21 Lutetia spectra and Osawa et al (2005) and RELAB spectra of PCA 91467 in the IR region, the similarity in the position of organic (in the 2.5 to 4 μm region) and *silicate* (in the 8 to 16 μm region) associated peaks has been shown. Several differences point towards a higher presence of aqueous alteration in Lutetia than in PCA 91467, which could be explained if the meteorite was ejected from the aqueously and thermally unaltered surface of its parent body.

6. It is proposed here that PCA 91467, and by extension the group of CH chondrites, proceed from a Lutetia-type asteroid, i.e., an asteroid with properties and evolutionary history resembling those of Lutetia. Those meteorites can possibly be considered as analogues for particularly primitive regions on the surface of Lutetia. This could imply that at a certain point on Lutetia's life a reservoir of CH-like material accumulated or formed on its surface, as a result of aggregation and/or impacts. PCA 91467 could then have been formed as a breccia on the cold surface of an asteroid similar to Lutetia. The parent fragments of CH chondrites were saved from differentiation due to the size and general properties of its parent asteroid, which prevented thermal metamorphism and partially aqueous alteration to reach the most outer layers of this object. After the meteorites were released to space, collisional processes broke the outer layers of the asteroid, revealing more aqueously altered and thermally *metamorphosed* regions. Therefore, the current heterogeneity on the surface of Lutetia would be showing different degrees of alteration and mineralogical evolution.

5 MECHANICAL PROPERTIES OF THE CHELYABINSK METEORITE

Abstract

In addition to the understanding about the formation and evolution of minor bodies and the predecessors of planets, the study of asteroids using meteorites has more practical motivations. Earth's neighborhood is constantly visited by comets and asteroids which orbits have a perihelion of less than 1.3 AU. Most of those so called Near-Earth Objects (NEOs) are actually asteroids, and are therefore referred as NEAs. More than 16,000 NEAs have been identified so far and, although more are being discovered almost every day. Among them, there are currently ~1,800 whose orbits have minimum intersection distance of less than 0.05 AU with Earth's orbit, or a size of about 150 m or larger. Since this implies a potential threat to our planet, they are known as Potentially Hazardous Asteroids (PHAs). In order to study NEAs and PHAs, most of which are S- or Q-type asteroids, representative samples are required. The Chelyabinsk meteorite is a highly shocked, low porosity OC, and therefore can be a good example of the materials composing S- and Q-type asteroids. The nanoindentation technique was used on Chelyabinsk in this chapter in order to obtain key data to understand the physical properties of NEAs. Tests at different length scales provide information about the local mechanical properties of the minerals forming this meteorite: reduced *Young's modulus*, *hardness*, *elastic recovery*, and *fracture toughness*. Those tests are also useful to

understand the potential to deflect threatening asteroids using a kinetic projectile. It was found that the differences in mechanical properties between regions of the meteorite, which increase or reduce the efficiency of impacts, are not a result of compositional differences. A low mean particle size, attributed to repetitive shock, can increase *hardness*, while low porosity promotes a higher momentum multiplication. Momentum multiplication is the ratio between the change in momentum of a target due to an impact, and the momentum of the projectile, and, therefore higher values imply more efficient impacts. In the Chelyabinsk meteorite, the properties of the light-colored *lithology* materials facilitate obtaining higher momentum multiplication values, compared to the other regions described for this meteorite. A low value of *fracture toughness* was obtained for the shock-melt veins of Chelyabinsk, which would promote the ejection of material after an impact and, therefore, increase the momentum multiplication. These results are relevant considering the growing interest in missions to test asteroid deflection, such as the recent collaboration between the European Space Agency and NASA, known as the Asteroid Impact and Deflection Assessment mission. The results of this chapter have been published in the *Astrophysical Journal* (Moyano-Cambero et al., 2017a)

5.1 Introduction

Although the probability of an asteroid causing a catastrophic impact is statistically small (Atkinson et al., 2000), the public concern about impact hazard increased in 2013, when a small asteroid overflew the Russian region of Chelyabinsk, producing a large airburst accompanied by thousands of meteorite specimens falling, with a total mass of ~1000 kg (Nazarov et al., 2013; Ruzicka et al., 2015). The asteroid diameter, estimated at ~18 meters (Brown et al., 2013), was relatively small compared with kilometer-sized bodies capable of producing a mass extinction. Nevertheless, the shockwave released caused significant damage to buildings, and ~1500 people were injured. The Chelyabinsk event shows that even if a highly destructive impact has a very low probability of occurrence, airburst effects can still be dangerous (see e.g. Wasson 2003). Such events can be expected on a once in a decade-to-century scale (see e.g. Atkinson et al. 2000) due to collisions with objects coming directly from the main asteroid belt, or also to disruptive processes that occurred in near-Earth space (Trigo-Rodríguez et al., 2007).

There is an ongoing discussion concerning the best strategy to deal with any potential threatening asteroid (Morrison, 2010). Some techniques, such as using a gravity tractor, require years or even decades to be effective (Lu & Love, 2005). Kinetic impact strategies, which imply using a projectile to slightly change the orbit of a NEA, are technologically more advanced and require a much shorter time scale (Ahrens & Harris, 1992). Due to the controversy related to the use of nuclear weapons, non-explosive projectiles are preferred (Koenig & Chyba, 2007). Between 2005 and 2007 the European Space Agency (ESA) proposed the Don Quijote mission (Carnelli et al., 2006), with the aim of testing the feasibility of using a kinetic projectile to deflect an asteroid, and also to properly observe and analyze the consequences on the target asteroid. The mission was not adopted, but aspects of it were incorporated in the Asteroid Impact and Deflection Assessment (AIDA) mission. AIDA has been a collaboration between ESA and NASA to develop two complementary spacecraft: the *Asteroid Impact Mission (AIM),* by ESA, and the *Double Asteroid Redirect Test (DART),* by NASA (Michel et al., 2015a; Michel et al., 2016). The two missions were planned to travel to the binary NEA (65803) Didymos, composed of a primary 800 m asteroid and a 150 m satellite. The latter will be impacted by the 300 kg *DART* spacecraft, while *AIM* would characterize the system before and after such event (Michel et al., 2015a). However, AIM did not receive the necessary funding in December, 2016, and, therefore, the future of AIDA is unclear.

The success of AIDA and similar concepts depends on the knowledge of the physical (i.e., mechanical) properties of the NEA to be deflected. A proper characterization of these objects is, therefore, required to avoid, or minimize, unexpected outcomes such as a multiple fragmentation (Holsapple & Ryan, 2002). In this chapter a laboratory approach using meteorite specimens is presented, in order to quantify, in controlled small-scale experiments, mechanical parameters that might be used to predict the effects caused by a projectile on the surface of an asteroid. Nanoindentation is selected here as an almost nondestructive technique, compared to impact tests. The Chelyabinsk meteorite was selected as a good example of the different materials that form small NEAs such as (65803) Didymos. The results obtained using quasistatic conditions from a Chelyabinsk specimen, are interpreted in view of their correlation with dynamic mechanical parameters that play a role during an impact between the asteroid and an external body.

5.2 Sample selection and experimental techniques

Chelyabinsk has been classified as an LL5 and LL6 OC breccia exhibiting different *lithologies* (Bischoff et al. 2013; Kohout et al. 2014; Ruzicka et al. 2015). The most abundant is the light-colored *lithology*, constituting ~65% of the meteorite. It shows a typical equilibrated chondritic texture and contains *recrystallized* chondrules that are deformed or broken, plus very thin inter-granular metal and *troilite* veins (Galimov et al. 2013; Kohout et al. 2014; Righter et al. 2015; Ruzicka et al. 2015). Some LL6 fragments with rare chondrule relicts and highly *recrystallized* LL5/6 or LL6 regions, with and without shock veins, have been classified as part of the light-colored *lithology*, but also as different *lithologies* (Bischoff et al., 2013b). The following most common *lithology* is the dark-colored (or shock-darkened), in which only a small fraction of the original equilibrated chondritic texture remains. The light- and dark-colored *lithologies* are rarely found in the same specimen (Kohout et al., 2014). A third *lithology* is often encountered together with any of the other two: a fine-grained dark impact-melt *lithology* containing finely dispersed metal and *troilite* droplets, and variable abundances of mineral and *lithic* clasts (Bischoff et al. 2013; Galimov et al. 2013; Kohout et al. 2014; Righter et al. 2015). Due to their similar color, the dark-colored and the impact-melt *lithologies* have often been considered together as a single *lithology* (Reddy et al. 2014; Ruzicka et al. 2015). The three *lithologies* have roughly similar compositions (Galimov et al. 2013; Kohout et al. 2014;), with *olivine* (~Fa_{28}) being two to four times more abundant than *pyroxene* (~Fs_{23}). Although both minerals are mostly homogeneous in composition (Galimov et al. 2013; Kohout et al. 2014; Righter et al. 2015; Ruzicka et al. 2015), *pyroxene* is mainly *orthopyroxene*, in a proportion superior to 2:1 over *clinopyroxene* (Galimov et al. 2013; Ruzicka et al. 2015). Opaque minerals consist of 6-7 wt% of *troilite* and 2-4 wt% of metal phase, the latter being mostly *kamacite* (~5 wt% of Ni) and *taenite* (~35 wt% of Ni) (Galimov et al. 2013; Popova et al. 2013; Ruzicka et al. 2015). *Chromite*, *phosphate* (*apatite*), and *ilmenite*, among others, are *accessory* minerals (Galimov et al., 2013).

As an LL-type OC, Chelyabinsk can be easily connected with most NEAs, usually associated with S- or Q-class asteroids (Binzel et al., 2001; Vernazza et al., 2008; Reddy et al., 2014). In fact, it has been suggested that ~2/3 of NEAs show a better match with LL chondrites than with the other OC types (Vernazza et al., 2008). It has been found that S- and Q- asteroids probably form as rubble piles (Holsapple, 2001) and, therefore, should show a considerable degree of shock and brecciation, similar to

what has been seen in the Chelyabinsk meteorite (Bischoff et al. 2013; Ruzicka et al. 2015). Didymos, in particular, has been classified as an S-type asteroid, and it also has been spectroscopically connected to L/LL-type meteorites (Dunn et al., 2013b). As a binary system, the formation of Didymos as a rubble pile is logical (Walsh & Richardson, 2006). As well as being a good analog for Didymos, Chelyabinsk also allows for testing the effects of shock on the mechanical properties of OC-forming minerals. Such chondrites probably originated from the catastrophic disruption of moderately large asteroids, whose fragments formed families with complex collisional histories (Bottke Jr. et al., 2015; Michel et al., 2015b).

In this chapter one of the specimens of Chelyabinsk, the polished thin (~30 μm) section PL 13049, kindly provided by Addi Bischoff, was analyzed. The section was polished to mirror-like appearance using diamond paste, and studied by optical microscopy with the Zeiss Scope Axio petrographic microscope described in chapter 2. RL and TL images of the whole Chelyabinsk PL 13049 section were obtained at 50× magnification, and the TL images were merged to create a high-resolution mosaic to be used as a reference map (Figure 5.1). The Zeiss Merlin FE SEM at the UAB was used to study the microstructure of the sample at 1.20 kV. The chemical composition of the different regions was determined by EDS, using both the Inca 250 SSD XMax20 working at accelerating voltages of 20 kV, and the Zeiss Merlin SEM, which also allowed for the acquisition of EDS patterns working at accelerating voltages of 15 kV.

The mechanical properties of the specimen were evaluated by nanoindentation with the UMIS from Fischer-Cripps Laboratories at the UAB, operated in the load control. As explained in chapter 2 the indenter pushes the surface of the samples while increasing load, and when the indenter is unloaded, the sample surface pushes back. In this case, the thermal drift during nanoindentation was kept below 0.05 nm s^{-1}. A load-displacement curve was obtained for every measurement, showing both loading and unloading. After applying corrections for the contact area, initial penetration depth, and instrument compliance, the *hardness* (H) and reduced *Young's modulus* (E_r) were obtained using the conventional method (Oliver & Pharr 1992). From the initial unloading slope, the contact stiffness, S, is determined as:

$$S = \frac{dP}{dh} \tag{1}$$

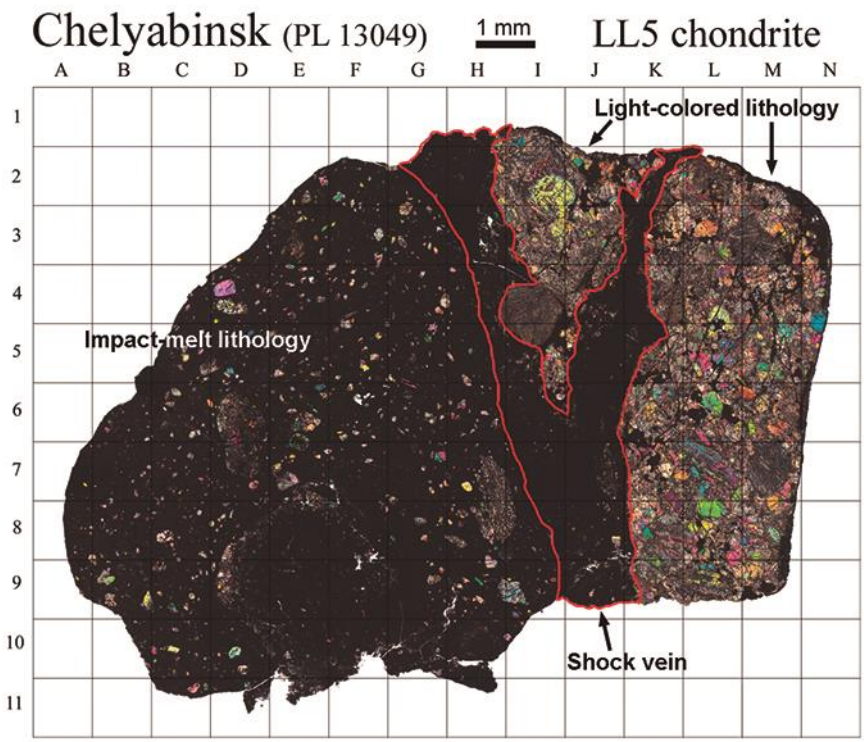

Figure 5.1: High resolution TL with crossed nicols mosaic of the Chelyabinsk PL 13049 thin section. The three different regions studied here are highlighted.

where P and h denote the applied force and the penetration depth during nanoindentation, respectively. The reduced *Young's modulus* is evaluated based on its relationship with the contact area, A, and the contact stiffness:

$$S = \beta' \frac{2}{\sqrt{\pi}} E_r \sqrt{A} \tag{2}$$

Here, β' is a constant that depends on the geometry of the indenter (β'= 1.034 for a Berkovich indenter according to Fischer-Cripps 2004). E_r is defined as follows:

$$\frac{1}{E_r} = \frac{1-\nu^2}{E} + \frac{1-\nu_i^2}{E_i} \tag{3}$$

The reduced *Young's modulus* takes into account the elastic displacements that occur in both the specimen, with *Young's modulus* E and Poisson's ratio ν, and the diamond indenter, with elastic constants E_i and ν_i. Note that for diamond, E_i = 1140 GPa and ν_i = 0.07. *Hardness* can be calculated using the following expression:

$$H = \frac{P_{Max}}{A} \tag{4}$$

where P_{Max} is the maximum force applied during nanoindentation. The *elastic recovery* is evaluated as the ratio between the elastic and the total (plastic + elastic) energies during nanoindentation, W_{el}/W_{tot}, as explained in chapter 2.

Indentations with a maximum applied force of 20 mN (low-load) were performed on the different mineral phases comprised in this OC, in order to obtain the local mechanical properties. The results served to test the consistency with previous studies, and as a reference for mechanical properties assessed using higher applied forces. The average mechanical properties of the material composing the Chelyabinsk meteorite as a whole are also important to model the eventual response of NEAs to impacts. Thus, larger indentations were also performed, applying the maximum available force for the indenter used in this chapter, 500 mN (high-load). Such configuration gets rid of the indentation size effect, which is a progressive increase of *hardness* observed for low indentation forces and ascribed to a variety of factors (see, e.g. Nix & Gao 1998; Gerberich et al. 2002). Thus, the results obtained from indentations performed using 500 mN should be more representative of the real behavior. An array of 16 large indentations was performed on each of the *lithologies* and regions identified on the selected specimen (Figure 5.1): the light-colored and the impact-melt *lithologies*, and a thick black shock-melt vein consisting of a fine-grained *silicate matrix* with abundant metal and *troilite* inside (Bischoff et al. 2013; Ruzicka et al. 2015). In order to calculate their mean mechanical properties, the results of the large indentations performed on the *silicates* of each region (*olivine*, *pyroxene*, and *plagioclase*) were averaged, as these minerals account for ~90% of the material in Chelyabinsk (Galimov et al., 2013). This combination of several indentations can provide a good estimation of the average mechanical properties of each region. All indentations reached depths between 0.2 and 2 μm, but the compressive stresses caused by the indenter are not limited to the size of the indent. Therefore, the depth affected and measured by the nanoindentations can go down to ~5 μm for 20 mN loads, and to 20 μm for the 500 mN loads, not deep enough to be disturbed by the properties of the *glass* supporting the sample (Fischer-Cripps, 2004).

5.3 Results

5.3.1 Low-load indentations

A summary of the calculated mechanical properties of the main minerals obtained after local low-load indentations is presented in Table 5.1, and representative load-displacement curves acquired from each mineral phase are shown in Figure 5.2. According to the results obtained in this chapter, *olivine* shows higher *hardness* and reduced *Young's modulus* than *pyroxene*, while both properties notably decrease for *plagioclase*. It has to be taken into account that the indented *olivine* included inter-granular metal and *troilite* veins, which probably increase the variability in mechanical properties. Lower average values of both mechanical parameters were obtained for *troilite*. For metal grains, composed of *kamacite* and *taenite* in variable proportion, rather low *hardness* and relatively low reduced *Young's modulus* were found. *Taenite* has a lower reduced *Young's modulus* and similar (but slightly lower) *hardness* than *kamacite*. The last mineral phase indented was *chromite*, which shows high values of both H and E_r. Concerning the *elastic recovery*, the highest mean values are achieved in regions where *pyroxene* and *plagioclase* are mixed. *Chromite* also shows a high *elastic recovery*, whereas *troilite* and metal inclusions show much lower values.

Table 5.1: Average mechanical properties of Chelyabinsk minerals. Reduced *Young's modulus* (E_r), *hardness* (H) and *elastic recovery* (W_{el}/W_{tot}) of the same mineral phases shown at Figure 5.2. Each was calculated by averaging the results obtained from several low-load indentations.

Mineral Phase	E_r (GPa)	H (GPa)	W_{el}/W_{tot}
Olivine	136 ± 5	13.6 ± 0.9	0.551 ± 0.023
Pyroxene	122 ± 11	11.9 ± 2.2	0.59 ± 0.03
Pyroxene + Plagioclase	71 ± 5	9.6 ± 1.0	0.720 ± 0.025
Troilite	71 ± 8	5.1 ± 0.8	0.45 ± 0.05
Taenite	82 ± 6	3.05 ± 0.29	0.232 ± 0.007
Kamacite	127 ± 16	3.58 ± 0.24	0.20 ± 0.06
Chromite	131 ± 3	15.9 ± 1.3	0.666 ± 0.016

Table 5.2: Average mechanical properties of Chelyabinsk regions. Reduced *Young's modulus* (E_r), *hardness* (H) and *elastic recovery* (W_{el}/W_{tot}) were calculated averaging the results obtained from several high-load indentations.

Region	E_r (GPa)	H (GPa)	W_{el}/W_{tot}
Light-colored *lithology*	69 ± 8	9.7 ± 2.1	0.65 ± 0.07
Impact-melt *lithology*	71 ± 8	12.2 ± 2.2	0.69 ± 0.05
Shock-melt vein	77 ± 8	11.8 ± 2.3	0.679 ± 0.027

5.3.2 High-load indentations

The results after performing high-load indentations (maximum load of 500 mN) to obtain combined mechanical properties are summarized in Table 5.2, while representative indentation curves for each *lithology* or region are shown in Figure 5.3. The impact-melt *lithology* shows the highest *hardness*, while the highest values of reduced *Young's modulus* correspond to the black shock-melt vein. The three regions show very similar values of *elastic recovery*.

Remarkably, small cracks are sometimes formed at the edges of the indentations performed at high-load. These cracks are the result of localized fracture, and are almost only observed in the shock-melt vein, as can be seen in Figure 5.4. Whenever cracks are formed after indentations, the formation and length of these cracks can be correlated with *fracture toughness* of the indented regions. For a Berkovich indentation impression, the *fracture toughness*, K, can be given as (Fischer-Cripps, 2004):

$$K = k\left(\frac{E}{H}\right)^{n}\frac{P}{c^{3/2}} \tag{5}$$

where k is an empirical constant close to 0.016, P is the applied indentation force, $n = ½$ and c is the length from the center of the indentation to the end of the crack. Longer cracks thus result in lower *fracture toughness* values.

The length of the most significant cracks found in this chapter is between 7 and 13 μm, from the center of the indentation to the end of the crack. Thus, with an average *c* of ~10 μm, a *fracture toughness* of 0.62 ± 0.12 MPa·m$^{1/2}$ is obtained.

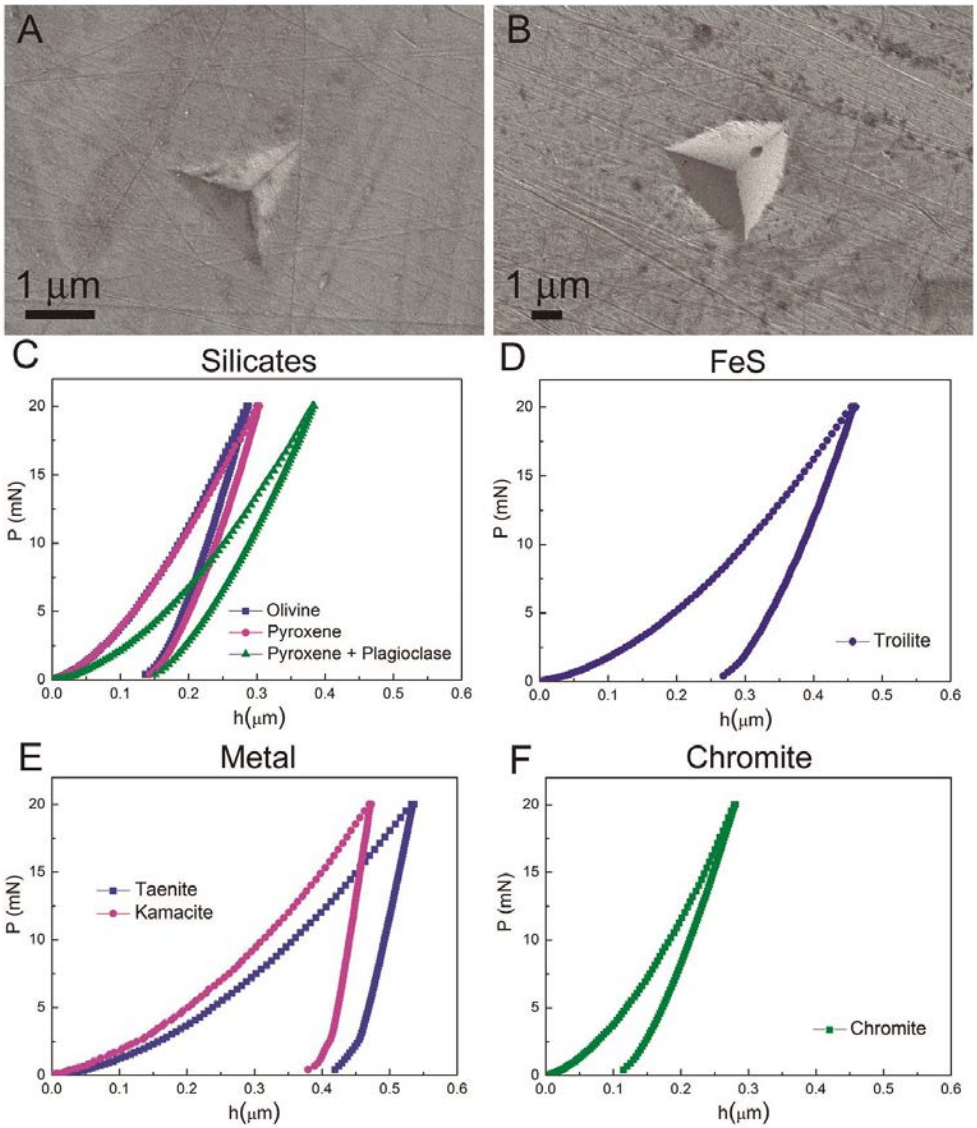

Figure 5.2: Low-load indentations performed on the Chelyabinsk PL 13049 sample. At the top, BSE SEM images show indentations on: *olivine* (A), and metal (B, *taenite* or *kamacite*). Indentation curves for different mineral phases are shown below. *Silicates* (C): *Olivine* (Fo$_{75}$, plus tiny *troilite* veins), *Pyroxene* (En$_{80}$), and *pyroxene + plagioclase* (*pyroxene* plus a small amount of Ab$_{90}$ *plagioclase*). *Troilite* (D): contains ~54% of atomic S. Metal grains (E): *taenite* (~35% of atomic Ni) and *kamacite* (~5% of atomic Ni, plus a small amount of *troilite*). The *chromite* curve is shown in (F). The selected curves are considered representative of the mean mechanical properties of each mineral phase (shown in Table 5.1).

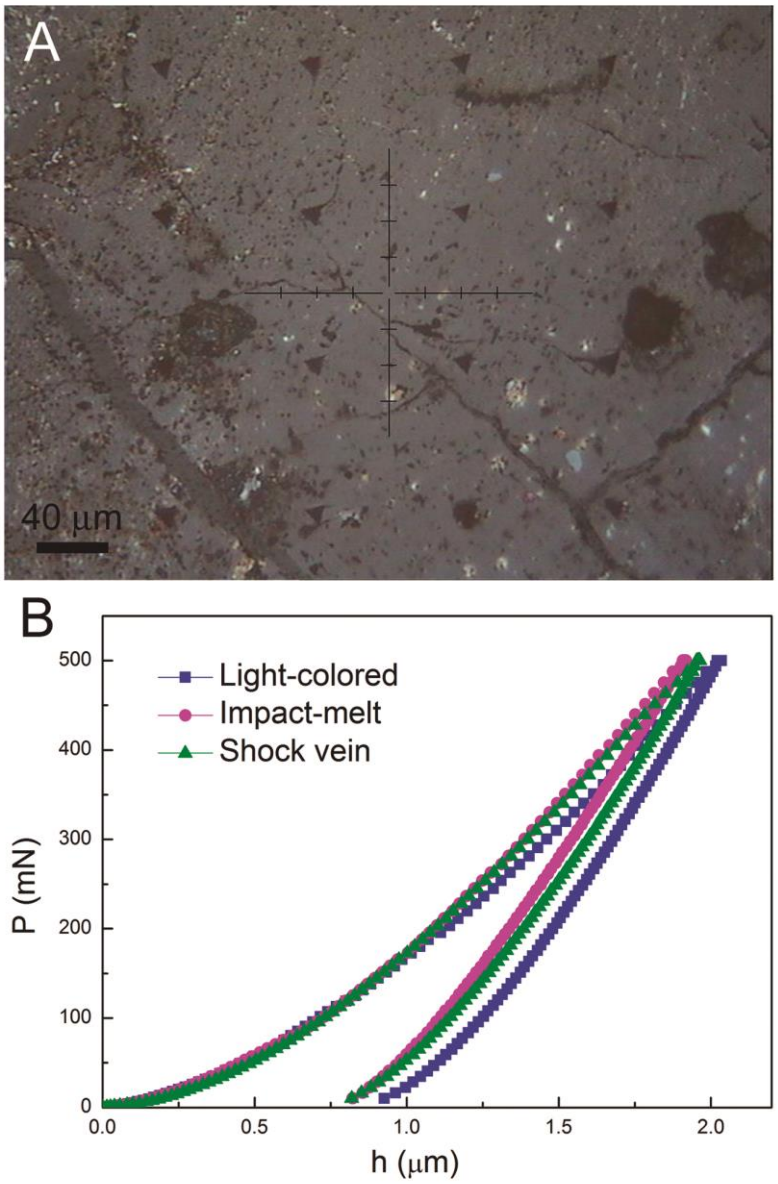

Figure 5.3: High-load indentations on the Chelyabinsk *lithologies*. At the top, an optical image (A) shows an array of 16 high-load indentations on the shock-melt vein. Below (B), three indentation curves representative of the mean mechanical properties obtained from the three regions analyzed with the high-load indentations (see data in Table 5.2).

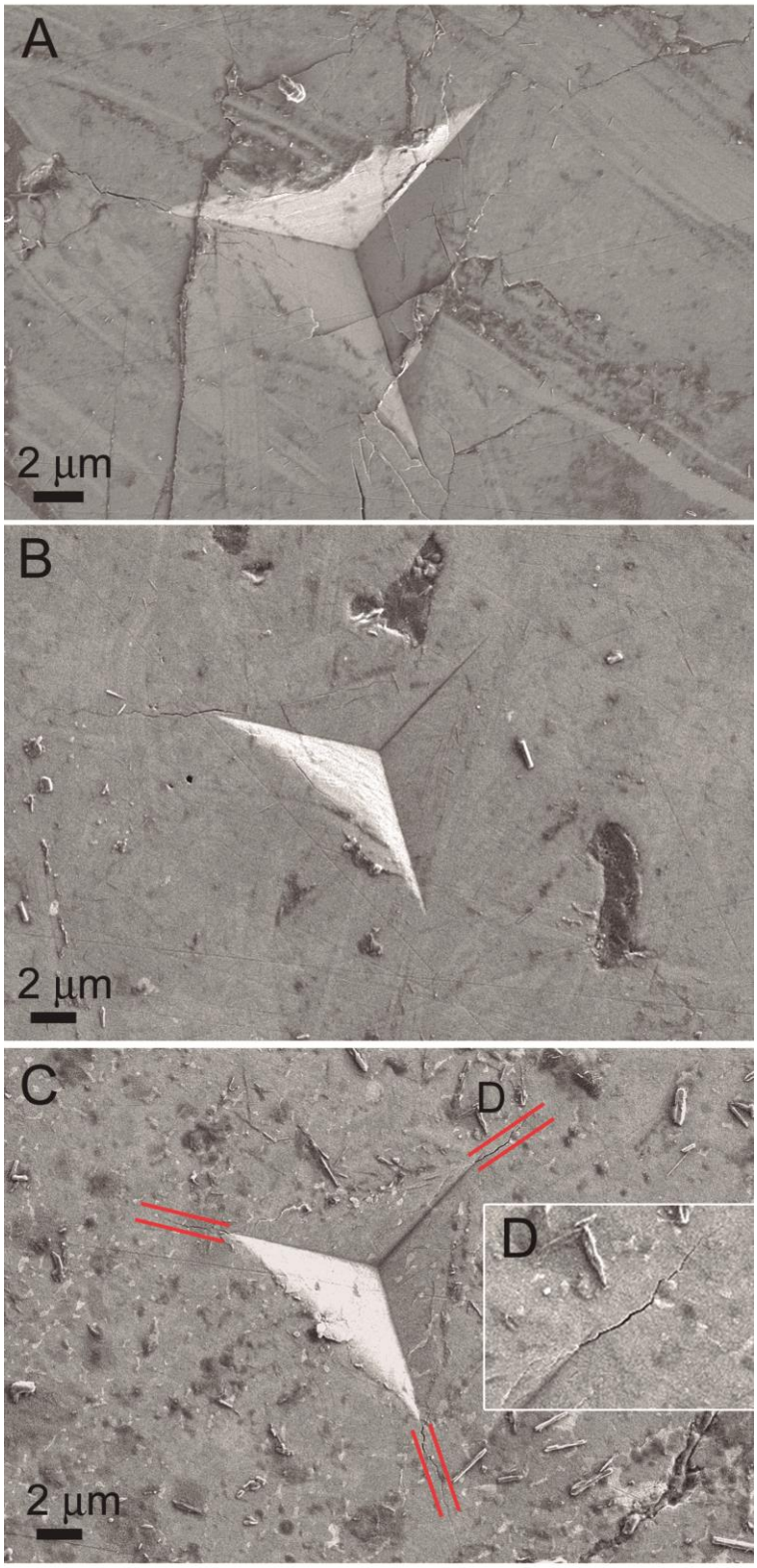

Figure 5.4: Fractures after high-load (up to 500 mN) indentations on the three regions analyzed on this Chelyabinsk specimen. Three BSE images show high-load indentations on: (A) the light-colored *lithology*; (B) the impact-melt *lithology*; (C) the shock-melt vein. Fractures can only be clearly identified in the shock-melt vein (surrounded by parallel red lines in (C), and shown in more detail in (D).

5.3.3 Comparison with previous studies

The reduced *Young's modulus* can be easily related with the *Young's modulus* (*E*) if one knows the Poisson's ratio (*v*) of the indented material, as shown in Equation 1. Considering the Poisson's ratio defined for OCs in previous studies (see e.g. Yomogida & Matsui 1983), the reduced *Young's modulus* values obtained here for the Chelyabinsk meteorite are consistent with the *Young's modulus* measured previously for ordinary chondrites, between 10 and 140 GPa (see e.g. Yomogida & Matsui 1983; Flynn 2005). As expected, the results of this chapter indicate that Chelyabinsk has a much higher average reduced *Young's modulus* than the reported for CCs, typically around 20 GPa (Britt et al. 2016). Concerning *hardness*, there is a dearth of previous studies where nanoindentation is applied to meteorites, hence preventing a proper comparison with the literature. However, the measurements of *hardness* performed here in *kamacite* and *taenite* seem to be as expected (Brusnitsyna et al., 2016), thus making the results of this chapter reliable. Similar to reduced *Young's modulus*, the nanoindentation *hardness* of CCs must be orders of magnitude lower than that of Chelyabinsk, mainly due to the high porosity of CCs, which can exceed 30% (Consolmagno et al., 2008; Pellicer et al., 2012). OCs typically show porosities around 5%-10% (Consolmagno et al., 2008), and indeed the values reported for Chelyabinsk range between 2% and 11%, with an average value of ~6%. However, the porosity is almost identical all around Chelyabinsk (Kohout et al., 2014), and, therefore, changes in porosity cannot be considered the cause for the measured differences in mechanical properties between the different investigated regions.

5.4 Discussion

5.4.1 Mechanical properties of the Chelyabinsk sample

As an LL5-6 OC breccia, Chelyabinsk can be considered representative of the properties exhibited by the surface of a heterogeneous asteroid with distinguishable *lithologies*, at least at mm size scale. The two *lithologies* and the shock-melt vein studied in this chapter are rather similar in chemical composition, mineralogy, and porosity (Galimov et al. 2013; Kohout et al. 2014). Therefore, the differences in mechanical properties between them have to be ascribed to other factors. Also, it does not seem that the *hardness* values obtained are strongly affected by the value of the applied indentation load (Nix & Gao, 1998), since the values of *H* at 20 mN and 500

mN are not significantly different. This could mean that these loads are already high enough to avoid the apparent hardening phenomena related to the indentation size effects. However, the results reveal that when jumping from the in-situ properties of mineral phases (Table 5.1, Figure 5.2) to the overall behavior of *lithologies* or shock-melt veins (Table 5.2, Figure 5.3), there is an evident decrease in reduced *Young's modulus*. Porosity can explain this decrease with applied indentation load (Asmani et al., 2001). As the load is increased, the influence of porosity is exacerbated since the probability to encounter voids in the sample increases. For the same reason, *hardness* obtained with larger load indentations would probably be smaller than what is shown here (Palchik & Hatzor, 2004). The presence of various minor phases and their interaction with the *matrix*, mainly the melt veins filled with both *troilite* and metal, possibly alter the resulting mechanical properties of the *lithologies*, too. In this sense, indentations performed using 500 mN are more representative of the real behavior than those carried out using 20 mN, and are, therefore, better to calculate average bulk properties of the *lithologies*, as expected. In turn, repetitive shock in the impact-melt *lithology* and the shock-melt vein can induce a refinement of the mean particle size while also increasing the amount of structural defects (e.g., dislocations), hence leading to mechanical hardening with respect to the light-colored *lithology*, due to the Hall-Petch strengthening relationship (Gil Sevillano et al., 1980). Finally, it should be noted that the extrapolation of material properties to length scales much larger than the micrometer-sized regions sampled by the 500 mN indentations should be made with caution. It is well known that the strength of bulk materials consisting of multiple phases with dissimilar properties can be very nonlinear (see, e.g., Tullis et al. 1991, Durham et al. 2009). The strain rate flow law for an aggregate does not necessarily follow a simple power law, as for monomineralic aggregates. However, here, the mechanically hard phases (*olivine*, *pyroxene*) constitute the majority phases in the meteorite and, therefore, the polyphase aggregate can be considered, in a first approximation, as a load-bearing strong framework with a relatively small volume proportion of weaker phases (*troilite*, *taenite*, *kamacite*). In such a case (i.e., with no obvious connection between the weak inclusions), deformation of the aggregate involves strain of the stronger *matrix*, while not much concentration of strain can occur in the inclusions. This is possibly why the *hardness* of the different *lithologies* (with values ranging between 9.7 GPa and 12.2 GPa, Table 5.2) is close to that of the mechanically hard phases (Table 5.1), since a load-bearing framework of the stronger

material is formed. Otherwise the behavior of the aggregate bulk material would be similar to that of the weak phase alone, as reported by Tullis et al. (1991).

5.4.2 Momentum multiplication factor

In order to take into account these results in impact scenarios, the key parameter to be considered is the β parameter, known as the momentum multiplication factor. It is defined as the momentum change divided by the momentum input:

$$\beta = \frac{\Delta p_t}{M_p v_p} = \frac{M_p v_p + M_e v_e}{M_p v_p} = 1 + \frac{M_e v_e}{M_p v_p} \tag{6}$$

Here Δp_t is the momentum change of the target due to the impact. M_p and v_p are the total mass and average velocity of the projectile, whereas M_e and v_e are the total mass and average velocity (on anti-impact direction) of the ejected material. If $\beta > 1$ there are fragments ejected after the impact, and the efficiency of an impact would be larger, since the attained Δv would be also more significant. This effect is called "momentum multiplication" and has been studied by several authors (Hoerth et al., 2015).

Several models have tried to account for the effects of collision and impact on the momentum multiplication in brittle, porous materials (Benz & Jutzi 2006; Hoerth et al. 2015), and in all these models material parameters play a key role. Momentum multiplication can be assessed considering its dependence on porosity and strength of the target (Hoerth et al., 2015), besides from the influence of impact velocities and densities (or masses) of the colliding objects, their size, and other properties (see e.g. Schultz 1993; Holsapple & Housen 2012; Jutzi & Michel 2014; among many others). In solids with low porosity, like the Chelyabinsk meteorite, momentum multiplication is more pronounced, since material ejection is then more directional and no impact energy is dissipated in the form of pore compaction (Hoerth et al., 2015). Then, the role of strength can be considered using the strength-dominated cratering model, which provides the following scaling relation (Holsapple & Housen, 2012):

$$\beta - 1 \approx \left(v_p \sqrt{\frac{\rho_t}{Y}} \right)^{3\mu - 1} \left(\frac{\rho_t}{\rho_p} \right)^{1 - 3\nu} \tag{7}$$

Where v_p is the projectile velocity, ρ_t and ρ_p are the densities of the target and the projectile, Y is some measure of the strength of the target, μ is a scaling parameter close to 0.55 for non-porous materials and between 1/3 and 0.4 for highly porous materials,

and ν is a constant close to 0.4 for most target materials (Holsapple & Housen, 2007). Different definitions of strength (compressive strength, yield strength, ultimate strength, etc.) can be used to substitute *Y*, but they all can be related on predictable ways (Holsapple, 2009). The compressive yield stress (σ_C) was selected for this chapter because it can be related to *hardness* following the typical expression in constrained materials (free from porosity):

$$H = C\sigma_C \tag{8}$$

Also, this relationship between *hardness* and compressive yield stress holds for the case of dynamic tests (Subhash et al., 1999). *C* is the constraint factor and attains typical values close to 1.6 for rocks and 3 for metals (Buddhue, 1945). The values of σ_C that can be inferred from those typical *C* and the measurements of *H* performed here, would be much higher than the compressive strengths found in some previous studies, which are of the order of 10 to a few hundred MPa (Kimberley & Ramesh, 2011). Although σ_C and compressive strength are not the same, they should be fairly similar. The apparent discrepancy with previous works comes from the specific correlation between *H* and σ_C, which varies for different materials, scales, and techniques. Due to the size of nanoindentations, porosity, interactions between different phases, and cracks, are not perceived on these measurements. Also, *C* can attain values as high as 180 for ceramics and other brittle materials (Zhang et al., 2011). Altogether, those factors can imply a much higher *H*, and therefore σ_C, than expected for the same materials at larger scales (Palchik & Hatzor, 2004; Pellicer et al., 2012). Considering those points, a value of σ_C representative of a real asteroid cannot be calculated from the measurements of *H* presented here, and therefore β could not be calculated. However, and since *H* and σ_C can be related through a specific constrain factor *C*, for two similar materials A and B (and assuming the same *C*, density, and μ), their ratio of β-1 can be calculated as follows:

$$\frac{(\beta-1)_A}{(\beta-1)_B} \approx \left(\frac{Y_B}{Y_A}\right)^{\frac{3\mu-1}{2}} = \left(\frac{\sigma_{CB}}{\sigma_{CA}}\right)^{\frac{3\mu-1}{2}} = \left(\frac{H_B}{H_A}\right)^{\frac{3\mu-1}{2}} \tag{9}$$

That ratio provides an idea of which of those materials would grant a higher momentum multiplication and a more efficient impact.

5.4.3 Extrapolation to asteroids

According to this model, a lower porosity increases the momentum multiplication, and hence an impact on an asteroid like Chelyabinsk would be more effective in deflecting its trajectory than on NEAs with higher porosity. Also, for a given porosity, meteorites with lower *hardness* (and, therefore, lower strength) will lead to larger values of β and higher efficiency of the impact, since the formation of the impact crater is promoted (see Equation 7).

With respect to the different *lithologies* in Chelyabinsk, and assuming a scaling parameter (μ) between 0.4 and 0.55, β -1 of the light-colored *lithology* would be between 5% and 20% higher than for the impact-melt *lithology* (see Equation 9). For Chelyabinsk-like asteroids this implies that an impact in objects enriched in light-colored *lithology* would be more efficient than in others where the impact-melt *lithology* predominates. The light-colored *lithology* can be easily distinguished spectroscopically from the dark-colored and the impact-melt *lithologies*, due to the remarkable darkening of the latter two (Popova et al. 2013; Reddy et al. 2014). This would allow an asteroid impact mission to select the most suitable region to be targeted in order to obtain a more efficient deflection.

The results presented here also show that although the reduced *Young's modulus* of the two *lithologies* and the shock-melt vein are rather similar, the prominent formation of cracks after indentations on the latter is indicative of the ease to create fractures within these veins. It is likely that the amount of mass ejected after an impact depends on *fracture toughness*, with low *fracture toughness* values promoting larger ejecta mass, and, therefore, higher momentum multiplication (Walker & Chocron, 2015). Not many studies calculate the *fracture toughness* of meteorites, but the result of 0.62 ± 0.12 $MPa \cdot m^{1/2}$ shown before is clearly lower than the 2 $MPa \cdot m^{1/2}$ estimated by some other authors (Walker & Chocron, 2015). This is indicative of the ease with which these shock-melt veins can be broken, which would promote the fracturation and consequent ejection of surface materials, and therefore increase the momentum multiplication.

In order to use these results in the frame of an impact deflection mission such as the AIDA, it is necessary to understand the connection between quasistatic indentations and dynamic indentations or impacts. Although it has been observed that for most brittle materials dynamic *hardness* values are larger than quasistatic values, typically by 10-25% (Anton & Subhash, 2000; Wheeler, 2009), the relationship between *hardness* and

compressive yield stress holds for the case of dynamic tests, as explained before. The difference in scale between a centimeter-sized sample and an asteroid can also have an important effect on the effective mechanical properties. Although several studies have already considered how *hardness*, strength, and momentum multiplication are affected by variations in size (Schultz, 1993; Holsapple & Housen, 2012; Jutzi & Michel, 2014), a deeper understanding provided by real-scale experiments is required for a proper extrapolation of properties from meteorites to asteroids.

5.5 Conclusions

The mechanical properties of one thin sample of the Chelyabinsk meteorite were studied in this chapter using the nanoindentation technique. Since this meteorite is an LL5-6 OC breccia, it is a good proxy for the surface materials of heterogeneous NEAs with distinguishable *lithologies* and some of the most abundant chondritic materials impacting the Earth. Its study provides constraints to improve our understanding of the mechanical response of such bodies. The main conclusions of this chapter are as follows:

1. The measurements and results presented in this chapter represent a first step in the use of nanoindentation to acquire additional insight into the mechanical properties of chondritic bodies. Although dynamic impact tests would be more representative of impacts on asteroids, they require much larger samples than nanoindentation, which are not available for most types of meteorites, especially considering that impact test require at least a partial destruction of the sample. As an almost non-destructive technique, nanoindentation is a remarkable option to acquire the necessary data to support AIDA and other future asteroid deflection missions in order to palliate unexpected impact hazard on human beings.

2. The value of the applied indentation load (20 mN or 500 mN) does not significantly affect *hardness*, but reduced *Young's modulus* decreases notably when moving from the in-situ properties of mineral phases to the overall behavior of *lithologies* or shock-melt veins. Porosity can explain this decrease, since with larger loads the probability to encounter voids in the sample increases.

3. The differences in mechanical properties between the two *lithologies* and the shock-melt vein studied in this chapter cannot be attributed to variations in chemical composition, but the presence of minor phases and melt veins can possibly affect them. Also, lower mean particle size produced by repetitive shock implies increasing the structural defects and, therefore, the mechanical hardening, which increases the *hardness* of the impact-melt *lithology* and the shock-melt.

4. Indentations produce cracks in the shock-melt vein, providing as a result a low *fracture toughness* value, which is indicative of the ease to create fractures within these veins. Low *fracture toughness* can promote the ejection of surface materials after an impact, therefore increasing momentum multiplication. The shock-melt veins are, therefore, one important structural weakness of Chelyabinsk-like asteroids.

5. Since for a given porosity lower *hardness* implies larger momentum multiplication, asteroids dominated by light-colored *lithology* would be easier to deflect than asteroids mainly composed of the impact-melt *lithology*. As they can be easily distinguished spectroscopically, an asteroid impact mission would be able to select the region where an impact would be more efficient.

6 SHOCK DARKENING IN CHELYABINSK AS A PROXY OF POTENTIALLY HAZARDOUS ASTEROIDS

Abstract

In the previous chapter, one thin sample of the Chelyabinsk meteorite was studied as a proxy for the materials composing most NEAs, and particularly the PHAs. The analysis of chondrite samples provides extensive data about the composition, mineralogy and mechanical properties of the studied meteorite, which become clues about its parent asteroid. However, in order to apply this data to better understand the properties of a specific asteroid, it is required to know to what extent the selected meteorite is representative of the asteroid being studied. In chapter 4 the process to determine the similitudes and possible connection between a CC and an asteroid was studied into detail. As explained, spectroscopic techniques are particularly useful to have some insight about the composition of an asteroid's surface. Most of the relatively small bodies that reach Earth's surface are the product of significant collisional processing taking place in the surface of asteroids since they formed, which implies disruption, excavation, and the production of fragments that are delivered from the MB to the NEA region, thanks to planetary resonances and non-gravitational forces. This impact processing has affected asteroid albedos and the reflectance that can be perceived with

spectroscopic techniques. In this chapter, the effects of shock and brecciation in samples of the Chelyabinsk OC are studied, together with its reflective properties, while taking into consideration the results from chapter 5. The results of this chapter have been published in the book *Assessment and Mitigation of Asteroid Impact Hazards: Proceedings of the 2015 Barcelona Asteroid Day* (Moyano-Cambero et al., 2017c)

6.1 Introduction

Every asteroid has suffered a peculiar evolution and their bulk physical properties result from all kinds of processing (Britt et al., 2002). NEAs are usually asteroids that travelled from the MB to the near-Earth region, mainly delivered via main-motion resonances and non-gravitational effects (Morbidelli & Nesvorný, 1999). Asteroids crossing these resonances are typically small (less than one km in diameter), and are fragments produced in catastrophic impacts. Indeed, most of them have intense collisional histories due to the events occurring during their dynamic transport.

As mentioned in chapter 5, the PHAs are bodies larger than 150 m in diameter and whose Minimum Orbit Intersection Distance (MOID) with the Earth is 0.05 AU or less (Trigo-Rodríguez & Williams, 2017). These encounters are not always close enough to hit the Earth and become catastrophic (Milani et al., 2002), but tidal effects can affect the weak structure of rubble piles. These close approaches with terrestrial planets have been envisioned as a pathway to release meter-sized rocks from asteroidal surfaces that could produce meteorite-dropping bolides (Trigo-Rodríguez et al., 2007). Some surviving boulders detached from the surface of these asteroids can evidence a complex history of continuous impacts and brecciation that is well exemplified in the heterogeneity of Almahata Sitta meteorites associated with the fall of the asteroid 2008 TC_3 (Bischoff et al., 2010; Zolensky et al., 2010; Goodrich et al., 2014; Horstmann & Bischoff, 2014). The determination of the heliocentric orbit of meteorite-dropping bolides is an excellent way to identify the source of these rocks, usually coming from the MB, but with the a probable origin in the near-Earth population (Dmitriev et al., 2015; Trigo-Rodríguez et al., 2015).

OCs usually exhibit unequivocal features of shock metamorphism (Bischoff & Stöffler, 1992; Bischoff et al., 2006; Bischoff et al., 2013a; Bischoff et al., 2013b), defined as the mechanical deformation and transformation of rocks by shock wave compression without substantial movement of the rock constituents (e.g., Stöffler et al.

1991; Bischoff and Stöffler 1992). On the other hand, a significant number of chondritic meteorites have been found to be breccias (Bischoff et al., 2006). Actually, energetic impacts producing shock effects usually involve mass transport and substantial implantation of foreign *lithologies* in the surviving rock fragments that leads to progressive brecciation and ejection of materials present at the surfaces of asteroids (Bischoff et al., 2006). Also, collisions might compact loose surface materials to produce the frequent regolith breccias (e.g., Bischoff et al., 1983). Therefore, the mineralogical study of these meteorites provides clues on the processes experienced by their parent bodies (e.g., Bischoff et al., 1993; Bischoff et al., 2006).

Even NEAs being a few tens of meters in diameter are expected to have experienced a significant degree of shock and brecciation (Binzel et al., 2001). These processes make them to be weak, fractured bodies easily disrupted by the entrance through Earth's atmosphere (Bland & Artemieva, 2003), and therefore meteorites reaching the Earth's surface are biased towards high-strength materials (Trigo-Rodríguez & Blum, 2009). Despite of that, their entrance through Earth's atmosphere is still capable of sending a high-energy shock wave and a large amount of meteorites to the ground, being a significant source of hazard to humans (Brown et al. 2013; Moreno-Ibáñez et al. 2015). The most recent example was the Chelyabinsk superbolide, which penetrated the atmosphere at a velocity of ~19 km/s (Borovička et al., 2013) and exploded several times, releasing an energy of ~500 kT of TNT (Brown et al., 2013).

In this chapter the shock-modified minerals of some samples of the Chelyabinsk meteorite are studied with the micro-Raman technique. Also, the reflectance spectra in the ultraviolet to near-infrared wavelengths of different *lithologies* of this meteorite are compared to spectra from other OCs and asteroids, in order to understand how the different *lithologies*, processes and degree of shock metamorphism modify the spectra.

6.2 Sample selection and experimental techniques

The Chelyabinsk meteorite shows a relatively high S4 degree of shock (Ruzicka et al., 2015), according to the weak *mosaicism* on *olivine* and the presence of *crystalline plagioclase* instead of *maskelynite* (Stöffler et al. 1991). Chelyabinsk is a well-*lithified polymict genomict* breccia only containing *lithologies* related to LL OCs (Bischoff et al., 2006; Bischoff et al., 2013b), in contrast to other breccias such as Almahata Sitta, which contain foreign fragments of both chondritic and ureilitic origins (e.g., Bischoff et al. 2010, Goodrich et al. 2014, Horstmann and Bischoff 2014), and Kaidun (Zolensky

& Ivanov, 2003). This represents an advantage in order to study the effects of shock on the materials composing LL OCs, since this meteorite contains similar materials affected by shock to different extents. This way, the light-colored *lithology* exhibits an intermediate shock state, with abundant shock veins, although light-colored fragments with minor or no shock veins are also common (Righter et al., 2015). The highly *recrystallized* LL6 dark clasts also contain abundant shock veins. The dark-colored *lithology* is described as shock-darkened fragments, and contains a large amount of inter- and intra-granular thin melt veins of opaque material (metal and *troilite*) probably due to shock mobilization (Bischoff et al. 2013; Galimov et al. 2013; Kohout et al. 2014; Reddy et al. 2014; Righter et al. 2015). Indeed, in some of these shock-darkened areas all *silicates* are completely embedded by a FeS-metal network dominated by *sulfides*. The impact-melt *lithology*, on the other hand, does not contain high-pressure phases, and shock veins in this *lithology* are less abundant than in the others, or missing (Bischoff et al., 2013b; Righter et al., 2015). Small *anhedral plagioclase* (~Ab_{86}) grains also show the consequences of shock, and indeed in the dark-colored *lithology* the isotropy of *plagioclase* is complete (Galimov et al. 2013; Ruzicka et al. 2015). Both *olivine* and *pyroxene* in the different *lithologies* are strongly affected by shock (Galimov et al., 2013; Ruzicka et al., 2015).

Table 6.1: Ordinary chondrites from which the UV-NIR spectra were obtained. Although Kilabo is a pure LL6 OC, differing from Chelyabinsk with most of it being LL5, it can be seen in Figure 6.4 that their spectra are comparable.

Meteorite	Type	Place	Recovery	Total Known Weight
Chelyabinsk	LL5-6	Chelyabinsk (Russia)	2013	~1000 kg
Travis County (b)	H4	Travis County (USA)	1937	5.9 kg
Bassikounou	H5	Hodhech Chargui (Mauritania)	2006	29.56 kg
Tieschitz	H/L3.6	Olomoucký (Czech Republic)	1878	28 kg
Gold Basin	L4	Arizona (USA)	1995	61 kg
Kilabo	LL6	Jigawa (Nigeria)	2002	19 kg

For this chapter, two polished thin sections of the Chelyabinsk meteorite (PL13049 and PL13050) and a thicker section, kindly provided by Addi Bischoff, were studied by

optical microscopy with the Zeiss Scope Axio petrographic microscope described in chapter 2. RL and TL images of both thin sections were obtained at 50× magnification to create the high-resolution mosaics, like described in chapter 5 (see Figure 5.1, as an example). The mosaics allowed establishing target features to be characterized by petrographic microscopy, SEM and micro-Raman techniques. The FEI Quanta 650 FEG working in low-vacuum BSED mode at the ICN2 was used to observe the shock features and the differences between *lithologies* into detail. Micro-Raman spectra were acquired with the Jobin-Yvon T-64000 Raman spectrometer (ICMAB-CSIC), operated as described in chapter 2. In this case, the laser power onto the sample was kept below 0.5 mW to avoid degradation due to overheating. Finally, several ultraviolet to near-infrared spectra (~0.2 to 2.0 μm) were obtained from the different *lithologies* of the Chelyabinsk meteorite and the other meteorites shown in Table 6.1, with the Shimadzu UV3600 UV-Vis-NIR spectrometer (UPC) described in chapter 2.

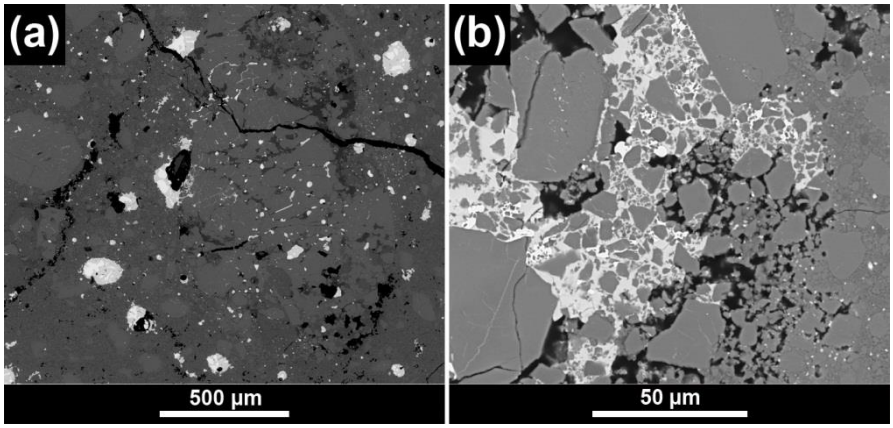

Figure 6.1: Two SEM BSE images from the studied sections of the Chelyabinsk meteorite, showing: (a) texture of the interior of an impact melt breccia: *Mafic silicate* fragments (medium grey) are enclosed in *plagioclase*-normative interstitial material (dark grey). The light roundish objects consist of metal (white) and *troilite* (light grey), which are often intergrown. (b) in some shock-darkened areas *silicates* (grey) are completely embedded in (mainly) *sulfides* (pale grey) and metal (white).

6.3 Results

6.3.1 Micro-Raman study

The thin sections studied here contain representative shock-darkening veins through their OC *lithologies* (see e.g. Figure 5.1). After SEM observation of the different areas

around the thin sections (Figure 6.1) it was seen that, besides from the tiny melt *troilite* + metal veins that can be found all around the meteorite, the impact-melt *lithology* was a very good candidate for the study of shock melted minerals. Raman spectroscopy was applied on this *lithology*, on the thin sample PL 13049, in order to identify shock minerals. The spots analyzed are shown on Figure 6.2, while the Raman spectra can be seen in Figure 6.3. Also, the different minerals recognized by this technique are listed on Table 6.2. Spot C was recognized as *jadeite*, previously reported in Chelyabinsk meteorite (Ozawa et al., 2014), with main frequencies at 379, 700 and 1039 cm^{-1}. In spot E a mixture of *oldhamite* (or another Ca-rich *sulfide*), with main frequencies at 185, 215, and 285 cm^{-1}, and *troilite*, which has main frequencies at 160, 290, and 335 cm^{-1}, was tentatively identified. High-pressure (High-P) *merrillite* was also identified nearby shock veins with its characteristic intense peaks at 956 and 972 cm^{-1} (Trigo-Rodríguez et al., 2014b). Spot F spectrum shows peaks close to those of an iron oxide such as *hematite*, but an alteration phase formed by terrestrial weathering could not be ruled out. In several *olivine* spectra (like e.g. spot B in Table 6.2 and Figure 6.3) there is a small shift in the *olivine* peaks.

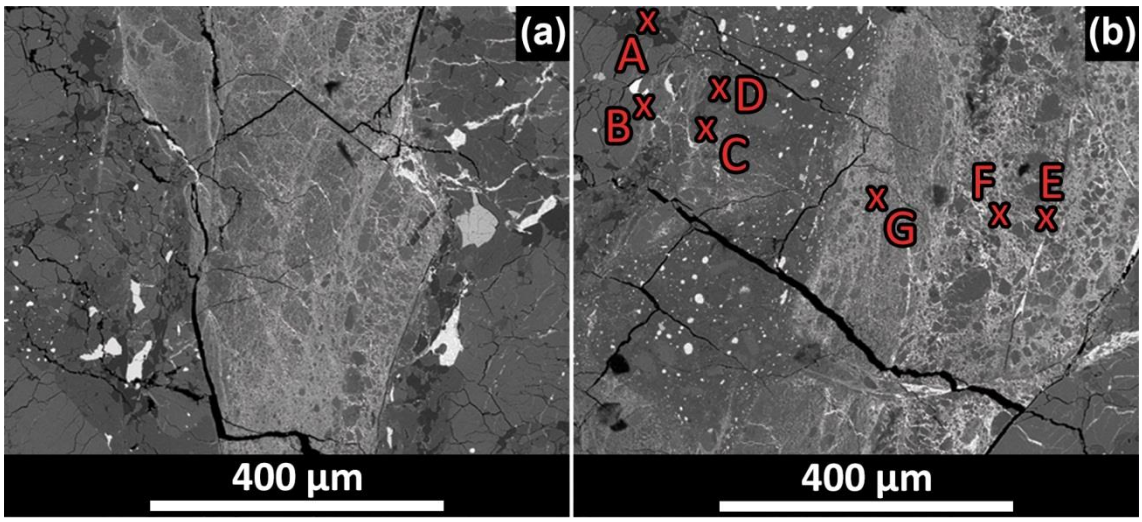

Figure 6.2: SEM BSE images showing two selected areas of the analyzed thin section where the shock veins are evident. In (b) the selected Raman (A-G) points were marked. Their spectra and interpretation are shown at Figure 6.3 and Table 6.2 respectively.

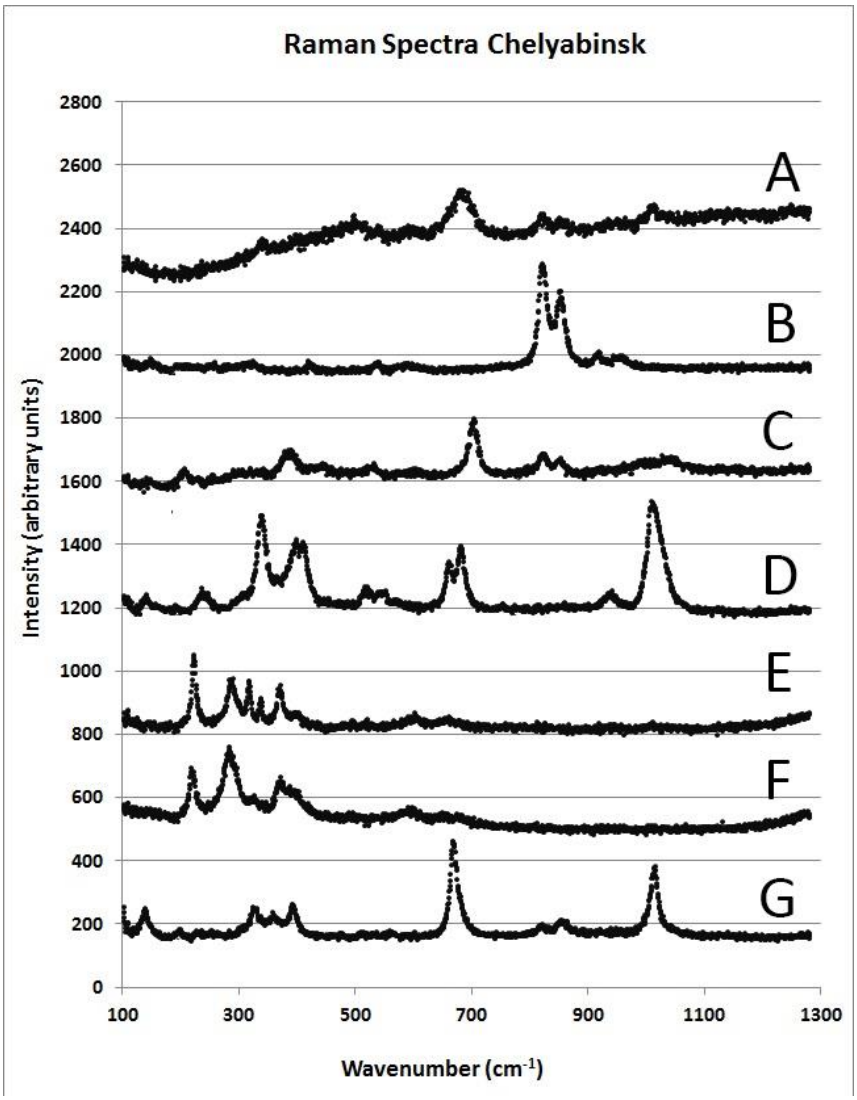

Figure 6.3: Raman spectra obtained from Chelyabinsk sample PL 13049, measured at the points indicated in Figure 6.2 (b). The spectra are shifted to avoid superposition. See also Table 6.2 for the identification of the spectra.

6.3.2 UV-Vis-NIR spectrometry

The Chelyabinsk samples studied in this chapter mainly contain the light-colored and the impact-melt *lithologies*, and therefore the dark-colored *lithology* could not be studied appropriately. The distinction between the two available *lithologies* of this meteorite was found to be consistent with previous studies (Britt & Pieters, 1991; Keil et al., 1992; Britt & Pieters, 1994). Thus, reflectance spectra of both *lithologies* were obtained from different regions of the thick and thin sections, in order to get clues on how shock metamorphism affects the reflectance of this meteorite, and hence the reflectance of related asteroids and possible NEAs.

Table 6.2: Main minerals found listed by alphabetical order, their theoretical frequencies in terrestrial unshocked rocks (except for *merrillite* and *ringwoodite* that are high-P phases), and the frequencies measured here in Chelyabinsk (see the spectra in Figure 6.3).

Mineral	Characteristic Raman Frequencies cm^{-1}	Measured frequencies in Chelyabinsk cm^{-1}	Comments	Raman spectrum
Chromite[a]	493, 685	497, 681	High-P phase Peaks drifted +4 cm^{-1}	A
Diopside[a]	139, 325, 357, 560, 667, 855, 1013	139, 324, 357, 561, 667, 854, 1014	High-P phase[a]	G
Low-Ca *orthopyroxene*[b]	331, 654, 673, 1001	337, 660, 679, 1008	Peaks drifted +6 cm^{-1}	D
Hematite?[c,d]	227, 377, 411, 497, 612	222, 370, 400, 498, 595	Peaks drifted	F
Jadeite[c]	204, 370, 429, 522, 695, 982, 1036	207, 389, 444, 528, 699, 989, 1038	High-P phase ≥ 4 cm^{-1}	C
Merrillite[e,f,g]	956, 972	956, 972	High-P phase	-
Olivine[c]	818, 846	821, 852	Peaks drifted +3-6 cm^{-1}	B
Ca- and Fe-*sulfides*?[c,h]	165, 225, 285, 310, 365	108, 222, 285, 316, 368		E
Ringwoodite[a]	794, 843	794, 843	High-P phase	-

[a]Handbook of Minerals Raman spectra hosted by University of Lyon (http://www.ens-lyon.fr/LST/Raman/)

[b](Chen & Xie, 1992)

[c](Lafuente et al., 2015)

[d](Wachs & Routray, 2012)

[e](Xie et al., 2002)

[f](Llorca & Trigo-Rodríguez, 2004)

[g](Trigo-Rodríguez et al., 2014a)

[a](Avril et al., 2013)

The spectra obtained are shown in Figure 6.4, where they are compared with other OCs. Chelyabinsk is particularly *olivine*-rich and *pyroxene* depleted (Galimov et al., 2013). The spectrum of a theoretical Fo_{70} + En_{75} (in a proportion 2:1) was created with data from the RELAB database, which is close to the average composition of the Chelyabinsk meteorite (Galimov, 2013; Kohout et al., 2014; Righter et al., 2015). In most of the OC and Chelyabinsk spectra the main feature in the working range presented here is the characteristic 1 μm *olivine* absorption band, together with the *forsterite* bands at ~0.5 μm. Afterwards 1.5 μm the pyroxene absorption band bends again the spectra. The similarity between the Chelyabinsk spectra from the light-colored *lithology* and the theoretical *olivine* + *pyroxene* spectrum is clearly seen. In the impact-melt *lithology* the *olivine* and *pyroxene* characteristic bands become much more difficult to distinguish, and the reflectance has been significantly attenuated. With respect to the other OCs compared here (see Table 6.1 for details), the spectra from Chelyabinsk are easily related to the spectra from other LL meteorites, as expected. For H and L chondrites the differences between the two exemplary specimens show a similar behavior to the variation between Chelyabinsk's impact-melt and light-colored *lithologies*. However, between the darker and lighter *lithologies* of the Kilabo LL6 meteorite the change implies only a decrease in reflectance, but not an attenuation of the *olivine* bands. A similar behavior can probably be expected for the dark-colored *lithology* of the Chelyabinsk meteorite.

6.4 Discussion

Laboratory studies concerning meteorite reflectance spectra have been particularly useful to know the general trends that might be characteristic of their progenitor asteroids. In fact, remote spectroscopic observations of NEOs are used to constrain their mineral compositions in order to identify possible meteorite analogs (Gaffey, 1976; Grier et al., 2004; Trigo-Rodríguez et al., 2014a; Moyano-Cambero et al., 2016b). Today we know that the MB is the direct dynamic source for NEAs (Binzel et al., 2001). The asteroids composing this group have a full range of sizes, and very distinctive origins. The S-class is by far the most complex and populated group representing a significant fraction of MB asteroids that share similar reflectance spectra. They are characterized by stony compositions revealed by their 1 and 2 μm bands,

associated with *olivine* and *pyroxene*, and they are moderately bright (Pieters & McFadden, 1994; Bus & Binzel, 2002a; Clark et al., 2010).

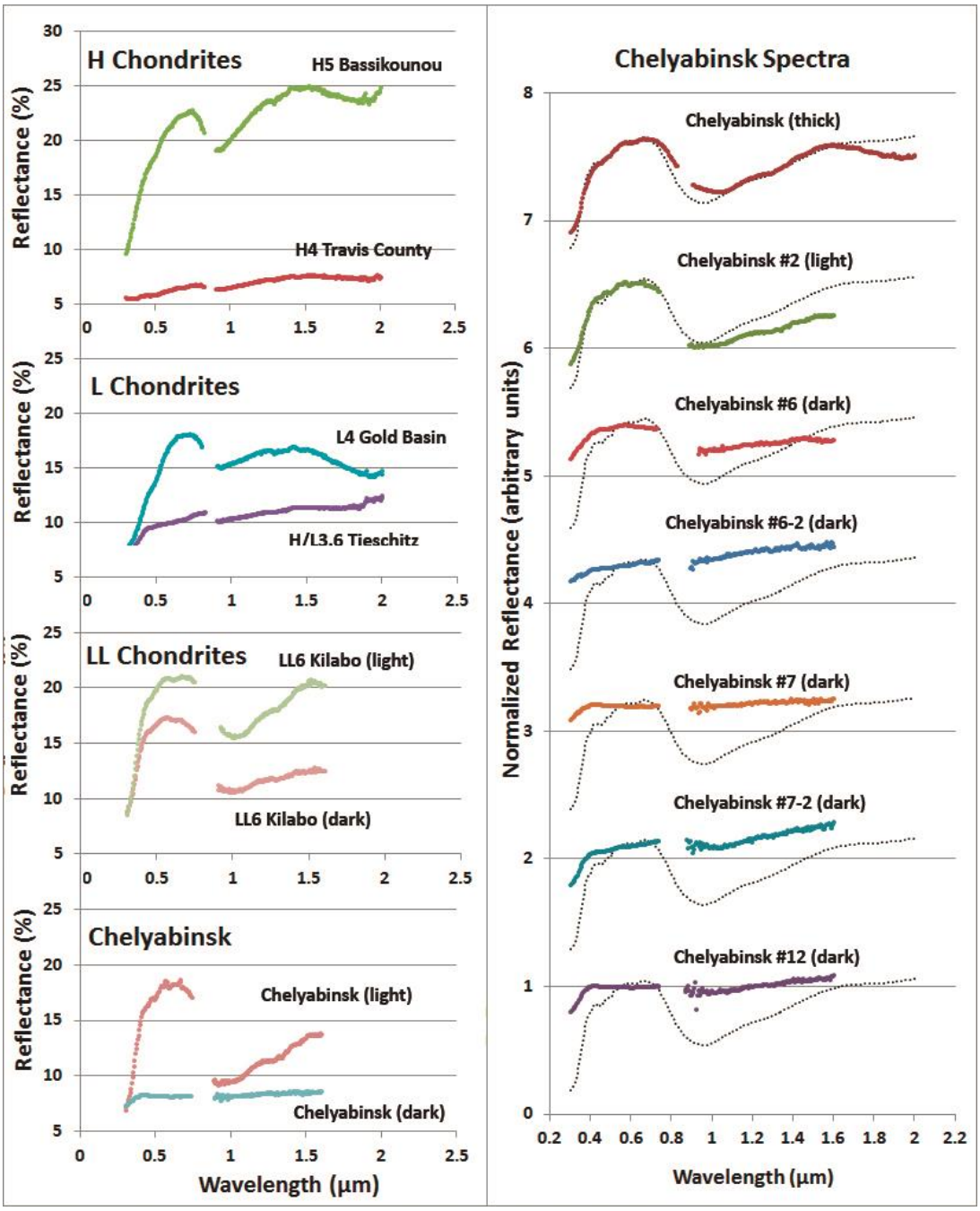

Figure 6.4: Several reflectance spectra of Chelyabinsk and the other meteorites in Table 6.1. At left, spectra of H, L and LL chondrites, showing the relatively common changes in OCs spectra, which imply lower reflectance and often, but not always, attenuation of the 1 and 2 *µ*m bands. At right, we compare the Chelyabinsk spectra (shifted to avoid superposition) to a spectrum obtained from

the 2 to 1 mixture of *olivine* (Fo_{70}) and *pyroxene* (En_{75}) spectra from the RELAB database (dotted line).

Also related with stony meteorites (and with S-class asteroids) are the Q-class, which show subtle variations of depth and width in the 1 and 2 μm bands (Bus & Binzel, 2002a; DeMeo et al., 2009). However, Q-class asteroids have a much lower slope of the whole spectrum, even more pronounced at redder wavelengths. Such spectral distinction is almost absent in the inner of the MB, and in fact the Bus-DeMeo classification (2009) reports less than ten samples, with only a few being well-catalogued in modern surveys.

According to Figure 6.4, the dark-colored and the impact-melt *lithologies* have different effects in the spectral behavior of meteorites, assuming the dark-colored *lithology* in Kilabo is representative of similar *lithologies* in other OCs. While the dark-colored *lithology* implies a reduction of the overall reflectance, the main bands of *olivine* and *pyroxene* are strongly attenuated in the impact-melt. However, they could be described as the same effect, but at different extents, being stronger in the impact-melt than in the dark-colored *lithology*. The distinction between the light-colored and impact-melt *lithologies* in Chelyabinsk, and between the light- and dark-colored *lithologies* in Kilabo, can be tentatively connected to the distinction between S- and Q-type asteroids (overall similar shape but a noticeable decrease in slope and reflectance), as it has been done before between S- and C-type asteroids (Britt & Pieters, 1994; Grier et al., 2004). The similarity between the Kilabo LL6 (light) and the Chelyabinsk LL5 #2 (light) spectra seems to indicate that those variations are not particularly dependent on the petrologic type 5 to 6. One possible explanation is that these differences are a consequence of the progressive darkening associated with impacts, shock metamorphism and brecciation, which affect the reflectance properties (Britt & Pieters, 1994). That would be consistent with the optical darkening observed in the dark-colored *lithology* of Chelyabinsk due to higher degree of shock, and also with its definition as a breccia (Bischoff et al., 2013b). Other secondary processes have been associated with this overall variation. Space weathering can also have a deep influence in the reflectance properties (Pieters et al., 2000), and it has been suggested that the differences between OC meteorites and their S- or Q-type parent asteroids are a consequence of space weathering after surface exposition to the space environment for a long time (Gaffey et al., 1993). However, space weathering implies a stronger change in spectral slope than shock darkening (Kohout et al., 2014). Most NEOs could experience resurfacing due to

the regolith displacement, originated by the differential gravitational pull at each surface point after close approaches to the terrestrial planets (Binzel et al., 2010). Also, small asteroids could have been produced in relatively recent impacts, and due to their low gravitational fields these would not have significant regolith on their surfaces. In fact, Q-type asteroids are relatively small, with its largest member being 1866 Sisyphus, which has a diameter of about 10 km, probably indicating that sample size is crucial to allow an unbiased distinction.

The classification of Chelyabinsk as an LL5-6 *genomict* breccia with an S4 degree of shock makes it an ideal candidate to test whether impact processing and induced metamorphism is behind the spectral variation reported between S- and Q-type asteroids. The impact-melt *lithology*, together with the shock veins filled mainly with melt *troilite* and metal and *silicate* fragments, are common all over our meteorite sample (Bischoff et al., 2013b; Kohout et al., 2014), where they occur as dark to opaque areas in the TL mosaic (Figure 5.1, Figure 6.1, and Figure 6.2). Shocked minerals are also to be expected in this meteorite, but the phases formed depend on the degree of shock and elemental availability (Xie et al., 2001). As mentioned before, *oldhamite* was detected in the samples studied here with Raman spectroscopy. This mineral, previously unknown in OCs (Avril et al., 2013), was considered as one of the components identified on asteroid (2867) Šteins in the interpretation of reflectance spectra taken by ESA's Rosetta spacecraft (Weissman et al., 2008). Therefore, the identification of *oldhamite* in Chelyabinsk indicates that the reflectance spectra of shocked S asteroids might have a minor, but still distinctive, depth in this region (Burbine et al., 2002b), although the abundance due to shock would hardly be high enough to be apparent. The presence of *merrillite* and other high-pressure mineral indicates that Chelyabinsk experienced peak shock pressures higher than ~25 GPa, being consistent with the S4 shock stage already proposed (Stöffler et al., 1991; Bischoff & Stöffler, 1992; Bischoff et al., 2013b; Kohout et al., 2014). The small shift in *olivine* spectra was previously reported for L6 chondrite Yamato 7304, and was attributed to residual stress after an incomplete recovery from the shock deformation, or a local deviation from the static pressure induced by the shock wave during its quick transit through the meteorite (Miyamoto & Ohsumi, 1995). Also, the presence of *ringwoodite* has been reported for Chelyabinsk (Trigo-Rodríguez et al., 2014b). Although it was identified long ago as quite common in shocked L-chondrites (Binns et al., 1969), it has been rarely found in LL chondrites (Bischoff, 2002).

Those results can be considered together with the outcome of the nanoindentation technique from chapter 5. As described there, the *lithologies* studied have different mechanical behavior (see Table 5.2 and Figure 5.3) as a consequence of shock processes, such as refinement of particle size, increase in the amount of structural defects, the formation of shock-melt metal and *troilite* veins, and the transformation of some minerals into high-pressure phases. The results from this chapter show that shock processes have a noticeable effect on the reflectance UV-NIR spectra of meteorites, which with enough data could be properly measured and characterized. If that spectroscopic is variation is considered in the characterization of asteroids, a certain degree of shock together with an approximation of the mechanical properties can be inferred, at least from its surface materials. However, space weathering can affect the spectra in similar ways, and therefore a proper distinction between the effects of shock processes and space weathering is required, first.

6.5 Conclusions

The effects of shock processes in the different *lithologies* of the Chelyabinsk meteorite are shown in this chapter, after studying three different samples with the SEM and micro-Raman techniques. UV-NIR spectroscopy was used to see the differences in reflection between the *lithologies* found on the samples of Chelyabinsk, which have been affected by shock to different extents. Those spectra were also compared to similar effects in other meteorites. The main conclusions of this chapter are as follows:

1. The detection of high-pressure minerals in the Chelyabinsk samples studied here, such as *jadeite* and *ringwoodite*, indicate that the meteorite experienced peak shock pressures higher than ~25 GPa, consistently with the S4 shock stage. *Oldhamite*, which had not been found in ordinary chondrites before, was possibly identified in the asteroid (2867) Šteins, and therefore can be used to infer some degree of shock processing on the surface of asteroids. Other minerals exhibit shifts associated with residual stress due to the high pressure experienced by the body, like can be seen in *olivine*, *chromite*, *merrillite* and *diopside*. The association of the mineral phases described here with specific degrees of shock processing, provides clues about the level of shock suffered by an asteroid where those phases are spectroscopically identified.

2. Chelyabinsk UV-NIR reflectance spectra are dominated by *olivine* and *pyroxene* bands, but due to the presence of shock darkened regions on this meteorite the overall reflectance of large samples will be lower than the one from other OCs, varying as a function of the amount of dark- and impact-melt *lithologies*. Consequently, the collisional history has a deep influence in the reflectance of asteroids.

3. The different UV-NIR spectral behavior of the *lithologies* in Chelyabinsk resembles those of S and Q-type asteroids. Being relatively small and rare, Q-type asteroids could be the surviving fragments of strong collisional histories, which points towards a connection between the dark-colored *lithology* of Chelyabinsk, which is also the product of higher shock processes.

4. The UV-NIR spectra of the different *lithologies* of Chelyabinsk show important variations that can be easily distinguished. In combination with studies about the mechanical properties of meteorites, like chapter 5, the amount of shock processing and an approximation of the mechanical properties of the surface materials on asteroids, can be inferred from their spectra.

7 SUMMARY AND CONCLUSIONS

The study of the physico-chemical properties of meteorites and, more specifically, of chondrites, provides a unique opportunity to learn about the current and past population of asteroids and comets in the Solar System, but also about the formation of terrestrial planets. This thesis provides a multidisciplinary approach to the subject considering multiple experimental techniques at the same time, and also exploring the different properties of meteorites in order to understand the formation of their components at the early stages of the Solar System, and their posterior evolution until they fell on Earth.

7.1 Experimental methods

The Martian *orthopyroxenite* ALH 84001 has been studied extensively by many authors since it was found more than 30 years ago. In order to perform a study that could provide new information about the parent rock in which this meteorite was formed, and about the aqueous conditions that gave birth to the *carbonates* analyzed here, a very careful and detailed approach was necessary. This provided the opportunity to test several laboratory techniques commonly used in the study of meteorites, to develop the necessary skills to use them appropriately, and to understand the meaning of the results.

The three petrographic microscopes allowed obtaining a first glimpse to the different meteorite samples studied here. During the preparation of the high resolution mosaics the whole sample is observed into detail, which helps finding those features that will be useful for the study being performed. The mosaics became maps of the

sections, which simplifies finding the selected ROIs in order to study them into more detail with other techniques. Also, they are useful to understand the distribution and abundance of different inclusions and regions in a sample. In thin samples, TL is helpful to distinguish opaque phases, such as metals and shock darkened areas. Combined with polarization and a rotating platen, specific minerals can be described. SEM allows for a much more detailed observation and description of the ROIs, and therefore finding small features that cannot be seen with lower magnification. The chemical variation between regions can be observed with BSE, which is particularly useful to distinguish minerals containing elements with different atomic number. EDS provides in situ elemental characterization while the samples are being studied with SEM, but EMP guarantees higher precision and resolution to perform elemental analysis of specific spots in the samples. Also, EMP can be used to obtain continuous elemental profiles, and therefore a detailed description of progressive variations in composition.

CL has proven to be very useful as a support technique to find variations in composition and *crystallographic* structure, since it can detect even trace amounts of specific elements, but it is very dependent on the specific composition of the samples. Indeed, although it was only used to study a Martian meteorite here, CL has been used successfully before in the analysis of chondrites. Since Fe quenches the luminescence, this technique can be used to distinguish between Fe-poor and Fe-rich chondrules, with those last glowing in red. It has also been observed that CL of chondrites changes with petrographic type: *olivine* is Fe-free in low petrographic type chondrites, and therefore shows red luminescence, but with increasing petrographic type iron diffuses into *olivine* grains, which quenches the red luminescence, and *feldspar crystallizes* as a consequence of *metamorphism*, promoting a blue luminescence. Therefore, it can also help distinguishing parts in a breccia with distinct petrographic type.

Despite the usefulness of the techniques mentioned above, micro-Raman spectroscopy, UV-NIR and IR spectroscopy, and Nanoindentation stand out above the others. Micro-Raman is an extensively used technique in mineralogy, and large databases exist with spectra from most known minerals, measured in different conditions and with small variation in composition. Thanks to that, this technique allows for a quick identification of most minerals, although it does not provide the exact chemical composition. Also, micro-Raman spectra are perceivably affected by shock, usually producing a shift in the peaks, and therefore this technique becomes useful to

identify shock affected minerals and to provide an approximate idea of the degree of shock suffered by the analyzed materials.

UV-NIR and IR spectroscopy are commonly used to obtain information from asteroids, which can be compared with data from meteorites, and the large spectral catalogues containing thousands of spectra from minerals and specific meteorites are very helpful to that end. In this thesis, the spectra in the UV-NIR range, ~0.2 to 2.2 μm, proved to be undoubtedly useful to understand the surface materials on asteroids, and to establish proper comparison with meteorites. Indeed, many studies have identified the reasons behind most of the spectral bands found at that range, and the effects that can modify spectral reflectance and slope, such as shock processing and space weathering. This way, clues about the composition and the evolution of specific asteroids and meteorites can be obtained with techniques working in that range. However, the spectra in the UV-NIR range obtained for this thesis are different from the spectra obtained in the same range by other authors, but they show the same albedo, slope and main features, and therefore are still directly comparable, as explained in chapter 4. Indeed, it is interesting to always compare the spectra obtained with the abundant data from the existing catalogues, whenever possible. In the 2.5 to 30.0 μm spectral range (4000 to 333 cm^{-1}, approximately), several features associated to mineralogy, and more specifically to organics and aqueous alteration, can be studied. However, the specific technique used here, ATR, has not been commonly used in the study of meteorites and asteroids, and major parts of the spectra obtained with this technique cannot be directly compared with IR spectra from other type of spectrometers. In any case, spectroscopic techniques working in the UV-NIR or in the IR range require prior knowledge of the bulk properties of the object being studied, and about the particularities of the specific technique being used, in order to determine the meaning of the spectra with reasonable certainty.

From the laboratory techniques used in this thesis, nanoindentation is the least used in the study of meteorites, so far. Here the utility of this technique is demonstrated measuring *hardness*, *Young's modulus* and *elastic recovery* of several different minerals on a Chelyabinsk sample. Although it is not as representative as a large dynamic impact test, nanoindentation is an almost non-destructive technique that requires only very small samples to provide valuable data. With the capability of changing indentation load, it can measure both the very specific mechanical properties of a small mineral inclusion, and the reaction of larger areas. In combination with the study of the

composition and mineralogical structure of the samples, it helps understanding how the evolution suffered by regions of a sample can affect its properties. Also, the appearance of cracks in the borders of some indentations provides information about the *fracture toughness*, and the ease to break the specific mineral phase being studied.

7.2 The Physico-chemical properties of chondrites

In this thesis a CC, the CH3 PCA 91467, and an OC, the Chelyabinsk LL5-6 breccia, have been studied in detail with diverse laboratory techniques. Spectroscopy, both in the UV-NIR and in the IR, provided information about the composition of the samples studied here, but also about aqueous alteration, thermal metamorphism, shock processes, and even space weathering. In the UV-NIR, the level of absolute reflectance is commonly different between OCs and CCs. OCs usually show the relatively high reflecting spectra of a combination of *olivine* and *pyroxene*, with the bands and shape of this minerals being easily recognizable. In the case of CCs, the spectra tend to be mostly flat and almost featureless as descending to lower petrographic types, due to the increasing abundance of fine-grained opaque minerals (such as *magnetite* and organics) finely-dispersed in their *matrix* (Cloutis et al., 1990; Cloutis et al., 2011a). However, in CCs from the CR clan the metal grains (mostly Fe-Ni) produce an increase in the reflectance and a reddening of the spectra, as can be observed in the spectra of the CH3 PCA 91467. This increase in reflectance is different on each group of metal-rich CCs, being stronger in CBs and weaker in CRs, and therefore those groups can be spectroscopically distinguished in the UV-NIR range. Despite of this higher reflectance, the bands remain week CCs from the CR clan. In the CH3 studied in this thesis the *enstatite* bands at 0.9 and 1.9 μm are the stronger and, in fact, very low content in Fe can be estimated just from the shape of the spectra. With a good resolution other fainter bands can also be tentatively identified. This way, minor bands associated to the Fe^{3+} spin forbidden and Fe^{3+} charge transfer transition in iron oxides are found in the spectra of PCA 91467 (Figure 4.4). In OCs, like Chelyabinsk, *olivine* is the main rock-forming phase, followed by *pyroxene*, and then the bands of these minerals at 0.5, 1.0 and beyond 1.5 μm should be dominant. Therefore, once the composition of such a meteorite is known, its spectrum can be approximated combining the spectra of those minerals (Figure 6.4). However, it has been shown in this thesis that regions strongly affected by shock metamorphism are predominantly dark, which attenuates the absorption bands and reduces the overall reflectance.

Working in the IR range, between 2.5 and 25.0 μm (4000 to 333 cm^{-1}, approximately), the Christiansen peak, the Reststrahlen bands and the transparency features are usually studied. Unfortunately, ATR IR spectroscopy could only be used to find the position of the Christiansen peak, but thanks to catalogues and previous studies other IR spectra were used to gain insight in the properties of the PCA 91467. Indeed, the position of the Christiansen peak is consistent with the presence of specific *silicates*. With data from previous studies (Osawa et al., 2005), the main features of CH chondrites in the 2.5 to 4 μm (4000 to 2500 cm^{-1}) spectral region, could be analyzed. Peaks related to the free O-H stretching vibrations of *phyllosilicates*, the presence of hydrated *phyllosilicates*, and widespread aqueous alteration, are common in CH chondrites. Peaks attributed to the symmetric and asymmetric C-H stretching vibrations of *aliphatic* organics were also found in CH chondrites, although those peaks could be a consequence of terrestrial contamination. At higher wavelengths, the only spectrum from the RELAB catalogue belonging to a CH chondrite, PCA 91467, was used. The peaks found in this region for PCA 91467 (Figure 4.7) mostly indicate the presence of *silicates*, in the form of *amorphous olivines*, *enstatite*, possibly *crystalline forsterite*, and *crystalline enstatite.* Consistently with the results in the UV-NIR range, some bands could be indicative of the presence of the *talc*, considering hydration of *enstatite*. Above 16 μm (625 cm^{-1}), grain size and technique specifications can modify the general shape and slope of the spectra, but that possibility was not studied here.

Micro-Raman spectroscopy was applied to the Chelyabinsk OC, and also to the Martian meteorite ALH 84001. In the case of Chelyabinsk, this technique was successfully used to find mineral phases produced as a consequence of high shock pressures (Figure 6.3, Table 6.2). *Jadeite* and *ringwoodite*, high-pressure phases of *pyroxene* and *olivine*, respectively, were found, which is indicative of the degree of shock suffered by this meteorite (more than 25 GPa) and consistent with previous studies. *Olivine*, *chromite*, *merrillite* and *diopside* show their micro-Raman spectra shifted to higher cm^{-1}, which is also indicative of the high pressure experienced by the meteorite. This technique proved to be very helpful to determine whether a meteorite has suffered a higher or lower degree of shock, and in the same way that was done here for Chelyabinsk, can be used with any chondrite. Also, it allowed for differentiation between *carbonates* in the chapter about the Martian meteorite ALH 84001 (Figure 3.5, Table 3.1). Indeed, and thanks to combination of the existing micro-Raman spectra catalogues (like the very extensive RRUFF catalogue) and the Crystalsleuth software,

this technique was used to certify the presence of specific minerals in meteorite samples, although the exact composition and state of minerals required the use of other methods, such as EMP. Minor mineral phases can be detected thanks to the lateral spatial resolution of 1 μm. That was the case for *magnetite* in the *orthopyroxenite* ALH 84001, and for *hematite* in both the Martian meteorite and Chelyabinsk.

The chemical composition and mineralogy of most chondrites has been studied extensively. The mechanical properties, however, are much more difficult to determine. It is particularly interesting to know how a body of specific materials would react to an impact, and to the ablation induced by quick deceleration when penetrating the Earth's atmosphere. Those investigations are usually approached with kinetic impacts on synthetic materials with properties that resemble those of a specific meteorite, because these experiments result in the partial, or almost complete, destruction of the sample. Although thousands of meteorites have been recovered, they tend to be small and each can contain new clues to understand their formation and parent bodies, and therefore the destruction of these samples is always a significant loss. Nanoindentation, by the other hand, is an almost non-destructive technique, that only produces few μm size holes in the samples, and therefore can be applied to most of the know meteorites without implying destruction of unique samples. Chelyabinsk, being a breccia, allows for measuring the variations in mechanical properties between materials that have experienced different degrees of shock and metamorphism. The mechanical properties found here with nanoindentation are consistent with those found previously for OCs, and differ from those of CCs, as expected. According to the results presented in chapter 5, *olivine* and *pyroxene* show *hardness*, *Young's modulus* and *elastic recovery* values that tend to be higher than those of the less abundant materials found on OCs, except for *chromite*. Therefore, high abundances of those less typical materials would reduce the *hardness* of OCs. With respect to the overall behavior of the *lithologies* in this sample of Chelyabinsk, the impact-melt shows the highest *hardness* while the highest values of reduced *Young's modulus* correspond to the black shock-melt vein, but the three regions show very similar values of *elastic recovery*. The light-colored *lithology*, the impact melt *lithology*, and the shock-melt vein are rather similar in chemical composition, mineralogy and porosity, and therefore the differences have to be ascribed to other factors, like the presence of minor phases and high-pressure minerals and their interaction with the *matrix*, or the refinement of the mean particle size and increase of the amount of structural defects due to repetitive shocks produced in the parent asteroid

of this meteorite. The *hardness* values obtained for indentations with different loads are very similar, while *Young's modulus* values are clearly lower in high-load indentations. This is probably due to porosity, since larger-load indentations encounter more voids, and therefore are more influenced by porosity, which, at even larger loads, would probably decrease *hardness*, too. It has also been shown that the average *hardness* of each region tends to be close to that of *olivine* and *pyroxene*, which can imply that ordinary chondrites such as Chelyabinsk behave mechanically in a way similar to that of the major phases, with only a strong contribution of minor phases, since not much strain lies on them. Finally, high-load indentations formed cracks at their edges in some cases in the shock-melt vein, which was indicative of the ease of these veins to break, in comparison with the impact melt and light-colored *lithologies*. The shock-melt veins are therefore weak spots in the structure of meteorites similar to Chelyabinsk.

7.3 Studying chondrites to understand asteroids and rocky planets

In this thesis the properties of the CH3 PCA 91467 and the LL5-6 Chelyabinsk are compared to specific asteroids or asteroid types. Most of the information available about the chemical composition and mineralogy of asteroids comes from the study of their spectra in the UV-NIR to IR range, and therefore the spectral comparison with meteorites is key to establish possible links. In the case of PCA 91467, several bands in the UV-NIR range and features in the IR range talk about a possible connection between CH chondrites and 21 Lutetia or similar asteroids. First, Lutetia spectra are mostly featureless in the UV-NIR range, consistently with CCs, but show a high albedo that could be explained by a relatively high content in metal grains, similarly to what happens with PCA 91467. With respect to specific spectral bands, both the CH meteorite and Lutetia show features associated with the Fe^{3+} spin forbidden transition and charge transfer transitions in iron oxides, the presence of *enstatite*, peaks associated to the free O-H stretching vibrations of *phyllosilicates*, hydrated *silicates*, widespread aqueous alteration, *aliphatic* organics, *amorphous olivine*, and *crystalline forsterite*, and the Christiansen peak seems to be consistent. Other features from the meteorite were only found on some Lutetia spectra, like the 3 μm band commonly (but not only) associated to aqueous alteration, and there are variations in spectral slope. Indeed, the spectral data obtained from the surface of Lutetia is very heterogeneous, varying with the amount of area scanned and the specific position in the asteroid, often showing some difference with the PCA 91467 spectra. This discrepancy does not necessarily imply

that PCA 91467 cannot be associated to 21 Lutetia or similar asteroids, and its rather exemplary of the difficulties to connect the meteorite samples to specific asteroids. First, the size of the areas scanned spectroscopically in an asteroid is much larger than those measured in meteorite samples, and therefore encompasses higher mineralogical variability. Also, the grain size of the fine regolith that covers the surface of an asteroid can modify the spectral slope and hide some features that would be seen in the polished surface of a meteorite sample. Moreover, the evolutionary divergence between a meteorite and its parent asteroid can produce spectral variations. Considering Lutetia as an equivalent of the parent body of PCA 91467, a plausible scenario suggests that water was present in the asteroid before the meteorite was released, in the form of internal ice, brought by CC-materials accreted into the surface, or deposited through a water-rich object that impacted Lutetia at low speed, avoiding water vaporization. Internal heating by radiative decay would produce thermal metamorphism in the interior of the asteroid, and aqueous alteration closer to its surface. PCA 91467 would have formed in the surface of such an asteroid, with very low aqueous alteration. Collisions would create brecciated material in the surface, as can be seen in PCA 91467, and increase the formation of *phyllosilicates*. At that point, the parent fragment of this meteorite would be ejected from the asteroid, and both would experience different evolutionary processes. Subsequent collisions in the asteroid would reshape its surface, uncovering layers with more aqueous alteration and even deeper ones affected by thermal metamorphism, which would gave as a result a high heterogeneous surface. The described collisional history would imply increasing the temperature of the asteroid's surface materials, which could explain the spectral bluing with respect to PCA 91467, and the disappearance of some spectral features. Future studies would require obtaining more spectra from CH meteorites, and compare them to a larger selection of Lutetia spectra.

In the case of the Chelyabinsk OC, the spectra obtained from the light-colored *lithology* shows the typical OC reflectance behavior, with predominance of the *olivine* and *pyroxene* bands (Figure 6.4). This is consistent with the typical spectra of S-type asteroids (DeMeo, 2010). The impact melt *lithology* has been affected to a larger extent by shock metamorphism, according to the data described in chapter 6. The spectra from this *lithology* (and presumably also from the dark-colored *lithology*) show these bands strongly attenuated, becoming mostly featureless and with a flattened slope. Other OCs studied show similar behaviors, although in some cases the change only implies

decrease in the level of reflectance, but not a strong attenuation of the bands. The overall behavior of a large sample would then show intermediate spectra between these two possibilities, with decrease of the reflectance and attenuation of the bands as a function of the amount of shock darkened regions. This way, the collisional history experienced by an asteroid has an important influence in its spectra, providing the opportunity to potentially determine the amount of shock suffered by an asteroid through the study of its spectra, and the possible presence of high pressure and shock modified mineral phases. This model could explain the difference in the spectra between S-type asteroids and the small and rare Q-type asteroids, considering the latter as the surviving fragments of strong collisional processes suffered by S-type asteroids. Combining those results with the mechanical properties obtained with nanoindentation for the Chelyabinsk meteorite, which vary between the different *lithologies* and the shock-melt vein, the average mechanical properties of an asteroid with a determined combination of light and dark-colored *lithologies* could potentially be determined. These properties are particularly interesting to evaluate impact-deflection strategies of PHA. In the hypothetic case that each *lithology* was clearly separated in the surface of an asteroid, selecting the light-colored, with lower *hardness*, as the target of an impact would increase the momentum multiplication and consequently the deviation from its initial trajectory. With Chelyabinsk being an LL5-6 OC breccia with an S4 degree of shock, it can be considered representative of the surface materials of most NEAs and PHAs. If those objects share the abundance of shock-melt veins, they will tend to break and create fragments easier than suggested by their forming materials, since those veins with low *fracture toughness* represent structural weaknesses of asteroids. Although the results described here already provide interesting information to be considered in asteroid-deflection missions, the extrapolation to asteroid scales would require, first, applying nanoindentation to a large population of OCs to have a representative amount of data, and also a better understanding of the internal structure and mechanical behavior of asteroids, which could be provided by real-scale experiments such as the AIDA NASA-ESA joint impact deflection test on the satellite of the asteroid Didymos.

The study of ALH 84001 differs from the previous in that the sample analyzed is not a chondrite, but a Martian achondrite. As explained in chapter 1, chondritic material aggregated progressively to form the planetary embryos, some of which survived to form the rocky planets between the Sun and the MB. Most of that material was probably of OC composition. It is believed that the accretion of carbonaceous chondritic material

provided the necessary amounts of water and carbon to promote the formation of oceans and life on Earth. Similarly, impacts produced by water-rich asteroids on Mars would have set the conditions to allow a wet environment on the early stages of the planet. The study of ALH 84001 serves thus two different purposes in the study of chondrites, besides from developing instrumental capabilities. First, it represents sort of a last stage in the evolution of chondrites, which aggregate until their size is large enough to produce differentiation and the disappearance of chondrules. Also, it is exemplary of the shock and aqueous alteration processes that can take place in the largest asteroids of the Solar System, some of which are at intermediate differentiation stages, still conserving some undifferentiated material. With respect to Mars, this meteorite formed ~4 Gyr ago is a unique source of information on the environmental conditions of early Mars. This thesis focused in the *carbonates* globules formed by precipitation in aqueous conditions. According to the results presented here, at least two precipitation events from different fluids were necessary to create the *carbonates*. Shock processes in the parent rock of this meteorite created large fractures with holes were most of *carbonates* precipitated. The first precipitation compresses layers #1 to #4. A shock event produced the fractures in those layers and introduced a second fluid, which precipitated to form, at least, layers #5 and #6. Indeed, small fractures do not extend from layer #4 to #5, and those two layers are separated by *euhedral* shapes containing small inclusions, suggesting an undetermined time interval between the formations of those layers. A sharp change in composition between those layers and the different compositional trends identified also suggest two distinct events. The appropriate scenario would require a temporally differentiated fluid environment within the region of the Martian crust were the studied sample was formed, with *carbonate* precipitation changing the aqueous environment to promote the precipitation of more Fe-rich *carbonates*, followed by Mg-rich ones. The composition of those *carbonates* is uncommon on Earth, being different from the known solid solutions and evolving across the immiscibility areas between Fe-, Mg- and Ca-rich *carbonates*. These are metastable phases that would require future studies providing detailed characterization.

Summarizing, this thesis has shown how, applying a wide selection of instrumental techniques, the physico-chemical properties of chondrites can be explored into detail and, with a careful approach, they can be extrapolated to specific asteroid, which will provide very valuable information for practical applications such as the deflection of threatening asteroids.

8 REFERENCES

Agee C. B., Wilson N. V., McCubbin F. M., Ziegler K., Polyak V. J., Sharp Z. D., Asmerom Y., Nunn M. H., Shaheen R., Thiemens M. H., Steele A., Fogel M. L., Bowden R., Glamoclija M., Zhang Z. and Elardo S. M. (2013) Unique meteorite from early Amazonian Mars: Water-rich basaltic breccia Northwest Africa 7034. *Science* **339**, 780–785.

Ahrens T. J. and Harris A. W. (1992) Deflection and fragmentation of near-Earth asteroids. *Nature* **360**, 429–433.

Akridge D. G., Akridge J. M. C., Batchelor J. D., Benoit P. H., Brewer J., DeHart J. M., Keck B. D., Jie L., Meier A., Penrose M., Schneider D. M., Sears D. W. G., Symes S. J. K. and Yanhong Z. (2004) Photomosaics of the cathodoluminescence of 60 sections of meteorites and lunar samples. *J. Geophys. Res. E Planets* **109**, 1–10.

Alexander C. M. O., Bowden R., Fogel M. L., Howard K. T., Herd C. D. K. and Nittler L. R. (2012) The Provenances of Asteroids, and Their Contributions to the Volatile Inventories of the Terrestrial Planets. *Science* **337**, 721–723.

Alexander C. M. O., Fogel M. L., Yabuta H. and Cody G. D. (2007) The origin and evolution of chondrites recorded in the elemental and isotopic compositions of their macromolecular organic matter. *Geochim. Cosmochim. Acta* **71**, 4380–4403.

Allègre C. J., Manhés G. and Göpel C. (1995) The age of the Earth. *Geochim. Cosmochim. Acta* **59**, 1445–1456.

Amelin Y., Krot A. N., Hutcheon I. D. and Ulyanov A. A. (2002) Lead Isotopic Ages of Chondrules and Calcium-Aluminum – Rich Inclusions. *Science* **297**, 1678–1683.

Anders E. and Grevesse N. (1989) Abundances of the elements: Meteoritic and solar. *Geochim. Cosmochim. Acta* **53**, 197–214.

Anton R. J. and Subhash G. (2000) Dynamic Vickers indentation of brittle materials. *Wear* **239**, 27–35.

Asmani M., Kermel C., Leriche A. and Ourak M. (2001) Influence of porosity on Young's modulus and Poisson's ratio in alumina ceramics. *J. Eur. Ceram. Soc.* **21**, 1081–1086.

Atkinson H., Tickell C. and Williams D. A. (2000) *Report of the Task Force on Potentially Hazardous Near Earth Objects*., London.

Avril C., Malavergne V., Caracas R., Zanda B., Reynard B., Charon E., Bobocioiu E., Brunet F., Borensztajn S., Pont S., Tarrida M. and Guyot F. (2013) Raman spectroscopic properties and Raman identification of CaS-MgS-MnS-FeS-Cr2FeS4 sulfides in meteorites and reduced sulfur-rich systems. *Meteorit. Planet. Sci.* **48**, 1415–1426.

Baldridge A. M., Hook S. J., Grove C. I. and Rivera G. (2009) The ASTER spectral library version 2.0. *Remote Sens. Environ.* **113**, 711–715.

Bandfield J. L., Glotch T. D. and Christensen P. R. (2003) Spectroscopic identification of carbonate minerals in the martian dust. *Science* **301**, 1084–1087.

Barber D. J. and Scott E. R. D. (2002) Origin of supposedly biogenic magnetite in the Martian meteorite Allan Hills 84001. *Proc. Natl. Acad. Sci. U. S. A.* **99**, 6556–61.

Barucci M. A., Belskaya I., Fornasier S., Fulchignoni M., Clark B. E., Coradini A., Capaccioni F., Dotto E., Birlan M., Leyrat C., Sierks H., Thomas N. and Vincent J.-B. (2012) Overview of Lutetia's surface composition. *Planet. Space Sci.* **66**, 23–30.

Barucci M. A., Capria M. T., Coradini A. and Fulchignoni M. (1987) Classification of Asteroids Using G-Mode Analysis. *Icarus* **72**, 304–324.

Barucci M. A., Fornasier S., Dotto E., Lamy P. L., Jorda L., Groussin O., Brucato J. R., Carvano J. M., Alvarez-Candal A., Cruikshank D. and Fulchignoni M. (2008) Asteroids 2867 Steins and 21 Lutetia: surface composition \nfrom far infrared observations with the Spitzer space telescope. *Astron. Astrophys.* **477**, 665–670.

Barucci M. A., Fulchignoni M., Fornasier S., Dotto E., Vernazza P., Birlan M., Binzel

R. P., Carvano J. M., Merlin F., Barbieri C. and Belskaya I. (2005) Asteroid target selection for the new Rosetta mission baseline 21 Lutetia and 2867 Steins. *Astron. Astrophys.* **317**, 313–317.

Beitz E., Blum J., Parisi M. G. and Trigo-Rodríguez J. M. (2016) The collisional evolution of undifferentiated asteroids and the formation of chondritic meteoroids. *Astrophys. J.* **824**, 18.

Beitz E., Güttler C., Nakamura A. M., Tsuchiyama A. and Blum J. (2013) Experiments on the consolidation of chondrites and the formation of dense rims around chondrules. *Icarus* **225**, 558–569.

Belskaya I., Fornasier S., Krugly Y. N., Shevchenko V. G., Gaftonyuk N. M., Barucci M. A., Fulchignoni M. and Gil-Hutton R. (2010) Puzzling asteroid 21 Lutetia: our knowledge prior to the Rosetta fly-by. *Astron. Astrophys.* **515**, 1–8.

Benz W. and Jutzi M. (2006) Collision and impact simulations including porosity. *Proc. Int. Astron. Union* **2**, 223.

Berk W. van, Ilger J.-M., Fu Y. and Hansen C. (2011) Decreasing CO2 partial pressure triggered Mg-Fe-Ca carbonate formation in ancient Martian crust preserved in the ALH84001 Meteorite. *Geofluids* **11**, 6–17.

Binns R. A., Davis R. J. and Reed S. J. B. (1969) Ringwoodite, Natural (Mg,Fe)2SiO4 Spinel in the Tenham Meteorite. *Nature* **221**, 943–944.

Binzel R. P., Lupishko D. F., Martino M. Di, Whiteley R. and Hahn G. J. (2001) Physical properties of near-earth objects: open problems eds. W. F. Bottke Jr., A. Cellino, P. Paolicchi, and R. P. Binzel. *Adv. Sp. Res.* **28**, 1103–1106.

Binzel R. P., Morbidelli A., Merouane S., DeMeo F. E., Birlan M., Vernazza P., Thomas C. A., Rivkin A. S., Bus S. J. and Tokunaga A. T. (2010) Earth encounters as the origin of fresh surfaces on near-Earth asteroids. *Nature* **463**, 331–334.

Birlan M., Barucci M. A., Vernazza P., Fulchignoni M., Binzel R. P., Bus S. J., Belskaya I. and Fornasier S. (2004) Near-IR spectroscopy of asteroids 21 Lutetia, 89 Julia, 140 Siwa, 2181 Fogelin and 5480 (1989YK8), potential targets for the Rosetta mission; remote observations campaign on IRTF. *New Astron.* **9**, 343–351.

Birlan M., Vernazza P., Fulchignoni M., Barucci M. A., Descamps P., Binzel R. P. and Bus S. J. (2006) Near infra-red spectroscopy of the asteroid 21 Lutetia: I. New results of long-term campaign. *Astron. Astrophys.* **454**, 677–681.

Bischoff A. (2002) Discovery of Purple-Blue Ringwoodite Within Shock Veins of an LL6 Ordinary Chondrite from Northwest Africa. In *33rd Lunar and Planetary Science Conference* p. Abstract 1264.

Bischoff A., Dyl K. A., Horstmann M., Ziegler K., Wimmer K. and Young E. D. (2013a) Reclassification of Villalbeto de la Peña-Occurrence of a winonaite-related fragment in a hydrothermally metamorphosed polymict L-chondritic breccia. *Meteorit. Planet. Sci.* **48**, 628–640.

Bischoff A., Horstmann M., Pack A., Laubenstein M. and Haberer S. (2010) Asteroid 2008 TC3-Almahata Sitta: A spectacular breccia containing many different ureilitic and chondritic lithologies. *Meteorit. Planet. Sci.* **45**, 1638–1656.

Bischoff A., Horstmann M., Vollmer C., Heitmann U. and Decker S. (2013b) Chelyabinsk - Not only another ordinary LL5 chondrite, but a spectacular chondrite breccia. *Meteorit. Planet. Sci.* **48**, A1–A394.

Bischoff A., Palme H., Schultz L., Weber D., Weber H. W. and Spettel B. (1993) Acfer 182 and paired samples, an iron-rich carbonaceous chondrite: Similarities with ALH85085 and relationship to CR chondrites. *Geochim. Cosmochim. Acta* **57**, 2631–2648.

Bischoff A., Rubin A. E., Keil K. and Stöffler D. (1983) Lithification of gas-rich chondrite regolith breccias by grain boundary and localized shock melting. *Earth Planet. Sci. Lett.* **66**, 1–10.

Bischoff A., Schirmeyer S., Palme H., Spettel B. and Weber D. (1994) Mineralogy and Chemistry of the Carbonaceous Chondrite PCA 91467 (CH). *Meteoritics* **29**, 444.

Bischoff A., Scott E. R. D., Metzler K. and Goodrich C. A. (2006) Nature and origins of meteoritic breccias. In *Meteorites and the Early Solar System II* (eds. D. S. Lauretta and H. Y. J. McSween). Univ. of Arizona Press, Tucson. pp. 679–712.

Bischoff A. and Stöffler D. (1992) Shock metamorphism as a fundamental process in the evolution of planetary bodies: Information from meteorites. *Eur. J. Mineral.* **4**, 707–755.

Bischoff A., Vogel N. and Roszjar J. (2011) The Rumuruti chondrite group. *Chemie der Erde - Geochemistry* **71**, 101–133.

Bland P. A., Alard O., Benedix G. K., Kearsley A. T., Menzies O. N., Watt L. E. and

Rogers N. W. (2005) Volatile fractionation in the early solar system and chondrule/matrix complementarity. *Proc. Natl. Acad. Sci.* **102**, 13755–13760.

Bland P. A. and Artemieva N. A. (2003) Efficient disruption of small asteroids by Earth's atmosphere. *Nature* **424**, 288–291.

Blum J. (2004) Grain growth and coagulation. In *Astrophysics of Dust, ASP Conference Series* (eds. A. N. Witt, G. C. Clayton, and B. T. Draine). Estes Park, Colorado. pp. 369–391.

Blum J. and Münch M. (1993) Experimental Investigation on Aggregate-Aggregate Collisions in the Early Solar Nebula. *Icarus* **106**, 151–167.

Blum J., Schrapler R., Davidsson B. J. R. and Trigo-Rodríguez J. M. (2006) The Physics of Protoplanetesimal Dust Agglomerates. I. Mechanical Properties and Relations to Primitive Bodies in the Solar System. *Astrophys. J.* **652**, 1768–1781.

Blum J. and Wurm G. (2000) Experiments on Sticking, Restructuring, and Fragmentation of Preplanetary Dust Aggregates. *Icarus* **143**, 138–146.

Blum J., Wurm G., Kempf S., Poppe T., Klahr H., Kozasa T., Rott M., Henning T., Dorschner J., Schrapler R., Keller H. U., Markiewicz W. J., Mann I., Gustafson B. A. S., Giovane F., Neuhaus D., Fechtig H., Grun E., Feuerbacher B., Kochan H., Ratke L., El Goresy A., Morfill G., Weidenschilling S. J., Schwehm G., Metzler K. and Ip W.-H. (2000) On Growth and Form of Planetary Seedlings: results from a microgravity aggregation experiment. *Phys. Rev. Lett.* **85**, 2426–2429.

Bogard D. D. and Johnson P. (1983) Martian Gases in an Antarctic meteorite? *Science* **221**, 651–654.

Borg L. E., Connelly J. N., Nyquist L. E. and Shih C.-Y. (1999) Pb-Pb Age of the carbonates in the Martian meteorite ALH 84001. *30th Lunar Planet. Sci. Conf.*, Abstract 1430.

Borovička J., Spurný P., Brown P. G., Wiegert P., Kalenda P., Clark D. and Shrbený L. (2013) The trajectory, structure and origin of the Chelyabinsk asteroidal impactor. *Nature* **503**, 235–237.

Bottke Jr. W. F., Broz M., O'Brien D. P., Campo Bagatín A., Morbidelli A. and Marchi S. (2015) The Collisional Evolution of the Main Asteroid Belt. In *Asteroids IV* (eds. P. Michel, F. E. DeMeo, and W. F. Bottke Jr.). University of Arizona Press, Tucson. pp. 701–724.

Bouvier A. and Wadhwa M. (2010) The age of the Solar System redefined by the oldest Pb – Pb age of a meteoritic inclusion. *Nat. Geosci.* **3**, 637–641.

Bouwman J., Meeus G., de Koter A., Hony S., Dominik C. and Waters L. B. F. M. (2001) Processing of silicate dust grains in Herbig Ae / Be systems. *Astron. Astrophys.* **375**, 950–962.

Boynton W. V. (1975) Fractionation in the solar nebula: condensation of yttrium and the rare Earth elements. *Geochim. Cosmochim. Acta* **39**, 509–584.

Boynton W. V., Ming D. W., Kounaves S. P., Young S. M. M., Arvidson R. E., Hecht M. H., Hoffman J., Niles P. B., Hamara D. K., Quinn R. C., Smith P. H., Sutter B., Catling D. C. and Morris R. V. (2009) Evidence for calcium carbonate at the Mars Phoenix landing site. *Science* **325**, 61–64.

Boynton W. V. and Wark D. A. (1985) Refractory Rims: Evidence for High Temperature Events in the Post-formation History of Ca, Al-rich Inclusions. *Meteoritics* **20**, 613.

Bradley J., McSween H. Y. and Harvey R. P. (1998) Epitaxial growth of nanophase magnetite in Martian meteorite Allan Hills 84001: implications for biogenic mineralization. *Meteorit. Planet. Sci.* **33**, 765–73.

Brearley A. J. and Jones R. H. (1998) Chodritic meteorites. In *Planetary Materials, vol. 36: Reviews in Mineralogy* (ed. J. J. Papike). Mineralogical Society of America, Washington, D.C. pp. 3-1-3–398.

Bridges J. C., Catling D. C., Saxton J. M., Swindle T. D., Lyon I. C. and Grady M. M. (2001) Alteration assemblages in Martian meteorites: Implications for near-surface processes. *Space Sci. Rev.* **96**, 365–392.

Bridges J. C. and Grady M. M. (2000) Evaporite mineral assemblages in the nakhlite (martian) meteorites. *Earth Planet. Sci. Lett.* **176**, 267–279.

Britt D. T., Abreu N. M., Asphaug E. I., Campins H., Gertsch L., Sercel J. and Zacny K. (2015) *Boulder Physical Properties*.,

Britt D. T. and Pieters C. M. (1991) Black ordinary chondrites: An analysis of abundance and fall frequency. *Meteoritcs* **26**, 279–285.

Britt D. T. and Pieters C. M. (1994) Darkening in black and gas-rich ordinary chondrites: The spectral effects of opaque morphology and distribution. *Geochim.*

Cosmochim. Acta **58**, 3905–3919.

Britt D. T., Yeomans D., Housen K. R. and Consolmagno G. J. (2002) Asteroid density, porosity, and structure. In *Asteroids III* (ed. W. F. Bottke). Univ. of Arizona Press, Tucson. pp. 485–500.

Brodie K., Fettes D., Harte B. and Schmid R. (2007) A systematic nomenclature for metamorphic rocks: 3. Structural terms including fault rock terms. In *Recommendations by the IUGS Subcommission on the Systematics of Metamorphic Rocks* p. 14.

Brown P. G., Assink J. D., Astiz L., Blaauw R., Boslough M. B., Borovička J., Brachet N., Brown D., Campbell-Brown M., Ceranna L., Cooke W., de Groot-Hedlin C., Drob D. P., Edwards W., Evers L. G., Garces M., Gill J., Hedlin M., Kingery A., Laske G., Le Pichon A., Mialle P., Moser D. E., Saffer A., Silber E., Smets P., Spalding R. E., Spurný P., Tagliaferri E., Uren D., Weryk R. J., Whitaker R. and Krzeminski Z. (2013) A 500-kiloton airburst over Chelyabinsk and an enhanced hazard from small impactors. *Nature* **503**, 238–241.

Brownlee D. E. (2001) The Origin and Properties of Dust Impacting the Earth. In *Accretion of Extraterrestrial Matter Throughout Earth's History* (eds. B. Peucker-Ehrenbrink and B. Schmitz). Springer US, New York. pp. 1–12.

Brownlee D. E., Tsou P., Aleon J., Alexander C. M. O., Araki T., Bajt S., Baratta G. A., Bastien R., Bland P. A., Bleuet P., Borg J., Bradley J. P., Brearley A. J., Brenker F., Brennan S., Bridges J. C., Browning N. D., Brucato J. R., Bullock E. S., Burchell M. J., Busemann H., Butterworth A. L., Chaussidon M., Cheuvront A., Chi M., Cintala M. J., Clark B. E., Clemett S. J., Cody G. D., Colangeli L., Cooper G., Cordier P., Daghlian C., Dai Z., D'Hendecourt L., Djouadi Z., Dominguez G., Duxbury T., Dworkin J. P., Ebel D. S., Economou T. E., Fakra S., Fairey S. A. J., Fallon S., Ferrini G., Ferroir T., Fleckenstein H., Floss C., Flynn G. J., Franchi I. A., Fries M. D., Gainsforth Z., Gallien J.-P., Genge M., Gilles M. K., Gillet P., Gilmour J., Glavin D. P., Gounelle M., Grady M. M., Graham G. A., Grant P. G., Green S. F., Grossemy F., Grossman L., Grossman J. N., Guan Y., Hagiya K., Harvey R. P., Heck P., Herzog G. F., Hoppe P., Horz F., Huth J., Hutcheon I. D., Ignatyev K., Ishii H., Ito M., Jacob D., Jacobsen C., Jacobsen S., Jones S., Joswiak D., Jurewicz A., Kearsley A. T., Keller L. P., Khodja H., Kilcoyne A. L. D., Kissel J., Krot A. N., Langenhorst F., Lanzirotti A., Le L., Leshin L. A., Leitner J.,

Lemelle L., Leroux H., Liu M.-C., Luening K., Lyon I. C., Macpherson G. J., Marcus M. A., Marhas K. K., Marty B., Matrajt G., McKeegan K. D., Meibom A., Mennella V., Messenger K., Messenger S., Mikouchi T., Mostefaoui S., Nakamura T., Nakano T., Newville M., Nittler L. R., Ohnishi I., Ohsumi K., Okudaira K., Papanastassiou D. A., Palma R., Palumbo M. E., Pepin R. O., Perkins D., Perronnet M., Pianetta P., Rao W., Rietmeijer F. J. M., Robert F., Rost D., Rotundi A., Ryan R., Sandford S. A., Schwandt C. S., See T. H., Schlutter D., Sheffield-Parker J., Simionovici A., Simon S. B., Sitnitsky I., Snead C. J., Spencer M. K., Stadermann F. J., Steele A., Stephan T., Stroud R. M., Susini J., Sutton S. R., Suzuki Y., Taheri M., Taylor S., Teslich N., Tomeoka K., Tomioka N., Toppani A., Trigo-Rodríguez J. M., Troadec D., Tsuchiyama A., Tuzzolino A. J., Tyliszczak T., Uesugi K., Velbel M., Vellenga J., Vicenzi E., Vincze L., Warren J., Weber I., Weisberg M. K., Westphal A. J., Wirick S., Wooden D., Wopenka B., Wozniakiewicz P. J., Wright I. P., Yabuta H., Yano H., Young E. D., Zare R. N., Zega T. J., Ziegler K., Zimmerman L., Zinner E. K. and Zolensky M. E. (2006) Comet 81P/Wild 2 Under a Microscope. *Science* **314**, 1711–1716.

Brusnitsyna E. V., Grokhovsky V. I. and Minin M. G. (2016) Nanoindentation of Different Structures Within the Metallic Part of the Seymchan Pallasite PMG. *Meteorites Planet. Sci.* **51**, A144.

Buddhue J. D. (1945) The Compressive Strength of Meteorites. *Contrib. Soc. Res. Meteorites* **3**, 39–40.

Burbine T. H., McCoy T. J., Meibom A., Gladman B. and Keil K. (2002a) Meteoritic Parent Bodies : Their Number and Identification. In *Asteroids III* (eds. W. F. Bottke Jr., A. Cellino, P. Paolicchi, and R. P. Binzel). University of Arizona Press, Tucson. pp. 653–667.

Burbine T. H., Mccoy T. J., Nittler L. R., Benedix G. K., Cloutis E. A. and Dickinson T. L. (2002b) Spectra of extremely reduced assemblages: Implications for Mercury. *Meteoric* **37**, 1233–1244.

Burns R. G. (1993) *Mineralogical Applications of Crystal Field Theory*. 2nd ed., Cambridge University Press, London.

Bus S. J. and Binzel R. P. (2002a) Phase II of the Small Main-Belt Asteroid Spectroscopic Survey: A Feature-Based Taxonomy. *Icarus* **158**, 146–177.

Bus S. J. and Binzel R. P. (2002b) Phase II of the Small Main-Belt Asteroid Spectroscopic Survey: The Observations. *Icarus* **158**, 106–145.

Caffee M. W., Hohenberg C. M., Swindle T. D. and Goswani J. N. (1987) Evidence in meteorites for an active early Sun. *Astrophys. J.* **313**, L31–L35.

Cameron A. G. W. (1993) Nucleosynthesis and star formation. In *Protostars and planets III* (eds. E. H. Levy and J. I. Lunine). University of Arizona Press, Tucson, AZ. pp. 47–73.

Cameron A. G. W. (1963) The Formation of the Solar Nebula. In *Origin of the Solar System* (eds. R. Jastrow and A. G. W. Cameron). Academic Press, New York. pp. 85–94.

Cameron A. G. W. and Truran J. W. (1977) The Supernova Trigger for Formation of the Solar System. *Icarus* **30**, 447–461.

Campbell A. J. and Humayun M. (2004) Formation of metal in the CH chondrites ALH 85085 and PCA 914671. *Geochim. Cosmochim. Acta* **68**, 3409–3422.

Carnelli I., Gàlvez A. and Ongaro F. (2006) Learning to Deflect Near-Earth Objects: Industrial Design of the Don Quijote mission. *57th Int. Astronaut. Congr.*

Carr R. H., Grady M. M., Wright I. P. and Pillinger C. T. (1985) Martian atmospheric carbon dioxide and weathering products in SNC meteorites. *Nature* **314**, 248–250.

Chan Q. H. S., Zolensky M. E. and Martínez J. (2015) Scaffold of Asymmetric Organic Compounds - Magnetite Plaquettes. *46th Lunar Planet. Sci. Conf.*, Abstract #1150.

Chang L. L. Y., Howie R. A. and Zussman J. (1996) *Rock forming minerals. volume 5B: Non-silicates: sulphates, carbonates, phosphates and halides*. 2nd ed., Geological Society of London, London.

Chapman C. R. (2004) Space Weathering of Asteroid Surfaces. *Annu. Rev. Earth Planet. Sci.* **32**, 539–567.

Chemtob S. M. and Glotch T. D. (2007) Linear deconvolution of attenuated total reflectance infrared spectra of fine-grained mineral mixtures. *38th Lunar Planet. Sci. Conf.*, Abstract #1097.

Chen M. and Xie X. (1992) Raman spectra of orthopyroxene in two natural shocked H chondrites. *Meteoritics* **27**, 209.

Clark B. E., Binzel R. P., Howell E. S., Cloutis E. A., Ockert-Bell M. E., Christensen P.

R., Barucci M. A., DeMeo F. E., Lauretta D. S., Connolly H. C., Soderberg A., Hergenrother C., Lim L. F., Emery J. P. and Mueller M. (2011) Asteroid (101955) 1999 RQ36: Spectroscopy from 0.4 to 2.4 μm and meteorite analogs. *Icarus* **216**, 462–475.

Clark B. E., Fanale F. P. and Salisbury J. W. (1992) Meteorite-asteroid spectral comparison: The effects of comminution, melting, and recrystallization. *Icarus* **97**, 288–297.

Clark B. E. and Johnson R. E. (1996) Interplanetary Weathering : Surface Erosion in Outer Space. *Eos (Washington. DC).* **77**, 141–148.

Clark B. E., Ziffer J., Nesvorný D., Campins H., Rivkin A. S., Hiroi T., Barucci M. A., Fulchignoni M., Binzel R. P., Fornasier S., DeMeo F. E., Ockert-Bell M. E., Licandro J. and Mothé-Diniz T. (2010) Spectroscopy of B-type asteroids: Subgroups and meteorite analogs. *J. Geophys. Res.* **115**, 22.

Clayton R. N. and Mayeda T. K. (1999) Oxygen isotope studies of carbonaceous chondrites. *Geochim. Cosmochim. Acta* **63**, 2089–2104.

Clayton R. N. and Mayeda T. K. (1991) Oxygen isotope studies of ordinary chondrites. *Geochim. Cosmochim. Acta* **55**, 2317–2337.

Cloutis E. A., Gaffey M. J., Smith D. G. W. and Lambert R. S. J. (1990) Reflectance spectra of "Featureless" materials and the surface mineralogies of M- and E-class asteroids. *J. Geophys. Res.* **95**, 281–293.

Cloutis E. A., Hardersen P. S., Bish D. L., Bailey D. T., Gaffey M. J. and Craig M. A. (2010) Reflectance spectra of iron meteorites: Implications for spectral identification of their parent bodies. *Meteorit. Planet. Sci.* **45**, 304–332.

Cloutis E. A., Hiroi T., Gaffey M. J., Alexander C. M. O. and Mann P. (2011a) Spectral reflectance properties of carbonaceous chondrites: 1. CI chondrites. *Icarus* **212**, 180–209.

Cloutis E. A., Hudon P., Hiroi T. and Gaffey M. J. (2012a) Spectral reflectance properties of carbonaceous chondrites: 3. CR chondrites. *Icarus* **217**, 389–407.

Cloutis E. A., Hudon P., Hiroi T. and Gaffey M. J. (2012b) Spectral reflectance properties of carbonaceous chondrites 4: Aqueously altered and thermally metamorphosed meteorites. *Icarus* **220**, 586–617.

Cloutis E. A., Hudon P., Hiroi T., Gaffey M. J. and Mann P. (2011b) Spectral reflectance properties of carbonaceous chondrites: 2. CM chondrites. *Icarus* **216**, 309–346.

Cloutis E. A., Hudon P., Hiroi T., Gaffey M. J. and Mann P. (2012c) Spectral reflectance properties of carbonaceous chondrites: 8. " Other" carbonaceous chondrites: CH, ungrouped, polymict, xenolithic inclusions, and R chondrites. *Icarus* **221**, 984–1001.

Connolly Jr. H. C. (2005) Refractory Inclusions and Chondrules : Insights into a Protoplanetary Disk and Planet Formation. In *Chondrites and the Protoplanetary Disk, ASP Conference Series* (eds. A. N. Krot, E. R. D. Scott, and B. Reipurth). Astronomical Society of the Pacific, San Francisco. pp. 215–224.

Connolly Jr. H. C., Jones B. D. and Hewins R. H. (1998) The flash melting of chondrules: An experimental investigation into the melting history and physical nature of chondrule precursors. *Geochim. Cosmochim. Acta* **62**, 2725–2735.

Consolmagno G. J., Britt D. T. and Macke R. J. (2008) The significance of meteorite density and porosity. *Chemie der Erde - Geochemistry* **68**, 1–29.

Cooney T. F., Scott E. R. D., Krot A. N., Sharma S. K. and Yamaguchi A. (1999) Vibrational spectroscopic study of minerals in the Martian meteorite ALH 84001. *Am. Mineral.* **84**, 1569.

Coradini A., Capaccioni F., Erard S., Arnold G., De Sanctis M. C., Filacchione G., Tosi F., Barucci M. A., Capria M. T., Ammannito E., Grassi D., Piccioni G., Giuppi S., Bellucci G., Benkhoff J., Bibring J. P., Blanco A., Blecka M., Bockelee-Morvan D., Carraro F., Carlson R., Carsenty U., Cerroni P., Colangeli L., Combes M., Combi M., Crovisier J., Drossart P., Encrenaz E. T., Federico C., Fink U., Fonti S., Giacomini L., Ip W.-H., Jaumann R., Kuehrt E., Langevin Y., Magni G., McCord T., Mennella V., Mottola S., Neukum G., Orofino V., Palumbo P., Schade U., Schmitt B., Taylor F., Tiphene D. and Tozzi G. (2011) The Surface Composition and Temperature of Asteroid 21 Lutetia As Observed by Rosetta/VIRTIS. *Science* **334**, 492–494.

Corrigan C. M. and Harvey R. P. (2004) Multi-generational carbonate assemblages in Martian meteorite Allan Hills 84001; implications for nucleation, growth, and alteration. *Meteorit. Planet. Sci.* **39**, 17–30.

Corrigan C. M., Niles P. B., Leshin L. A., Harvey R. P., Guan Y. and McKeegan K. D. (2003) Oxygen Isotopic Compositions of Unique Carbonates in Martian Meteorite Allan Hills 84001. *66th Annu. Meteorit. Soc. Meet.*, 5269.

Cuzzi J. N., Hogan R. C. and Bottke W. F. (2010) Towards Initial Mass Functions for Asteroids and Kuiper Belt Objects. *Icarus* **208**, 518–538.

Davis A. M. and MacPherson G. J. (1996) Thermal processing in the solar nebular: Constraints from refractory inclusions. In *Chondrules and the Protoplanetary Disk* (eds. R. H. Hewins, R. H. Jones, and E. R. D. Scott). Cambridge University Press, Cambridge. pp. 71–76.

Davis D. R., Weidenschilling S. J., Farinella P., Paolicchi P. and Binzel R. P. (1989) Asteroid collisional history: Effects on sizes and spins. In *Asteroids II* (eds. R. P. Binzel, T. Gehrels, and M. S. Matthews). University of Arizona Press, Tucson, AZ. pp. 805–826.

Davison T. M., O'Brien D. P., Ciesla F. J. and Collins G. S. (2013) The early impact histories of meteorite parent bodies. *Meteorit. Planet. Sci.* **48**, 1894–1918.

DeMeo F. E. (2010) The compositional variation of small bodies across the Solar System. Observatoire de Paris.

DeMeo F. E., Binzel R. P., Slivan S. M. and Bus S. J. (2009) An extension of the Bus asteroid taxonomy into the near-infrared. *Icarus* **202**, 160–180.

Dmitriev V., Lupovka V. and Gritsevich M. (2015) Orbit determination based on meteor observations using numerical integration of equations of motion. *Planet. Space Sci.* **117**, 223–235.

Dorschner J., Begemann B., Henning T., Jäger C. and Mutschke H. (1995) Steps toward interstellar silicate mineralogy II. Study of Mg-Fe-silicate glasses of variable composition. *Astron. Astrophys.* **300**, 503–520.

Drake J. (2001) Presidential Adress: The eucrite/Vesta story. *Meteorit. Planet. Sci.* **36**, 501–513.

Drummond J. D., Conrad A., Merline W. J., Carry B., Chapman C. R., Weaver H. A., Tamblyn P. M., Christou J. C. and Dumas C. (2010) The triaxial ellipsoid dimensions, rotational pole, and bulk density of ESA/NASA Rosetta target asteroid (21) Lutetia. *eprint arXiv* **1005**, 5353.

Dunn T. L., Burbine T. H., Bottke W. F. and Clark J. P. (2013a) Mineralogies and source regions of near-Earth asteroids. *Icarus* **222**, 273–282.

Dunn T. L., Burbine T. H., Bottke W. F. and Clark J. P. (2013b) Mineralogies and Source Regions of near Earth Asteroids. *Lunar Planet. Sci. Conf.*, 1997.

Dyar M. D., Glotch T. D., Lane M. D., Wopenka B., Tucker J. M., Seaman S. J., Marchand G. J., Klima R. L., Hiroi T., Bishop J. L., Pieters C. P. and Sunshine J. M. (2011) Spectroscopy of Yamato 984028. *Polar Sci.* **4**, 530–549.

Ehlmann B. L., Mustard J. F., Murchie S. L., Poulet F., Bishop J. L., Brown A. J., Calvin W. M., Clark R. N., Des Marais D. J., Milliken R. E., Roach L. H., Roush T. L., Swayze G. A. and Wray J. J. (2008) Orbital Identification of Carbonate-Bearing Rocks on Mars Bethany. *Science* **322**, 1828–1832.

Eiler J. M., Valley J. W., Graham C. M. and Fournelle J. (2002) Two populations of carbonate in ALH84001 : Geochemical evidence for discrimination and genesis. *Geochim. Cosmochim. Acta* **66**, 1285–1303.

de Elía G. C. and Brunini A. (2007) Collisional and dynamical evolution \n of the main belt and NEA population. *Astron. Astrophys.* **466**, 1159–1177.

Eugster O., Herzog G. F., Marti K. and Caffee M. W. (2006) Irradiation Records, Cosmic-Ray Exposure Ages, and Transfer Times of Meteorites. In *Meteorites and the Early Solar System II* (eds. D. S. Lauretta and H. Y. J. McSween). University of Arizona Press, Tucson, AZ. pp. 829–851.

Feierberg M. A., Lebofsky L. A. and Tholen D. J. (1985) The nature of C-Class asteroids from 3-μm spectrophotometry. *Icarus* **63**, 183–191.

Fernández-Remolar D. C., Sánchez-Roán M., Hill A. C., Gómez-Ortíz D., Ballesteros O. P., Romanek C. S. and Amils R. (2011) The environment of early Mars and the missing carbonates. *Meteorit. Planet. Sci.* **46**, 1447–1469.

Fischer-Cripps A. C. (2004) *Nanoindentation*. ed. F. F. Ling, Springer, New York.

Flynn G. J. (2005) Physical Properties of Meteorites and Interplanetary Dust Particles: Clues to the Properties of the Meteors and Their Parent Bodies. *Earth. Moon. Planets* **95**, 361–374.

Fornasier S., Lantz C., Barucci M. A. and Lazzarin M. (2014) Aqueous alteration on main belt primitive asteroids: Results from visible spectroscopy. *Icarus* **233**, 163–

178.

Frey H. V. (2008) Ages of very large impact basins on Mars: Implications for the late heavy bombardment in the inner solar system. *Geophys. Res. Lett.* **35**, 1–4.

Gaffey M. J. (2010) Space weathering and the interpretation of asteroid reflectance spectra. *Icarus* **209**, 564–574.

Gaffey M. J. (1976) Spectral Reflectance Characteristics of the Meteorite Classes. *J. Geophys. Res.* **81**, 905–920.

Gaffey M. J., Bell J. F., Brown R. H., Burbine T. H., Piatek J. L., Reed K. L. and Chaky D. A. (1993) Mineralogical variations within the S-type asteroid class. *Icarus* **106**, 573–602.

Gaffey M. J., Cloutis E. A., Kelly M. S. and Reed K. L. (2002) Mineralogy of Asteroids. In *Asteroids III* (eds. W. F. Bottke, A. Cellino, P. Paolicchi, and R. P. Binzel). University of Arizona Press, Tucson. pp. 183–204.

Gail H.-P., Trieloff M., Breuer D. and Spohn T. (2014) Early Thermal Evolution of Planetesimals and its Impact on Processing and Dating of Meteoritic Material. In *Protostars and planets IV* (eds. H. Beuther, R. S. Klessen, C. P. Dullemond, and T. Henning). University of Arizona Press, Tucson. pp. 571–593.

Galimov E. M. (2013) Chelyabinsk meteorite—an LL5 chondrite. *Sol. Syst. Res.* **47**, 255–259.

Galimov E. M., Kolotov V. P., Nazarov M. A., Kostitsyn Y. a., Kubrakova I. V., Kononkova N. N., Roshchina I. A., Alexeev V. A., Kashkarov L. L., Badyukov D. D. and Sevast'yanov V. S. (2013) Analytical results for the material of the Chelyabinsk meteorite. *Geochemistry Int.* **51**, 522–539.

Gerberich W. W., Tymiak N. I., Grunlan J. C., Horstemeyer M. F. and Baskes M. I. (2002) Interpretations of Indentation Size Effects. *J. Appl. Mech.* **69**, 433–442.

Gil Sevillano J., van Houtte P. and Aernoudt E. (1980) Large strain work hardening and textures. *Prog. Mater. Sci.* **25**, 69–134.

Golden D. C., Ming D. W., Schwandt C. S., Lauer H. V., Socki R. A., Morris R. V., Lofgren G. E. and McKay G. A. (2001) A simple inorganic process for formation of carbonates, magnetite, and sulfides in Martian meteorite ALH84001. *Am. Mineral.* **86**, 370–375.

Golden D. C., Ming D. W., Schwandt C. S., Morris R. V., Yang S. V. and Lofgren G. E. (2000) An experimental study of kinetically-driven precipitation of calcium-magnesium-iron carbonates from solution: Implications for the low-temperature fromation of carbonates in Martian meteorite Allan Hills 84001. *Meteorit. Planet. Sci.* **35**, 457–465.

Gomes R., Levison H. F., Tsiganis K. and Morbidelli A. (2005) Origin of the cataclysmic Late Heavy Bombardment period of the terrestrial planets. *Nature* **435**, 466–469.

Goodrich C. A., Bischoff A. and O'Brien D. P. (2014) Asteroid 2008 TC3 and the fall of Almahata sitta, a unique meteorite breccia. *Elements* **10**, 31–37.

Göpel C., Gerard M. and Allègre C. J. (1994) U-Pb systematics of phosphates from equilibrated ordinary chondrites. *Geochim. Cosmochim. Acta* **121**, 153–171.

Götze J., Krbetschek M. R., Habermann D. and Wolf D. (2000) High-resolution cathodoluminescence studies of feldspar minerals. In *Cathodoluminescence in Geosciences* (eds. M. Pagel, V. Barbin, P. Blanc, and D. Ohnenstetter). Springer-Verlag Berlin Heildelberg. pp. 245–270.

Greaves J. S. (2005) Disks Around Stars and the Growth of Planetary Systems. *Science* **307**, 68–71.

Greenwood R. C., Franchi I. A., Kearsley A. T. and Alard O. (2010) The relationship between CK and CV chondrites. *Geochim. Cosmochim. Acta* **74**, 1684–1705.

Greshake A., Krot A. N., Meibom A., Weisberg M. K., Zolensky M. E. and Keil K. (2002) Heavily-hydrated lithic clasts in CH chondrites and the related, metal-rich chondrites Queen Alexandra Range 94411 and Hammadah al Hamra 237. *Meteorit. Planet. Sci.* **37**, 281–293.

Grier J. A., Kring D. A., Swindle T. D., Rivkin A. S., Cohen B. A. and Britt D. T. (2004) Analyses of the chondritic meteorite Orvinio (H6): Insight into the origins and evolution of shocked H chondrite material. *Meteorit. Planet. Sci.* **39**, 1475–1493.

Grimm R. E. and McSween H. Y. J. (1993) Heliocentric zoning of the asteroid belt by aluminum-26 heating. *24th Lunar Planet. Sci. Conf.*, 577–578.

Grimm R. E. and McSween H. Y. J. (1989) Water and the Thermal Evolution of Carbonaceous Chondrite Parent Bodies. *Icarus* **82**, 244–280.

Grossman J. N., Rubin A. E., Nagahara H. and King E. A. (1988) Properties of chondrules. In *Meteorites and the early Solar System* (eds. J. F. Kerridge and M. S. Ž. . Matthews). University of Arizona Press, Tucson, AZ. pp. 619–659.

Gundlach B. and Blum J. (2013) A new method to determine the grain size of planetary regolith. *Icarus* **223**, 479–492.

Halevy I., Fischer W. W. and Eiler J. M. (2011) Carbonates in the Martian meteorite Allan Hills 84001 formed at 18 +- 4 ºC in a near-surface aqueous environment. *Proc. Natl. Acad. Sci.* **108**, 16895–16899.

Hall A. (1987) *Igneous Petrology*., Longman Scientific & Technical, London.

Hamilton V. E., Christensen P. R., McSween H. Y. and Bandfield J. L. (2003) Searching for the source regions of Martian meteorites using MGS TES: Integrating Martian meteorites into the global distribution of igneous materials on Mars. *Meteorit. Planet. Sci.* **38**, 871–885.

Hardersen P. S., Cloutis E. A., Reddy V., Mothé-Diniz T. and Emery J. P. (2011) The M-/X-asteroid menagerie: Results of an NIR spectral survey of 45 main-belt asteroids. *Meteorit. Planet. Sci.* **46**, 1910–1938.

Harvey R. P. and McSween H. Y. J. (1996) A possible high-temperature origin for the carbonates in the Martian meteorite ALH 84001. *Nature* **382**, 49–51.

Hendrix A. R. and Vilas F. (2006) The effects of space weathering at UV wavelengths: S-Class asteroids. *Astron. J.* **132**, 1396–1404.

Henke S., Gail H.-P., Trieloff M., Schwarz W. H. and Kleine T. (2012) Thermal evolution and sintering of chondritic planetesimals. *Astron. Astrophys.* **537**, 19.

Hewins R. H. and Connolly Jr. H. C. (1996) Peak temperatures of flash-melted chondrules. In *Chondrules and the Protoplanetary Disk* (eds. R. H. Hewins, R. H. Jones, and E. R. D. Scott). Cambridge University Press, Cambridge. pp. 197–204.

Hewins R. H., Yu Y., Zanda B. and Bourot-Denise M. (1997) Do nebular fractionations, evaporative losses, or both, influence chondrule compositions? *Antarct. Meteor. Res.* **10**, 275–298.

Hiroi T., Pieters C. M., Zolensky M. E. and Lipschutz M. E. (1993) Evidence of thermal metamorphism on the C, G, B, and F asteroids. *Science* **261**, 1016–1018.

Hoerth T., Schäfer F. K., Hupfer J., Millon O. and Wickert M. (2015) Momentum Transfer in Hypervelocity Impact Experiments on Rock Targets. *Procedia Eng.* **103**, 197–204.

Holland G., Lyon I. C., Saxton J. M. and Turner G. (1999) Evidence for an unusual generation of carbonate in Allan Hills 84001. *Meteorit. Planet. Sci.* **34**, A55.

Holland G., Saxton J. M., Lyon I. C. and Turner G. (2005) Negative delta18O values in Allan Hills 84001 carbonate: Possible evidence for water precipitation on Mars. *Geochim. Cosmochim. Acta* **69**, 1359–1369.

Holsapple K. A. (2001) Equilibrium Configurations of Solid Cohesionless Bodies. *Icarus* **154**, 432–448.

Holsapple K. A. (2009) On the "' strength '" of the small bodies of the solar system : A review of strength theories and their implementation for analyses of impact disruptions. *Planet. Space Sci.* **57**, 127–141.

Holsapple K. A. and Housen K. R. (2007) A crater and its ejecta: An interpretation of Deep Impact. *Icarus* **191**, 586–597.

Holsapple K. A. and Housen K. R. (2012) Momentum transfer in asteroid impacts. I. Theory and scaling. *Icarus* **221**, 875–887.

Holsapple K. A. and Ryan E. (2002) Asteroid Impacts : Laboratory Experiments and Scaling Laws. In *Asteroids III* (eds. W. F. Bottke Jr., A. Cellino, P. Paolicchi, and R. P. Binzel). University of Arizona Press, Tucson. pp. 443–462.

Horstmann M. and Bischoff A. (2014) The Almahata Sitta polymict breccia and the late accretion of asteroid 2008 TC3. *Chemie der Erde - Geochemistry* **74**, 149–183.

Humayun M., Nemchin A., Zanda B., Hewins R. H., Grange M., Kennedy A., Lorand J.-P., Göpel C., Fieni C., Pont S. and Deldicque D. (2013) Origin and age of the earliest Martian crust from meteorite NWA 7533. *Lett. to Nat.* **503**, 513–517.

Hunt G. R. and Ashley R. P. (1979) of Altered Rocks in the Visible and Near Infrared. *Econ. Geol.* **74**, 1613–1629.

Huss G. R., Rubin A. E. and Grossman J. N. (2006) Thermal Metamorphism in Chondrites. *Meteorites early Sol. Syst. II*, 567–586.

Itoh S., Rubin A. E., Kojima H., Wasson J. T. and Yurimoto H. (2002) Amoeboid olivine aggregates and AOA-bearing chondrule from Y-81020 CO 3.0 chondrite:

Distribution of oxygen and magnesium isotopes. *33rd Lunar Planet. Sci. Conf.*, Abstract #1490.

Izawa M. R. M., King P. L., Flemming R. L., Peterson R. C. and McCausland P. J. A. (2010) Mineralogical and spectroscopic investigation of enstatite chondrites by X - ray diffraction and infrared reflectance spectroscopy. *J. Geophys. Res.* **115**, 18.

Jäger C., Molster F. J., Dorschner J., Henning T., Mutschke H. and Waters L. B. F. M. (1998) Steps toward interstellar silicate mineralogy IV. The crystalline revolution. *Astron. Astrophys.* **339**, 904–916.

Jenniskens P., Shaddad M. H., Numan D., Elsir S., Kudoda A. M., Zolensky M. E., Le L., Robinson G., Friedrich J. M., Rumble D., Steele A., Chesley S. R., Fitzsimmons A., Duddy S., Hsieh H. H., Ramsay G., Brown P. G., Edwards W. N., Tagliaferri E., Boslough M. B., Spalding R. E., Dantowitz R., Kozubal M., Pravec P., Borovicka J., Charvat Z., Vaubaillon J., Kuiper J., Albers J., Bishop J. L., Mancinelli R. L., Sandford S. A., Milam S. N., Nuevo M. and Worden S. P. (2009) The impact and recovery of asteroid 2008 TC3. *Nature* **458**, 485–488.

Johnson T. V. and Fanale F. P. (1973) Optical Properties of Carbonaceous Chondrites and Their Relationship to Asteroids. *J. Geophys. Res.* **78**, 8507–8518.

Jones R. H. (2012) Petrographic constraints on the diversity of chondrule reservoirs in the protoplanetary disk. *Meteorit. Planet. Sci.* **47**, 1176–1190.

Jones R. H., Lee T., Connolly Jr. H. C., Love S. G. and Shang H. (2000) Formation of Chondrules and CAIs: Theory VS. Observation. *Protostars planets IV*, 927–962.

Jones R. H., Saxton J. M., Lyon I. C. and Turner G. (1998) Oxygen Isotope Analyses of Chondrule and Isolated Olivine Grains in the CO3 Chondrite, ALHA 77307. *29th Lunar Planet. Sci. Conf.*, Abstract #1795.

Jull A. J. T., Eastoe C. J., Xue S. and Herzog G. F. (1995) Isotopic composition of carbonates in the SNC meteorites Allan Hills 84001 and Nakhla. *Meteoritcs* **30**, 311–318.

Jutzi M. and Michel P. (2014) Hypervelocity impacts on asteroids and momentum transfer I. Numerical simulations using porous targets. *Icarus* **229**, 247–253.

Kallemeyn G. W., Rubin A. E., Wang D. and Wasson J. T. (1989) Ordinary chondrites: Bulk compositions, classification, lithophile-element fractionations and

composition-petrographic type relationships. *Geochim. Cosmochim. Acta* **53**, 2747–2767.

Kallemeyn G. W., Rubin A. E. and Wasson J. T. (1991) The compositional classification of chondrites: V. The Karoonda (CK) group of carbonaceous chondrites. *Geochim. Cosmochim. Acta* **55**, 881–892.

Kallemeyn G. W., Rubin A. E. and Wasson J. T. (1994) The compositional classification of chondrites: VI. The CR carbonaceous chondrite group. *Geochim. Cosmochim. Acta* **58**, 2873–2888.

Kallemeyn G. W. and Wasson J. T. (1981) The compositional classification of chondrites-I. The carbonaceous chondrite groups. *Geochim. Cosmochim. Acta* **45**, 1217–1230.

Keil K. (1968) Mineralogical and chemical relationships among enstatite chondrites. *J. Geophys. Res.* **73**, 6945–6976.

Keil K., Bell J. F. and Britt D. T. (1992) Reflection spectra of shocked ordinary chondrites and their relationship to asteroids. *Icarus* **98**, 43–53.

Keil K., Haack H. and Scott E. R. D. (1994) Catastrophic fragmentation of asteroids: evidence from meteorites. *Planet. Space Sci.* **42**, 1109–1122.

Keil K., Stöffler D., Love S. G. and Scott E. R. D. (1997) Constraints on the role of impact heating and melting in asteroids. *Meteorit. Planet. Sci.* **32**, 349–363.

Kimberley J. and Ramesh K. T. (2011) The dynamic strength of an ordinary chondrite. *Meteorit. Planet. Sci.* **46**, 1653–1669.

Kita N. T., Huss G. R., Tachibana S., Amelin Y., Nyquist L. E. and Hutcheon I. D. (2005) Constraints on the Origin of Chondrules and CAIs from Short- lived and Long-lived Radionuclides. In *Chondrites and the Protoplanetary Disk, ASP Conference Series* (eds. A. N. Krot, E. R. D. Scott, and B. Reipurth). Astronomical Society of the Pacific, San Francisco. pp. 558–587.

Klima R. L., Pieters C. M. and Dyar M. D. (2007) Spectroscopy of synthetic Mg-Fe pyroxenes I : Spin-allowed and spin-forbidden crystal field bands in the visible and near-infrared. *Meteorit. Planet. Sci.* **42**, 235–253.

Koenig J. D. and Chyba C. F. (2007) Impact Deflection of Potentially Hazardous Asteroids Using Current Launch Vehicles. *Sci. Glob. Secur.* **15**, 57–83.

Kohout T., Gritsevich M., Grokhovsky V. I., Yakovlev G. A., Haloda J., Halodova P., Michallik R. M., Penttilä A. and Muinonen K. (2014) Mineralogy, reflectance spectra, and physical properties of the Chelyabinsk LL5 chondrite - Insight into shock-induced changes in asteroid regoliths. *Icarus* **228**, 78–85.

Krause M., Blum J., Skorov Y. V. and Trieloff M. (2011) Thermal conductivity measurements of porous dust aggregates: I. Technique, model and first results. *Icarus* **214**, 286–296.

Kring D. A. and Gleason J. D. (1997) Magmatic temperatures and composition on early Mars as inferred from the orthopyroxene silica assemblage in ALH 84001. *Meteorit. Planet. Sci.* **32**, A74.

Krot A. N., Hutcheon I. D., Yurimoto H., Cuzzi J. N., McKeegan K. D., Scott E. R. D., Libourel G., Chaussidon M., Aléon J. and Petaev M. I. (2005) Evolution of oxygen isotopic composition in the inner solar nebula. *Astrophys. J.* **622**, 1333–1342.

Krot A. N., Meibom A., Weisberg M. K. and Keil K. (2002) The CR chondrite clan: Implications for early solar system processes. *Meteorit. Planet. ...* **37**, 1451–1490.

Krot A. N., Petaev M. I., Russell S. S., Itoh S., Fagan T. J., Yurimoto H., Chizmadia L., Weisberg M. K., Komatsu M., Ulyanov A. A. and Keil K. (2004) Amoeboid olivine aggregates and related objects in carbonaceous chondrites: records of nebular and asteroid processes. *Chemie der Erde* **64**, 185–239.

Laetsch T. A. and Downs R. T. (2006) Software for identification and refinement of cell parameters from powder diffraction data of minerals using the RRUFF Project and American Mineralogist Crystal Structure Databases. *Progr. Abstr. 19th Gen. Meet. Int. Mineral. Assoc.*, 152.

Lafuente B., Downs R. T., Yang H. and Stone N. (2015) The power of databases: the RRUFF project. In *Highlights in Mineralogical Crystallography* (eds. T. Armbuster and R. M. Danisi). De Gruyter, Berlin (Germany). pp. 1–30.

Lamy P. L., Groussin O., Fornasier S., Jorda L., Kaasalainen M. and Barucci M. A. (2010) Thermal properties of asteroid 21 Lutetia from Spitzer Space Telescope observations. *Astron. Astrophys.* **516**, A74.

Lane M. D., Glotch T. D., Dyar M. D., Pieters C. M., Klima R. L., Hiroi T., Bishop J. L. and Sunshine J. M. (2011) Midinfrared spectroscopy of synthetic olivines: Thermal

emission, specular and diffuse reflectance, and attenuated total reflectance studies of forsterite to fayalite. *J. Geophys. Res.* **116**, 20.

Lapen T. J., Righter M., Brandon A. D., Debaille V., Beard B. L., Shafer J. T. and Peslier A. H. (2010) A younger age for ALH 84001 and its geochemical link to shergottite sources in Mars. *Science* **328**, 347–351.

Lazzarin M., Marchi S., Magrin S. and Barbieri C. (2004) Visible spectral properties of asteroid 21 Lutetia , target of Rosetta Mission Letter to the Editor. *Astron. Astrophys.* **425**, L25–L28.

Lazzarin M., Marchi S., Moroz L. V. and Magrin S. (2009) New visible spectra and mineralogical assessment of (21) Lutetia, a target of the Rosetta mission. *Astron. Astrophys.* **498**, 307–311.

Lebofsky L. A. (1978) Asteroid 1 Ceres: evidence for water of hydration. *Mon. Not. R. Astron. Soc.* **182**, 17p–21p.

de León J., Duffard R., Lara L. M. and Lin Z. Y. (2011) Photometric and spectroscopic observations of asteroid (21) Lutetia three months before the Rosetta fly-by⋆(Research Note). *Astron. Astrophys.* **42**, 4–9.

Lewis J. S. (1995) *Physics and Chemistry of the Solar System*., Academic Press, San Diego.

Lim L. F., McConnochie T. H., Bell III J. F. and Hayward T. L. (2005) Thermal infrared (8–13 μm) spectra of 29 asteroids: the Cornell Mid-Infrared Asteroid Spectroscopy (MIDAS) Survey. *Icarus* **173**, 385–408.

Llorca J. and Trigo-Rodríguez J. M. (2004) Raman spectroscopy of merrilite in Villalbeto de la Peña L6 Ordinary Chondrite. *37th Lunar Planet. Sci. Conf.*, Abstract 1055.

Llorca J., Trigo-Rodríguez J. M., Ortiz J. L., Docobo J. A., García-Guinea J., Castro-Tirado A. J., Rubin A. E., Eugster O., Edwards W., Laubenstein M. and Casanova I. (2005) The Villalbeto de la Peña meteorite fall: I. Fireball energy, meteorite recovery, strewn field, and petrography. *Meteorit. Planet. Sci.* **40**, 795–804.

Lu E. T. and Love S. G. (2005) Gravitational tractor for towing asteroids. *Nature* **438**, 177–178.

Machel H. G., Mason R. A., Mariano A. N. and Mucci A. (1991) Causes and emission

of luminescence in calcite and dolomite. In *Luminescence Microscopy and Spectroscopy* (eds. C. E. Barker, R. C. Burruss, O. C. Kopp, H. G. Machel, D. J. Marshall, P. Wright, and H. Y. Colbum). SEPM (Society for Sedimentary Geology), Tulsa, OK. pp. 9–25.

Macke R. J., Consolmagno G. J., Britt D. T. and Hutson M. L. (2010) Enstatite chondrite density, magnetic susceptibility, and porosity. *Meteorit. Planet. Sci.* **45**, 1513–1526.

Macpherson G. J. (2003) Calcium-Aluminum-Rich Inclusions in Chondritic Meteorites. In *Treatise on Geochemistry, Volume 1.* (ed. A. M. Davis). Elsevier. pp. 201–246.

Macpherson G. J. and Russell S. S. (1997) Origin of aluminum-rich chondrules: Constraints from major element chemistry. *Meteorit. Planet. Sci.* **32**, A83.

Macpherson G. J., Wark D. A. and Armstrong J. T. (1988) Primitive material surviving in chondrites - Refractory inclusions. In *Meteorites and the early Solar System* (eds. J. F. Kerridge and M. S. Matthews). University of Arizona Press, Tucson, AZ. pp. 746–807.

Martínez-Jiménez M., Moyano-Cambero C. E., Trigo-Rodríguez J. M., Alonso-Azcárate J. and Llorca J. (2017) Asteroid Mining: Mineral Resources in Undifferentiated Bodies from the Chemical Composition of Carbonaceous Chondrites. In *Assessment and Mitigation of Asteroid Impact Hazards. Astrophysics and Space Science Proceedings, vol 46.* (eds. J. M. Trigo-Rodríguez, M. Gritsevich, and H. Palme). Springer, Cham, Switzerland. pp. 73–101.

Marvin U. B. (1983) The discovery and initial characterization of Allan Hills 81005: The first lunar meteorite. *Geophys. Res. Lett.* **10**, 775–778.

McCord T. B. and Sotin C. (2005) Ceres: Evolution and current state. *J. Geophys. Res.* **110**, 14.

McCoy T. J., Keil K., Bogard D. D., Garrison D. H., Casanova I., Lindstrom M. M., Brearley A. J., Kehm K., Nichols R. H. and Hohenberg C. M. (1995) Origin and history of impact-melt rocks of enstatite chondrite parentage. *Geochim. Cosmochim. Acta* **59**, 161–175.

McCoy T. J., Keil K., Scott E. R. D., Benedix G. K., Ehlmann A. J., Mayeda T. K. and Clayton R. N. (1994) Low-FeO Ordinary Chondrites: A Nebular Origin and New

Chondrite Parent Body. *25th Lunar Planet. Sci. Conf.*, 865–866.

McKay D. S., Gibson E. K., Thomas-Keprta K. L., Vali H., Romanek C. S., Clemett S. J., Chillier X. D., Maechling C. R. and Zare R. N. (1996) Search for past life on Mars: possible relic biogenic activity in martian meteorite ALH84001. *Science* **273**, 924–930.

McKay G. A. and Lofgren G. E. (1997) Carbonates in ALH 84001: Evidence for Kinetically Controlled Growth. *28th Lunar Planet. Sci. Conf.*, Abstract 1799.

McSween H. Y. J. (1994) What we have learned about Mars from SNC meteorites. *Meteoritics* **29**, 757–779.

Melosh H. J. (1984) Impact Ejection, Spallation, and the Origin of Meteorites. *Icarus* **59**, 234–260.

Meyer C. (2012) ALH 84001, Orthopyroxenite, 1931 grams. *Martian Meteor. Compend.*, 23.

Michalski J. R. and Niles P. B. (2010) Deep crustal carbonate rocks exposed by meteor impact on Mars. *Nat. Geosci.* **3**, 751–755.

Michel P., Cheng A. F., Küppers M., Pravec P., Blum J., Delbo M., Green S. F., Rosenblatt P., Tsiganis K., Vincent J.-B., Biele J., Ciarletti V., Hérique A., Ulamec S., Carnelli I., Galvez A., Benner L. A. M., Naidu S. P., Barnouin O. S., Richardson D. C., Rivkin A. S., Scheirich P., Moskovitz N., Thirouin A., Schwartz S. R., Campo Bagatín A. and Yu Y. (2016) Science case for the Asteroid Impact Mission (AIM): A component of the Asteroid Impact & Deflection Assessment (AIDA) Mission. *Adv. Sp. Res.* **57**, 2529–2547.

Michel P., Cheng A. F., Ulamec S. and Team the A. (2015a) Asteroid Impact and Deflection Assessment (AIDA) Mission: Science return and mitigation relevance. *4th IAA Planet. Def. Conf.*, IAA-PDC-15-04-01.

Michel P., Richardson D. C., Durda D. D., Jutzi M. and Asphaug E. I. (2015b) Collisional Formation and Modeling of Asteroid Families. In *Asteroids IV* (eds. P. Michel, F. E. DeMeo, and W. F. Bottke Jr.). University of Arizona Press, Tucson. p. 785.

Milani A., Chesley S., Chodas P. W. and Valsecchi G. B. (2002) Asteroid Close Approaches: Analysis and Potential Impact Detection. In *Asteroids III* pp. 55–69.

Mittlefehldt D. W. (1994) ALH 84001, a cumulate orthopyroxenite member of the Martian meteorite clan. *Meteoritcs* **29**, 214–221.

Mittlefehldt D. W. (1997) Macroscopic Description of Allan Hills 84001 and the Relative Timing of Events in Its History. *Meteorit. Planet. Sci.* **32**, A93.

Miyamoto M. and Ohsumi K. (1995) Micro Raman spectroscopy of olivines in L6 chondrites : Evaluation of the degree of shock. *Geoph* **22**, 437–440.

Montmerle T., Augereau J.-C., Chaussidon M., Gounelle M., Marty B. and Morbidelli A. (2006) Solar System Formation and Early Evolution: the First 100 Million Years. *Earth. Moon. Planets* **98**, 39–95.

Morbidelli A., Levison H. F., Tsiganis K. and Gomes R. (2005) Chaotic capture of Jupiter's Trojan asteroids in the early Solar System. *Nature* **435**, 462–465.

Morbidelli A. and Nesvorný D. (1999) Numerous Weak Resonances Drive Asteroids toward Terrestrial Planets Orbits. *Icarus* **139**, 295–308.

Moreno-Ibáñez M., Gritsevich M. and Trigo-Rodríguez J. M. (2015) New methodology to determine the terminal height of a fireball. *Icarus* **250**, 544–552.

Morlok A., Bischoff A., Stephan T., Floss C., Zinner E. and Jessberger E. K. (2006) Brecciation and chemical heterogeneities of CI chondrites. *Geochim. Cosmochim. Acta* **70**, 5371–5394.

Morlok A., Lisse C. M., Mason A. B., Bullock E. S. and Grady M. M. (2014) Mid-infrared spectroscopy of components in chondrites : Search for processed materials in young Solar Systems and comets. *Icarus* **231**, 338–355.

Morris R. V., Ruff S. W., Gellert R., Ming D. W., Arvidson R. E., Clark B. C., Golden D. C., Siebach K., Klingelhöfer G., Schröder C., Fleischer I., Yen A. S. and Squyres S. W. (2010) Identification of carbonate-rich outcrops on Mars by the Spirit rover. *Science* **329**, 421–424.

Morrison D. (2010) Impacts and Evolution: Protecting Earth from Asteroids. *Proc. Am. Philos. Soc.* **154**, 439–450.

Moyano-Cambero C. E., Nittler L. R., Trigo-Rodríguez J. M., Alexander C. M. O., Davidson J. and Stroud R. M. (2016a) A Space Oddity: A Nanosims Study of a Primitive Ultracarbonaceous Clast and Fine-Grained Matrix in the LaPaz Icefield 02342 CR Chondrite. *47th Lunar Planet. Sci. Conf.*, Abstract 2537.

Moyano-Cambero C. E., Pellicer E., Trigo-Rodríguez J. M., Williams I. P., Blum J., Michel P., Küppers M., Martínez-jiménez M., Lloro I. and Sort J. (2017a) Nanoindenting the Chelyabinsk meteorite to learn about impact deflection effects in asteroids. *Astrophys. J.* **835**, 9.

Moyano-Cambero C. E., Trigo-Rodríguez J. M., Benito M. I., Lee M. R., Mestres N., Martínez-Jiménez M., Martín-Torres F. J. and Fraxedas J. (2017b) Petrographic and geochemical evidence for multiphase formation of carbonates in the Martian orthopyroxenite Allan Hills 84001. *Meteorit. Planet. Sci.*, 1–18.

Moyano-Cambero C. E., Trigo-Rodríguez J. M., Benito M. I., Mestres N. and Alonso-Azcárate J. (2014) Raman Spectroscopy Study of the Carbonate Globules in Allan Hills 84001 to Better Understand their Mineralogy. *45th Lunar Planet. Sci. Conf.*, Abstract 1844.

Moyano-Cambero C. E., Trigo-Rodríguez J. M. and Llorca J. (2013) UV-NIR spectra of the most reflective carbonaceous chondrite groups: CH, CR and R. *44th Lunar Planet. Sci. Conf.*, Abstract 1533.

Moyano-Cambero C. E., Trigo-Rodríguez J. M., Llorca J., Fornasier S., Barucci M. A. and Rimola A. (2016b) A plausible link between the asteroid 21 Lutetia and CH carbonaceous chondrites. *Meteorit. Planet. Sci.* **51**, 1795–1812.

Moyano-Cambero C. E., Trigo-Rodríguez J. M., Pellicer E., Martínez-Jiménez M., Llorca J., Mestres N. and Sort J. (2017c) Chelyabinsk Meteorite as a Proxy for Studying the Properties of Potentially Hazardous Asteroids and Impact Deflection Strategies. In *Assessment and Mitigation of Asteroid Impact Hazards. Proceedings of the 2015 Barcelona Asteroid Day. Astrophysics and Space Science Proceedings, vol 46.* (eds. J. M. Trigo-Rodríguez, M. Gritsevich, and H. Palme). Springer International Publishing, Cham, Switzerland. pp. 219–241.

Mueller M., Harris A. W., Bus S. J., Hora J. L., Kassis M. and Adams J. D. (2006) The size and albedo of Rosetta fly-by target 21 Lutetia from new IRTF measurements and thermal modeling. *Astron. Astrophys.* **447**, 1153–1158.

Nakamura T., Noguchi T., Tanaka M., Zolensky M. E., Kimura M., Tsuchiyama A., Nakato A., Ogami T., Ishida H., Uesugi M., Yada T., Shirai K., Fujimura A., Okazaki R., Sandford S. A., Ishibashi Y., Abe M., Okada T., Ueno M., Mukai T., Yoshikawa M. and Kawaguchi J. (2011) Itokawa dust particles: a direct link

between S-type asteroids and ordinary chondrites. *Science* **333**, 1113–1116.

Nazarov M. A., Badyukov D. D., Kononkova N. N. and Kubrakova I. V. (2013) Chelyabinsk Meteoritical Bulletin: Entry for Chelyabinsk; Available at: http://www.lpi.usra.edu/meteor/metbull.php?code=57165.

Nedelcu D. A., Birlan M., Vernazza P., Descamps P., Binzel R. P., Colas F., Kryszczynska A. and Bus S. J. (2007) Near infra red spectroscopy of the asteroid 21 Lutetia II Rotationally resolved spectroscopy of the surface. *Astron. Astrophys.* **470**, 1157–1164.

Neumann W., Breuer D. and Spohn T. (2012) Differentiation and core formation in accreting planetesimals. *Astron. Astrophys.* **543**, 21.

Neumann W., Breuer D. and Spohn T. (2014) Differentiation of Vesta: Implications for a shallow magma ocean. *Earth Planet. Sci. Lett.* **395**, 267–280.

Niles P. B., Leshin L. A. and Guan Y. (2005) Microscale carbon isotope variability in ALH84001 carbonates and a discussion of possible formation environments. *Geochim. Cosmochim. Acta* **69**, 2931–2944.

Niles P. B., Zolotov M. Y. and Leshin L. A. (2009) Insights into the formation of Fe- and Mg-rich aqueous solutions on early Mars provided by the ALH 84001 carbonates. *Earth Planet. Sci. Lett.* **286**, 122–130.

Niles P. B., Zolotov M. Y. and Leshin L. A. (2006) The role of CO2 in aqueous alteration of ultra-mafic rocks and the formation of Mg-Fe-rich aqueous solutions on early Mars. *37th Lunar Planet. Sci. Conf.*, Abstract #1440.

Nix W. D. and Gao H. J. (1998) Indentation size effects in crystalline materials: A law for strain gradient plasticity. *J. Mech. Phys. Solids* **46**, 411–425.

Nyquist L. E., Bogard D. D., Shih C.-Y., Greshake A., Stöffler D. and Eugster O. (2001) Ages and geologic histories of Martian meteorites. *Space Sci. Rev.* **96**, 105–164.

O'Keefe J. D. and Ahrens T. J. (1985) Impact and explosion crater ejecta, fragment size, and velocity. *Icarus* **62**, 328–338.

Ockert-Bell M. E., Clark B. E., Shepard M. K., Isaacs R. A., Cloutis E. A., Fornasier S. and Bus S. J. (2010) The composition of M-type asteroids : Synthesis of spectroscopic and radar observations. *Icarus* **210**, 674–692.

Ockert-Bell M. E., Clark B. E., Shepard M. K., Rivkin A. S., Binzel R. P., Thomas C. A., Demeo F. E., Bus S. J. and Shah S. (2008) Observations of X / M asteroids across multiple wavelengths. *Icarus* **195**, 206–219.

Ogliore R. C., Huss G. R., Nagashima K., Butterworth A. L., Gainsforth Z., Stodolna J., Westphal A. J., Joswiak D. and Tyliszczak T. (2012) Incorporation of a Late-forming Chondrule into Comet Wild 2. *Astrophys. J. Lett.* **745**, L19–L23.

Oliver W. C. and Pharr G. M. (1992) An improved technique for determining hardness and elastic modulus using load and displacement sensing indentation experiments. *J. Mater. Res.* **7**, 1564–1583.

Osawa T., Kagi H., Nakamura T. and Noguchi T. (2005) Infrared spectroscopic taxonomy for carbonaceous chondrites from speciation of hydrous components. *Meteorit. Planet. Sci.* **40**, 71–86.

Owen T., Biemann K., Rushneck D. R., Biller J. E., Howarth D. W. and Lafleur A. L. (1977) The Composition of the Atmosphere at the Surface of Mars. *J. Geophys. Res.* **82**, 4635–4639.

Ozawa S., Miyahara M., Ohtani E., Koroleva O. N., Ito Y., Litasov K. D. and Pokhilenko N. P. (2014) Jadeite in Chelyabinsk meteorite and the nature of an impact event on its parent body. *Sci. Rep.* **4**, 5033.

Pack A., Yurimoto H. and Palme H. (2004) Petrographic and oxygen-isotopic study of refractory forsterites from R-chondrite Dar al Gani 013 (R3.5-6), unequilibrated ordinary and carbonaceous chondrites. *Geochim. Cosmochim. Acta* **68**, 1135–1157.

Palchik V. and Hatzor Y. H. (2004) The Influence of Porosity on Tensile and Compressive Strength of Porous Chalks. *Rock Mech. Rock Eng.* **37**, 331–341.

Patzold M., Andert T. P., Asmar S. W., Anderson J. D., Barriot J.-P., Bird M. K., Hausler B., Hahn M., Tellmann S., Sierks H., Lamy P. L. and Weiss B. P. (2011) Asteroid 21 Lutetia: Low Mass, High Density. *Science* **334**, 491–492.

Pellicer E., Pané S., Panagiotopoulou V., Fusco S., Sivaraman K. M., Suriñach S., Baró M. D., Nelson B. J. and Sort J. (2012) Localized electrochemical deposition of porous Cu-Ni microcolumns: Insights into the growth mechanisms and the mechanical performance. *Int. J. Electrochem. Sci.* **7**, 4014–4029.

Perna D., Dotto E., Lazzarin M., Magrin S., Fulchignoni M., Barucci M. A., Fornasier S., Marchi S. and Barbieri C. (2010) Inhomogeneities on the surface of 21 Lutetia,

the asteroid target of the Rosetta mission. *Astron. Astrophys.* **513**, 3.

Pieters C. M. and McFadden L. A. (1994) Meteorite and Asteroid Reflectance Spectroscopy: Clues to Early Solar System Processes. *Annu. Rev. Earth Planet. Sci.* **22**, 457–497.

Pieters C. M., Taylor L. A., Noble S. K., Keller L. P., Hapke B. W., Morris R. V., Allen C. C., McKay D. S. and Wentworth S. J. (2000) Space weathering on airless bodies: Resolving a mystery with lunar samples. *Meteorit. Planet. Sci.* **35**, 1101–1107.

Popova O. P., Borovička J., Hartmann W. K., Spurný P., Gnos E., Nemtchinov I. and Trigo-Rodríguez J. M. (2011) Very low strengths of interplanetary meteoroids and small asteroids. *Meteorit. Planet. Sci.* **46**, 1525–1550.

Popova O. P., Jenniskens P., Emel'yanenko V. V., Kartashova A. P., Biryukov E. E., Khaibrakhmanov S., Shuvalov V. V., Rybnov Y., Dudorov A., Grokhovsky V. I., Badyukov D. D., Yin Q.-Z., Gural P. S., Albers J., Granvik M., Evers L. G., Kuiper J., Kharlamov V. A., Solovyov A. and Rusakov Y. S. (2013) Chelyabinsk Airburst, Damage Assessment, Meteorite Recovery, and Characterization. *Science* **342**, 1069–1073.

Reames D. V. (1995) Coronal abundances determined from epnergetic articles. *Adv. Sp. Res.* **15**, 41–51.

Reddy V., Dunn T. L., Thomas C. A., Moskovitz N. A. and Burbine T. H. (2015) Mineralogy and Surface Composition of Asteroids. In *Asteroids IV* (eds. P. Michel, F. E. DeMeo, W. F. Bottke, and R. Dotson). University of Arizona Press, Tucson, AZ. pp. 43–64.

Reddy V., Sanchez J. A., Bottke W. F., Cloutis E. A., Izawa M. R. M., O'Brien D. P., Mann P., Cuddy M., Le Corre L., Gaffey M. J. and Fujihara G. (2014) Chelyabinsk meteorite explains unusual spectral properties of Baptistina Asteroid Family. *Icarus* **237**, 116–130.

Reipurth B. (1990) Fu Orionis eruptions and early stellar evolution. In *Flare stars in star clusters, associations and the solar vicinity* (ed. L. V. Mirzoyan). Kluwer Academic Publishers, Dordrecht, Netherlands. pp. 229–251.

Reipurth B. (2005) The Early Sun: Evolution and Dynamic Environment. In *Chondrites*

and the Protoplanetary Disk, ASP Conference Series pp. 1–24.

Righter K., Abell P. A., Agresti D., Berger E. L., Burton A. S., Delaney J. S., Fries M. D., Gibson E. K., Haba M. K., Harrington R., Herzog G. F., Keller L. P., Locke D., Lindsay F. N., McCoy T. J., Morris R. V., Nagao K., Nakamura-Messenger K., Niles P. B., Nyquist L. E., Park J., Peng Z. X., Shih C.-Y., Simon J. I., Swisher C. C., Tappa M. J., Turrin B. D. and Zeigler R. A. (2015) Mineralogy, petrology, chronology, and exposure history of the Chelyabinsk meteorite and parent body. *Meteorit. Planet. Sci.* **50**, 1790–1819.

Rimstidt J. D., Balog A. and Webb J. (1998) Distribution of trace elements between carbonate minerals and aqueous solutions. *Geochim. Cosmochim. Acta* **62**, 1851–1863.

Rivkin A. S., Clark B. E. and Ockert-Bell M. E. (2011) Observations of 21 Lutetia in the 2-4 Mm Region With the Nasa Irtf. In *42nd Lunar and Planetary Science Conference* p. Abstract 1439.

Rivkin A. S., Howell E. S., Vilas F. and Lebofsky L. A. (2002) Hydrated Minerals on Asteroids: The Astronomical Record. In *Asteroids III* (eds. W. F. Bottke, A. Cellino, P. Paolicchi, and R. P. Binzel). University of Arizona Press, Tucson. pp. 235–253.

Rosenberg P. E. (1967) Subsolidus relations in the system CaCO3-MgCO3-FeCO3 between 350degree and 550degree. *Am. Mineral.* **52**, 787–796.

Rotelli L., Trigo-Rodríguez J. M., Moyano-Cambero C. E., Carota E., Botta L., Di Mauro E. and Saladino R. (2016) The key role of meteorites in the formation of relevant prebiotic molecules in a formamide/water environment. *Nature, Sci. Reports* **6**, 7.

Rubin A. E. (2003) Chromite-plagioclase assemblages as a new shock indicator; Implications for the shock and thermal histories of ordinary chondrites. *Geochim. Cosmochim. Acta* **67**, 2695–2709.

Rubin A. E. (1998) Correlated petrologic and geochemical characteristics of CO3 chondrites. *Meteorit. Planet. Sci.* **33**, 385–391.

Rubin A. E. (2011) Origin of the differences in refractory-lithophile-element abundances among chondrite groups. *Icarus* **213**, 547–558.

Rubin A. E. (2000) Petrologic, geochemical and experimental constraints on models of

chondrule formation. *Earth-Science Rev.* **50**, 3–27.

Rubin A. E. (2010) Physical properties of chondrules in different chondrite groups: Implications for multiple melting events in dusty environments. *Geochim. Cosmochim. Acta* **74**, 4807–4828.

Rubin A. E. and Brearley A. J. (1996) A Critical Evaluation of the Evidence for Hot Accretion. *Icarus* **124**, 86–96.

Rubin A. E., Kallemeyn G. W., Wasson J. T., Clayton R. N., Mayeda T. K., Grady M. M., Verchovsky A. B., Eugster O. and Lorenzetti S. (2003) Formation of metal and silicate globules in Gujba: A new Bencubbin-like meteorite fall. *Form. Met. Silic. Globul. Gujba A new Bencubbin-like Meteor. fall* **67**, 3283–3298.

Rubin A. E. and Krot A. N. (1996) Multiple heating of chondrules. In *Chondrules and the Protoplanetary Disk* (eds. R. H. Hewins, R. H. Jones, and E. R. D. Scott). Cambridge University Press, Cambridge. pp. 173–180.

Rubin A. E., Trigo-Rodríguez J. M., Huber H. and Wasson J. T. (2007) Progressive aqueous alteration of CM carbonaceous chondrites. *Geochim. Cosmochim. Acta* **71**, 2361–2382.

Ruzicka A., Grossman J. N., Bouvier A., Herd C. D. K. and Agee C. B. (2015) The Meteoritical Bulletin, No. 102. **50**, 1–248.

Sahagian D. L. and Hewins R. H. (1992) The size of chondrule-forming events. *23rd Lunar Planet. Sci. Conf.*, Abstract #1197.

Salisbury J. W. (1993) Mid-infrared spectroscopy: Laboratory data. In *Remote Geochemical Analysis: Elemental and Mineralogical Composiotion* (eds. C. M. Pieters and P. A. J. Englert). Cambridge University Press, New York. pp. 79–98.

Sandford S. A., Allamandola L. J., Tielens A. G. G. M., Sellgren K., Tapia M. and Pendleton Y. (1991) The interestellar C-H stretching band near 3.4 microns: constraints on the composition of organic material in the diffuse interestellar medium. *Astron. J.* **371**, 607–620.

Saxton J. M., Lyon I. C. and Turner G. (1998) Correlated chemical and isotopic zoning in carbonates in the Martian meteorite ALH84001. *Earth Planet. Sci. Lett.* **160**, 811–822.

Van Schmus W. R. and Wood J. A. (1967) A chemical-petrologic classification for the

chondritic meteorites. *Geochim. Cosmochim. Acta* **31**, 747–765.

Schultz R. A. (1993) Brittle Strength of Basaltic Rock Masses with Applications to Venus. *J. Geophys. Res.* **98**, 10883–10895.

Schwandt C. S., McKay G. A. and Lofgren G. E. (1999) FESEM imaging reveals previously unseen detail and enhances interpretations of ALH84001 carbonate petrogenesis. *30th Lunar Planet. Sci. Conf.*, Abstract #1346.

Score R. and Macpherson G. J. (1985) Macroscopic and thin section description of ALH 84001. *Meteor. Newsl.* **8**, 5.

Scott E. R. D. and Krot A. N. (2003) Chondrites and Their Components. In *Treatise on Geochemistry* (ed. A. M. Davis). Elsevier, Amsterdam, Netherlands. pp. 143–200.

Scott E. R. D. and Krot A. N. (2005) Chondritic meteorites and the high-temperature nebular origins of their components. *Chondrites protoplanetary Disk - ASP Conf. Ser. Vol. 341* **341**, 15–53.

Scott E. R. D., Krot A. N. and Yamaguchi A. (1998) Carbonates in fractures of Martian meteorite Allan Hills 84001 : Petrologic evidence for impact origin. *Meteorit. Planet. Sci. Planet. Sci.* **33**, 709–719.

Scott E. R. D., Yamaguchi A. and Krot A. N. (1997) Petrological evidence for shock melting of carbonates in the martian meteorite ALH84001. *Nature* **387**, 377–379.

Sears D. W. G., Grossman J. N., Melcher C. L., Ross L. M. and Mills A. A. (1980) Measuring metamorphic history of unequilibrated ordinary chondrites. *Nature* **287**, 791–795.

Shepard M. K., Clark B. E., Nolan M. C., Howell E. S., Magri C., Giorgini J. D., Benner L. A. M., Ostro S. J., Harris A. W., Warner B. D., Pray D. P., Pravec P., Fauerbach M., Bennett T., Klotz A., Behrend R., Correia H., Coloma J., Casulli S. and Rivkin A. S. (2008) A radar survey of M- and X-class asteroids. *Icarus* **195**, 184–205.

Shepard M. K., Clark B. E., Ockert-Bell M. E., Nolan M. C., Howell E. S., Magri C., Giorgini J. D., Benner L. A. M., Ostro S. J., Harris A. W., Warner B. D., Stephens R. D. and Mueller M. (2010) A radar survey of M- and X-class asteroids II. Summary and synthesis. *Icarus* **208**, 221–237.

Shu F. H., Najita J. R., Shang H. and Li Z.-Y. (2000) X-winds: theory and observations.

In *Protostars and planets IV* (ed. V. Mannings). University of Arizona Press, Tucson, AZ. pp. 789–813.

Shu F. H., Shang H., Glassgold A. E. and Lee T. (1997) X-rays and Fluctuating X-Winds from Protostars. *Science* **277**, 1475–1479.

Shu F. H., Shang H., Gounelle M., Glassgold A. E. and Lee T. (2001) The origin of chondrules and refractory inclusions in chondritic meteorites. *Astrophys. J.* **548**, 1029–1050.

Sierks H., Lamy P. L., Barbieri C., Koschny D., Rickman H., Rodrigo R., A'Hearn M. F., Angrilli F., Barucci M. A., Bertaux J.-L., Bertini I., Besse S., Carry B., Cremonese G., Da Deppo V., Davidsson B., Debei S., De Cecco M., De León J., Ferri F., Fornasier S., Fulle M., Hviid S. F., Gaskell R. W., Groussin O., Gutierrez P., Ip W.-H., Jorda L., Kaasalainen M., Keller H. U., Knollenberg J., Kramm R., Kührt E., Küppers M., Lara L. M., Lazzarin M., Leyrat C., Lopez Moreno J. J., Magrin S., Marchi S., Marzari F., Massironi M., Michalik H., Moissl R., Naletto G., Preusker F., Sabau L., Sabolo W., Scholten F., Snodgrass C., Thomas N., Tubiana C., Vernazza P., Vincent J.-B., Wenzel K.-P., Andert T. P., Pätzold M. and Weiss B. P. (2011) Images of asteroid 21 Lutetia: a remnant planetesimal from the early Solar System. *Science* **334**, 487–490.

Steele A., Fries M. D., Amundsen H. E. F., Mysen B. O., Fogel M. L., Schweizer M. and Boctor N. Z. (2007) Comprehensive imaging and Raman spectroscopy of carbonate globules from Martian meteorite ALH 84001 and a terrestrial analogue from Svalbard. *Meteorit. Planet. Sci.* **42**, 1549–1566.

Stöffler D., Keil K. and Scott E. R. D. (1991) Shock metamorphism of ordinary chondrites. *Geochim. Cosmochim. Acta* **55**, 3845–3867.

Subhash G., Koeppel B. J. and Chandra A. (1999) Dynamic indentation hardness and rate sensitivity in metals. *J. Eng. Mater. Technol.* **121**, 257–263.

Sugiura N. (2000) Petrographic evidence for in-situ hydration of the CH chondrite PCA 91467. *31st Lunar Planet. Sci. Conf.*, Abstract #1503.

Tholen D. J. (1989) Asteroid taxonomic classifications. In *Asteroids II* (eds. R. P. Binzel, T. Gehrels, and M. S. Matthews). University of Arizona Press, Tucson, AZ. pp. 1139–1150.

Tomkinson T., Lee M. R., Mark D. F. and Smith C. L. (2013) Sequestration of Martian CO2 by mineral carbonation. *Nat. Commun.* **4**, 1–6.

Treiman A. H. (1995) A petrographic history of Martian meteorite ALH 84001: Two shocks and an ancient age. *Meteoritcs* **30**, 294–302.

Treiman A. H. (1998) The history of Allan Hills 84001 revised: Multiple shock events. *Meteorites early Sol. Syst. II* **33**, 753–764.

Treiman A. H., Amundsen H. E. F., Blake D. F. and Bunch T. E. (2002) Hydrothermal origin for carbonate globules in Martian meteorite ALH84001: A terrestrial analogue from Spitsbergen (Norway). *Earth Planet. Sci. Lett.* **204**, 323–332.

Treiman A. H., Gleason J. D. and Bogard D. D. (2000) The SNC meteorites are from Mars. *Planet. Space Sci.* **48**, 1213–1230.

Trigo-Rodríguez J. M. and Blum J. (2009) Tensile strength as an indicator of the degree of primitiveness of undifferentiated bodies. *Planet. Space Sci.* **57**, 243–249.

Trigo-Rodríguez J. M., Llorca J., Alonso-Azcárate J., Rivkin A. S., Fornasier S., Belskaya I., Binzel R. P., Moyano-Cambero C. E., Dergham J. and Cortés-Comellas J. (2012) IR reflectance spectra of antarctic carbonaceous chondrites to better characterize the surfaces of asteroids targetted by sample return missions. *43rd Lunar Planet. Sci. Conf.*, Abstract #1443.

Trigo-Rodríguez J. M., Lyytinen E., Gritsevich M., Moreno-Ibáñez M., Bottke W. F., Williams I. P., Lupovka V., Dmitriev V., Kohout T. and Grokhovsky V. I. (2015) Orbit and dynamic origin of the recently recovered Annama's H5 chondrite. *Mon. Not. R. Astron. Soc.* **449**, 2119–2127.

Trigo-Rodríguez J. M., Lyytinen E., Jones D. C., Madiedo J. M., Castro-Tirado A. J., Williams I. P., Llorca J., Vítek S., Jelínek M., Troughton B. and Gálvez F. (2007) Asteroid 2002NY40 as a source of meteorite-dropping bolides. *Mon. Not. R. Astron. Soc.* **382**, 1933–1939.

Trigo-Rodríguez J. M., Moyano-Cambero C. E., Llorca J., Fornasier S., Barucci M. A., Belskaya I., Martins Z., Rivkin A. S., Dotto E., Madiedo J. M. and Alonso-Azcárate J. (2014a) UV to far-IR reflectance spectra of carbonaceous chondrites - I. Implications for remote characterization of dark primitive asteroids targeted by sample-return missions. *Mon. Not. R. Astron. Soc.* **437**, 227–240.

Trigo-Rodríguez J. M., Moyano-Cambero C. E., Mestres N. and Bischoff A. (2014b) A

Raman Study of Chelyabinsk LL5-6 Chondrite Breccia: Investigating the Signatures of Shock-Induced Melting in Near-Earth Asteroids. *45th Lunar Planet. Sci. Conf.*, Abstract 1729.

Trigo-Rodríguez J. M. and Williams I. P. (2017) Dynamic sources of contemporary hazard from meteoroids and small asteroids. In *Assessment and Mitigation of Asteroid Impact Hazard* (eds. J. M. Trigo-Rodríguez, M. Gritsevich, and H. Palme). Springer, New York. pp. 1–9.

Tsiganis K., Gomes R., Morbidelli A. and Levison H. F. (2005) Origin of the orbital architecture of the giant planets of the Solar System. *Nature* **435**, 459–461.

Valley J. W., Eiler J. M., Graham C. M., Gibson E. K., Romanek C. S. and Stolper E. M. (1997) Low-temperature carbonate concretions in the Martian meteorite ALH84001: evidence from stable isotopes and mineralogy. *Science* **275**, 1633–1638.

Vernazza P., Binzel R. P., Thomas C. A., DeMeo F. E., Bus S. J., Rivkin A. S. and Tokunaga A. T. (2008) Compositional differences between meteorites and near-Earth asteroids. *Nature* **454**, 858–860.

Vernazza P., Lamy P. L., Groussin O., Hiroi T., Jorda L., King P. L., Izawa M. R. M., Marchis F., Birlan M. and Brunetto R. (2011) Asteroid (21) Lutetia as a remnant of Earth's precursor planetesimals. *Icarus* **216**, 650–659.

Vilas F. and Gaffey M. J. (1989) Phyllosilicate absorption features in main-belt and outer-belt asteroid reflectance spectra. *Science* **246**, 790–2.

Wachs I. E. and Routray K. (2012) Catalysis science of bulk mixed oxides. *ACS Catal.* **2**, 1235–1246.

Walker J. D. and Chocron S. (2015) Damage Modeling , Scaling and Momentum Enhancement for Asteroid and Comet Nucleus Deflection. *Procedia Eng.* **103**, 636–641.

Walsh K. J. and Richardson D. C. (2006) Binary near-Earth asteroid formation: Rubble pile model of tidal disruptions. *Icarus* **180**, 201–216.

Warren P. H. (1998) Petrologic Evidence for Low-Temperature, Possible Flood-Evaporitic origin of Carbonates in the ALH 84001 Meterorite. *61st Annu. Meteorit. Soc. Meet.*, Abstract #5204.

Wasson J. T. (1993) Constraints on chondrule origins. *Meteoritics* **28**, 14–28.

Wasson J. T. (2003) Large Aerial Bursts: An Important Class of Terrestrial Accretionary Events. *Astrobiology* **3**, 163–179.

Wasson J. T. (1985) *Meteorites: Their record of early solar-system history*., W H Freeman & Co (Sd), New York.

Wasson J. T., Isa J. and Rubin A. E. (2013) Compositional and petrographic similarities of CV and CK chondrites: A single group with variations in textures and volatile concentrations attributable to impact heating, crushing and oxidation. *Geochim. Cosmochim. Acta* **108**, 45–62.

Wasson J. T. and Kallemeyn G. W. (1990) Allan Hills 85085: A subchondritic meteorite of mixed nebular and regolithic heritage. *Earth* **101**, 148–161.

Wasson J. T., Krot A. N., Lee M. S. and Rubin A. E. (1995) Compound chondrules. *Geochim. Cosmochim. Acta* **59**, 1847–1869.

Weaver H. A., Feldman P. D., Merline W. J., Mutchler M. J., A'Hearn M. F., Bertaux J.-L., Feaga L. M., Parker J. W., Slater D. C., Steffl A. J., Chapman C. R., Drummond J. D. and Stern S. A. (2010) Ultraviolet and visible photometry of asteroid (21) Lutetia using the Hubble Space Telescope. *Astron. Astrophys.* **518**, 14.

Weidenschilling S. J. and Cuzzi J. N. (1993) Formation of planetesimals in the solar nebula. In *Protostars and planets III* (eds. E. H. Levy and J. I. Lunine). University of Arizona Press, Tucson, AZ. pp. 1031–1060.

Weisberg M. K., McCoy T. J. and Krot A. N. (2006) Systematics and Evaluation of Meteorite Classification. *Meteorites early Sol. Syst. II*, 19–52.

Weisberg M. K., Prinz M., Clayton R. N. and Mayeda T. K. (1997) CV3 chondrites: Three subgroups not two. *Meteorit. Planet. Sci.* **32**, A138–A139.

Weisberg M. K., Prinz M., Clayton R. N., Mayeda T. K., Sugiura N., Zashu S. and Ebihara M. (2001) A new metal-rich chondrite grouplet. *Meteorit. Planet. Sci.* **36**, 401–418.

Weiss B. P., Elkins-Tanton L., Barucci M. A., Sierks H., Snodgrass C., Vincent J.-B., Marchi S., Weissman P. R., Pätzold M., Richter I., Fulchignoni M., Binzel R. P. and Schulz R. (2012) Possible evidence for partial differentiation of asteroid

Lutetia from Rosetta. *Planet. Space Sci.* **66**, 137–146.

Weiss B. P., Vali H., Baudenbacher F. J., Kirschvink J. L., Stewart S. T. and Shuster D. L. (2002) Records of an ancient Martian magnetic field in ALH84001. *Earth Planet. Sci. Lett.* **201**, 449–463.

Weissman P. R., Hicks M. D., Abell P. A., Choi Y.-J. and Lowry S. C. (2008) Rosetta target asteroid 2867 Steins: An unusual E-type asteroid. *Meteorit. Planet. Sci.* **914**, 905–914.

Wheeler J. M. (2009) Nanoindentation under Dynamic Conditions. .

Williams J. P. (2010) The Astrophysical Environment of the Solar Birthplace. *Contemp. Phys.* **51**, 18.

Williams J. P. and Cieza L. A. (2011) Protoplanetary Disks and Their Evolution. *Annu. Rev. Astron. Astrophys.* **49**, 67.

Woolfson M. (2000) The origin and evolution of the Solar System. *Astron. Geophys.* **41**, 1.12-1.19.

Wray J. J., Murchie S. L., Ehlmann B. L., Milliken R. E., Seelos K. D., Noe Dobrea E. Z., Mustard J. F. and Squyres S. W. (2011) Evidence for Regional Deeply Buried Carbonate-Bearing Rocks on Mars. *Lunar Planet. Inst. Sci. Conf. Abstr.* **42**, 2635.

Wurm G. and Blum J. (1998) Experiments on Preplanetary Dust Aggregation. *Icarus* **132**, 125–136.

Wurm G., Paraskov G. and Krauss O. (2005) Growth of planetesimals by impacts at ~25 m/s. *Icarus* **178**, 253–263.

Wurm G., Paraskov G. and Krauss O. (2004) On the Importance of Gas Flow through Porous Bodies for the Formation of Planetesimals. *Astrophys. J.* **606**, 983–987.

Xie X., Chen M., Dai C., El Goresy A. and Gillet P. (2001) A comparative study of naturally and experimentally shocked chondrites. *Earth Planet. Sci. Lett.* **187**, 345–356.

Xie X., Minitti M. E., Chen M., Mao H. K., Wang D., Shu J. and Fei Y. (2002) Natural high-pressure polymorph of merrillite in the shock veins of the Suizhou meteorite. *Geochim. Cosmochim. Acta* **66**, 2439–2444.

Yomogida K. and Matsui T. (1984) Multiple parent bodies of ordinary chondrites. *Earth*

Planet. Sci. Lett. **68**, 34–42.

Yomogida K. and Matsui T. (1983) Physical Properties of Ordinary Chondrites. *J. Geophys. Res.* **88**, 9513–9533.

Zaikowski A., Knacke R. F. and Porco C. C. (1975) On the presence of phyllosilicate minerals in the interestellar grains. *Astrophys. Space Sci.* **37**, 97–115.

Zellner B. (1979) Asteroid taxonomy and the distribution of the compositional types. In *Asteroids* (ed. T. Gehrels). University of Arizona Press, Tucson, AZ. pp. 783–806.

Zhang P., Li S. X. and Zhang Z. F. (2011) General relationship between strength and hardness. *Mater. Sci. Eng. A* **529**, 62–73.

Zolensky M. E., Bland P. A., Brown P. G. and Halliday I. (2006) Flux of Extraterrestrial Materials. In *Meteorites and the Early Solar System II* (eds. D. S. Lauretta and H. Y. J. McSween). University of Arizona Press, Tucson, AZ. pp. 869–888.

Zolensky M. E., Herrin J., Mikouchi T., Ohsumi K., Friedrich J. M., Steele A., Rumble D., Fries M. D., Sandford S. A., Milam S., Hagiya K., Takeda H., Satake W., Kurihara T., Colbert M., Hanna R., Maisano J., Ketcham R., Goodrich C. A., Le L., Robinson G., Martinez J., Ross K., Jenniskens P. and Shaddad M. H. (2010) Mineralogy and petrography of the Almahata Sitta ureilite. *Meteorit. Planet. Sci.* **45**, 1618–1637.

Zolensky M. E. and Ivanov A. (2003) The Kaidun Microbreccia Meteorite: A Harvest from the Inner and Outer Asteroid Belt. *Chemie der Erde - Geochemistry* **63**, 185–246.

Zolensky M. E., Mittlefehldt D. W., Lipschutz M. E., Wang M.-S., Clayton R. N., Mayeda T. K., Grady M. M., Pillinger C. T. and Barber D. J. (1997) CM chondrites exhibit the complete petrologic range from type 2 to 1. *Geochim. Cosmochim. Acta* **61**, 5099–5115.

Zolensky M. E., Weisberg M. K., Buchanan P. C. and Mittlefehldt D. W. (1996) Mineralogy of carbonaceous chondrite clasts in HED achondrites and the Moon. *Meteorit. Planet. Sci.* **31**, 518–537.

9 APPENDIX

9.1 Glossary

Accessory mineral: Any mineral that is present in small amounts in a rock, but is not considered to be characetristic of such rock.

Albite (Ab, for short): A *plagioclase feldspar* mineral, sodium-rich endmemeber of the *plagioclase* solid solution. Pure *albite* has the formula $NaAlSi_3O_8$.

Aliphatic compounds: Hydrocarbons that do not form the especially stable rings of atoms that can be found in aromatic compounds. Methane and butane are examples of *aliphatic* compounds.

Amorphous mineral: A mineral with no definite *crystalline* structure.

Anhedral: A mineral grain that has no well-formed *crystal* faces. Ir ocurs in a competitive environment with no free space for the formation of *crystal* faces.

Anhydrous: A substance containing no water.

Ankerite: A *carbonate* of the group of rhombohedral *carbonates* with formula $Ca(Fe,Mg,Mn)(CO_3)_2$. Closely related to *dolomite*.

Anorthite (An, for short): A *plagioclase feldspar* mineral, calcium-rich endmemeber of the *plagioclase* solid solution. Pure *anorthite* has the formula $CaAl_2Si_2O_8$.

Augite: A very common *clinopyroxene* mineral in *mafic igneous* rocks with formula $(Ca,Na)\ (Mg,Fe,Al,Ti)(Si,Al)_2O_6$.

Apatite: A group of *phosphate* minerals with high concentrations of OH^-, F^- and Cl^-

ions, and with general formula $Ca_{10}(PO_4)_6(OH,F,Cl)_2$.

Basalt: Dark-coloured *mafic igneous* rocks, mostly composed of calcic *plagioclase* and *clinopyroxene*.

Bremsstrahlung effect: Electromagnetic radiation produced by deceleration of a charged particle when deflected by another charged particle, typically an electron by an atomic nucleus. The moving particle loses kinetic energy, which is converted into a photon to satisfy the law of conservation of energy.

Calcite: A common rock-forming *carbonate* mineral with a perfect rhombohedral cleavage, and general formula $CaCO_3$.

Carbonate: Minerals and rocks dominated by the *carbonate* polyatomic ion CO_3^{2-}. This salts of carbonic acid (H_2CO_3) are extremely varied and ubiquitous in chemically precipitated *sedimentary* rocks.

Chlorite: A *phyllosilicate* compound containing the chlorine dioxide anion ClO_2^-, and with general formula $(Mg,Fe)_3(Si,Al)_4O_{10}(OH)_2 \cdot (Mg,Fe)_3(OH)_6$.

Chromite: A mineral of the *spinel* group of general formula $(Fe,Mg)(Cr,Al)_2O_4$. The iron and magnesium endmembers are $FeCr_2O_4$ and $MgCr_2O_4$. When Al substitutes Cr, it is called hercynite: $FeAl_2O_4$

Chrysotile: Soft, fibrous *silicate* mineral in the *serpentine* subgroup of *phyllosilicates*, with idealized formula $Mg_3(Si_2O_5)(OH)_4$.

Clinopyroxene: A group name for *pyroxenes crystallizing* in the monoclinic system and usually containing Ca or Na.

Cryptocrystalline: A rock texture defined by small *crystals* that are only vaguely revealed under a microscope in thin section with polarized light.

Crystal, crystalline: Solid material whose constituents are arranged in a highly ordered microscopic structure, with single *crystals* showing geometrical shapes and flat faces with specific orentations.

Cumulate rock: An *igneous* rock formed by the accumulation of *crystals* that settle out from a magma by the action of gravity. They are named according to their texture, which is diagnostic of the conditions of formation of this rocks.

Diopside: A *clinopyroxene* mineral with composition $MgCaSi_2O_6$. It is found in *mafic igneous rocks*, but also in a variety of *metamorphic* rocks.

Dolomite: An *anhydrous carbonate* mineral with ideal formula $CaMg(CO_3)_2$.

Dunite: A coarse-grained *igneous* rock *anhedrally crystallized* from slowly cooling magma at great depth below the surface, and composed mainly of *olivine*, with *accessory chromite*.

Elastic recovery: A measure of the ability of a material to return to its orignal shape when a load applied to it is removed.

Enstatite (En, for short): A common rock-forming mineral of the *orthopyroxene* group and general formula $MgSiO_3$.

Euhedral: A mineral grain completely bounded by its own well-formed, easily recognised faces, and whose growth was not interfered by adjacent grains, because was formed in a cavity or early in the *crystallization* of magma.

Fayalite (Fa, for short): The Fe-rich endmember of the *olivine* solid-solutions series, with ideal composition Fe_2SiO_4.

Feldspar: The most widespread rock-forming mineral in rocky planets, which *crystallizes* from magma as veins in *igneous* rocks, and also present in *metamorphic* rocks. Its general formula is $XAl(Al,Si)_3O_8$, where X is commonly K, Na or Ca.

Ferrosilite (Fs, for short): A common rock-forming mineral of the *orthopyroxene* group and general formula $FeSiO_3$.

Forsterite (Fo, for short): The Mg-rich endmember of the *olivine* solid-solutions series, with ideal composition Mg_2SiO_4.

Fracture toughness: A property describing the ability of a material containing cracks to resist fracture.

Fusion crust: A *glassy* thin layer produced by the cooling of viscous minerals produced by the ablation of a meteorite during its deceleration in the atmosphere of a planet, and with a typical thickness of less than a millimeter.

Genomict breccia: Meteorite breccia formed by materials of the same compositional group, but with different petrographic type or alteration history.

Glass: A non-*crystalline amorphous* solid.

Hardness: A measure of how resistant is solid matter to various kinds of permanent

shape change after applying a compressive force.

Hematite: The mineral form of Fe^{3+} oxide, with general formula Fe_2O_3.

Igneous rock: Also called magmatic rocks, they solidified from molten or partly molten material, such as magma or lava, below (intrusive) or above (extrusive) the surface.

Ilmenite: A titanium-iron oxide mineral with idealized formula $FeTiO_3$.

Jadeite: A *clinopyroxene* mineral with composition $NaAlSi_2O_6$. It is formed in *metamorphic* rocks in relatively low temperature conditions when applying high pressure on *pyroxene albite*.

Kamacite: An alloy of iron and nickel (NiFe) only found on meteorites, with a proportion of iron-nickel between 90-10 and 95-5, and small quantities of other elements, such as cobalt or carbon. It is some times intermixed with *taenite*.

Late Heavy Bombardment: Event though to have ocurred 4.1-3.8 Gyr ago, which implied a large number of asteroids colliding with the early terrestrial planets of the Inner Solar System, i.e., Mercury, Venus, Earth (and the Moon), and Mars, after they had already accreted most of its mass. It is consistent with the Nice model and evidence found on lunar samples brought back by the Apollo missions.

Lithic: Pieces of rocks eroded to sand size and included in *sedimentary* rocks.

Lithified: Said of the sediments compacted under pressure in a process that destroys porosities, gradually forming a solid rock.

Lithology: Description of the physical characteristics, such as colour, texture, grain size and composition, of a rock unit. It is commonly used to subdivide a rock into parts with differences in their formation or evolution processes.

Lithophile element: Elements that remain on or close to the surface because they combine readily with oxygen, forming compounds that do not sink into the core. Mainly consist in highly reactive metals which form very stable ions.

Lizardite: *Silicate* mineral in the *serpentine* subgroup of *phyllosilicates*, with idealized formula $Mg_3(Si_2O_5)(OH)_4$, closely related to *chrysotile*.

Mafic: Said of a *silicate* or *igneous* rock mainly composed of one or more Fe- and Mg-rich minerals, such as *olivine* or *pyroxene*.

Magnesite: A *carbonate* of the rhombohedral group with formula $MgCO_3$.

Magnetite: An strongly magnetic iron oxide of the *spinel* group, with general formula Fe_3O_4, and ocurring naturally in most *igneous* and *metamorphic* rocks.

Maskelynite: A common *noncrystalline* mineral in meteorites formed by *plagioclase glass* modified by the effect of shock, and retaining the external features of *crystalline plagioclase*.

Matrix: The finer-grained material enclosing or filling the interstices between the larger grains or particles of a *sedimentary* rock, or a meteorite.

Melilite: A *silicate* mineral with general formula $(Ca, Na)_2(Al, Mg, Fe^{2+})[(Al, Si)SiO_7]$.

Merrillite: An unusual form of calcium *phosphate* with general formula $Ca_9(Mg,Fe^{2+})(PO_4)_6(PO_3OH)$, and relatively common in chondritic meteorites.

Metamorphic rock: A rock transformed by the combined effect of heat and pressure, with profound physical and/or chemical changes.

Mosaicism: A microscopic form of shock *metamorphism* which appears as an irregular mottled optical extinction pattern.

Oldhamite: An *accessory* calcium magnesium *sulfide* mineral in meteorites with general formula (Ca, Mg)S, although it may contain ferrous iron.

Olivine: A magnesium iron *silicate* mineral with general formula $(Mg,Fe)_2SiO_4$. It forms the solid-solution series of *forsterite* (Mg-rich endmember) and *fayalite* (Fe-rich endmember). Its composition is commonly expressed as molar percentatges of *forsterite* (Fo) and *fayalite* (Fa).

Olivine-phyric: An *olivine* formed by large *crystals* in a *porphyritic* way.

Orthopyroxene: A group of low-Ca, Fe- and Mg-rich *pyroxenes crystallizing* in the orthorhombic system. Most are in the solid-solution series of *enstatite* (Mg-rich endmember) and *ferrosilite* (Fe-rich endmember), and therefore its composition is commonly expressed as molar percentatges of *enstatite* (En) and *ferrosilite* (Fs).

Phosphate: A mineral compound containing the *phosphate* polyatomic ion PO_4^{3-}, and usually being derivates of phosphoric acid (H_3PO_4).

Plagioclase: A group of *silicate feldspars* of general formula: $(Na,Ca)Al(Si,Al)Si_2O_8$. They form the solid-solution series of *albite* (Na-rich endmember) and *anorthite* (Ca-rich endmember). Their composition is commonly expressed as molar

percentatges of *albite* (Ab) and *anorthite* (An).

Polymict breccia: Meteorite breccia formed by materials of various types, with clasts and/or matrix showing different compositions.

Porphyritic: Said of the texture of a rock in which larger *crystals* are set in a finer-grained groundmass, which may be *crystalline*, or *glassy* or both.

Protostar: A star in the earliest phase of stellar evolution, still gathering mass from its parent molecular cloud.

Pyrite: A very common *sulfide* mineral with general formula FeS_2, usually associated with other *sulfides* or oxides.

Pyroxene: A common group of mantle rock-forming *silicate* minerals, closely related in *crystal* form and composition and having the general formula $XYSi_2O_6$, where X can be Ca, Na, Mg or Fe^{+2}, and Y is typically Mg, Fe^{+2}, Fe^{+3}, Fe, Cr, Mn or Al, and with Al ocasionally substituing Si. They *crystallize* in the monoclinic (*clinopyroxenes*) and orthorhombic (*orthopyroxenes*) systems.

Pyrrhotite: A common iron *sulfide* mineral with some lacking ferrous iron and general formula $Fe_{1-x}S$ (with x between 0 and 0.2). It is a magnetic variant of *troilite*.

Refractory: A material chemically and physically stable at high temperatures, and therefore with a high melting point.

Ringwoodite: A high-pressure phase of *forsterite* formed at high temperatures, and able to contain hydroxide ions within its structure. It has been found in shocked chondritic meteorites replacing *olivine* as a consequence of shock *metamorphism*.

Sedimentary rock: A rock formed by the deposition of sediment by a geologic process.

Serpentine: A common group of rock-forming hydrous magnesium iron *phyllosilicates* resulting from the hydrothermal alteration of ferromagnesian *silicates*, and with general formula $(Mg, Fe)_3Si_2O_5(OH)_4$, although they may contain minor amounts of elements such as Mn or Ni.

Siderite: A *carbonate* of the group of rhombohedral *carbonates* with formula $FeCO_3$.

Silica: The chemically resistant dioxide of silicon that is omnipresent in achondritic meteorites and has the general formula SiO_2.

Silicate: Compound containing anionic silicon, usually the anion SiO_4^{4-}. They constitute most of the crust of terrestrial planets, rocky moons and asteroids.

Spinel: A group of minerals of general formulation XY_2O_4, with X and Y being typically (but not always) atoms with charges +2 and +3, respectively. X and Y can also be the same metal with different valences, like in *magnetite*. The name *spinel* can also refer to the magnesium aluminium member of the *spinel* group of minerals, with formula $MgAl_2O_4$.

Subhedral: A mineral grain that is bounded by its own well-formed faces but also by surfaces formed against preexisting grains by *crystallization* or *recrystallization*.

Sulfate: A salt of sulfuric acid (H_2SO_4) characterized by the *sulfate* radical SO_4^{2-}, and that can be hydrous or *anhydrous*.

Sulfide: A compound formed with the inorganic anion of sulfur S^{2-}.

Taenite: An alloy of iron and nickel (NiFe) only found on meteorites, with a proportion of iron-nickel between 80-20 and 35-65. Although it is some times intermixed with *kamacite*, *taenit*e is the major constituent of iron meteorites.

Talc: A metamorphic magnesium *phyllosilicate* with formula $Mg_3Si_4O_{10}(OH)_2$, and formed in the presence of water or carbon dioxide.

Troilite: An iron sulfide mineral with formula FeS, rarely found on Earth but abundant on meteorites. Is the Fe-rich endmember of the *pyrrhotite* group.

T Tauri star: Star in the pre-main-sequence phase of stellar evolution, contracting towards the main sequence until nuclear fusion begins. They have intense and variable X-ray and radio emissions and many have very powerful stellar winds.

Volatiles: Chemical elements exhibiting low boiling points.

Wollastonite (Wo, for short): A calcium *silicate* mineral with general formula $CaSiO_3$, (although may contain small amounts of Fe, Mg and Mn substituting Ca) generally formed under high temperature and pressure. It is structurally different from *pyroxene* but chemically similar, and sometimes they are associated to the point that in the composition of a specific *pyroxene* the molar percentatges of *wollastonite* is included.

Young's modulus: A measure of the rigidity and flexibility of a solid material, also known as elastic modulus. It defines the relationship between applied force and deformation of a material, in such a way that a high *Young's modulus* implies high rigidity.